REACTOR MATERIALS

A Quarterly Technical Progress Review

Prepared for DIVISION OF TECHNICAL INFORMATION, U. S. ATOMIC ENERGY COMMISSION,
by BATTELLE MEMORIAL INSTITUTE

ST. LOUIS PUBLIC LIBRARY
FEB 19 1968
APPLIED SCIENCE DEPT.

Winter 1967-1968

● VOLUME 10

● NUMBER 4

TECHNICAL PROGRESS REVIEWS

The United States Atomic Energy Commission publishes the Technical Progress Reviews to meet the needs of industry and government for concise summaries of current nuclear developments. Each journal digests and evaluates the latest findings in a specific area of nuclear technology and science. *Nuclear Safety* is a bimonthly journal; the other three are quarterly journals.

Isotopes and Radiation Technology
P. S. Baker, A. F. Rupp, and Associates
Isotopes Information Center, Oak Ridge National Laboratory

Nuclear Safety
Wm. B. Cottrell, W. H. Jordan, J. P. Blakely, and Associates
Nuclear Safety Information Center, Oak Ridge National Laboratory

Reactor and Fuel-Processing Technology
Argonne National Laboratory

Reactor Materials
E. M. Simons and Associates
Battelle Memorial Insti'ute

All are available from the U. S. Government Printing Office. See the back cover for ordering instructions.

The views expressed in this publication do not necessarily represent those of the United States Atomic Energy Commission, its divisions or offices, or of any Commission advisory committee or contractor.

Availability of Reports Cited in This Review

United States Atomic Energy Commission (USAEC) reports are available at USAEC depository libraries and are sold by the Clearinghouse for Federal Scientific and Technical Information (CFSTI), National Bureau of Standards, U. S. Department of Commerce, 5285 Port Royal Road, Springfield, Va. 22151. All reports sold by CFSTI are $3.00 for printed copy and $0.65 for microfiche. Each separately bound part of a report is priced as a separate report. Some reports may not be available because of their preliminary nature; however, the information contained in them will generally be found in later progress or topical reports on the subject.

Other U. S. Government agency reports identified in this journal generally are available from CFSTI.

Private-organization reports should be requested from the originator.

United Kingdom Atomic Energy Authority (UKAEA) and Atomic Energy of Canada Limited (AECL) reports are available at USAEC depository libraries. UKAEA reports are sold by Her Majesty's Stationery Office, London; AECL reports are sold by the Technical Information Officer, Atomic Energy of Canada Limited, Chalk River, Ontario, Canada. UKAEA and AECL reports issued after March 1, 1967, are sold by CFSTI to purchasers in the United States and its territories.

Contents

Reactor Materials

Vol. 10, No. 4, Winter 1967–1968

Fuel and Fertile Materials (Section I)

Uranium Metal and Alloys . . . 203
Plutonium . . . 205
Thorium . . . 208
Metal–Ceramic Fuels . . . 208
Uranium and Thorium Oxides . . . 209
Carbide and Nitride Fuels . . . 209
Fuel–Water Reactions . . . 211
Basic Studies of Irradiation Effects in Fuel Materials . . . 212
References . . . 215

Moderator and Control Materials (Section II)

Graphite . . . 217
Beryllium and Beryllium Alloys . . . 218
Beryllium Oxide . . . 220
Solid Hydrides . . . 220
Metallic Poison Materials . . . 221
Dispersion and Nonmetallic Poison Materials . . . 222
References . . . 223

Cladding and Structural Materials (Section III)

Corrosion by Aqueous and Gaseous Media . . . 225
Corrosion by Nonaqueous Liquids . . . 228
Metal–Water Reactions . . . 230
Radiation Effects in Structural Materials . . . 232
Metallurgy of Refractory Metals . . . 236
Metallurgy of Common Cladding and Structural Materials . . . 244
Nonfuel Refractories . . . 249
Concrete . . . 252
Ceramic Technology . . . 252
References . . . 252

Special Fabrication Techniques (Section IV)

Cast and Wrought Materials . . . 257
Powder-Metallurgy Materials . . . 259
Pressure Bonding . . . 260
Plating . . . 260
Explosion Forming . . . 261
Welding and Brazing . . . 262
Nondestructive Testing . . . 264
References . . . 265

Index

Volume 10 . . . 267

Reactor Materials

is one of a series of technical progress reviews broadly covering the field of nuclear science and technology. Under the auspices of the USAEC Division of Technical Information, *Reactor Materials* is prepared by Battelle personnel from worldwide literature. It covers properties, behavior, and fabrication processes of materials applicable to nuclear reactor components and associated equipment.

The reader will recognize that the scope of this Review is too broad to permit detailed coverage of every topic. Rather, the authors and editors attempt to combine the highlights of significant new developments into an information summary of current research for both management and the technical specialist. As a rule, enough of the results are presented to define the research and summarize the findings. For readers desiring more information on any particular topic, a complete set of references is provided at the end of each section.

Each quarter a number of bibliographies, monographs, and books appear on subjects within the scope of *Reactor Materials*. Although the main purpose of this Review is to call attention to findings that are new and significant, such publications are noted in the text because they often represent excellent compilations of available information on important materials topics.

E. M. SIMONS
S. W. POREMBKA, JR.
D. L. KELLER

Battelle Memorial Institute

Issued quarterly by the U. S. Atomic Energy Commission. Use of funds for printing this publication approved by the Director of the Bureau of the Budget on July 8, 1966.

Section I

Reactor Materials

Fuel and Fertile Materials

Uranium Metal and Alloys

Unalloyed Uranium

The Polish[1] have studied the interdiffusion of uranium and copper at 510 to 910°C and have noted the effect of uranium crystal structure on the growth of the UCu_5 phase. Formation of UCu_5 proceeded according to the volume diffusion law $x^2 = kt$, where x is the thickness of the diffusion layer, k is a constant, and t is time. The constant k varied with temperature according to $k = k_0 \exp(-Q/RT)$, where Q is the activation energy of diffusion. The following values of k_0 and Q were obtained for the formation of UCu_5 from the three allotropic forms of uranium.

Uranium form	Temp., °C	k_0, cm²/hr	Q, cal/gram atom
α	<667	1.1×10^{-1}	26,000
β	667–770	1.2×10^{-2}	20,000
γ	>770	5.0×10^{-2}	21,000

Nuclear Metals[2] has investigated the extrusion of uranium at high alpha-phase temperatures. They found that extrusion conditions can be selected so that extruded uranium rod transforms to the beta phase as it leaves the die and thereby acquires a structure that is ordinarily obtained by a separate postextrusion heat-treatment. This beta structure may be present throughout the rod or it may constitute a core surrounded by a rim of fine-grained material that has not transformed into the beta phase. This rim has a preferred orientation and also very fine grains; the latter may help minimize in-pile bumping of the surface by the coarse core grains. The thickness of the fine-grained rim can be controlled through cooling of the rim of the extrusion billet (through contact with the extrusion tools). The beta-treated structure achieved directly by extrusion presumably would behave in an isotropic manner under irradiation.

The oxidation of beta uranium in CO_2 was studied by the British.[3] The oxide on the samples was cracked and oxidation was controlled by oxygen diffusion through a thin layer of UO_2. Self-heating occurred at ≤750°C, leading to rapid oxidation rates between 750 and 850°C. Between 900 and 1000°C the oxide was more compact; consequently, rates were not excessively high and self-heating was hardly significant. Around 700°C, carbon in the oxide was predominantly located near cracks, but as the temperature increased, the distribution became more uniform and high mobility led to the formation of multicomponent reaction-product layers.

A nonaqueous bath for electropolishing uranium has been developed by Rocky Flats.[4] The bath consists of 1,2-ethanediol saturated with NaH_2PO_2. The effects of water content, pH, temperature, and salt concentration on the electropolishing procedure were studied. Surface roughness was reduced to about 60% of the original value.

A study on the sintering mechanisms of uranium powder has been published by the French.[5] The observed behavior was related to the alpha, beta, and gamma phases.

Alpha-Phase Uranium Alloys

Hot hardness at 300 and 400°C and recrystallization of dilute uranium alloys were studied by Battelle–Northwest.[6] Ternary, quaternary, and quinternary alloys of uranium containing small additions of approximately 1000 ppm or less of Fe, Al, Si, and C and 0.05 to 2.0 wt.% Mo, Zr, or Nb were examined. It was concluded that Meyer hardness values for most of the alloys decrease markedly with an increase in test temperature from 300 to 400°C. It is possible that small molybdenum additions to alloys containing Fe, Al, Si, and C reduce this effect.

Gamma quenching produces a higher alloy hardness than does beta quenching. The difference in hardness, however, is quite small and may be due to the more rapid cooling rate experienced by the gamma-quenched alloys. It appears that gamma heat-treating produces a finer grain size and a smaller concentration of second-phase particles than that obtained by beta heat-treating. This is evidenced by a difference in recrystallization temperatures between gamma- and beta-heat-treated samples of the same alloy. There is some indication that the recrystallization temperature of uranium is affected more by the presence of silicon than by iron, aluminum, or carbon. However, carbon additions do have a noticeable effect on recrystallization behavior. One result of the study indicates that as the amount of silicon plus carbon is increased the recrystallization temperature of uranium decreases.

The French[7] have investigated the grain refinement and mechanical properties of U–0.10 to 0.25 wt.% V alloys. The 0.20 wt.% vanadium alloy was found to have a fine, as-cast grain structure. The mechanical

characteristics of this alloy were determined at room temperature. Italian[8] studies have concerned the metastable phases in U–1 to 5 wt.% Nb alloys.

Gamma-Phase Uranium Alloys

The transformations and structures in high-uranium alloys of the U–Re system were examined by workers at Iowa State University.[9] Figure I-1 shows the effect of cooling rate and quenching temperature on the crystal structure of these alloys. The metastable transition states observed were: orthorhombic α', monoclinic α'', and tetragonal γ°. The relation between metastability in U–Re alloys and other uranium systems in which metastable states are observed was discussed. Also obtained was a comparison of grain sizes (Fig. I-2) and of hardness values after various thermal treatments (Fig. I-3).

The beta-to-alpha transformation in the U–Re system was found to proceed via an isothermal martensitic reaction or by a sluggish nucleation and growth process. The delta (U_2Re) phase forms by a sluggish peritectoid reaction. A single-phase alloy of stoichiometric composition was obtained by a 6-month heat-treatment. Evidence presented indicates that a delta-prime transition exists which is intermediate between the ordered γ_b° tetragonal phase and the stable delta phase. The effect of aging treatments on hardness and structure of a metastable gamma-quenched U–10 wt.% Re alloy is given in Fig. I-4.

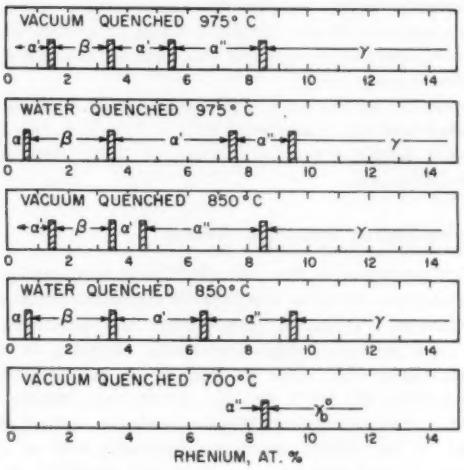

Fig. I-1 Effect of cooling rate and quenching temperature on the crystal structure produced in the U–Re system.[9]

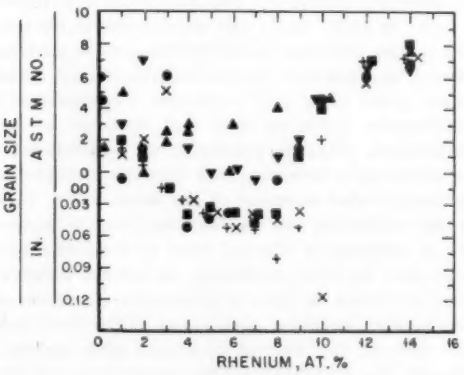

Fig. I-2 Comparison of grain-size measurements after various thermal treatments.[9] ×, water quenched 975°C; +, vacuum quenched 975°C; ●, water quenched 850°C; ■, vacuum quenched 950°C; ▲, vacuum quenched 662°C; ▼, cooled 25°C/hr from 825°C.

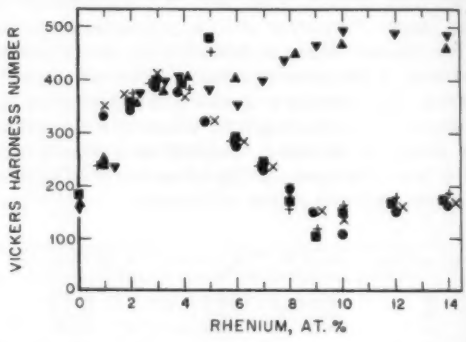

Fig. I-3 Comparison of hardness values after various thermal treatments.[9] ×, water quenched 975°C; +, vacuum quenched 975°C; ●, water quenched 850°C; ■, vacuum quenched 850°C; ▲, vacuum quenched 662°C; ▼, cooled 25°C/hr from 825°C.

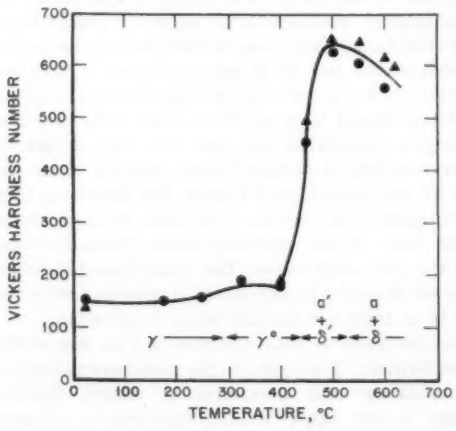

Fig. I-4 Hardness and structural changes accompanying the heat-treating of the 10 at.% rhenium retained-gamma alloy (vacuum quenched 850°C) after 1 hr at temperatures shown.[11] The hardness changes for the 10 at.% rhenium alloy water quenched from 975°C are also shown. ●, vacuum quenched 850°C; ▲, water quenched 975°C.

General

A new section of the continuing bibliography, "Radiation Effects on Solid, Uranium-Based Nuclear Fuel Materials,"[10] has been compiled. (M. S. Farkas)

Plutonium

Plutonium Metal and Alloys

The rate of oxidation at 90°C of unalloyed plutonium over a number of desiccants can be significantly decreased only if the humidity is decreased[11] to less than 2%. Results of studies concerned with the solubility of C, Ta, W, and Re in liquid plutonium at 750 to 950°C showed that the mole fractions of the solute could be expressed by the equation

$$\log N_x = A + BT^{-1}$$

where N_x = solute mole fraction and T = °K. At 950°C the mole fractions of the solutes were 0.0447, 0.00352, 0.000379, and 0.0405 for C, Ta, W, and Re, respectively.

After considerable research in batch electrorefining of plutonium, Rocky Flats[12] has designed and built new production and research facilities. The production facilities have a capability of refining over 100 kg of plutonium per month and will employ the two-piece ceramic crucible and hinged-top cell designs developed at Rocky Flats.

Mound[13] has investigated the U–Pu–Zr system. Most of the data were obtained by differential thermal analysis. The solidus and liquidus contours of the plutonium-rich corner of the ternary system are shown in Fig. I-5. Note that the addition of zirconium increases the solidus and liquidus temperatures and at 15 wt.% zirconium the range between the liquidus and solidus temperature has increased to approximately 200°C.

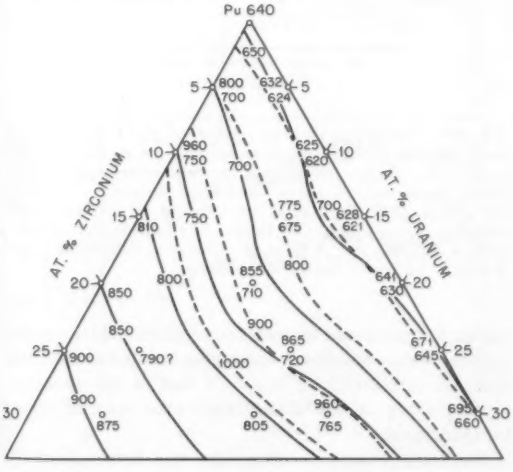

Fig. I-5 Liquidus and solidus temperature in the plutonium corner of the U–Pu–Zr system.[13] ——, solidus contours; – – –, liquidus contours.

Heat-capacity measurements at Mound on electrorefined plutonium yielded a value of 8.50 ± 0.27 cal/(g)(°C) for the ΔH of the delta-prime phase. Further interpretation of data indicates that the latent heat of the delta-to-delta-prime transformation required only 7 ± 3 cal/gram atom. Mound is also investigating the density of Pu–Ce alloys. Figure I-6 shows the densities of two Pu–Ce alloys as a function of temperature. The densities for both of the alloys were within 1% of the value calculated for the mixing of an ideal solution.

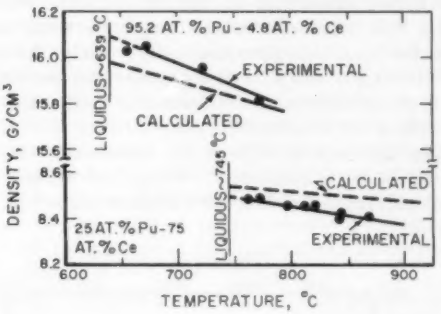

Fig. I-6 Liquid densities of two Pu–Ce alloys as a function of temperature.[13]

Argonne[14,15] has conducted preliminary studies of diffusion between U_2Ti and 304 stainless steel. A liquid phase is formed at 800°C. Replacing some of the uranium with plutonium lowers the temperature required for liquid-phase formation. Fuels of U–15 wt.% Pu–10 wt.% Zr have been prepared for irradiation to 10 at.% burnup with jacket temperatures up to 500°C. In addition, several Th–U and Th–U–Pu fuel alloys jacketed in V–20 wt.% Ti are being irradiated in CP-5 to determine the swelling behavior of the fuels, restraint characteristics of the jacket, and the maximum burnup attainable before jacket failure.

A very complete compilation of data sheets on ^{238}Pu has been published by Mound.[16] (N. E. Daniel)

Plutonium Compounds

Argonne has reported the only comprehensive data available on the sulfides and phosphides of plutonium.[17] The compounds PuS and PuP were prepared by reacting H_2S or PH_3 gas with partially decomposed plutonium hydride. Specimens of 90% theoretical density were obtained by sintering in argon at 1800 and 1900°C for PuS and PuP, respectively. Vacuum sintering was attempted but was discontinued because of

high weight losses observed. Microstructural examination and X-ray lattice measurements verified that the monosulfide and monophosphide can exist as substoichiometric compounds. Density, melting point, thermal expansion, microhardness, Seebeck coefficient, electrical resistivity, thermal diffusivity, heat capacity, and thermal conductivity were determined.

Knudsen-cell evaporation studies were performed by Argonne[15] on hypostoichiometric PuO_{2-x} with O/M ratios of 1.825 and 1.875. The data reported in Fig. I-7 indicate that the small compositional difference between the two specimens evaluated did not cause a significant difference in the rate of evaporation of each. The measured weight-loss rates were linear, and the final compositions were nearly the same (O/M = 1.820 and 1.794). It appears that the congruently evaporating composition has an O/M ratio close to 1.80 in the temperature range 2070 to 2360°K.

The Babcock & Wilcox Co. observed plutonium pickup of 20 to 23% Pu/(U + Pu) in both gel and fired UO_2 microspheres after two 10-min contact periods with a *p*H 0.3 Pu(IV) nitrate solution.[18] Alpha autoradiography of calcined 800-μ-diameter spheres showed uniform distribution of plutonium within each sphere.

The thermal diffusivity of $(U_{0.8}Pu_{0.2})O_{2.00}$ and $(U_{0.8}Pu_{0.2})O_{1.92}$ was measured to 1200°C by Battelle–Northwest[19] using a laser heat-pulse apparatus. The thermal conductivity of $(U_{0.8}Pu_{0.2})O_{2.00}$ was calculated (Figs. I-8 and I-9). The results indicate that anion vacancies produced by hydrogen reduction of the mixed oxides were effective scattering centers, reducing thermal diffusivity by one-half that of the stoichiometric oxide at 100°C and somewhat less at higher temperatures.

Similarly, thermal diffusivity was determined for $(U_{0.8}Pu_{0.2})N$ of 85% theoretical density.[19] X-ray diffraction analysis indicated the presence of 2 to 4% $(U,Pu)O_2$. The thermal conductivity was calculated

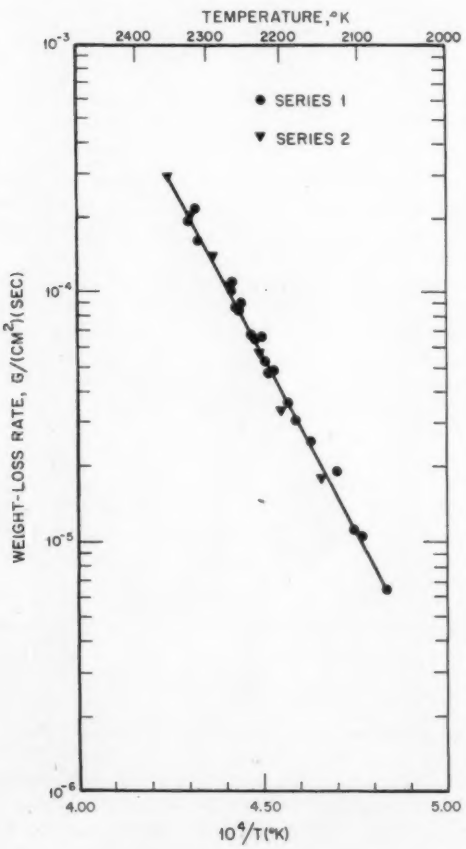

Fig. I-7 Weight losses per second of $PuO_{1.825}$ (Series 1) and $PuO_{1.875}$ (Series 2) in Knudsen-cell runs.[15]

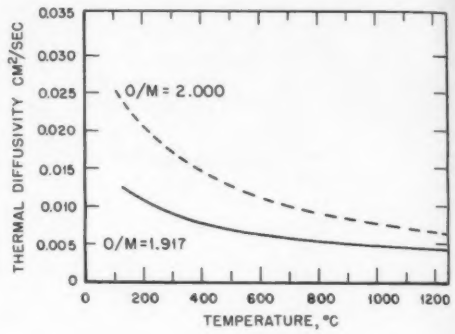

Fig. I-8 Thermal diffusivity–temperature relation[19] *of pneumatically impacted $(U_{0.8}Pu_{0.2})O_{2\pm x}$ for two oxygen-to-metal ratios (O/M).*

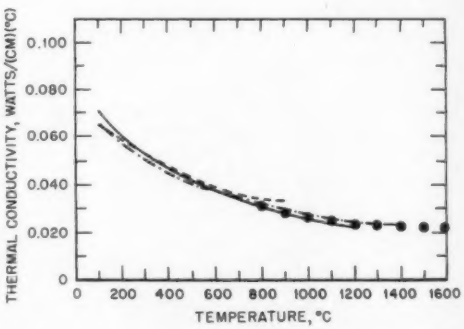

Fig. I-9 Calculated thermal conductivity of $(U_{0.8}Pu_{0.2})O_{2.00}$ as a function of temperature (other data shown for comparison).[19] ——, *$(U_{0.8}Pu_{0.2})O_{2.00}$ (Battelle–Northwest) pneumatic impacted, 96.1% of theoretical density;* – – –, *$(U_{0.8}Pu_{0.2})O_{2.00}$, (ETI, Karlsruhe) sintered, 96.4% of theoretical density;* —·—, *$UO_{2.00}$, Oak Ridge, 93.4% of theoretical density;* ●, *$(U_{0.8}Pu_{0.2})O_{2.00}$ (General Electric, Vallecitos), sintered, 93 to 96% of theoretical density.*

and corrected to 100% of the theoretical density (Figs. I-10 and I-11).

The reaction of uranium and plutonium carbides with residual nitrogen in a "pure" argon glove-box atmosphere has been investigated by the French.[20] Powdered and low-density UC was rapidly transformed into the nitride, but the reaction was slower with dense UC. PuC, even when powdered, was difficult to nitride. Materials were subjected to repeated grinding and sintering operations in "purified" argon which contained between 5000 and 50,000 ppm nitrogen.

The compatibility of 304 stainless steel with unstabilized hypostoichiometric $(U_{0.8}Pu_{0.2})C$, which contained 4.40 to 4.50 wt.% carbon, and hypostoichiometric (U,Pu)C stabilized with iron or $Cr_{23}C_6$ has been studied by Westinghouse.[21] Free uranium and plutonium were observed in the pellets which were prepared by grinding and sintering. In the iron-stabilized carbides, $(U,Pu)Fe_2$ and iron were observed; in the $Cr_{23}C_6$-stabilized fuel, $Cr_{23}C_6$ was observed. Compatibility couples of both unstabilized and iron-stabilized (U,Pu)C were helium bonded to 304 stainless steel and tested for 1000 hr at 650 and 800°C. Unstabilized, iron-stabilized, and $Cr_{23}C_6$-stabilized (U,Pu)C were sodium bonded and tested at 800°C for 1440 hr. No fuel–cladding interactions were observed in any of these couples when subjected to metallographic evaluation.

Electron-microscopic examination of vibrationally compacted $(U_{0.8}Pu_{0.2})C$ specimens irradiated to an approximate average burnup of 6.9 at.% was performed by Argonne.[14] Since the UC was not enriched, the PuC burnup approaches 35 at.%. Numerous fission-gas bubbles with an average diameter of 2 μ were present in the PuC phase. Spherical second-phase particles, generally <1 μ in diameter and assumed to be associated with solid fission products, were observed in the PuC. UC_2 platelets originally observed in the unirradiated UC phase disappeared in a zone approximately 6 μ wide where the UC was adjacent to the PuC. This phenomenon was believed to be due either to the effect of fission recoils from adjoining PuC or to diffusion of PuC into UC and altered phase equilibria.

Phase relations in the high-carbon portion of the U–Pu–C system are being investigated by Los Alamos using high-temperature differential thermal analysis (DTA), X-ray diffraction, and metallographic techniques.[22] Lattice parameters and transition temperatures are reported in Tables I-1 and I-2. There

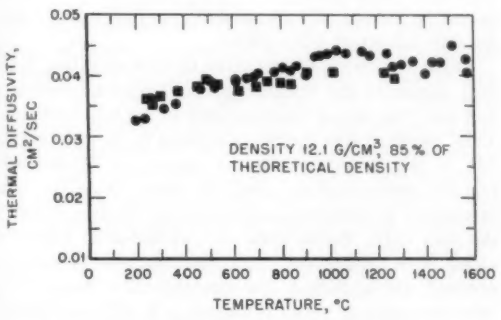

Fig. I-10 Thermal diffusivity of sintered $(U_{0.8}Pu_{0.2})N$ as a function of temperature.[19] ●, *temperature increasing;* ■, *temperature decreasing.*

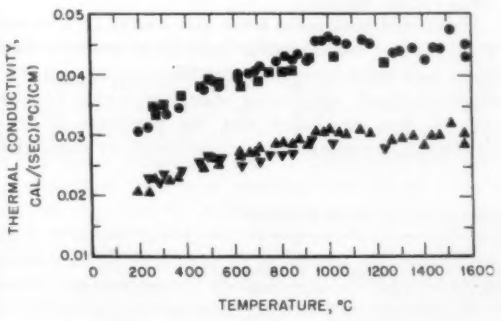

Fig. I-11 Thermal conductivity of $(U_{0.8}Pu_{0.2})N$ as calculated from thermal-diffusivity data (data also shown corrected to 100% theoretical density).[19] *85% theoretical density:* ▲, *heating;* ▼, *cooling. Corrected to 100% theoretical density:* ●, *heating;* ■, *cooling.*

Table I-1 LATTICE PARAMETERS IN THE M_2C_3 AND MC_2 SYSTEMS[22]

Bcc M_2C_3			Tetragonal MC_2		
	Lattice dimension, A			Lattice dimension, A	
Composition, mole % Pu_2C_3	>60 at. % C*	<60 at. % C†	Composition, mole % PuC_2	*a*	*c*
0	8.088		0	3.520	5.985
6	8.090		6	3.529	6.006
11	8.091	8.090	19	3.534	5.997
22	8.093		30	3.552	6.022
26		8.094	36	3.553	6.020
39	8.100		58	3.573	6.051
49	8.104	8.099	60	3.574	6.050
59	8.108		78	3.601	6.076
69	8.113	8.108	92	3.613	6.105
79	8.119		97	3.611	6.101
89	8.126		100	3.606	6.106
100	8.133	8.125			

*Samples annealed at 1700°C for 17 hr.
†Samples annealed at 1550°C for 17 hr.

appears to be solid solution between U_2C_3 (bcc) and Pu_2C_3 (bcc) over the entire range of composition. Apparently there is also complete solid solubility of the tetragonal PuC_2 and UC_2 structures. Attempts to produce cubic PuC_2 and cubic $(U,Pu)C_2$ were unsuccessful. The first transition observed by DTA and metallography was interpreted as the M_2C_3 + C/MC_2 transition, the second as melting of Pu_2C_3, and the

third as melting of MC_2. Apparently the first transition temperature was not strongly dependent on composition in the range of 10 to 80 mole % U_2C_3. The uniform rise in melting temperature of the MC_2 phase with increasing UC_2 concentration confirmed the solid solution with PuC_2 previously indicated by X-ray analysis.

Table I-2 TRANSITION TEMPERATURES OBSERVED BY DIFFERENTIAL THERMAL ANALYSIS[22]

Composition	Transition temperatures, °C		
	1st	2nd	3rd
$PuC_{1.56}$	1650	1980	
$PuC_{1.78}$	1650	1980	
$PuC_{2.0}$	1640	Absent	2210
$PuC_{2.3}$	1645	Absent	2220
PuC_4	1650	Absent	2230
PuC_9	1645	Absent	2230
$(U_{0.1}Pu_{0.9})C_3$	1690	Absent	2260
$(U_{0.25}Pu_{0.75})C_3$	1730	Absent	2300
$(U_{0.4}Pu_{0.6})C_3$	1740	Absent	2325
$(U_{0.5}Pu_{0.5})C_3$	1750	Absent	2345
$(U_{0.6}Pu_{0.4})C_3$	1750	Absent	2350
$(U_{0.75}Pu_{0.25})C_3$	1725	Absent	2420
$(U_{0.8}Pu_{0.2})C_3$	1720	Absent	2425

(D. F. Askey)

Thorium

Zircaloy-2-clad Th–2.5 wt.% U–1.0 wt.% Zr tubular fuel elements are being irradiated by Battelle–Northwest.[19] Accumulated exposures of 2500 to 17,700 Mwd/ton of fuel alloy with corresponding volume changes varying from 0.5 to 3.1% have been achieved. The rate of swelling is roughly 2% per 10,000 Mwd/ton, which is slightly greater than a value calculated by considering the conversion of ^{232}Th atoms to more-dense ^{233}U atoms and the conversion of ^{235}U atoms to less-dense fission-product atoms. Irradiation conditions include a surface temperature of 300°C and a maximum centerline temperature of 500°C.

Diffusion of ^{238}Th, ^{231}Pa, and ^{233}U in polycrystalline alpha thorium has been measured in the range 690 to 810°C by German investigators.[23] A technique employing a solid electrolyte was used to keep the surface of the specimens free of oxide. Alpha-spectrum degradation was employed as the nondestructive technique, and the diffusion coefficients as functions of temperature were found to be

$$D_{Th} = 3.95 \times 10^2 \exp(-71{,}600/RT) \text{ cm}^2/\text{sec}$$

$$D_{Pa} = 1.26 \times 10^2 \exp(-74{,}700/RT) \text{ cm}^2/\text{sec}$$

$$D_U = 2.21 \times 10^4 \exp(-74{,}300/RT) \text{ cm}^2/\text{sec}$$

Thorium self-diffusion follows the empirical rules for vacancy diffusion in fcc metals. (R. L. Martin)

Metal–Ceramic Fuels

Dispersion Fuels (Less Than 50 Vol.% Ceramic Phase)

Idaho Nuclear[24] has investigated the swelling of fuel plates containing dispersions of 37 wt.% UO_2–stainless steel. These plates consisted of a 0.005-in.-thick 347 stainless-steel cladding roll bonded to a 0.031-in.-thick dispersion core. The dispersion contained burnable poison of natural ZrB_2 particles and a low-density spherical UO_2 powder.

Table I-3 shows the relation of core swelling in the fuel plates to the burnup received during irradiation and the void space incorporated in the fuel particles. This swelling was further analyzed by calculating the $^4He + {}^7Li$ generated by the burnup of ^{10}B and subtracting the resulting swelling effect from the total measured to obtain an approximate swelling effect of the fuel only. These data are presented in Table I-4 along with values for core swelling due to fission-product accumulation for theoretically dense UO_2. This theoretical value is based on 6.38% core swelling for each 10^{21} fissions/cm³ of core. Since the measured fission-product swelling averages only approximately 40% of that for theoretically dense UO_2, it was concluded that the fabrication porosity within the fuel particles accommodates fission products and is beneficial to fuel stability.

Irradiated specimens were also heated in a furnace at increasing temperatures until they blistered. When these data were compared with the blistering of UO_2–stainless-steel specimens observed during irradiation, it was concluded that the presence of boron significantly reduced the temperature at which blis-

Table I-3 CORE SWELLING IN STAINLESS STEEL–UO_2 FUEL PLATES[24]

Plate	As-fabricated UO_2 fuel density, g/cm³	UO_2 void fraction, %	Average core burnup, 10^{20} fissions/cm³	Initial core volume, cm³	Measured ΔV, cm³	Measured core swelling, ($\Delta V/V \times 100$)
A-29-927	8.87	18.1	12.0	2.584	0.085	3.27
A-29-928	9.04	16.5	11.0	2.577	0.076	2.92
A-29-929	8.99	17.0	12.5	2.571	0.088	3.40
A-29-936	9.12	15.8	10.5	2.562	0.084	3.25
A-29-938	9.42	13.0	11.5	2.547	0.132	5.18
A-29-939	9.05	16.4	10.5	2.505	0.073	2.90

Table I-4 EFFECT OF ^{10}B ON CORE SWELLING[24]

Plate	Boron, mg	Swelling due to $^{7}Li + {}^{4}He$, cm^3	Measured swelling due to Li + He, %	Swelling due to ^{235}U fission products, %	Theoretically expected core swelling from dense UO_2, %	Theoretical swelling due to fission products, %
A-29-927	26.0	0.0092	10.8	2.93	7.54	38.9
A-29-928	26.0	0.0092	12.1	2.59	6.97	37.2
A-29-929	26.0	0.0092	10.4	3.06	7.85	39.0
A-29-936	41.0	0.0145	17.3	2.71	6.59	41.1
A-29-938	39.7	0.0140	10.6	4.63	7.34	63.1
A-29-939	1.3	0.005	0.6	2.90	6.59	44.0

tering occurred. For each 10 mg of natural boron burned up or 5.4 ml (at STP) of helium thus formed, the blister temperature is lowered by approximately 22°C. (D. E. Lozier)

Uranium and Thorium Oxides

Properties and Behavior

German investigators[25] have studied thermal diffusion of CeO_2 in UO_2 in a temperature gradient between 1400 and 2200°C. The CeO_2 concentrations of 3.7, 5.6, and 13.3 wt.% were used. It was found that CeO_2 migrates to the higher temperature region by thermal diffusion, with the concentration decreasing in the lower temperature region. The diffusion data for UO_2 containing 13.3 wt.% CeO_2 at 2050°C can be summarized in terms of the diffusion coefficient

$$D = 5.4 \times 10^{-8}\ cm^2/sec$$

and the thermal diffusion coefficient

$$D_t = 1.6 \times 10^{-10}\ cm^2/(sec)(°K)$$

The activation energy was found to be about 110 kcal/gram mole. (R. H. Barnes)

Preparation of Fuel Bodies

A "flame reactor" usually employed for the conversion of UF_6 to UF_4 is being utilized at Oak Ridge[26] for the direct conversion of UF_6 to UO_2. The apparatus, which utilizes the heat of reaction of hydrogen and fluorine, has been modified to include mixing UF_6, H_2, O_2, and F_2 at low pressure to produce submicron urania powders. Powders obtained to date consist of 60 wt.% UO_2, 37 wt.% U_3O_8, and 3 wt.% unknown contaminants. The process has the potential for reprocessing uranium fuels to fine uranium oxide powder at the rate of 5 kg/day.

Oak Ridge investigators[27] are also successfully extruding clays derived from UO_2 and ThO_2 sols. The most successful UO_2 material employed has been a 9.75*M* sol blended in methyl alcohol with 30 wt.% −325-mesh fired UO_2 powder. This mixture became plastic at a moisture content of approximately 12 wt.% and was easily extruded without cracking. Sol–gel ThO_2, ranging in diameter from 0.166 to 0.426 in., has also been extruded. Most of these extrusions were made with concentrated ThO_2 sols containing 1 to 37.5 wt.% fired ThO_2. The sintering behavior and microstructures of these materials were not discussed. (T. R. Wright)

Carbide and Nitride Fuels

Properties and Behavior

Uranium monocarbide reacts with small amounts of iridium and rhodium to form U_2IrC_2 and U_2RhC_2, respectively. Reaction of UC with more than the stoichiometric amount of iridium or rhodium required to form these ternary compounds causes the formation of graphite and the respective compounds UIr_3 and URh_3. Uranium monocarbide and ThC also react with an excess of gold to form UAu_3 and graphite or $ThAu_3$ and graphite, respectively. At reduced pressures, UN reacts with gold to form UAu_3 and nitrogen gas. At atmospheric pressure, layers of U_2N_3 and UAu_3 would be expected between UN and gold, but only U_2N_3 and gold were found in the products by X-ray examination.[28]

Venard has prepared a critical review of the literature with reference to the use of UC clad with an SAP aluminum alloy in an organic-cooled heavy-water-moderated reactor.[29] Data from the literature are presented on plots of the logarithm of the time required for an unacceptable amount of reaction to occur vs. temperature. This type of plot assumes that the reaction observed occurs as the result of a rate process such as diffusion rather than an interface process such as the breakdown of an oxide film. It is concluded that hypostoichiometric and stoichiometric UC are not suitable for use in contact with SAP aluminum for 10,000 hr at 500°C. On the other hand, it is suggested that hyperstoichiometric UC might be suitable for such use if the temperature of the interface is limited to 510°C.

Using a molten fluoride salt as an electrolyte, Satow[30] has measured cell voltages for the Th–C

system at temperatures from 720 to 950°C. From these results, the thermodynamic data shown in Table I-5 and Fig. I-12 have been calculated. The thermal-expansion coefficient of $ThC_{0.76}$ is 6.6×10^{-6}/°C from 830 to 950°C, whereas that of $ThC_{0.96}$ is 8.5×10^{-6}/°C from 700 to 950°C (Ref. 31). The free energies of formation at 1172°K of ThP, Th_3P_4, ThS, Th_7S_{12}, and ThS_2 are −72, −58, −109, −96, and −88 kcal/gram atom of phosphorus or sulfur, respectively.[32]

Table I-5 PARTIAL MOLAR FREE ENERGIES, ENTROPIES, AND ENTHALPIES OF Th–C ALLOYS[30]

C/Th ratio	$-\Delta\bar{G}_{Th}$, kcal/mole			$-\Delta\bar{S}_{Th}$, cal/(mole)(°K)	$-\Delta\bar{H}_{Th}$, kcal/mole
	1000°K	1100°K	1200°K		
2.43	29.4	28.8	28.2	5.9	35.2
2.10	29.3	28.8	28.2	5.9	35.2
1.92	28.4	27.8	27.2	6.4	34.9
1.85	26.9	26.2	25.5	6.7	33.6
1.77	25.0	24.3	23.6	7.1	32.1
1.60	23.1	22.4	21.7	7.3	30.4
1.35	23.4	22.6	21.9	7.4	30.7
1.02	23.5	22.7	22.0	7.4	30.8
0.92	22.7	22.0	21.2	7.0	29.7
0.87	19.3	18.8	18.3	5.2	24.5
0.83	14.4	14.0	13.7	3.7	18.1
0.79	10.2	9.9	9.7	2.5	12.7
0.76	7.0	6.9	6.7	1.1	8.1
0.72	2.6	2.6	2.5	0.6	3.3
0.60	0.26	0.26	0.25		
0.35	0.19	0.18	0.17		
0.13	0.22	0.21	0.21		

A series of refractory fuels is being irradiated at extremely high specific power levels (33 kw/ft). A pellet of hyperstoichiometric, cast UC, 4 in. long and 0.3 in. in diameter, clad in 20 mils of 348 stainless steel sustained a burnup of 2.3×10^{20} fissions/cm^3 with no measurable dimensional changes and a gas release of 0.55%. The fuel was gas bonded to the cladding, which had an estimated surface temperature of 490 to 570°C (Ref. 33).

At somewhat lower, although still high, power levels (19 to 30 kw/ft), at higher temperatures (570 to 680°C), and after burnups of 5.6 to 8.9×10^{20} fissions/cm^3, Argonne has recovered three specimens of UC–20% PuC essentially intact.[34] Two 80% dense specimens 0.3 in. in diameter and clad in 25-mil-thick stainless steel showed insignificant dimensional changes. The third specimen was 86% dense and was clad in 24-mil-thick vanadium. This specimen received the highest exposure at the highest power level and temperature and showed a density decrease of 1.5%.

Wullaert et al.[35] have prepared a critical review of the literature with reference to the irradiation behavior of UC and UC–PuC. Swelling and gas-release data are presented as a function of temperature, burnup, composition, and initial density. It was concluded that at centerline temperatures below 1000°C a UC specimen containing 4.8 to 5.0 wt.% carbon would, on the average, grow only about 0.5 vol.% per 10^{20} fissions/cm^3. Below 1000°C, growth was a linear function of burnup to at least 11×10^{20} fissions/cm^3. Alloys containing less than 4.8 wt.% carbon showed appreciably higher swelling rates than those containing more than 4.8 wt.% carbon. Up to 10% porosity produced no significant trend with regard to either the swelling or gas-release behavior of the carbides.

It has been noted that, when bulk UN is allowed to evaporate freely in a vacuum at temperatures above 1800°C, it decomposes to nitrogen and liquid uranium metal.[36] However, in a vacuum below 1800°C, a kinetic barrier to the free evaporation of nitrogen develops. The partial pressure of nitrogen gas measured under these conditions is nearly two orders of magnitude lower than it should be on the basis of nitrogen pressures measured under equilibrium (non-kinetic) conditions. This implies an "evaporation coefficient" of about 0.01. The kinetic barrier is believed to be related to the necessity to form nitrogen molecules from nitrogen atoms on the surface of UN. This kinetic barrier causes the vapors over UN below 1800°C to contain almost twice as many moles of uranium as nitrogen, so that liquid uranium forms very slowly or not at all in the UN. This "congruent" evaporation is apparently a kinetic rather than an equilibrium process.

Gradients of fission-gas-bubble sizes from axial center to surface and from midplane to end in cylindrical samples of both single-crystal and polycrystalline UN have been observed by workers at Battelle–Columbus.[37] These gradients were attributed to the radial and axial temperature profiles of the specimens during irradiation and to the temperature dependence of swelling. At a section near the end of

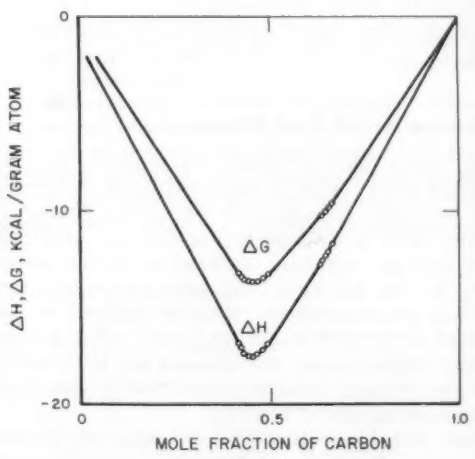

Fig. I-12 Free energy (ΔG) and heat of formation (ΔH) of the Th–C system at 1100°K (Ref. 30).

a single crystal, the bubble volume varied from 5% near the surface to 10% at the axis. At a section near the longitudinal midplane of this crystal, the bubble volume varied from 10% near the surface to 35% at the axis. The temperatures of the claddings were 500 to 750°C, and burnups were 5 to 6 at.%. (W. Chubb)

Preparation and Fabrication

Russell has reviewed[38] studies at Harwell and other sites concerning the fabrication of UC and UN by sintering. The oxidation of these materials in protective atmospheres is described, and its deleterious effect on the sintering behavior and composition changes that occur during sintering are considered.

British patents were recently awarded for the preparation and fabrication of carbide, nitride, and carbonitride fuels. A process for the preparation of UC and UC–ZrC, which employs the carbothermic reduction of the oxides in either a vacuum or flowing atmosphere of inert gas, is the subject of one patent.[39] The second patent[40] describes a process for the production of UN or UC–UN sintered bodies. The requirements for the starting powders are:

1. Particle size 0.1 to 5.0 μ
2. Nitrogen or nitrogen + carbon content 48 to 52 at.%
3. Oxygen content below 1 wt.%

The powder is compacted into pellets, and the pellets are sintered in an inert atmosphere containing less than 10 ppm by weight of oxygen and less than 10 ppm by weight of water vapor. This process is also considered applicable to mixtures of PuN, PuC, ThN, and/or ThC with the uranium carbides and nitrides.

A process for the production of spherical UC_2 particles containing a high volume dilution of porosity is being investigated at General Atomic.[41] The process uses spheroidal UO_2–C particles. Results indicate that complete conversion to UC_2 is possible, although the effects of binder, residual carbon content, and conversion temperature on porosity remain to be defined.

The feasibility of producing UN by chemical vapor-deposition techniques was demonstrated at Oak Ridge.[42] Employing lithium vapor as a reducing agent, the reaction

$$UF_6(g) + 6Li(g) \rightarrow U(s) + 6LiF(g)$$

produces a very fine uranium powder that reacts with the nitrogen injected into the reaction zone, which is maintained at 900 to 1200°C, to form UN. Also found in the reaction product, however, were small amounts of alpha uranium, UO_2, LiF, $Li_{13}UF_7$, $Li_7U_6F_{31}$, and an unknown phase. The potential of the process remains to be developed since no attempts at optimization were made in this study. (J. T. Lowder)

Fuel–Water Reactions

General Electric[43] has continued investigations into the oxidation of UO_2 by steam. A thermobalance was employed to determine gravimetrically the extent of reaction between 1100 and 1500°C. Solid cylinders of UO_2 ($UO_{2.004}$ by chemical analyses) sintered at 1700°C for 5 hr in hydrogen were used in these tests. Experiments were performed in steam flowing at a rate of 300 STD ml/min. The oxygen partial pressure in the steam was calculated to be a maximum of 5×10^{-6} atm and was considered to have negligible effects upon the O/U ratio at the experimental temperatures. Prior to entering the steam, the test specimens (1.27 cm in diameter and in length) were brought to temperature using argon as a sweep gas to preclude oxidation of the samples. A similar procedure was employed during cooling.

The results of the experiments indicated that the samples had gained weight at an initially high rate (early time data) followed by a lower rate, in approximate agreement with parabolic kinetics. For long times, there was a leveling off in the curve for the weight gain vs. time curve as a limiting composition was reached. From these measurements parabolic rate constants were determined. These calculated parabolic rate constants are shown in Table I-6 and are plotted in the form of an Arrhenius plot

Table I-6 RESULTS OF UO_2 ($UO_{2.004}$) REACTION WITH STEAM[43]

Temp., °C	Test time, sec	Initial weight, g	Weight gain,* g	Parabolic rate, $mg^2(O_2)/(cm^4)(sec)$
1500	1,140	16.4467	0.0876	0.120
1500	2,400	16.2287	0.1009	0.0760
1500	4,560	16.1417	0.1226	0.0587
1400	5,700	16.0962	0.1206	0.0464
1400	6,900	16.3291	0.1029	0.0274
1200	7,020	20.6454	0.0649	0.00773
1200	10,800	20.5758	0.0735	0.00661
1100	10,500	16.9978	0.0331	0.00175
1100	10,860	16.5417	0.0187	0.00056

*From analytical balance weighings.

(log k vs. $1/T$) in Fig. I-13. As seen in Fig. I-13, considerable scatter existed in the data (a factor of 3 in some cases) when experiments were duplicated. It was concluded that the oxidation of UO_2 by steam can be represented by the equation (the solid line in Fig. I-13).

$$W^2/t = 1.64 \times 10^5 \exp \frac{-50,800 \pm 4800}{RT}$$

where W = weight gain, mg of oxygen/cm^2 of area
t = time, sec
R = gas constant, cal/(mole)(°K)
T = absolute temperature, °K

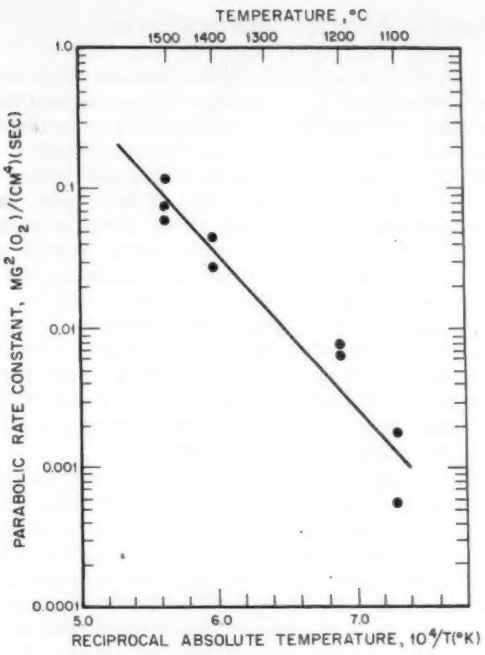

Fig. I-13 Oxidation of UO_2 by steam.[43]

(J. M. Genco)

Basic Studies of Irradiation Effects in Fuel Materials

Metals

The swelling of metallic uranium caused by the coalescence of fission-gas bubbles and by crack formation has been examined by the Japanese.[44] From the experimental results reported, it appears that, at temperatures near the melting point, gas bubbles coalesce through both surface-diffusion migration and the growth of larger bubbles due to the resolution of smaller bubbles. At lower temperatures, only the surface-diffusion mechanism is operative. It was concluded that the largest contribution to the swelling of uranium was probably the migration of grain boundaries, which controls the migration of bubbles. The conditions for crack formation in irradiated uranium were discussed along with various experiments that dealt with the swelling of uranium caused by conditions other than irradiation.

A study has been conducted at Battelle–Columbus[45] on the collisional coalescence of spherical gas-filled pores moving through a solid matrix. Both random and biased migration were considered under circumstances in which the migration mechanism was the diffusion of matrix atoms around the surface of the pores. The results were compared with the computerized studies of collisional coalescence conducted by Gruber.[46] Possible applications of similar analytical techniques to the case in which vapor transport, rather than surface diffusion, makes the dominant contribution to bubble mobility were also considered.

Fission-product behavior and characteristics have been investigated at Oak Ridge[47] to develop mathematical models that will predict the extent of fission-product release for a specific set of conditions. A model has been developed for predicting the release of some fission products from molten fuels. This model is based on the theories of Fonda[48] and Langmuir[49] and can be applied to the release of fission products from reactor fuels if it is assumed that in the presence of a cover gas a boundary layer exists around the fuel and that diffusion through this boundary layer is the rate-controlling step. The model relates the following variables to the amount of fission products released: (1) composition and pressure of the cover gas, (2) temperature, surface area, and amount of molten fuel, (3) the time that the fuel is in the molten state, and (4) the chemical form of the fission product. The model also can be used to characterize fuel vaporization and fission-product release from UO_2 below the UO_2 melting point. The model has been tested with data from several sources and satisfactorily explains the observed behavior of fission products and fuel.

A study of the vaporization of fission products from molten nuclear materials is being conducted at Brookhaven.[50] The objective of this work is to develop a model for predicting fission-product release as a function of time, temperature, liquid depth, and fission-product solubility in the condensed phase. Previous studies of the release of fission-product iodine from molten uranium have demonstrated that the release rate is a function of the liquid depth. A series of experiments with irradiated uranium showed further that gas-phase diffusion is not the rate-controlling process in the vaporization of the highly volatile fission-product iodine. The rate of iodine release from molten-uranium pools (0.91 cm in diameter by various thicknesses) was examined in the range 1350 to 1450°C at a gas flow rate of 200 cm^3/min. The results are illustrated in Fig. I-14, in which the percentage of iodine released is plotted as a function of time. Comparison of the curves shows a large difference in time to obtain a given percentage release. The spread is believed to be due to mixing in the liquid, which is induced by a combination of thermal convection and induction heating of the sample. It was concluded that the release of fission-product iodine from molten uranium is controlled by diffusion in the liquid phase.

An IBM-7090 computer program, FIZDIZ, written in FORTRAN-IV, has been developed by the British[51]

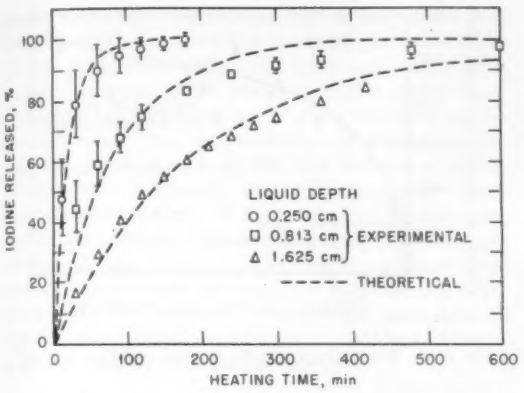

Fig. I-14. Release of fission-product iodine from molten uranium.[50]

to be used as an aid in calculating the release of fission-gas activity from a punctured fuel element. With this program it is possible to calculate the rate of escape of fission-gas activity from a hole in a fuel can as a fraction of the total fission-gas activity released from the fuel into the space between the fuel and the fuel can. However, the absolute release rate of fission-gas activity from the hole cannot be calculated unless the rate of release into the fuel/fuel-can interspace is known. This program contains a facility that allows such a calculation to be inserted as a subroutine, if desired, and has been written to apply to the diffusion of long-lived fission gases, the diffusion lengths of which are of the same order or longer than the linear dimensions of the fuel element. The fission-gas fraction can be calculated for many combinations of hole dimensions, bar dimensions, fission-gas diffusion coefficients, and radioactive-decay constants.

A one-dimensional, multigroup transport burnup code, DTF-BURN, has been developed at Los Alamos.[52] The code computes the neutron-flux distribution as a discrete-ordinates solution of the Boltzmann transport equation at the beginning of each specified time step. This calculated flux distribution is then used to determine the change in nuclide concentrations during the time interval. Nuclides considered in the burnup routine are ^{235}U, ^{236}U, ^{238}U, ^{239}Np, ^{239}Pu, ^{240}Pu, ^{241}Pu, ^{242}Pu, and FP, a pseudo fission-product pair. The program was designed especially for a survey of life-history analyses of plutonium-fueled fast-reactor systems. DTF-BURN is written in FORTRAN-IV and employs variable dimensioning so that a problem with any number of neutron-energy groups and spatial intervals may be computed provided the available core storage is not exceeded.

A two-parameter analysis of the charged particles' population associated with the thermal-neutron fission of ^{235}U has been performed in Poland[53] by means of a semiconductor telescope. The presence of protons, deuterons, tritons, and ^{6}He particles in the fission phenomenon was established. Events were also observed which were attributed to the passage of heavier particles such as ^{8}He, lithium, and beryllium nuclei through the telescope counter.

Ceramics

The effect of small amounts of additives of different valence (Y_2O_3 or Nb_2O_5) on xenon migration and on radiation-induced trapping in ThO_2 has been studied by Matzke.[54] The ThO_2 was chosen because it has the same lattice structure as UO_2. Also, the valence of Th^{4+} is unlikely to change in order to compensate for the different valence of the impurity. The diffusion of ^{233}U was measured at 1400 and 1550°C in both doped and undoped ThO_2. More rapid diffusion in Nb_2O_5-doped ThO_2 and less rapid diffusion in Y_2O_3-doped ThO_2 were observed, indicating that doping was effective in producing extrinsic behavior. Xenon was introduced into the specimens by ion bombardment. At low bombardment dose, doping did not appreciably affect the release, thus indicating that xenon does not diffuse via single vacancies on either sublattice. Diffusion via interstitial sites or in small vacancy clusters of constant size remained as alternatives. Temporary trapping (retarded gas release) was observed to be dependent upon impurities at higher doses; this retardation was decreased by additions of Nb_2O_5 but was increased by additions of Y_2O_3.

The results of studies on the diffusion of rare gases in solids have been summarized by Felix.[55] These results were obtained since a prior report[56] was submitted to the Third International Conference on the Peaceful Uses of Atomic Energy, held in Geneva in 1964. Among the various materials considered were UO_2, UC, and ThO_2. Observed deviations from ideal diffusion kinetics, due to vaporization of the sample, and the effects of rare-gas traps were discussed in detail. It was concluded that rare-gas traps can be effective even at very low irradiation exposure, especially if the radiation damage due to fission causes self-capture. A list of references concerning diffusion measurements on UO_2 and UC is given in the appendix to this report.

The dragging of gas bubbles by grain boundaries in irradiated arc-cast UC (4.7 wt.% carbon) has been observed by MacDonald.[57] A string of small bubbles outlined the UC grain boundary, whereas larger bubbles marked the boundary's earlier positions. Data from these observations were used in conjunction with the theoretical analysis of Speight and Greenwood[58] to obtain an activation energy of about 1.5 ev for the surface diffusion of the more slowly moving species in U–4.7 wt.% C.

High-resolution gamma spectrometry has been performed in Sweden[59] on slices of irradiated UO_2 pellets using a lithium-drifted germanium detector. It was shown that this technique is useful for studying the migrational benavior of solid fission products. Approximate correlation of the fission-product distribution curves across the specimen diameters with the metallographic structure of the specimens was obtained.

The behavior of fission products in pneumatically impacted UO_2-PuO_2 fuels has been studied at Battelle–Northwest.[60] It was found that fission products migrate to preferred locations at the higher fuel temperatures. Of the fission products studied, Zr–^{95}Nb, ^{90}Sr, and Ce–^{144}Pr migrated the least, whereas ^{137}Cs and ^{106}Ru migrated the most. Fission-gas-release values of about 90% were obtained for average volumetric fuel-rod temperatures of approximately 2200°C.

An electron-probe microanalyzer has been used by Jeffery[61] to examine white, rounded inclusions in UO_2 irradiated to 4.6 at.% burnup. Some solid fission products were found to be segregated and were usually identifiable with the inclusions, whereas others were detected in a homogeneous distribution throughout the UO_2 matrix. Three kinds of inclusions were found that contained molybdenum and/or barium as the main constituents. The molybdenum-bearing inclusions invariably contained Rh, Ru, Tc, and Nd; Te and Pd were also detected in small amounts. Barium-rich inclusions were always associated with enrichments of cerium, zirconium, and strontium. Uranium was detected in every inclusion, the smallest uranium concentration being in those free of barium. The UO_2 matrix was found to contain a homogeneous distribution of La, Ce, Pr, Nd, and Zr, although enhanced concentrations of cerium and zirconium were found associated with barium-rich inclusions.

The ejection of uranium atoms from sintered UO_2 pellets of stoichiometric composition and grain size of ~10 μ has been measured by Rogers.[62] The results are illustrated in Fig. I-15. The large primary ejection rate was attributed to the passage of fission fragments through small grains on the fuel surface; this resulted in the evaporation of these grains. The secondary rate was ascribed to knock-ons caused by hard-sphere collisions between the fission fragments and the atoms near the surface of the UO_2 emitter.

Swelling data for U_3Si_2, UAl_2, U_3O_8, niobium-coated UO_2, and UAl_3 have been published by Idaho Nuclear.[63] In general, the cores with the lowest theoretical densities (largest amount of fabrication voids) showed the least swelling. The coated UO_2 system had the highest swelling rate. With this system there was insufficient provision for fission-product accomodation within the particle because of high particle density; also, the particles could not conform to any fabrication voids that might be present because of

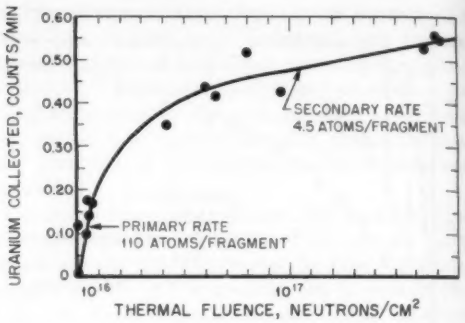

Fig. I-15 Uranium ejected from sintered UO_2 surface.[62]

the rigidity of the hard spherical niobium shells around the particles. Tests have shown, and continue to show, that the temperature at which accelerated (or breakaway) swelling occurs depends upon what is used for the dispersant fuel. For example, at 10^{20} fissions/cm^2, the accelerated swelling temperature of UO_2 dispersed in aluminum is about 250°C, whereas that of UAl_3 is about 500°C.

A method for the measurement of fission gases retained in irradiated mixed oxide and carbide fuel specimens has been described by the British.[64] Samples with masses between 1 and 3 g are dissolved in acid under reflux; helium is passed through the apparatus, and the liberated fission gases are trapped and dried in activated charcoal at liquid-nitrogen temperature. Gases other than krypton and xenon are almost entirely removed by distillation from the cold trap. The gas fraction containing krypton and xenon is collected and measured by an automatic Toepler system. An aliquot of this fraction is analyzed by mass spectrometry, and the measured krypton and xenon can be related to the weight of fuel dissolved, as determined by chemical analysis and mass spectrometry.

A computer code, FREVAP-8, has been developed at General Atomic[65] as a formulation of a fission-product-release code for two absorber regions, taking into account multicomponent sorption behavior and assuming steady-state diffusion. The basic limiting process considered in FREVAP is the evaporation of fission-product nuclides into the coolant stream at a graphite–coolant interface. This process in turn is limited by the sorption of fission products in the graphite between the fuel holes and the coolant holes and in the carbon sorbent material surrounding the fuel particles in the fuel hole. Finally, the process is limited by the release of fission products from the fuel particles themselves.

Procedures have been specified by Westinghouse[66] for using the CYGRO-1 computer program to evaluate the results of irradiation tests of Zircaloy-clad bulk-oxide fuel rods and to determine the adequacy of related fuel-rod designs. The most limiting cases

encountered when performing evaluation of fuel-rod designs were compared with the most probable values of the irradiation tests. The input and output for a sample program were also given. The major input variables of CYGRO-1 were (1) dimensions of the element (plug, fuel, and cladding); (2) elastic-plastic and creep properties of the fuel and the cladding; (3) thermal conductivity and expansion coefficient of the fuel and cladding; (4) dependence of swelling rate of fuel and cladding upon temperature and hydrostatic pressure; and (5) power, coolant pressure, and coolant temperature history. The major output variables were (1) temperature in fuel and cladding sections, (2) stresses and strains in fuel and cladding sections, and (3) dimensional changes.

(A. J. Markworth)

References

1. H. Matyja and S. Gabrycki, Effect of Crystal Structure of Uranium on the Kinetics of Growth of the Intermetallic Phase UCu_5 (in Russian), Polish Report 648/XIV, Institute for Nuclear Research, 1965.
2. A. D. Donaldson, S. Isserow, and R. B. Russell, Structures of Uranium Extruded High in the Alpha Phase, *J. Nucl. Mater.*, 22: 16-21 (1967).
3. J. J. Stobbs and A. J. Woodward, Oxidation of Pure Uranium in CO_2 Between 700 and 1000°C, *Corros. Sci.*, 6: 499-507 (November–December 1966).
4. E. L. Childs and F. E. Evans, Nonaqueous Electropolishing Bath for Uranium, USAEC Report RFP-816, Dow Chemical Co., Rocky Flats Division, Dec. 21, 1966.
5. B. Pinteau, Contribution to the Study of the Sintering Mechanisms of Uranium Powders in the Alpha, Beta, and Gamma Phases (in French), French Report CEA-R-2992, 1966.
6. R. E. Robbins, Recrystallization and Hot Hardness Studies of Uranium-Base Alloys, USAEC Report BNWL-CC-498, Battelle–Northwest, Feb. 16, 1966. (Classified)
7. R. Reisse, C. Collot, and D. Francois, Alloys of Uranium with Low Vanadium Concentrations: Refining of the Grain and Mechanical Properties (in French), *Compt. Rend., Ser. C*, 263: 1348-1351 (Nov. 28, 1966).
8. F. Coppola and C. Fizzotti, Metastable Phases in Uranium Alloys with Low Niobium Content and Their Thermal Decomposition (in Italian), Italian Report RT-MET-(66)2, 1966.
9. R. J. Jackson and W. L. Larsen, Transformations and Structures in the Uranium–Rhenium System, *J. Nucl. Mater.*, 21 (1967).
   I. Metastable α', α'' and γ° Structures, pp. 263-276.
   II. The $\beta \rightleftharpoons \alpha$ Transformation, pp. 277-281.
   III. Formation and Structure of $S(U_2Re)$, pp. 282-286.
10. A. Nystroem, Radiation Effects on Solid, Uranium-Based Nuclear Fuel Materials, Vol. 6, No. 2, A Bibliography, USAEC file No. NP-16522, December 1966.
11. B. G. Russell (Ed.), Plutonium Abstracts, USAEC Report BNWL-423, Battelle–Northwest, Mar. 31, 1967.
12. J. L. Long and R. D. Schweikhardt, Plutonium Electrorefining at Rocky Flats, USAEC Report RFP-871, Dow Chemical Co., Rocky Flats Division, Apr. 17, 1967.
13. L. J. Wittenberg and G. R. Grove, Reactor Fuels and Materials Development Plutonium Research: January–March 1966, USAEC Report MLM-1346, Mound Laboratory, Apr. 7, 1967.
14. Argonne National Laboratory, Reactor Development Program Progress Report, January 1967, USAEC Report ANL-7302.
15. Argonne National Laboratory, Reactor Development Program Progress Report, April 1967, USAEC Report ANL-7329, June 16, 1967.
16. Mound Laboratory, ^{238}Pu and ^{210}Po Data Sheets. Supplement to Mound Laboratory Isotopic Power Fuels Programs, October–December 1966, USAEC Report MLM-1387 (Suppl.), Mar. 1, 1967. (Classified)
17. O. L. Kruger and J. B. Moser, Sintering Characteristics and Properties of PuS and PuP, *J. Amer. Ceram. Soc.*, 49: 661-667 (December 1966).
18. E. C. Moncrief (Comp.), Gel-Addition Process Chemical Studies, Quarterly Progress Report No. 3, January–March, 1967, USAEC Report BAW-3714-3, Babcock & Wilcox Co., May 1967.
19. F. W. Albaugh et al., Battelle–Northwest, unpublished, June 1967.
20. R. Lorenzelli, A. Martin, and R. Schickel, The Reaction of Uranium and Plutonium Carbides with Nitrogen, USAEC Report BNWL-tr-20 (from French Report CEA-R-2997, March 1966).
21. W. R. Jacoby, R. G. Palm, and W. E. Ray, Compatibility of Stabilized Hypostoichiometric Uranium–Plutonium Monocarbide Fuels with Stainless Steel, USAEC Report WCAP-3791-3, Westinghouse Electric Corporation, Advanced Reactors Division, April 1967.
22. J. G. Reavis, M. W. Shupe, C. W. Bjorklund, and J. A. Leary, Phase Relations in the High-Carbon Portion of the U–Pu–C System, paper presented at the 1967 Annual Meeting of the American Nuclear Society, San Diego, California, June 11–15, 1967; *Trans. Amer. Nucl. Soc.*, 10(1): 111-112 (June 1967).
23. F. Schmidt and M. Fock, Diffusion of Thorium, Protactinium, and Uranium in Face-Centered Cubic Thorium, *J. Nucl. Mater.*, 21(3): 317-322 (March 1967).
24. Idaho Nuclear Corp., Nuclear Technology Branches Quarterly Report, October 1–December 31, 1966, USAEC Report IN-1083, May 1967.
25. H. Beisswenger, M. Bober, and G. Schumacher, Thermal Diffusion in the UO_2–CeO_2 System, USAEC Report WAPD-Trans-53 [from *J. Nucl. Mater.*, 21: 38-52 (1967)].
26. P. Patriarca (Comp.), Oak Ridge National Laboratory, unpublished, May 1967.
27. Oak Ridge National Laboratory, unpublished, Apr. 6, 1967.
28. N. H. Krikorian, The Reaction of Some Noble and Transition Metals with Refractory Carbides, *J. Nucl. Mater.*, 21: 236-238 (February 1967).
29. J. T. Venard, Compatibility of Dispersion Strengthened Aluminum with Uranium Monocarbide. A Review of the Literature, USAEC Report ORNL-TM-1705, Oak Ridge National Laboratory, January 1967.
30. T. Satow, Thermodynamic Properties and Nonstoichiometry of ThC and ThC_2, *J. Nucl. Mater.*, 21: 249-262 (1967).
31. T. Satow, Electrical Resistivity, Magnetic Susceptibility, and Thermal Expansion of ThC, *J. Nucl. Mater.*, 21: 343-344 (1967).
32. J. R. Weeks (Comp.), Brookhaven National Laboratory, unpublished, March 1967.
33. R. E. Schreiber, Irradiation of Refractory Fuel Compounds, UO_2 and UC, at High Specific Power to High Burnups, Report WCAP-2972 (NASA-CR-72019), Westinghouse Electric Corporation, Atomic Power Division, Aug. 1, 1966.
34. Argonne National Laboratory, Reactor Development Program Progress Report, February 1967, USAEC Report ANL-7308, Mar. 28, 1967.
35. R. A. Wullaert, J. M. Fackelmann, and W. Chubb, An Evaluation of UC–PuC for Sodium-Cooled Fast Reactors, USAEC Report BMI-1799, Battelle Memorial Institute, Apr. 13, 1967.
36. C. A. Alexander, Battelle Memorial Institute, Columbus Laboratories, private communication, May 1967.

37. A. J. Markworth, Battelle Memorial Institute, Columbus Laboratories, private communication, May 1967.
38. L. E. Russell, The Fabrication of Pyrophoric Materials by Sintering, British Report AERE-R-5410, February 1967 (soon to be published by the Institute of Metals).
39. N. R. Williams, Improvements in or Relating to the Production of Uranium Carbide, British Patent No. 1,052,084, Dec. 21, 1966.
40. J. R. McLaren, Improvements in or Relating to the Production of Nuclear Fuel Materials, British Patent No. 1,053,786, Jan. 4, 1967.
41. General Atomic Division, General Dynamic Corp., HIGR Base Program, Quarterly Progress Report for the Period Ending February 28, 1967, USAEC Report GA-7801, Apr. 20, 1967.
42. W. C. Robinson, Jr., and W. R. Martin, A Feasibility Study: Formation of Uranium Nitride Compounds Using Chemical-Vapor Deposition Techniques, USAEC Report ORNL-TM-1812, Oak Ridge National Laboratory, May 1967.
43. General Electric Company, Nuclear Materials and Propulsion Operation, High-Temperature Materials Programs. Part A. Sixth Annual Report, Physico-Chemical Studies of Clad UO_2 in Potential Meltdown Environment, USAEC Report GEMP-475A, Mar. 31, 1967.
44. R. Nagasaki and S. Kawasaki, Swelling of Metallic Uranium, Japanese Report JAERI-4037, April 1966.
45. E. M. Baroody, Calculations on the Collisional Coalescence of Fission-Gas Bubbles in Solid Fuels, USAEC Report BMI-1805, Battelle Memorial Institute, June 13, 1967.
46. E. E. Gruber, Calculated Size Distributions for Gas Bubble Migration and Coalescence in Solids, *J. Appl. Phys.*, 38(1): 243-250 (January 1967).
47. C. E. Miller, Jr., Light Bulb Model of Fission Product Release from Reactor Fuels, USAEC Report ORNL-4060, Oak Ridge National Laboratory, April 1967.
48. G. R. Fonda, Evaporation of Tungsten Under Various Pressures of Argon, *Phys. Rev.*, 31: 260-266 (February 1928).
49. I. Langmuir, Convection and Conduction of Heat in Gases, *Phys. Rev.* (Series I), 34(6): 401-422 (June 1912).
50. I. N. Tang and A. W. Castleman, Jr., On the Transport of Fission-Product Iodine from Molten Uranium, *Trans. Amer. Nucl. Soc.*, 10(2): (November 1967).
51. H. R. Brooks and R. L. D. French, FIZDIZ: A FORTRAN-IV Computer Program for Calculating the Diffusion of Radioactive Fission Gases from a Hole in a Reactor Fuel Element, British Report PG-Report-778, 1967.
52. J. J. Prabulos, Jr., DTF-BURN: A Multigroup Transport Theory Burnup Program Written in FORTRAN-IV, USAEC Report LA-3671, Los Alamos Scientific Laboratory, Jan. 20, 1967.
53. M. Sowinski, J. Chwaszczewska, M. Dakowski, T. Krogulski, and E. Piasecki, Emission of Long-Range Charged Particles in the Fission of ^{235}U Induced by Thermal Neutrons, Polish Report INR-765/IA/PL, October 1966.
54. H. Matzke, Xenon Migration and Trapping in Doped ThO_2, *J. Nucl. Mater.*, 21(2): 190-198 (February 1967).
55. F. Felix (Comp.), Diffusion of Rare Gases in Solids, USAEC–Euratom Report EURAEC-1650, Hahn-Meitner-Institut für Kernforschung, February 1966.
56. F. Felix, T. Lagerwall, D. Schmeling, and K. E. Zimen, Rare Gas Release from Solids with Special Attention to Nuclear Fuel Materials, in *Proceedings of the Third International Conference on the Peaceful Uses of Atomic Energy, Geneva, 1964*, Vol. 2, pp. 363-369, United Nations, New York, 1965.
57. R. D. MacDonald, Sweeping of Bubbles by Grain Boundaries in Irradiated UC, *J. Nucl. Mater.*, 22(1): 109-111 (April 1967).
58. M. V. Speight and G. W. Greenwood, Grain Boundary Mobility and Its Effects in Materials Containing Inert Gases, *Phil. Mag.*, 9: 683-689 (1964).
59. R. S. Forsyth, W. H. Blackadder, and N. Ronqvist, Burnup Determination by High Resolution Gamma Spectrometry: Fission Product Migration Studies, Swedish Report AE-272, April 1967.
60. W. J. Bailey and M. D. Freshley, Irradiation Properties of High Energy Rate Pneumatically Impacted UO_2–PuO_2 Fuels, USAEC Report BNWL-356, Battelle–Northwest, April 1967.
61. B. M. Jeffery, Microanalysis of Inclusions in Irradiated UO_2, *J. Nucl. Mater.*, 22(1): 33-40 (April 1967).
62. M. D. Rogers, Ejection of Uranium Atoms from Sintered UO_2, *J. Nucl. Mater.*, 22(1): 103-105 (April 1967).
63. Idaho Nuclear Corp., Nuclear Technology Branches Quarterly Report, July 1–September 30, 1966, USAEC Report IN-1048, February 1967.
64. W. Jennison and M. L. Clark, Measurement of Kr and Xe Fission Product Retention in Irradiated Fuel Elements, British Report TRG-Report-1382, Nov. 30, 1966.
65. L. R. Zumwalt, FREVAP-8 Formulation Code for Estimating the Release of Metallic Fission Products from HTGR Fuel Elements, USAEC Report GAMD-7535(Rev.), General Atomic Division, General Dynamics Corp., Mar. 24, 1967.
66. E. Duncombe, A Procedure for Analysis of Zircaloy-Clad Bulk Oxide Rods Using the CYGRO-1 Computer Program, USAEC Report WAPD-TM-583(Add.1), Westinghouse Electric Corporation, Bettis Atomic Power Laboratory, April 1967.

Section II

Reactor Materials

Moderator and Control Materials

Graphite

An impregnation microradiography technique employed by Battelle–Northwest[1] should be useful in many investigations concerned with interconnected graphite pore networks. A sample for examination was vacuum impregnated with a mixture of tetrabromoethane and Maraglas resin (equal parts by volume). It was then mounted in a Maraglas resin and held at 160°F (71°C) for 16 hr to cure the resin and immobilize the tetrabromoethane. Sections of the sample were then cut and thinned to about 0.008 in. and ultrasonically cleaned to remove debris. These sections were then radiographed with a tungsten tube operated at 8 kv and 15 ma. The gas in the X-ray beam was helium. Resulting radiographs showed interconnected pore networks and the development of pore structure during gas corrosion of graphite.

New data on irradiation-induced dimensional changes in pyrolytic graphite were reported by Battelle–Northwest.[2] Pyrolytic graphites heat-treated at 2200 and 3400°C were irradiated at approximately 600°C. The 2200°C material expanded at a rate of 1.62% per 10^{21} neutrons/cm^2 and contracted at a rate of 0.622% per 10^{21} neutrons/cm^2 for the transverse and parallel orientations, respectively, over the range 0.19 to 2.0×10^{21} neutrons/cm^2 ($E > 0.18$ Mev). The 3400°C material expanded at a rate of 0.491% per 10^{21} neutrons/cm^2 and contracted at a rate of 0.033% per 10^{21} neutrons/cm^2 for the transverse and parallel orientations, respectively, over the range 0.23 to 0.58×10^{21} neutrons/cm^2. For all materials tested a higher processing temperature resulted in less contraction. This is consistent with the generalization that the more highly developed the crystal structure of the graphite, the less contraction is experienced.

Irradiation results for glassy carbon were also noted in this study. Several samples of glassy-carbon pipe and rods were irradiated to a fluence of 6.4×10^{20} neutrons/cm^2 ($E > 0.18$ Mev) at approximately 600°C. Samples from all three heat-treatments, 1000, 2000, and 3000°C, exhibited high contraction rates. However, as in conventional nuclear graphites, the contraction rate decreased with an increase in processing temperature. The length-change data are given in Table II-1.

The effects of electron and neutron irradiation at 77°K on the physical properties of nuclear graphite were examined by Goggin.[3] Changes in the electrical resistance, magnetoresistance, Hall constant, and dynamic and static Young's moduli were studied as a function of irradiation exposure and annealing. The rate of change of the properties as a function of the number of displaced atoms differed for the two types of irradiation. Inverse annealing effects were observed in the electrical properties in the range 100 to 160°K and in the mechanical properties in the range 200 to 280°K. The results were consistent (1) with a model of neutron damage in which the displaced atoms are in small, loosely coupled clusters of about 10 interstitials that are distributed along the paths of the primary knock-ons and (2) for electron irradiation in which the damage is mainly randomly distributed simple Frenkel pairs.

Irradiation of a variety of graphites in the temperature range 300 to 1500°C to fluences of 1.20 to 3.25×10^{21} neutrons/cm^2 ($E > 0.18$ Mev) has been investigated.[4] The materials included conventional needle-coke or Texas-coke graphites upgraded in density and strength by impregnation and near-isotropic graphites prepared by pressure baking. Changes in linear dimension, coefficient of thermal expansion, and apparent crystallite height were noted. A saturation of linear contraction in the direction normal to the layer planes was observed for anisotropic graphite irradiated in the temperature range 880 to 1270°C to 2 to 3×10^{21} neutrons/cm^2 ($E > 0.18$ Mev). This characteristic was not observed for the isotropic graphites irradiated under the same condition. The apparent crystallite height, L_c, saturated at a common value of 150 to 250 A for all graphites studied, regardless of original values or irradiation temperatures, except for samples irradiated at 615°C; the 615°C samples saturated in the range 300 to 400 A. Changes in bulk thermal-expansion coefficients were

Table II-1 RADIATION-INDUCED LENGTH CHANGES OF GLASSY CARBON[2]

Sample	Process temp., °C	Dimensional change, %	
		Length	Diameter
Pipe			
GC 10	1000	−4.99	−4.32
GC 20	2000	−2.16	−1.99
GC 30	3000	−1.68	−1.58
Rod			
GC 10	1000	−4.45	
GC 20	2000	−2.94	
GC 30	3000	−1.66	

either small or nonexistent except for graphites made with Texas-coke filler and samples irradiated at 300 to 400°C. All graphites studied exhibited a single linear relation between thermal expansion and bulk dimensional changes in the range 320 to 615°C. Between 840 and 1490°C a separate linear relation was observed for anisotropic and isotropic graphites. At high temperatures the linear relation was shifted toward higher contraction for the isotropic graphites.

Nongraphitizing impregnated carbon in the pores of an anisotropic needle-coke graphite increased its volume contraction, reduced the anisotropy of contraction, and retarded "turnaround" in the perpendicular direction when irradiated in the range 880 to 1230°C at 3.25×10^{21} neutrons/cm^2 ($E > 0.18$ Mev).

Irradiation-induced dimensional changes in three graphites provided expected, but interesting, correlations with orientation and crystallinity.[5] The samples included: pyrolytic carbon ($L_c \simeq 220$ A), hot-worked graphite ($L_c \simeq 600$ A), and annealed pyrolytic carbon ($L_c \simeq 1600$ A). Samples were irradiated to fluences of approximately 1.9×10^{21} neutrons/cm^2 ($E > 0.18$ Mev) at 1225°C. The pyrocarbon samples expanded 24% perpendicular to the layer planes and contracted 9% parallel to the layer plane. Changes in the hot-worked graphite and annealed pyrolytic carbon were lower by factors of 2 and 10, respectively. Thus the length changes decreased with increased crystallinity.

A second annual report on the hot isostatic process for fabricating graphite has been published by Battelle–Columbus.[6] The report contains new characterization data for graphites prepared by the unique process that can produce highly isotropic, high-density graphite. (M. C. Brockway)

Beryllium and Beryllium Alloys

Fabrication

JOINING

Bogowitz and Metcalf have studied the brazing of beryllium by capillary flow at Solar.[7] Four silver-base alloys with improved flow were developed. Titanium-base braze alloys were shown to wet beryllium better than any silver-base alloy, but optimization of these alloys was not completed. The alloys were evaluated on the basis of (1) flat beryllium sheet, (2) capillary flow over a vertical distance of 1 in., (3) vertical capillary flow at selected temperatures as a function of time, (4) structure, and (5) strength and stability of brazed joints. Brazing temperatures below 1550°F (843°C) are desired because of degradation of properties in beryllium sheet at high temperatures. The comparative results of these studies for the silver-base alloys in an argon atmosphere are presented in Table II-2. The recom-

Table II-2 COMPARATIVE RESULTS FOR CANDIDATE BRAZING ALLOYS*†
(Point Basis)

Braze alloy†	Tolerance		Braze characteristics		Interaction	Mechanical strength	
	Atmosphere (Ti/Be spacer)	Surface condition (etch depth)	Capillary flow‡	Braze temperature	(beryllide thickness§)	Joint shear	Beryllium tensile
Ag–Cu–Li (6)	2	2	3	2	3	3	2
Ag–Cu–Ti (6B1)	1	2	3	3	4	2	2
Ag–Cu–Be-(6C)	1	2	3	3	4	2	2
Ag–Cu–In–Ti (6H5)	4	2	2	3	3	2	1
Ag–Cu–Ge (6J)	4	1	1	2	1	2	2
Ag–Cu–Ge–Ti (6J5)	3	2	2	3	2	2	
Ag–Cu–Mn–Ge (6K6)	4	1	3	3	4	3	2
Ag–Cu–Mn–Ti (6K7)	2	2	3	1	5	1	1
Ag–Cu–Mn (6K9)	2	2	3	1	4	3	3
Ag–Cu–Mn–Ge–Ti (6K13)	2	2	3	3	5	3	3

PARAMETER BASIS FOR AWARD OF POINTS

Temperature change for 0.5-in. flow		Flow increase on flat plate		Vertical flow		Based on preferred temperature at 1550°F‖		Beryllide at interface		Shear strength		Base-metal strength	
Points	Change, °F	Points	Flow, %	Points	Flow, in.	Points	Temp., °F	Points	10^{-4} in.	Points	Strength, 1000 psi	Points	Strength, 1000 psi
1 =	>150	1 =	>20	1 =	<0.5	1 =	>1650	1 =	>10	1 =	<10	1 =	<40
2 =	>100, <150	2 =	<20	2 =	0.5–0.75	2 =	1551–1650	2 =	5–10	2 =	10–13	2 =	40–50
3 =	>50, <100			3 =	0.75–1.0	3 =	<1551	3 =	2–5	3 =	>13	3 =	>50
								4 =	1–2				
								5 =	<1				

*For argon atmosphere.
†The recommended braze temperatures and compositions (wt.%) are 1550°F for Ag–12.5 Cu–5 Mn–1 Ge–1 Ti, Ag–12.5 Cu–5 Mn–1 Ge, and Ag–12.5 Cu–1 Li; 1650°F for Ag–7.5 Cu–15 Mn.
‡10-min braze.
§Higher temperatures anneal out the desired structures.

mended compositions are indicated and their braze temperatures given.

Various fabrication techniques for the manufacture of wrought beryllium and IN-102 (ingot) alloy components for the SNAP-27 generator have been investigated.[8] Forming, machining, brazing, and welding techniques were developed. Electron-beam-welding procedures provided good joints with adequate tensile strength, but the welds contained some small cracks. All the other fabrication procedures were completely satisfactory. Tensile properties of the wrought beryllium were determined for both welds and the parent metal at room and elevated temperatures. Also, chemical analyses, metallographic examination, and coefficient of thermal expansion were determined.

MACHINABILITY

As part of a combined U. S. Air Force and U. K. Ministry of Aviation cooperative research and development program, General Electric investigated the machinability of beryllium.[9] The two machining methods that showed the most promise for processing beryllium were conventional machining followed by chemical etching and electrochemical machining. The advantages of conventional machining are: (1) there is a high rate of stock removal, (2) conventional tooling practices can be used, and (3) the surface damage can be removed by an inexpensive chemical treatment. The advantages of electrochemical machining are (1) tenable metal-removal rates, (2) very good surface finishes, (3) no metallurgical damage to the beryllium, and (4) no required post-treatment. Machinability data for conventional machining represent an experimental verification of previously accepted procedures.

Electrochemical machining (ECM) was accomplished using an electrolyte consisting of 4 lb of $NaNO_3$ per gallon of water at 100°F (38°C). The process constants were determined to be a metal-removal rate of 11.6×10^{-3} cu in./amp-min and a starting voltage of 4.5 volts with a specific resistance of 4.19 ohm-cm in fully aged electrolyte. Satisfactory surface finishes (50 μin.) and practical metal-removal rates can be expected for this ECM system when cutting under steady-state conditions. Operating conditions determined necessary for this process were working gaps of 0.008 to 0.020 in., feed rates of 0.020 to 0.100 in./min, and an electrolyte velocity of 30 to 110 ft/sec. Machining conditions chosen should not be a combination of the three lowest operating conditions.

Physical Metallurgy

SPLAT COOLED Be–4 WT.% Cu

Kaufmann is studying splat cooling as a means to produce fine-grained beryllium, unalloyed SR beryllium, and a 4 wt.% copper alloy.[10] In the consolidation process used, the powder is vacuum hot pressed, followed by rolling or extruding. Tensile testing of the extruded splat material produced yield strengths of 50,000 to 77,000 psi and ultimate strengths of 50,000 to 97,000 psi. Although low for the unalloyed material, elongation of the copper alloy was as high as 6%. All samples except those which were completely brittle showed well-defined yield points and frequently demonstrated a drop in load after yielding. Many of the 4% copper samples also had a period of easy glide following yielding. A Cottrell effect in which impurity atoms lock the dislocations up to the yield point was possibly the cause. Apparently the impurity causing the yield-point phenomenon tends to inhibit fracture on the $(11\bar{2}0)$ plane and thus strengthens the material. Generally the splat-source materials were more resistant to plastic deformation at 600 to 900°C than ordinary hot-pressed powder. This may be due to the fine grain size and unusual morphology or to incomplete bonding that would prevent plasticity across powder-particle boundaries.

COPPER ALLOYED INGOT SHEET

The Beryllium Corp. has been engaged in an investigation of solid-solution-strengthened, high-purity, beryllium-alloy sheet.[11] The alloy compositions being studied contained 0.008, 1.0, 2.79, and 4.65 wt.% copper. Ingots of these alloys have been extruded into slabs and rolled at 1000, 1200, and 1400°F (538, 649, and 760°C), yielding approximately 0.05-in.-thick sheet. An equiaxed average grain size of about 43 μ has been produced by annealing 1 hr at 1300°F (704°C) subsequent to rolling. Although formability and property characterizations have not been completed, the 0.008 wt.% copper alloy exhibited superior forming characteristics compared with the 1.0 wt.% copper alloy. Both of these alloys have shown elevated-temperature elongation values superior to those for the 2.79 and 4.65 wt.% copper alloys.

Mechanical Metallurgy

ANISOTROPY

Autonetics has examined the effects of forging variables on anisotropy in beryllium forgings.[12] Combinations of uniaxial forging by extrusion and biaxial forging by upsetting against the extrusion direction were studied. Properties measured included orientation, microstructure, strength, and thermal expansion. The initial experiments indicated that upset-forging reductions from 45 to 60% could minimize the anisotropy of material extruded at ratios ranging from 4 to 7. The preferred-orientation and mechanical-property data demonstrated that reasonably isotropic hot-pressed beryllium can first be made anisotropic through uniaxial forging and can then be made less anisotropic through subsequent biaxial forging at 90° from the uniaxial direction. The

thermal-expansion anisotropy of upset-forged beryllium was 1.14×10^{-6}/°F, and the extruded and upset-forged material had only 0.330 and 0.422×10^{-6}/°F, respectively. Decreasing the forging temperature from 1350 to 1250°F (732 to 677°C) increased the yield strength and ductility by modest amounts. Increasing the stress-relief temperature from 1250 to 1420°F (677 to 771°C) decreased the yield strength and the yield anisotropy but had no effect on ultimate tensile strength and elongation.

During the development of a beryllium-clad UO_2 fuel element, an unusual form of extremely brittle fracture of the beryllium can be observed as a result of tensile strains developed in the can by differential thermal contraction onto the UO_2 fuel at temperatures of 300°C or below.[13] The highly textured beryllium can be produced by a double-extrusion route failed by the audible propagation of a helical crack along the element; the helix angle was about 25° in all cases, and sometimes two helices of opposite sense caused the element to break into several pieces. Calculations showed that the fracture occurred after only 0.15% plastic strain, considerably less than the tensile ductility of an extruded rod at the same temperature (10% is typical).

The characteristic spiral form of fracture was caused by cleavage failure of the highly textured tube along $(11\bar{2}0)$ planes under biaxial stress, but the crystallography of the fracture did not reveal the cause of the unexpectedly low plasticity. Mechanical testing of the tubes revealed circumferential ductilities of about 1%, which were in agreement with values expected from the high degree of texture of the tube; axial ductilities were anomalously very low, about 0.2%. Thin filaments cut from the walls of double-extruded material gave much greater elongations than the whole tube, indicating that the material was not inherently brittle. Increasing the width of these curved specimens decreased the ductility. The brittleness was believed to be caused by premature failure following the action of a secondary deformation process that was activated by transverse loop stresses, arising from the plastic anisotropy of the material and the tube curvature. This process may involve twinning, which is known to lead to nonductile failure.

Oxidation Protection

The protection of beryllium from high-temperature oxidation by use of a chromate film was the objective of an investigation at Frankford Arsenal.[14] The presence of chromium ions in the chromic acid anodic coating was considered an important factor contributing to the resistance to oxidation. The chromate film was applied from a proprietary (U. S. Patent 2796371) chromating solution normally used for aluminum. The specimens were 1.3-cm-diameter by 1.2-cm-long cylinders of hot-pressed, extruded, and machined beryllium and were chromated at 25°C for 30 min. Chromated beryllium was unoxidized after 24 hr of exposure to moist air at 900°C, and untreated beryllium was catastrophically oxidized under the same conditions.

(H. D. Hanes and F. T. Zurey)

Beryllium Oxide

The pore structure in porous aggregates of BeO crystallites prepared by thermal decomposition of $Be(OH)_2$ has been studied by British investigators.[15] Since the sinterability of oxide powders is strongly influenced by aggregate structure, this work is of particular interest. Even more significant may be subsequently planned studies on the behavior of such pores and their effect upon crystallite growth during heat-treatment up to sintering temperatures. Such studies should be most helpful in elucidating the nature of enhanced sinterability of oxide powders formed by thermal decomposition. The present study indicated that of the total intra-aggregate pore volume, only about 20% was available to CCl_4 and about 50% available to nitrogen; hence there was a substantial volume of pores with diameters less than 6 A and 3 A, respectively. Such small pores render surface-area measurements from gas adsorption meaningless, cause a small irreversibility in nitrogen adsorption at low pressures, and exhibit measurable helium adsorption even at 100°C. Although of comparable molecular size to nitrogen, H_2O was able to penetrate most or all of the pores (an observation attributed to the higher interaction energy of H_2O with the oxide surface), and after desorption some of these pores became accessible to nitrogen. Similarly, H_2O adsorption and desorption increased the pore volume accessible to CCl_4, and various treatments (including decomposition of the hydroxide in the presence of H_2O vapor) led to a microstructure in which pores of less than about 6 A were virtually absent.

(M. C. Brockway)

Solid Hydrides

Titanium Hydride

The reaction between titanium and hydrogen at room temperature has been studied at Battelle–Columbus.[16] It was found that titanium will hydride if all the oxide has been carefully removed from the surface of the metal by heating in a vacuum at 1500°F (816°C) for at least 2 hr. In addition, it was necessary to remove all oxygen from the hydrogen by first passing it through a trap maintained at liquid-nitrogen temperature and then passing it over hot titanium foil. An alloy consisting of Ti–6 wt.% Al –4 wt.% V was

found to react more readily than titanium under these conditions, whereas an alloy with the composition Ti–5 wt.% Al–2.5 wt.% Sn reacted less readily.

Alkali-Metal Hydrides

Precise determinations of the heats of formation of the hydrides of Rb and Cs have been completed at Lawrence Radiation Laboratory.[17] In addition, values for the heats of formation of both the hydrides and deuterides of lithium, sodium, and potassium have been recalculated. The values are tabulated below.

Material	Heat of formation, kcal/mole
LiH	21.663 ± 0.052
LiD	21.742 ± 0.041
NaH	13.489 ± 0.040
NaD	13.302 ± 0.015
KH	13.820 ± 0.023
KD	13.200 ± 0.022
RbH	12.500 ± 0.031
CsH	12.915 ± 0.024

In view of the high purity of the materials used and the careful experimental work, the above values undoubtedly represent the best data available for these materials.

Shielding experiments with LiH–Pb combinations for gamma-ray attenuation have been carried out at Atomics International.[18] Two-cycle systems were used: the first cycle consisted of 2 in. of lead plus 3.75 in. of LiH, and the second cycle, 4 in. of lead plus 5.75 in. of LiH. Measurements were made with the lead regions first in each cycle and were then repeated with the LiH regions first. The results showed a 70% increase in dose rate when the lead was closest to the fission plate because of the secondary gammas generated under these conditions. In other experiments, neutron fluence measurements through LiH up to 74 cm thick gave an attenuation coefficient of 0.179/cm. Studies of the distribution of neutron fluence through LiH showed that high-energy neutrons (greater than 8 Mev) are the most penetrating and may become the dominant component in thick shields.

Compatibility of LiH with a tungsten alloy and with ZrH_2 at 800 and 1000°F (427 and 538°C) has been examined. After 4000 hr the only change observed was a darkening of the surface of some of the 1000°F specimens.

Rare-Earth Hydrides

Thermodynamic data on Er_2H_3 have been obtained by the French.[19] The standard heat of formation was determined to be −51.9 kcal/mole. Thermodynamic properties at higher temperatures are given in the following tabulation.

H/Er ratio	Temp., °K	*H*, kcal/mole	*S*, cal/(mole)(deg)	*F*, kcal/mole
1.48	998	−38.4	−25.9	−12.6
1.505	962	−39.0	−26.3	−13.7
1.52	941	−39.4	−26.5	−14.4
1.54	915	−40.0	−27.0	−15.3
1.57	873	−40.7	−27.4	−16.8

Hydrided Alloys

Electrical-resistivity data on SNAP fuel material were evaluated at Atomics International[20] to estimate the effect of the H/Zr ratio on the thermal conductivity. For the S8DR fuel, which will have an H/Zr ratio between 1.65 and 1.81, a value of about 13 Btu/(hr)(ft)(°F) was determined to be the best.

(H. H. Krause)

Metallic Poison Materials

The grain growth of hafnium at annealing temperatures of 700 to 1000°C, after cold working to strains of 2 to 12.5% at room temperature, has been studied.[21] The annealing times varied from 10 to 10,000 min. It was found that exaggerated grain growth did not occur in any specimens at annealing temperatures of 700 and 800°C. At annealing temperatures of 900, 950, and 1000°C, this effect was observed only in specimens that had received 2 and 4% of cold work. The exaggerated grain growth at 900°C is shown in Fig. II-1. An incubation period, which varied inversely with strain, was associated with this type of grain growth. The exaggerated grain growth at low values of cold work is explained by the fact that only a few grains recrystallize at low strains, and thus these grains can grow without much

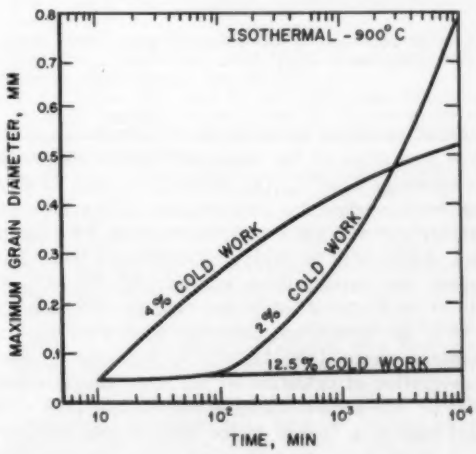

Fig. II-1 Influence of heat-treating at 900°C on grain size as a function of prior cold work.[21]

interference. A large number of grains recrystallize at large amounts of cold work because of high strains, and these impinge on one another and thus inhibit grain growth.

The Ta–Hf phase diagram is shown in Fig. II-2, and the relative room-temperature hardness of these alloys is illustrated in Fig. II-3 (Ref. 22). The increased hardness at about 10 wt.% tantalum results from formation of the hexagonal omega phase after annealing at 1100°C. The oxidation of Hf–Ta alloys has been studied by exposing the alloys to helium carrier gas with known oxygen contents.[23] No significant differences in oxidation resistance were found among the three alloys studied: Hf–27 wt.% Ta, Hf–20 wt.% Ta–2 wt.% Mo, and Hf–20 wt.% Ta–2 wt.% Zr. Isothermal oxidation tests over the temperature range 1200 to 2100°C indicated a sharp acceleration of oxidation for all three alloys at about 1700°C. The higher oxidation rates above 1700°C are attributed to a change in the HfO_2 crystal structure from monoclinic to tetragonal, with the tetragonal film being more easily penetrated by oxygen.

(M. Kangilaski)

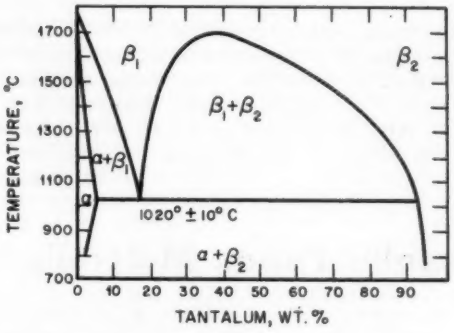

Fig. II-2 Phase diagram of Hf–Ta system in solid state.[22]

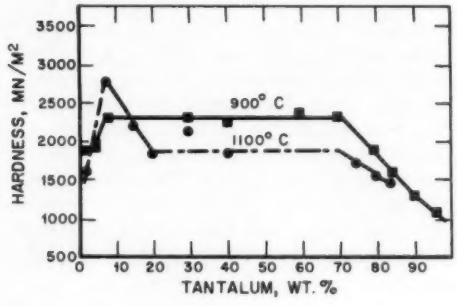

Fig. II-3 Hardness of Hf–Ta alloys annealed at 900 and 1100°C (Ref. 22).

Dispersion and Nonmetallic Poison Materials

Boron and Boron Compounds

Boronated graphite is being studied as a control-rod absorber material for the Public Service Company (PSC) of Colorado reactor.[24] Efforts are being concentrated on a model for irradiation damage which assumes that dimensional change in neutron-irradiated boronated graphite is due to a complex interaction of effects from fast-neutron damage, thermal-neutron capture by ^{10}B, and swelling of B_4C particles. The model, in conjunction with irradiation data, was used to calculate the dimensional change in an absorber compact (30 wt.% boron) for 6 years of service at 50% and 100% duty factors. The results of these calculations are shown in Table II-3.

Table II-3 DIMENSIONAL CHANGE OF TYPICAL 30 WT.% BORONATED-GRAPHITE ABSORBER COMPACT[24]

Forming method	Duty factor for 6 years, %	Probable range of dimensional change, %	
		Parallel to forming direction	Perpendicular to forming direction
Hot molding	50	+1.0 to +2.5	−1.0 to 0.0
	100	+2.0 to +5.0	0.0 to +0.5
Extrusion	50	0.0 to +0.5	0.0 to +1.0
	100	+0.5 to +1.0	0.0 to +2.0

Keihn and Keplin[25] determined the thermal expansions of certain Group IV and Group V diborides. The vacuum-sintered diborides were tested at temperatures above 1600°C by an X-ray method, and lattice constants were measured for each compound. Each exhibited the AlB_2-type hexagonal structure. Table II-4 illustrates the mean linear-thermal-expansion coefficients that were calculated from these tests.

The thermal and electrical conductivities of Groups IV, V, and VI transition metals and their borides at room temperature have been examined.[26] Certain regularities in the changes in thermal-conductivity coefficients in the diborides were illustrated. The thermal conductivities of diborides of Group IV elements were greater than those of diborides of Groups V and VI. Values for the Group IV metal diborides were higher than those for their pure metals, whereas with the Group V and, especially, the Group VI elements, the thermal conductivities of the pure metals were higher than those of their diborides.

Rare Earths

The irradiation behavior of Eu_2O_3–stainless-steel dispersions used in the SM-1 reactor was reviewed by Oak Ridge.[27] The compatibility problem between Eu_2O_3 and stainless steel containing silicon and the

Table II-4 LINEAR-THERMAL-EXPANSION COEFFICIENTS OF DIBORIDES[25]

Substance	Temp. range, °C	Expansion coefficient, 10^{-6}/°C
TiB_2	25–750	α_a = 6.63
TiB_2	25–750	α_c = 8.65
TiB_2	754–2041	α_a = 8.00
TiB_2	754–2041	α_c = 11.20
ZrB_2	25–750	α_a = 6.60
ZrB_2	25–750	α_c = 6.78
ZrB_2	754–1800	α_a = 8.62
ZrB_2	754–1800	α_c = 7.65
HfB_2	25–750	α_a = 6.39
HfB_2	25–750	α_c = 6.81
HfB_2	753–2041	α_a = 8.40
HfB_2	753–2041	α_c = 7.64
NbB_2	25–750	α_a = 5.51
NbB_2	25–750	α_c = 9.21
NbB_2	750–1700	α_a = 8.30
NbB_2	750–1700	α_c = 10.70
TaB_2	25–750	α_a = 5.85
TaB_2	25–750	α_c = 7.14
TaB_2	750–1700	α_a = 7.82
TaB_2	750–1700	α_c = 8.40

poor water-corrosion characteristics of Eu_2O_3 were discussed in relation to the method of control-rod fabrication.

Mass-spectrographic analyses of absorber test specimens were used to give an accurate measure of the burnup of europium. These analyses indicated that the actual burnup of europium was about an order of magnitude less than that predicted by unperturbed thermal fluence or ^{60}Co monitoring. Figure II-4 is a line graph of the burnup vs. the exposure for these specimens.

Workers at Oak Ridge[28] have studied the fabrication and thermal-expansion characteristics of Gd_2O_3–Al_2O_3 composition for the Molten Salt Reactor Experiment. A technique of first blending the powders of the eutectic composition (70 wt.% Gd_2O_3–30 wt.% Al_2O_3) and sintering for 2 hr at 1700°C in hydrogen was developed. The finished material was then ground to −325 mesh, pressed into pellets, and sintered at 1550°C in hydrogen for 2 hr. The thermal expansion of this material was measured between 25 and 905°C, and the average coefficient of thermal expansion was determined to be 0.24×10^{-5}/°C. (D. E. Lozier)

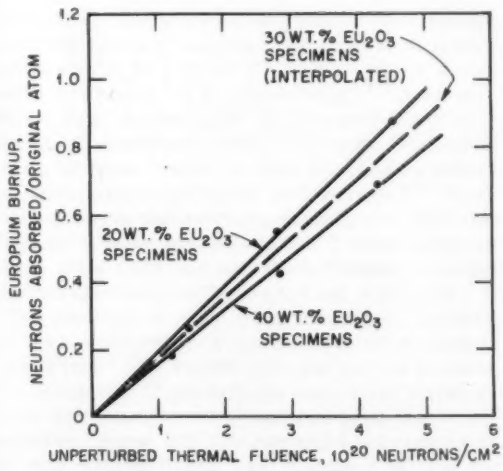

Fig. II-4 Burnup vs. exposure for Eu_2O_3–stainless-steel irradiation test specimens.[27]

References

1. Battelle–Northwest, Fueled Graphite Studies, Quarterly Progress Report, January–March 1967, USAEC Report BNWL-449, June 1967. (Classified)
2. F. W. Albaugh, S. H. Bush, J. J. Cadwell, D. R. deHalas, and D. C. Worlton, Battelle–Northwest, unpublished, June 1967.
3. P. R. Goggin, Some Effects of Irradiation at 77°K on the Physical Properties of Graphite, British Report AERE-R-5396, February 1967 (soon to be published in *Phil. Mag.*).
4. G. B. Engle, Dimensional and Property Changes of Impregnated and Isotropic Graphites Irradiated at 300 to 1500°C, USAEC Report GA-7326, General Atomic Division, General Dynamics Corp., Apr. 14, 1967.
5. General Atomic Division, General Dynamics Corp., HTGR Base Program Quarterly Progress Report for the Period Ending August 31, 1967, USAEC Report GA-8200, Sept. 30, 1967.
6. D. C. Carmichael, W. C. Chard, and M. C. Brockway, Dense Isotropic Graphite Fabricated by Hot Isostatic Compaction, USAEC Report BMI-1796, Battelle–Columbus, May 31, 1967.
7. R. G. Bogowitz and A. G. Metcalfe, Brazing Beryllium by Capillary Flow, Report AFML-TR-67-14, Solar, a Division of International Harvester Co., January 1967.
8. F. A. Harris, SNAP-27 Phase IIA Development Program, USAEC Report Y-1577, Union Carbide Corp., Nuclear Division, June 28, 1967. (Classified)
9. C. E. Glynn and J. Boyer, Machinability of Beryllium, Report AFML-TR-66-125, General Electric Company, October 1966.
10. A. R. Kaufmann, Improved Beryllium Alloys, Report NMI-8003.6, Whittaker Corp., Nuclear Metals Division, Jan. 10, 1967.
11. J. P. Denny, Development of Solid Solution Strengthened High-Purity Beryllium Alloy Sheet, Report NP-16732, The Beryllium Corp., Apr. 17, 1967.
12. A. G. Gross, Jr., and L. E. Colteryahn, Effects of Thermal–Mechanical Variables on the Anisotropy of Forged Beryllium, Report AFML-TR-66-333, Autonetics, September 1966.
13. G. Summer, Brittle Behavior in Extruded Beryllium, *Int. J. Fracture Mech.*, 2: 448-459 (June 1966).
14. F. Pearlstein, R. W. Wick, and A. Gallaccio, Protection of Beryllium Against High-Temperature Oxidation, Report A66-6, Frankford Arsenal, January 1966.
15. R. F. Horlock and P. J. Anderson, Studies on Molecular Size Pores in Beryllium Oxide Powders, *Trans. Faraday Soc.*, 63: 717 (1967); 63: 2316 (1967).
16. B. G. Koehl, W. Hodge, and D. N. Williams, An Investigation of the Reaction of Titanium with Hydrogen, Report NASA-CR-65456, Battelle Memorial Institute, July 14, 1966.
17. S. R. Gunn, The Heats of Formation at 25°C of the Crystalline Hydrides and Aqueous Hydroxides of Rubidium and Cesium, *J. Phys. Chem.*, 71(5): 1386-1390 (April 1967).
18. L. S. Mims, Progress Report for SNAP General Supporting Technology, November 1966–January 1967,

USAEC Report NAA-SR-12316, Atomics International, May 5, 1967.
19. J. F. Maurin, Study of Hydrides of Erbium and Yttrium, French Report NP-16610, February 1965.
20. L. M. Maki, SNAP Reactor Improvement Program, Progress Report, January–March 1967, USAEC Report NAA-SR-12378, Atomics International, May 19, 1967. (Classified)
21. C. D. Calhoun, Exaggerated Grain Growth in Reactor-Grade Hafnium After Small Deformations, USAEC Report KAPL-3193, Knolls Atomic Power Laboratory, Sept. 2, 1966.
22. V. N. Svechnikov, A. K. Shurin, and G. P. Dmitriyeva, Phase Equilibrium Diagram of the Hf–Ta System, Report NASA-TT-F-10, 280(N67-10209), translated from *Sb. Nauch. Rabot Inst. Metall., Akad. Nauk Ukr. SSR*, 19: 206-211 (1964).
23. J. B. Berkowitz-Mattuck, L. Kaufman, E. V. Clougherty, and R. Hopper, Oxidation of Hf–Ta Alloys, *Trans. Met. Soc. AIME*, 239: 750-753 (May 1967).
24. General Atomic Division, General Dynamics Corp., Public Service Company of Colorado 330-Mw(e) High-Temperature Gas-Cooled Reactor Research and Development Program, USAEC Report GA-7939, May 5, 1967.
25. F. G. Keihn and E. T. Keplin, High-Temperature Thermal Expansion of Certain Group IV and V Diborides, *J. Amer. Ceram. Soc.*, 50: 81-84 (Feb. 21, 1967).
26. P. I. Matl'kov, S. N. Livov, and V. F. Nemchenko, Thermal Conductivity of IV–VI Group Transition Metal Borides, in *Vysokotemperaturnye Neorganicheskie Soedineniya*, Izdatel'stvo Naukova Dumka, Kiev, 1965.
27. C. F. Leitten, Jr., A. E. Richt, and R. J. Beaver, Irradiation Behavior of Eu_2O_3–Stainless Steel Dispersions, USAEC Report ORNL-4104, Oak Ridge National Laboratory, June 1967.
28. P. E. Trent, Gadolinium Oxide–30 Wt.% Aluminum Oxide Compacts, USAEC Report Y-1571, Union Carbide Corp., Nuclear Division, Mar. 10, 1967.

Section III

Reactor Materials

Cladding and Structural Materials

Corrosion by Aqueous and Gaseous Media

Corrosion of Zirconium Alloys

ALLOY DEVELOPMENT

The corrosion and hydrogen-absorption properties in water and steam of zirconium-base alloys containing 0.5 to 1.0 wt. % Fe, Cr, Sn, and Nb have been studied at Westinghouse.[1] An alloy containing 0.5 wt. % Fe–1.0 wt. % Cr–0.5 wt. % Sn–0.5 wt. % Nb exhibited a low corrosion rate about equal to that of the Zircaloys, absorbed about one-half the amount of hydrogen as Zircaloy-4, and had a higher strength than the Zircaloys.

Modifications have been made in the Zr–3 wt. % Nb–1 wt. % Sn alloy to improve corrosion resistance in 400 to 450°C steam in studies conducted by Metallgesellschaft.[2] Alloy additions were less than 0.5 wt. %. Optimum corrosion resistance was obtained in tin-free alloys containing 0.2 wt. % antimony, 0.1 wt. % iron, or 0.5 wt. % chromium. However, the tin-free alloys generally exhibited poor creep behavior.

OXIDE FILMS

Electrical conductivities of anodized films formed on zirconium in a complex organic solution ranged from 2×10^{-14} to 2 to 3×10^{-15} $(\text{ohm-cm})^{-1}$ at thicknesses of 150 and 750 A, respectively.[3,4] Conductivities of film formed in 1% KOH were 5 to 8×10^{-14} $(\text{ohm-cm})^{-1}$ regardless of film thickness. Vacuum annealing of films formed in both solutions increased the conductivities to about 10^{-8} $(\text{ohm-cm})^{-1}$. Other work has shown that anodizing in phosphoric acid followed by a 64-hr exposure to 500°C steam produced weight gains only one-half those obtained with unanodized specimens or those anodized in 1% KOH.

The potential on oxide films forming on Zircaloy has been measured in a fused nitrate/nitrite bath at Chalk River.[5] The results indicated that, in the thin-film region (0 to 10 mg/dm^2), the oxidation of Zircaloy-2 was controlled by electronic transport at all temperatures. Below 400°C the potential fell steadily as the film thickened until ionic transport became the slower process. The potential on crystal-bar zirconium was always higher than on Zircaloy-2 at all temperatures, thus indicating electronic control. Zirconium–2.5 wt. % Nb alloys in the $(\alpha + \beta)$- and β-quenched conditions also exhibited high potentials and hence electronic control of the oxidation process at all temperatures. These results were used to discuss the relevancy of the 400°C steam test and the effects of irradiation and oxygen on the oxidation of zirconium alloys.

Workers at Chalk River have measured pores and cracks in ZrO_2 films with a pressurized mercury porosimeter.[6] The porosimeter results were correlated with capacitance curves for the aqueous corrosion of zirconium alloys. It was found that the onset of transition was accompanied by an increase in the number of large cracks and the appearance of small holes (10 to 20 A radius at 400°C and 100 A radius at 600°C). The large cracks then diminished, and the small holes predominated as the transition process propagated over the specimen surface. A rough correlation was found between the degree of fine porosity in the oxide film and the posttransition oxidation rate.

IRRADIATION

The effect of additives for *p*H control on the in-pile aqueous corrosion and hydriding behavior of zirconium alloys is being studied by Battelle–Northwest.[7] In *p*H 10 LiOH water, the oxidation of etched and prefilmed specimens was accelerated by in-flux exposure (36 days). On the other hand, similar specimens have been exposed 88 days to *p*H 10 NH_4OH-treated water at 270 to 280°C at a fast fluence of 6.9×10^{20} neutrons/cm^2 (>1 Mev) with only a slight increase in corrosion over that observed out-of-pile (a factor of less than 1.5).

WEAR

Chalk River has determined the wear rates of 157 material combinations as sleeve bearings in 80 and 160°F high-purity *p*H 7 water under loads of 20 to 250 lb and at speeds of 20 to 280 rpm for periods of 4 to 14 days.[8] The best materials were the hard oxides on zirconium alloys developed at Chalk River and a proprietary Ni–Sn–Bi alloy. In over half the tests, the wear rates decreased with increased sliding distance.

Corrosion of Aluminum Alloys

The effect of applied currents and additions to flowing water on the corrosion behavior of aluminum al-

loys has been studied at Argonne.[9] Colloidal, hydrated aluminum oxide significantly reduced the corrosion rate in 260°C water flowing at 7 m/sec. With applied currents, the corrosion in flowing 260°C water increased when the sample was made the cathode and decreased when it was made the anode. Promise was shown by AsO_3 as an effective corrosion inhibitor for aluminum in flowing high-temperature water.

The effect of irradiation on the transfer of corrosion products of aluminum and carbon steel from water into steam under boiling-water-reactor conditions has been reported by Russian scientists.[10] Neutron irradiation had no influence on the transfer of the corrosion products to the vapor state. It was believed that the governing factor in this transfer process was the radius of the hydrate molecule, which was not changed by neutron bombardment.

Corrosion of Stainless Steels

GENERAL

A translation of a Russian book titled *Water and Water Treatment in Nuclear Power Plants*[11] contains several chapters of interest. The fundamental corrosion processes and the corrosion behavior of steels and stainless steels are reviewed, and methods of protecting against corrosion are described. Deaeration, phosphate water treatments, and the protection of idle equipment are also discussed.

The behavior in 800 to 1100°C carbon dioxide of 20 wt. % Cr–25 wt. % Ni–Nb-stabilized steel containing 0.0 to 1.29 wt. % yttrium has been studied at Harwell.[12] All the yttrium additions reduced the overall attack and increased oxide adherence at all temperatures. In alloys containing >0.57 wt. % yttrium, there was a marked reduction in attack at 1000 and 1100°C, but appreciable intergranular oxidation at temperatures >900°C was observed.

STRESS-CORROSION CRACKING

U-bend specimens of 304 stainless steel have exhibited some stress-corrosion cracking (maximum depth 12 mils) after a 22-month exposure to the wet steam–water environment within the evaporator water boxes of the Elk River Reactor.[13] Exposure conditions were about 0.5 wt.% water in steam at 539°F (282°C) and 936 psig, which contained about 1100 ppm oxygen. Chloride in the reactor water was maintained at nondetectable levels (<35 ppb).

In studies conducted at Chalk River,[14] stress-corrosion cracking of a 316 stainless-steel threaded plug in a high-purity water loop has been attributed to chlorides from a fluorocarbon lubricant. A laboratory test with a 1-g sample of the fluorocarbon in 20 g of water at 500°F (260°C) revealed almost quantitative decomposition of the lubricant (187,000 μg of chlorine per gram of lubricant and 45,000 μg of fluorine per gram of lubricant).

The effect of cold work on the stress-corrosion-cracking behavior of 301, 304, 310, and 321 stainless steels has been studied at the Bureau of Standards.[15] Cold reductions ranged up to 50%. No cracking was detected in any of the specimens stressed to 90% of yield strength and exposed 452 days in a marine atmosphere. Laboratory studies in boiling 0.5*N* NaCl–0.1*N* $NaNO_2$ solution revealed a maximum in the curves for the threshold stress level necessary to produce cracking at 26% cold reduction (93,000 psi) for 304 stainless steel and at 33% cold reduction (113,000 psi) for 321 stainless steel. The threshold level for 301 stainless steel continued to increase with increasing cold work to 33% (166,000 psi). The 310 stainless steel generally did not crack in the above solution. Tests in boiling 42% $MgCl_2$ indicated that the annealed 310 stainless steel was more resistant to cracking than the cold-worked material.

Corrosion of Nickel-Base Alloys

The weight changes for nickel alloys and stainless steel exposed 6500 hr to 1200°F (649°C) steam containing oxygen and hydrogen have been investigated by Combustion Engineering.[16] Of the materials evaluated, Inconel 625, Inconel 600, and GE 2541 (Fe–24 wt. % Cr–4 wt. % Al–1 wt. % Y) appeared to have the best corrosion properties (weight gains of 20 to 25 mg/dm^2 after 6500 hr). Other alloys investigated included Hastelloy X, Inconel 800, IN-102, René 62, and 406 stainless steel.

The corrosion rates of Haynes 25, Hastelloy C, and Hastelloy N in seawater have been measured by the Naval Radiological Defense Laboratory[17] using the following techniques: (1) measurement of radioactivity leached into seawater from radioactive specimens, and (2) neutron activation analysis of corrosion products from inactive specimens exposed to seawater. Exposures were 95 days in aerated and deaerated seawater at 6°C at velocities up to 0.7 ft/sec. Average corrosion rates for Hastelloy C and Hastelloy N were 0.5×10^{-4} and 1×10^{-4} mil/year, respectively. Differential leaching occurred on Haynes 25. The corrosion rate based on cobalt release was 1×10^{-6} mil/year, and that based on chromium release was 4×10^{-4} mil/year. (W. E. Berry)

Corrosion of Refractory Metals

UNCOATED REFRACTORY METALS

Union Carbide[18] has studied the reaction rate of tungsten with oxygen at 2000 to 3000°K at pressures of 0.11 to 11.5 torrs. High gas-phase mass-transfer coefficients were obtained by impinging a high-velocity jet perpendicular to a flat surface. A maximum reaction rate was observed at each oxygen pressure, and the temperature corresponding to the maximum rate increased with increasing pressure. Below the temperature of the maximum, an apparent activation en-

ergy of 23 kcal/mole was observed. Appreciable diffusion effects were found only near the maxima. The data were correlated in terms of a two-layer oxygen-atom adsorption model for tungsten-oxidation kinetics.

The rates of volatilization of WO_2, $W_{18}O_{49}$, WO_3, and tungsten in atmospheres containing H_2O at 1050 to 1275°C have been investigated by Battles, St. Pierre, and Speiser.[19a] Rates were measured as a function of the partial pressure of H_2O and of oxygen potential (P_{H_2O}/P_{O_2}). The rate of volatilization of tungsten oxides decreased in the order $WO_3 > W_{18}O_{49} > WO_2$. Kinetic mechanisms for the experimental observations were proposed. Mass spectrographic analysis showed the volatile species to be $WO_3 \cdot H_2O$.

The oxidation of tungsten[19b] has been studied between 500 and 1100°C in CO_2 at pressures of 0.187, 0.42, and 1 atm. The results indicated that the oxidation rate was controlled by the equilibrium conditions of the W + CO_2 system, increased with increasing CO_2 pressure, and obeyed the parabolic law. The activation energy of the rate constant, determined at the lowest pressure, was 45.15 kcal/mole between 500 and 800°C and 83.2 kcal/mole between 800 and 1100°C.

The kinetics of absorption of oxygen and H_2O in niobium and tantalum, and evaporation of volatile oxides were the subjects of recent German investigations.[20,21] Steady states were investigated quantitatively at temperatures ranging from 1850 to 2560°C and pressures of 5×10^{-5} to 2×10^{-3} torr. Relations were established between oxygen or H_2O pressure, temperature, and oxygen concentration in the metal. Rates of oxygen absorption were determined.

In a Belgian study[19c] the kinetics of the reaction of tantalum with oxygen was followed using a mass spectrometer at temperatures of 1900 to 2900°K and oxygen pressures of 5×10^{-6} to 6×10^{-5} torr. The volatile oxides formed were TaO and TaO_2. The competition between oxygen solution and volatilization of oxides led to the establishment of a steady state from which rate constants and activation energies of formation of TaO and TaO_2 were deduced.

The rate of scale formation on tantalum in H_2O–H_2–Ar gas mixtures at temperatures between 840 and 1200°C has been related to gas composition and temperature.[22] At a given temperature it was found that the oxidation rate was determined by the partial pressure of H_2O and was independent of oxygen potential. The Ta_2O_5 scale formed was composed of an inner-lattice diffusion barrier and an outer layer of cracked, porous, nonprotective oxide. It was shown that a constant oxidation rate may prevail even with changing thickness of the inner scale layer.

Russian workers[23] have studied the reaction of tantalum with nitrogen at 800 to 1200°C and with air at 300 to 600°C for times up to 15 hr. The depth of nitrogen penetration increased with increasing temperature (especially above 900°C) and exposure time. The nitrogen-contaminated surface layer consisted of four zones: TaN, Ta_2N, a tetragonal phase, and a bcc phase next to the substrate. In the case of air, reaction started at 300°C and hardening was attributed to oxygen. Vacuum annealing of the reacted tantalum up to 1600°C homogenized both nitrogen and oxygen throughout the entire volume. This contamination strongly inhibited grain growth. Removal of the interstitials began at 1800 to 2000°C.

The oxidation behavior of niobium has been investigated at 400 to 600°C in superheated steam, steam plus air, and air.[19d] The oxides NbO, NbO_z, NbO_2, and Nb_2O_5 formed. The NbO_z was formed below 500°C at low oxygen pressure, and at high oxidation rates in air up to 600°C. Oxidation rates were determined by the properties of the different oxides. Below 600°C, Nb_2O_5 formed in air as a loose powder, but in steam or steam plus air, Nb_2O_5 was rather dense. The Nb_2O_5 scale flaked off on cooling. The NbO_z needles furnished better adherence to the substrate than NbO_2 and Nb_2O_5.

The effect of binary iron and cobalt additions on the oxidation of niobium in air at 500 to 900°C has been reported.[24] The addition of 30 wt. % iron or 30 wt. % cobalt increased the oxidation resistance of niobium by a factor of 100 at 900°C. X-ray analysis showed the presence of Nb_2O_5 + FeO + Fe or Nb_2O_5 + Co_3O_4 + CoO + Co in the scales.

The structure and composition of oxide phases in niobium and tantalum have been the object of recent studies.[25–27] The lower oxides of niobium have been reviewed.[28]

COATED REFRACTORY METALS

Illinois Institute of Technology[29] is developing coatings to protect tantalum-base alloys from oxidation above 3500°F (1927°C). In a slurry-sinter process, Hf–Ta coatings have been applied to tantalum using 3 to 4 wt. % Cu–Al or a fugitive vehicle. The process was capable of developing Hf–20 wt. % Ta coatings up to 20 mils thick. The coating was protective for 20 min at 3700°F (2040°C) in an O_2–H_2 torch flame. For protection at 2500°F (1371°C), the vehicle content had to be under 0.5%. At 3500°F the oxidation rate was about 20% greater in a ZrO_2 tube furnace as compared with torch heating. This behavior suggests that oxidation life could be extended if effective cooling of the subscale-interstitial contamination zone could be obtained. In the same program, duplex coatings of Ir–Hf–Ta with a copper vehicle have shown some protection of tungsten that was torch heated to 3300°F (1815°C).

Solar[30] has investigated the usefulness of sintered ThO_2 and HfO_2 coatings in the protection of tungsten and Ta–10 wt. % W nose caps for lifting reentry vehicles. Various composites were evaluated from 3800 to 5500°F (2095 to 3040°C) in a plasma-arc tunnel at Mach 2.0 to 2.5. Tungsten wire-mesh reinforcing of the coating was required, and this provided thermal-shock resistance sufficient to withstand heat-up rates up to 150°F (66°C)/sec. A vapor-deposited diffusion

barrier of tungsten in conjunction with ThO_2 or Y_2O_3-stabilized HfO_2 afforded adequate protection of Ta–10 wt. % W up to 4500°F (2482°C). Use of Hf–25 wt. % Ta limited protection to 3800°F. The ThO_2-coated tungsten demonstrated the maximum oxidation resistance for up to three typical 1-hr reentry cycles at temperatures up to 5300°F (2927°C). The HfO_2 was limited to 4900°F (2705°C).

Norwegian investigators have studied the oxidation of aluminum-coated tantalum and Ta–10 wt. % W and Al–Cr-coated tantalum at 1470 to 2910°F (799 to 1599°C) in 0.1 torr to 1 atm oxygen.[31] The 100-μ-thick coatings were applied by hot dipping. Evaluation techniques included thermogravimetric measurements, X-ray diffraction, metallography, and electron microprobe. Aluminum-coated substrates resisted 0.1 torr oxygen above 2010°F (1099°C), but breakaway oxidation occurred at 1470 to 1830°F (800 to 1000°C). Protection was provided by an alpha Al_2O_3 layer. At 1 atm oxygen, failure occurred at all temperatures. The Ta–Al phases that formed during interdiffusion were identified. The Al–Cr coatings gave improved protection. At 0.1 torr oxygen, Al–20 wt. % Cr and Al–30 wt. % Cr coatings provided excellent oxidation resistance above 1830°F and significantly retarded breakaway oxidation at the lower temperatures. The Al–30 wt. % Cr was protective for at least 50 hr at 2730°F (1500°C) in 1 atm oxygen. The increased oxidation protection was achieved by an Al_2O_3–Cr_2O_3 solid solution. The coating was not protective at 2910°F.

Battelle–Geneva[32] has conducted oxidation studies on unalloyed niobium coated with porous $NbSi_2$ impregnated with Sn–5 to 20 wt. % Al. The coating was made by reacting the substrate in a Sn–Al–Si bath. Oxidation resistance was similar to that provided by other silicide coatings, e.g., 10 to 100 hr in air at 2600°F (1427°C). The main advantage was the defect self-healing properties of the liquid phase held in place by $NbSi_2$. (B. C. Allen)

Corrosion by Nonaqueous Liquids

Nickel and Cobalt Alloys in Sodium

Some preliminary results are available from Brookhaven's thermal convection-loop program[33] to study corrosion of potential cladding materials for sodium-cooled fast-reactor fuels. To April 1967, three loops made of 321 stainless steel had each completed 1000 hr or more of operation. Weight changes of tab-type specimens removed from the hot legs (760°C) of the loops indicate that: (1) Incoloy 800 (32 Ni–21 Cr–46 Fe–0.3 Cu, by weight percent) and Multimet [20 Ni–21 Cr–32 Fe–20 Co–3 Mo–2.5 W–1 (Cb + Ta), by weight percent], the two high-nickel alloys, suffered the greatest weight losses; (2) the two cobalt-base alloys, S-1 (Co–20 Cr–10 Ni–7 Mo–2 Fe, by weight percent) and UMCO-51 (Co–28 Cr–19 Fe–2 Nb–0.3 C, by weight percent), had the lowest weight losses; and (3) in one loop where the diffusion cold trap was kept below the melting point of pure sodium, all the S-1 and Incoloy 800 specimens and some of the 316 stainless-steel specimens showed weight gains, rather than losses, after the first 1000 hr.

The nickel-base alloy Nimonic 80A was creep tested at Argonne[34] at 650°C in low-oxygen (<5 ppm) sodium and in vacuum (10^{-6} torr) under a stress of 46.2 kg/mm^2. The sodium reduced the rupture life and ductility by a factor of almost 4 (212 hr vs. 765 hr, and 1.2% vs. 4.6% true strain at fracture). This effect suggests that the surface energy of Nimonic 80A may be lowered by the penetration of liquid sodium into its grain boundaries.

Vanadium Alloys in Sodium

As indicated in previous reviews, Argonne has been studying the corrosion behavior of vanadium and its alloys in sodium up to 650°C. Briefly, it was found that when vanadium alloys containing chromium and/or titanium (5 to 20 wt. %) are exposed to flowing sodium cold trapped at 120°C or lower (<10 ppm oxygen) they gain weight very slowly as a result of the solution and inward diffusion of impurities (mostly oxygen) from the sodium. Some of the latest results[35] are shown in Table III-1. When exposed to sodium containing more than 10 ppm oxygen, the alloys lose weight rapidly as a result of the formation and loss of the nonadherent oxide ($VO_{0.9}$) at the specimen surfaces.

Table III-1 CORROSION OF VANADIUM ALLOYS[35] IN 550°C FLOWING SODIUM (6.1 m/sec)

Composition, wt. %	Weight gain, mg/cm^2, in indicated number of days					
	6.9	20.9	53.8	88.7	116.5	154.5
100 V	0	0.06	0.08	0.16	0.16	0.20
V–5 Cr	0	0.032	0.064	0.075	0.075	0.097
V–5 Cr	0	0.043	0.065	0.086	0.086	0.097
V–20 Ti	0.089	0.20	0.25	0.29	0.31	0.33
V–20 Ti	0.079	0.21	0.26	0.30	0.33	0.33
V–15 Ti–7.5 Cr	0.077	0.15	0.22	0.30	0.32	0.32
V–15 Ti–7.5 Cr	0.088	0.17	0.22	0.30	0.32	0.31
Oxygen in sodium, ppm		7.8	9.7	6.5	8.5	

It is interesting to note that both the weight gains and the differences between the various alloys shown in Table III-1 were much greater when the tests were run at 650°C than at 550°C.

Zirconium Alloys in Sodium

The French[36] exposed Zr–1 to 2.5 wt. % Cu alloys to sodium between 650 and 800°C in static capsules

made of austenitic stainless steel or Zircaloy and found very low corrosion rates. Corrosion of these Zr–Cu alloys and the alloys Zr–1.5 wt. % Al and Zr–1.5 wt. % Al–1.5 wt. % Mo–1.5 wt. % Sn in hot-trapped flowing sodium up to 550°C for as long as 2000 hr was also slight. In cold-trapped sodium the corrosion rates were increased by factors of 10 to 30. However, even with cold-trapped sodium, the steady-state rates (established after about 500 hr) were below 0.2 mg/(cm^2)(1000 hr) at 550°C and 2 mg/(cm^2) (1000 hr) at 700°C, and no breakaway occurred. The aluminum appeared to be beneficial at 700°C.

Braze Alloys in Sodium

British work on the behavior of braze alloys in liquid sodium[37] consisted in evaluating butt-brazed and fillet-brazed specimens of M316L steel (17.3 Cr–14 Ni–2.5 Mo–0.01 C, by weight percent) after 2 months' exposure to 650°C static or dynamic sodium containing 10 ppm oxygen. On the basis of weight changes, fillet brazes of Coast NP had corrosion resistance comparable to that of the parent metal, whereas Nicrobraz 30 and 50 had higher corrosion rates. All butt-brazed assemblies showed no worse corrosion than the unbrazed M316L controls.

Metallographic and microprobe examinations revealed little or no diffusion of braze elements into the steel matrix. There was some surface depletion of phosphorus and silicon from the Nicrobraz 30 and Coast NP brazes, and practically complete removal of phosphorus from the Nicrobraz 50. Overall, it appeared that Coast NP may be the most corrosion resistant of the three alloys in flowing sodium.

Graphite in Sodium

Some sodium–graphite compatibility results obtained some years ago by Atomics International[38] have been released for publication. The data can be used to predict the consequences of a flaw in the barrier between a graphite volume and a sodium-vapor contaminated gas. Sodium is absorbed by the graphite, even though the temperature of the communicating sodium surface is substantially lower than that of the graphite. However, the rate of absorption is several orders of magnitude lower than that calculated from data on gaseous diffusion through a graphite structure. Physical dilation of the graphite was found to be about 1 vol. %/wt. % sodium absorbed. Sodium vapor passing into the graphite is slowly "fixed" by reaction with the graphite, after which it cannot readily be removed by flushing with sodium-free gas.

Effects of Impurities in Sodium

Much has been written on the effects of impurities in sodium coolant on the structural materials and operation of sodium-cooled reactors. In general, impurities can interact with one another and with the container walls to cause corrosion, plugging of flow passages, and alterations in mechanical properties of the metals in contact with the sodium. On the basis of all available data, Hinze at Atomics International[39] has arrived at a set of sodium-purity requirements for a 30-year-life reactor system constructed of austenitic stainless steel and 2¼ wt. % Cr–1 wt. % Mo ferritic steel operating at a peak sodium temperature of 1200°F (649°C). He recommends hot gettering to maintain a 2-ppm limit on oxygen and prevent the fuel-element cladding from losing more than 2 mils during its 3-year (maximum) life. Other stipulations are:

1. Plugging temperature of 300°F (149°C) or less in secondary system
2. Carburizing potential of sodium low enough to keep surface of 304 stainless-steel tab below 0.5 wt. % carbon after 100 hr at 1200°F
3. Less than 5 ppm nitrogen in sodium
4. Concentration of neutron-absorbing impurities low enough to keep the macroscopic thermal-neutron absorption cross section below 0.0146 cm^2/g
5. Concentration of other impurities below the values (ppm)

Al 10	Halogens 20	Pb 10
Ba 10	K 200	Rb 50
Ca 20	Li 10	S 30
Cr 10	Mg 10	Si 10
Cs 6	Ni 10	Sn 10
Fe 25	P 20	Sr 10

Mating Materials in Sodium

As part of a program to supply engineering data needed to design mechanisms to operate in sodium to 650°C, workers at the Liquid Metal Engineering Center[40] have been exposing combinations of materials to hot sodium for periods to 2 months under static and sliding conditions. The following materials showed promise of being acceptable for rubbing surfaces in cold-trapped liquid sodium at 650°C: Stellites-3 and -6B, Hastelloy C, tungsten, some hard facings, and K-95 (WC). The tool steels AISI T-1, T-15, M-1, M-2, M-3, and M-43 had excellent wear resistance in sliding tests in sodium at 425°C but showed excessive wear and galling at 650°C. Titanium carbide suffered rapid oxidation attack in 650°C cold-trapped liquid sodium.

Brookhaven has been evaluating the Ordered Bed Fast Reactor (OBFR) concept, where the core consists of a rectangular container full of fuel spheres cooled by sodium. To screen potential cladding materials for resistance to sintering at the points of contact with other spheres, the workers subjected ¼-in.-diameter spheres of the cladding materials to compressive loads at 700°C in "purified" sodium for 1 week.[41] The presence of oxygen getters like Ti, Nb, Al, or Mo in 300- and 400-series stainless steels

prevented sintering. Thus, although almost all 304 and 410 stainless-steel balls sintered, their respective chromium–nickel analogs (321, 347, and 405) did not. Neither did 316—presumably because it contains molybdenum. Pure chromium sintered. Solid-solution alloys of aluminum and iron or aluminum and vanadium did not sinter because Al_2O_3 was formed. Thermal cycling did not affect the sintering results.

Corrosion by Indium

As part of the SNAP-8 materials investigation,[42] Aerojet-General found that indium (melting point, 160°C) did not react with 316 stainless steel under static, isothermal conditions up to 700°C. On this basis, molten indium was used to form a thermal bond between the thermocouples and thermowells in the mercury-vapor line of a laboratory boiler. Failure of two of the wells after 143 hr of loop operation at 600 to 700°C was attributed to diffusion, alloying, and possible intermetallic-compound formation between the indium and the stainless steel under the dynamic loop conditions. Consequently the use of indium for this application was discontinued.

Corrosion by Organics

In Canada, studies have been in progress[43] to determine whether low-neutron-absorption materials like sintered aluminum product (SAP) or zirconium alloys could be used to replace the stainless-steel pressure tubes or carbon-steel components of reactors cooled by organics like Santowax OM (Monsanto mixture of terphenyls) or HB-40 (hydrogenated terphenyls). It was found that, although SAP has excellent resistance to corrosion by organics, there are problems with quality control of the material and with its compatibility with UO_2. Tests with Zircaloy-2, Zircaloy-4, low-nickel Zircaloy-2, and Zr–2.5 wt. % Nb in Santowax OM up to 425°C showed that hydriding of the zirconium alloys can be substantially reduced by maintaining 50 ppm or more of water in the organic and keeping chlorine contamination to near-zero levels. However, even the best of these alloys (Zr–2.5 wt. % Nb) would become excessively hydrided after about 5 years, which is much too short for pressure-tube life in a large power reactor. Two new zirconium alloys that have been tested and appear more attractive are Zr–0.7 wt. % Cu–0.2 wt. % Fe and Zr–0.2 wt. % Sn–0.1 wt. % Fe–0.1 wt. % Ni–0.1 wt. % Nb (called Ozhennite 0.5).

Literature Reviews and Publications

An interpretive literature review has been published by Oak Ridge[44] on the effects of liquid and vapor cesium on structural materials. This was part of a study to compare cesium with potassium as a Rankine-cycle working fluid. It was concluded that the corrosion properties of cesium, like those of sodium and potassium, are intimately associated with the effects of interstitial impurities. Furthermore, if these impurities are kept at low levels, conventional and refractory metals behave qualitatively the same in cesium as they do in sodium and potassium. However, not enough attention has been paid to the impurity aspects in cesium studies to date, and more definitive research is needed.

In a separate report,[45] design and test experience with cesium and potassium components for space power plants has been reviewed and summarized. This report contains a complete bibliography of all published literature on the subject.

Summaries of the papers presented at the 1965 Symposium on Materials for Large Space Power Systems appeared in *Transactions of the American Nuclear Society*, 8(2): (1965). Several of the papers have now been published[46] in their entirety. These include Oak Ridge[46a] and Battelle–Columbus[46b] studies on refractory metals in lithium above 1000°C, Brookhaven work[46c] on the relative corrosiveness of boiling–refluxing Li, Na, K, Rb, and Cs in Nb–1 wt. % Zr capsules, and United Nuclear results[46d] on carbon and nitrogen transfer by molten potassium in a bimetallic system.

Weeks of Brookhaven has published summary descriptions[47] of various U. S. programs on the corrosion of steels, Incoloys, vanadium-base alloys, and cobalt-base alloys by sodium.

A supplement[48] has been issued to update the U. K. bibliography on liquid metals, listing 649 references for the years 1964 and 1965. (E. M. Simons)

Metal-Water Reactions

Isothermal studies of the nickel–steam reaction have been initiated at Argonne.[49] The experiments were conducted in a high-pressure furnace with Grade A nickel rod contained in impervious alumina crucibles. For all cases the steam flow rate past the samples was held constant at approximately 5 g/min. Experiments were conducted at three temperatures (1400, 1500, and 1600°C). At 1400°C the area of the samples exposed to steam was assumed to be the original geometric area. For experiments at 1500 and 1600°C, where nickel is molten, the area was assumed to be that of the inside diameter of the crucible. The reaction rate at 1400°C was found to be very low, i.e., an average reaction rate for a 100-min experiment was approximately 0.11 ml hydrogen (STP)/(cm^2)(min). Figure III-1 shows the results of experiments at the two other temperatures and indicates that molten nickel reacts approximately in accordance with the parabolic rate law. Experiments at 1500°C were performed at steam pressures of 1, 8, and 16 atm and indicate that there is no significant effect of pressure on the reaction rate.

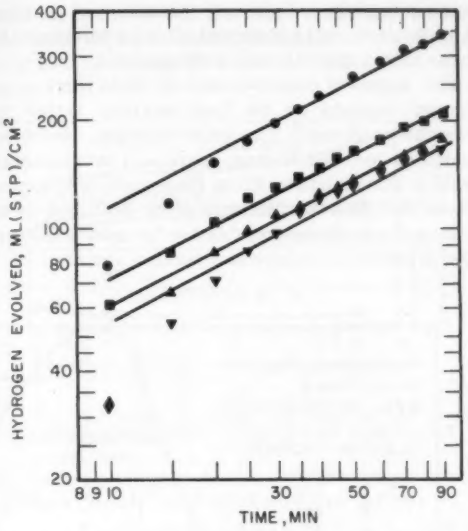

Fig. III-1 Hydrogen evolution as a function of time for the reaction between nickel and steam at various temperatures and pressures.[49] ●, 1600°C, 1 atm; ■, 1500°C, 16 atm; ▼, 1500°C, 8 atm; and ▲, 1500°C, 1 atm.

Isothermal steam-oxidation experiments with zirconium alloys were performed by General Electric[50] using a thermogravimetric technique previously described (*Reactor Materials*, Vol. 9, No. 4). The following alloys were tested: (1) Zircaloy-2 spheres at 1600°C; (2) Zircaloy-4 disks at 1250 and 1600°C; and (3) disks of Valoy* (a zirconium alloy) at 1200, 1400, and 1615°C. Parabolic rate constants were determined from these experiments and are shown in Fig. III-2, together with pertinent literature data.[51–53] Baker[51] performed oxidation experiments with zirconium metal, whereas Lemmon[52] and Bostrum[53] used Zircaloy-2. It was concluded in this study that the oxidation rate of zirconium, Zircaloy-2, Zircaloy-4, and Valoy in steam can be adequately expressed by the equation

$$W^2/t = 7.10 \times 10^5 \exp\left(\frac{-40{,}500 \pm 1200}{RT}\right)$$

where W = weight gain, mg of oxygen/cm²† of area
t = time, sec
R = gas constant, cal/(mole)(°K)
T = absolute temperature, °K

In addition to the aforementioned Zircaloy studies, General Electric researchers also investigated the

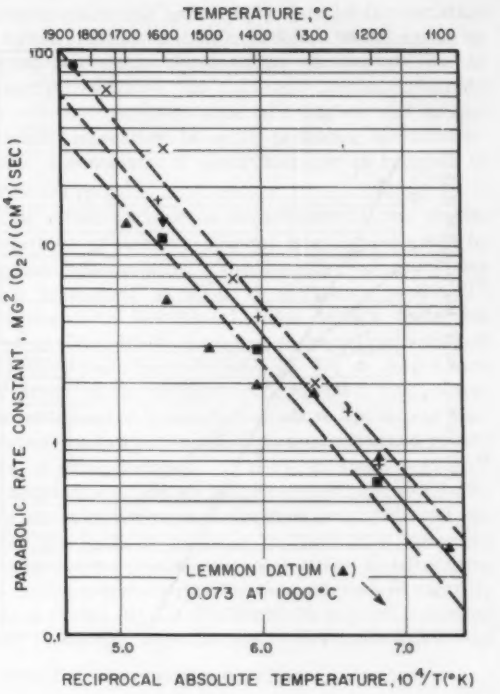

Fig. III-2 Oxidation of zirconium by steam.[50] ■, Zircaloy spheres; ▼, Zircaloy disks; ×, Valoy disks; ●, Baker;[51] ▲, Lemmon;[52] +, Bostrom.[53]

isothermal corrosion of 304 stainless steel by steam using the same thermogravimetric technique. The corrosion data showed a parabolic reaction rate, following an initial 6- to 28-min period of linear behavior, and a marked temperature dependence. Reaction-rate constants calculated from the parabolic portions of the curves for weight gain vs. time are shown in Table III-2 and are presented in the form of an Arrhenius plot in Fig. III-3. These data can be adequately represented by the equation

$$W^2/t = 2.4 \times 10^{12} \exp\left(\frac{-84{,}000 \pm 2400}{RT}\right)$$

where the nomenclature is the same as previously mentioned. For comparison purposes the parabolic

Table III-2 RESULTS OF OXIDATION OF 304 STAINLESS STEEL BY STEAM[50]

Temp., °C	Parabolic rate, $mg^2(O_2)/(cm^4)(sec)$	Temp., °C	Parabolic rate, $mg^2(O_2)/(cm^4)(sec)$
1000	0.0095	1200	0.800
1050	0.0302	1250	2.07
1100	0.0950	1300	4.38
1150	0.180	1350	12.97
1200	0.750		

*General Electric trademark for an alloy having the following composition: 2 at. % Cr; 0.16 at. % Fe; <70 ppm Ni; <100 ppm Sn; balance Zr.

†To convert W^2/t from $[mg^2(O_2)/(cm^4)(sec)]$ to $mg^2(Zr)/(cm^4)(sec)$, multiply by 8.126.

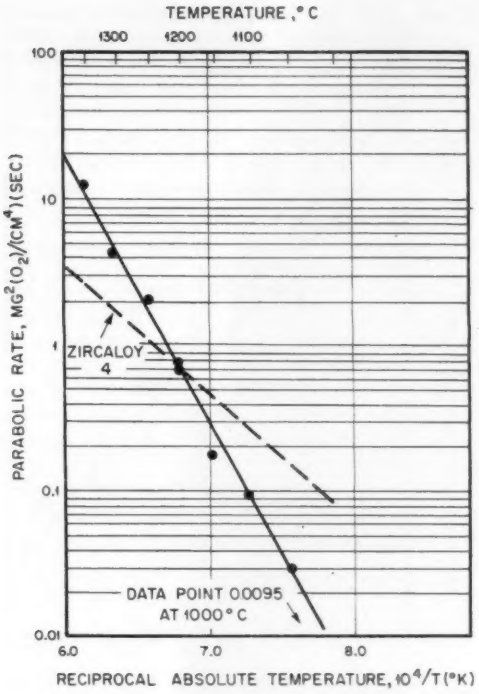

Fig. III-3 Oxidation of 304 stainless steel by steam.[50]

rate data for Zircaloy-4 are also shown. As seen in Fig. III-3, the temperature coefficient of reaction is much greater for stainless steel than for Zircaloy-4.

(J. M. Genco)

Radiation Effects in Structural Materials

Zirconium and Aluminum Alloys

A failure mechanism for cladding materials during irradiation has been proposed by O'Donnell.[54] This mechanism relates failure to the plastic instability that occurs after low strains in irradiated materials because of irradiation-induced losses in work-hardening capability of the material. Figure III-4 illustrates the agreement of the predicted theory with experimental results for failures of irradiated Zircaloy-2 cladding.[54,55] The Zircaloy-2 cladding was deformed by irradiation-induced swelling of uranium fuel. The increased strain, prior to plastic instability, was attributed to recovery of strain-hardening ability due to annealing out of irradiation damage at higher temperatures. The effect[56] of large fluences on the room-temperature mechanical properties of Zircaloy-2 is illustrated in Fig. III-5. Only minor increases in yield and ultimate strength, and decreases in elongation, were observed after irradiation to fluences higher than 2×10^{21} neutrons/cm^2.

The degree of embrittlement of oxide films on zirconium depends on the fast neutrons rather than thermal neutrons.[57] The embrittlement, which was evaluated by bend testing, increased with increasing neutron accumulation. From these results it was concluded that the embrittlement of the ZrO_2 film by fast neutrons may be responsible for the enhanced corrosion of zirconium alloys in a nuclear environment.

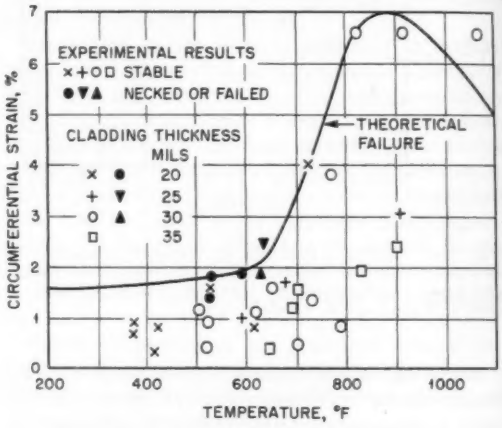

Fig. III-4 Nominal circumferential strain at instability ($\epsilon_\theta = n/2$) vs. temperature.[54,55]

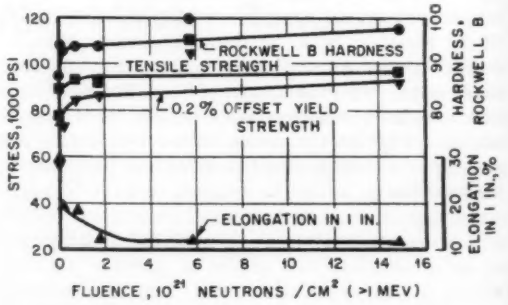

Fig. III-5 The effect[56] *of large fluences on the room-temperature mechanical properties of Zircaloy-2.*

The effects of large fluences (1.3×10^{22} neutrons/cm^2) on the mechanical properties of 2024, 6061, and 356 aluminum have been determined.[56] These aluminum alloys undergo decreasing elongation with increasing fluences, the strength values reach a maximum at a fluence of about 2×10^{21} neutrons/cm^2, after which they remain the same or decrease slightly.

Figure III-6 illustrates the room-temperature hardness, yield strength, ultimate strength, and elongation of 6061 aluminum as a function of fluence.

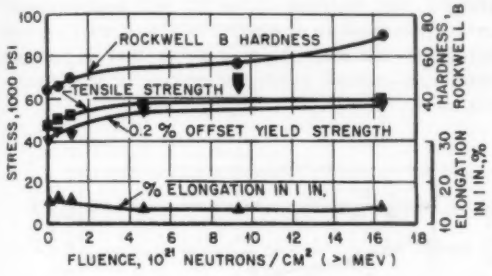
ROCKWELL B HARDNESS
TENSILE STRENGTH
0.2 % OFFSET YIELD STRENGTH
% ELONGATION IN 1 IN.
STRESS, 1000 PSI
HARDNESS, ROCKWELL B
ELONGATION IN 1 IN.,%
FLUENCE, 10^21 NEUTRONS / CM^2 (>1 MEV)

Fig. III-6 The effect of large fluences on the room-temperature mechanical properties of 6061 aluminum.[56]

Stainless Steels and Nickel-Base Alloys

Since most of the irradiation-induced ductility loss at 650°C takes place in uniform elongation, the theory describing linkup of helium bubbles at these temperatures as the cause of failure is questioned.[58] It is suggested that below about 700°C the fracture in irradiated materials is mainly caused by the initiation of wedge cracks and their subsequent stabilization by lithium atoms that decrease the surface energy. At temperatures above 700°C, where helium diffusivity and vacancy concentration are higher and grain-boundary migration is more probable, the helium-bubble mechanism of embrittlement is believed to predominate.

The effect of neutron irradiation on the tensile properties of Incoloy 800 has been investigated by Swedish researchers.[59] The Incoloy 800 specimens were irradiated at 40°C to a fluence of 2×10^{19} neutrons/cm^2. Results of these tensile tests are given in Table III-3. Annealing of the unirradiated and irradiated specimens at 650°C for 290 hr did not have any effect on the mechanical properties. The greater embrittlement at temperatures above 750°C was considered due to an increase in the nucleation and growth rate of grain-boundary cavities. In another study,[60] irradiation at elevated temperatures had no significant effect on the yield strength of Incoloy 800 but reduced the ductility as shown in Table III-4. Attempts to improve the postirradiation ductility by increasing the titanium content resulted in more severe ductility losses (Table III-5). The decrease in postirradiation total elongation with increasing titanium content was

Table III-3 EFFECT[59] OF IRRADIATION ON THE MECHANICAL PROPERTIES OF INCOLOY 800

Test temp., °C	Heat-treatment	Yield strength (0.2% offset), 1000 psi		Ultimate strength, 1000 psi		Uniform elongation, %		Total elongation, %	
		Unirradiated	Irradiated	Unirradiated	Irradiated	Unirradiated	Irradiated	Unirradiated	Irradiated
RT	None	25.6	32.6	71.7	80.5			47	47
650	None	17.8	16.6	43.5	35.9	40.0	28.5	45	29
750	None	16.6	15.6	25.6	22.7	17.0	10	28	12
820	None		15.6		18.5		8		11
RT	*		29.8		73.0		42		57
650	*	17.0	17.8	43.5	41.1	40.5		42	32
750	*	15.6	15.6	24.1	22.7	16	10	29	11
820	*	16.3	13.6	19.8	15.6	8	6	17	8

*Twelve days at 650°C.

Table III-4 EFFECT[60] OF NEUTRON IRRADIATION ON MECHANICAL PROPERTIES OF INCOLOY 800

Test temp., °C	Exposure conditions		Fluence, neutrons/cm^2		Postirradiation tests		Preirradiation tests	
	Temp., °C	Time, hr	Fast	Thermal	Yield strength (0.2% offset), kg/mm^2	Total elongation, %	Yield strength (0.2% offset), kg/mm^2	Total elongation, %
25	400	700	6×10^{19}	4.5×10^{19}	32	47	28	43
25	400	1340	4×10^{20}	3.0×10^{20}	33	36	29	38
25*	538	200	3.3×10^{20}		31	34	28	38
25	177	2500	1.2×10^{21}	1.6×10^{21}	63	32	22	50
25	704	5200	2.0×10^{21}	1.7×10^{21}	22	45	32	50
593	400	700	6×10^{19}	4.5×10^{19}	19	40	20	41
593	400	1340	4×10^{20}	3.0×10^{20}	20	23	20	35
593*	538	200	3.3×10^{20}		18	22	21	32
593	704	5200	2×10^{21}	1.7×10^{21}	15	14	14	41
593	177	5000	2.4×10^{21}	3.2×10^{21}	22	10	18	42
704*	538	200	3.3×10^{20}		15	13	17	63
704	704	630	3.5×10^{20}	3.0×10^{20}	14	25	15	47
704	704	5200	2.0×10^{21}	1.2×10^{21}	13	7	14	71

*Fast-neutron exposures in EBR-II. Values in many cases verified with duplicate coupons.

Table III-5 EFFECT[40] OF TITANIUM CONTENT ON THE POSTIRRADIATION TOTAL ELONGATION OF INCOLOY 800

Fluence, neutrons/cm²	Test temp., °C	Elongation, %, at indicated titanium content	
		0.2 wt. %	0.9 wt. %
3.5×10^{20}	593	22	1.0
2.0×10^{21}	704	7	>1.0

attributed to matrix hardening that caused the deformation to occur at the grain boundaries. These results suggest that greater losses in ductility occur in precipitation-hardened alloys than in solid-solution-hardened alloys because of irradiation.

The effect[50] of irradiation on the stress-rupture properties of Hastelloy N is shown in Fig. III-7. A good correlation of the Larson–Miller parameter as a function of stress was obtained for both unirradiated and irradiated Hastelloy N. The effect of irradiation on welded Hastelloy N is illustrated in Fig. III-8. It can be seen that welding itself reduces the stress-rupture properties significantly, and irradiation has no further effect.

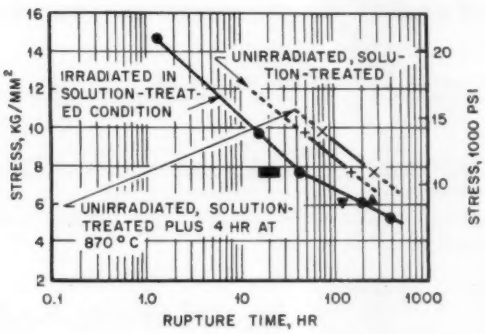

Fig. III-7 Stress-rupture properties[50] of Hastelloy N at 815°C.

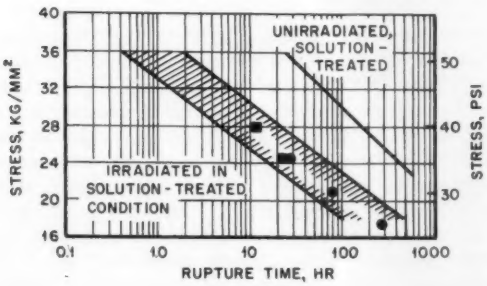

Fig. III-8 Stress-rupture properties[50] of welded Hastelloy N at 650°C. ●, unirradiated, as welded; ■, irradiation at 650°C, as welded. Fluence (thermal), 2.5×10^{20} neutrons/cm²; fluence (fast), 4.4×10^{19} neutrons/cm².

The effects[56] of long-term irradiations on the room-temperature mechanical properties of Inconel X are shown in Fig. III-9. The most significant irradiation-induced effect is the decrease of yield and ultimate strength with fluences above 2×10^{21} neutrons/cm². Since an increase in elongation is also occurring with increasing fluence, it is possible that significant irradiation-induced overaging may occur in the complex alloy.

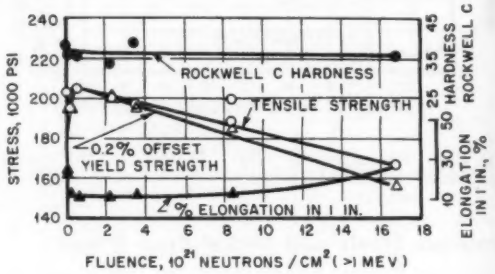
STRESS, 1000 PSI
ROCKWELL C HARDNESS
TENSILE STRENGTH
0.2% OFFSET YIELD STRENGTH
2% ELONGATION IN 1 IN.
HARDNESS ROCKWELL C
ELONGATION IN 1 IN., %
FLUENCE, 10²¹ NEUTRONS / CM² (>1 MEV)

Fig. III-9 Effect of irradiation on the mechanical properties[56] of Inconel X.

Vanadium Alloys

Room-temperature tensile tests[62] have been performed on V–20 wt.% Ti and V–15 wt.% Ti–7.5 wt.% Cr alloys that were irradiated, in a predominantly fast fluence in EBR-II, to up to 4.6×10^{21} neutrons/cm² at temperatures from 500 to 660°C. Results of these tests, as given in Table III-6, indicate that no changes in yield or ultimate strength occur as a result of irradiation. The only measured change was the reduction of elongation of the V–15 wt.% Ti–7.5 wt.% Cr alloys that were irradiated at the lower temperature. These minimal changes in tensile properties were related to the annealing out of irradiation damage at the irradiation temperatures.

Pressure-Vessel Steels

The sensitivity of A-302B steel to irradiation embrittlement was found to be controlled by irradiation-induced changes in σ_i (friction stress) and k_y (grain-boundary resistance).[63] The σ_i generally increased with increasing fluence; however, the steels sensitive to irradiation showed considerably greater increases of σ_i as a function of irradiation. The k_y values were observed to decrease with increasing irradiation, especially above 10^{18} neutrons/cm². The dependency of yield-strength recovery in irradiated A-212B steel as a function of irradiation temperature, fluence, and postirradiation annealing temperature is illustrated[3] in Fig. III-10. It has also been shown that the increase in yield stress of vacuum-melted iron irradiated to a constant fluence of 5×10^{18}

Table III-6 ROOM-TEMPERATURE TENSILE PROPERTIES[62] OF VANADIUM-BASE ALLOYS IRRADIATED IN EBR-II

Composition (balance vanadium), wt.%	Condition	Fluence at center of specimen, 10^{21} neutrons/cm^2	Irradiation temp., °C	Yield strength (0.2% offset), kg/mm^2	Ultimate tensile strength, kg/mm^2	Elongation, %	
						Uniform	Total
20 Ti	Unirradiated			63.2	75.2	20.0	25.8
20 Ti	Unirradiated 30 days, 550°C			52.6	64.8	15.0	20.4
20 Ti	Irradiated	1.8	540	49.5	60.7	15.8	22.5
20 Ti	Irradiated	3.2	600	53.5	64.6	15.4	21.7
20 Ti	Irradiated	4.8	650	57.6	67.5	14.2	19.9
20 Ti	Irradiated	4.6	660	56.9	67.7	13.0	18.2
15 Ti–7.5 Cr	Unirradiated			64.4	72.3	15.0	20.6
15 Ti–7.5 Cr	Unirradiated 30 days, 550°C			67.2	76.3	15.0	19.9
15 Ti–7.5 Cr	Irradiated	1.6	500	61.3	72.2	10.4	14.8
15 Ti–7.5 Cr	Irradiated	3.2	570	58.1	68.9	10.0	14.2
15 Ti–7.5 Cr	Irradiated	4.9	610	68.5	81.8	13.6	17.8
15 Ti–7.5 Cr	Irradiated	4.6	630	65.6	78.3	13.6	18.3

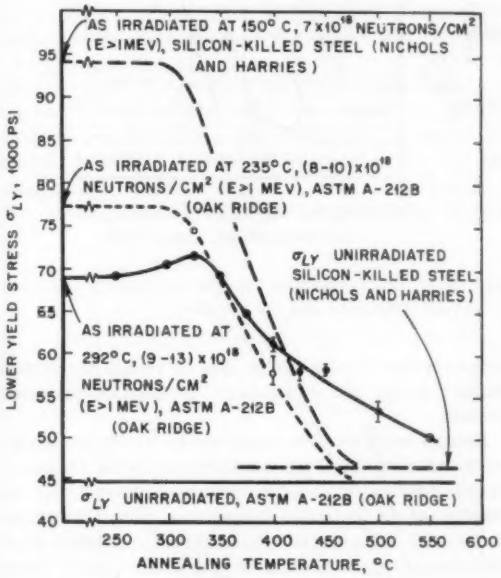
AS IRRADIATED AT 150° C, 7×10¹⁸ NEUTRONS/CM² (E>1MEV), SILICON-KILLED STEEL (NICHOLS AND HARRIES)
AS IRRADIATED AT 235°C, (8-10)×10¹⁸ NEUTRONS/CM² (E>1 MEV), ASTM A-212B (OAK RIDGE)
σLY UNIRRADIATED SILICON-KILLED STEEL (NICHOLS AND HARRIES)
AS IRRADIATED AT 292° C, (9-13) x 10¹⁸ NEUTRONS/CM² (E>1 MEV), ASTM A-212B (OAK RIDGE)
σLY UNIRRADIATED, ASTM A-212B (OAK RIDGE)
LOWER YIELD STRESS σLY, 1000 PSI
ANNEALING TEMPERATURE, °C

Fig. III-10 Recovery of lower yield stress of irradiated low-carbon pressure-vessel steels.[3]

neutrons/cm^2 at 95°C does not depend on the neutron flux in the range 2×10^{11} to 2×10^{13} neutrons/(cm^2)(sec).[3] The ^{10}B content of pressure-vessel steels affects the irradiation sensitivity of these steels.[64] Three sets of Fortiweld steel specimens containing equivalent amounts (exact amount not specified) of ^{11}B, natural boron, and ^{10}B were irradiated to equivalent fluences. The results of postirradiation impact tests shown in Fig. III-11 indicate that ^{10}B caused the largest shift in the transition temperature. This behavior is attributed to the helium which is generated from the ^{10}B by (n,α) reactions.

Impact tests were performed on surveillance specimens that were irradiated at 550°F (288°C) in front of the thermal shield in the Elk River Reactor. Results[65] of these impact tests are given in Fig. III-12. These results indicate that the irradiation-induced shift in the ductile-to-brittle transition temperature falls in the range of values given by the Naval Research Laboratory for similar irradiations. It was noted that only minor changes in tensile properties were induced by irradiation of the pressure-vessel and dissimilar-weld specimens, whereas the fatigue strengths were increased. Irradiation of A-302B steel to a fluence of 4×10^{17} neutrons/cm^2 reduced the fatigue life at high strains and increased the fatigue life at low strains.[66] The fatigue toughness (total energy to failure) increased with the number of cycles to failure.

The ductile-to-brittle transition temperature[3] in the heat-affected zone of welded A-212B C–Si steel is shifted the same amount as the base metal by irradiation at 70°C to 9×10^{18} neutrons/cm^2. About 65% of the shift in the transition temperature is recovered in the base metal by annealing at 300°C for 2 hr. However, only 30% of the shift is recovered in the heat-affected zone by an identical annealing treatment.

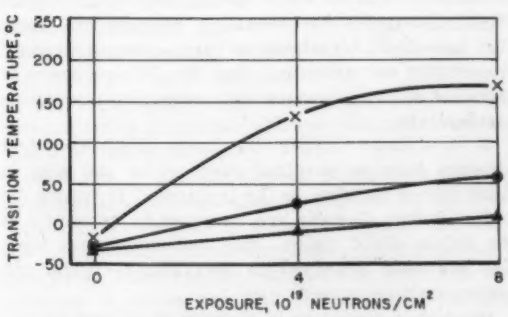

Fig. III-11 Influence of neutron irradiation and ^{10}B concentration on changes in transition temperature in Fortiweld steel.[64] *●, natural boron; ×, ^{10}B; ▲, ^{11}B.*

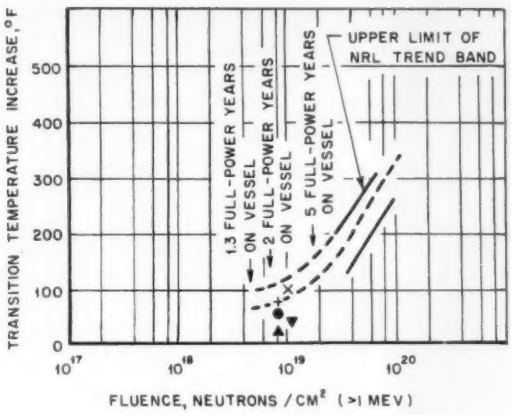

Fig. III-12 Shift in nil ductility transition temperature of Elk River Reactor surveillance specimens and vessel when irradiated[65] at 550°F, ▲, ▼, A-302B; ×, +, A 105-II; ●, A-212B.

Basic Mechanisms of Irradiation Damage

The size and distribution of irradiation-induced point defects is believed to depend on the homologous temperature of irradiation (irradiation temperature/melting temperature).[67] For example, it has been found that irradiation at 50°C to a fluence of 6×10^{18} neutrons/cm² results in defect clusters of 35, 60, and 100 A, respectively, in rhenium, molybdenum, and nickel. The density of these clusters was inversely proportional to their size. Increasing the fluence results in development of visible loops, which eventually lead to a tangled dislocation network. Introduction of interstitial atoms into molybdenum resulted in somewhat larger clusters than those observed in pure molybdenum after equivalent fluences. Annealing of the irradiated nickel, molybdenum, and rhenium at equivalent homologous temperatures resulted in growth of the defect clusters in nickel into loops, whereas the defects in rhenium and molybdenum increased in size as their density decreased. Figure III-13 illustrates the annealing kinetics for steels that have been irradiated at various temperatures.[3] Apparently the annealing time for 50% recovery of the yield stress increases with increasing irradiation temperature.

In irradiated copper the large (2000-A) defect clusters form in ultralong-range order and align in habit planes parallel to (1 1 1) planes.[68] In copper the 100-A defect clusters are removed by annealing in the 300 to 400°C range. This nonhomogeneous damage has been observed in both single-crystal and polycrystalline copper.

Irradiation hardening in niobium is considered dependent on the intersititial content.[69] In the 75 to 200°C temperature range, the oxygen interstitial is believed to cause irradiation hardening, whereas at

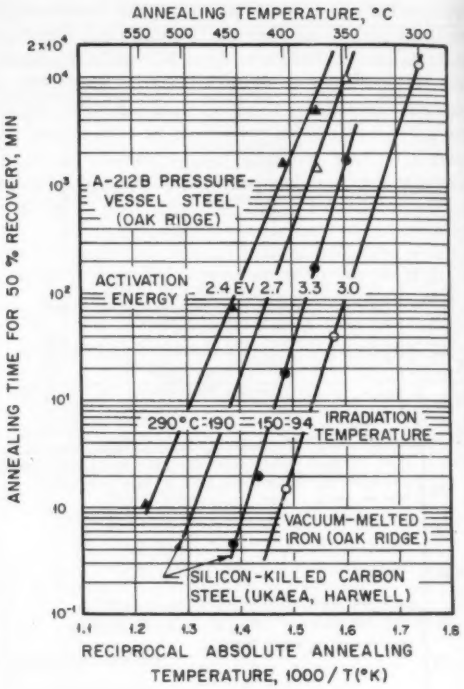

Fig. III-13 Annealing time for 50% recovery of the yield stress for irradiated iron and steel.[3]

temperatures in the 200 to 320°C range, the carbon atoms appear to stabilize irradiation-produced defects.

Helium bubbles were observed in irradiated Al–Li alloys as a result of the (n,α) reaction in the lithium.[70] These helium atoms precipitate preferentially as bubbles along subgrain boundaries and dislocations as well as along grain boundaries. The bubbles grow significantly upon heating at 400°C and above. After heating at 550°C, the size of the bubbles ranged from 10 to 1000 A. The shape of the bubbles was polyhedral after heating at 400°C, and the number of planes that bound the polyhedral increased with increasing annealing temperature. After annealing at 550°C, a large number of spherical bubbles were observed. (M. Kangilaski)

Metallurgy of Refractory Metals

Chromium

During an X-ray investigation of Cr–Mo alloys by the Dutch,[71] the pattern showed, in addition to the bcc reflections of the solid solution, strong extra lines that could be indexed on a cubic cell with lattice con-

stant a_β = 4.65 A. The ratio between the lattice constants of both phases (a_β/a_α = 1.58) was practically the same as the ratio between beta tungsten (a = 5.036 A) and bcc tungsten (a_α = 3.158 A), which is a_β/a_α = 1.59. From intensity calculations of the X-ray pattern, it was concluded that this structure is ordered, with six chromium atoms situated on the 6(c) sites and two oxygen atoms on the 2(a) sites of an A15 cell. Therefore it was determined that the phase found was an oxide with the formula $(Cr,Mo)_3O$.

Investigators at General Electric[72] have successfully prepared a number of chromium-base alloys. Figures III-14 and III-15 show the strength and ductility of the strongest of the alloys developed in this program. Several dilute carbide-containing and boride-containing alloys exhibited considerable ductility at room temperature and measurable plastic flow at 0°F (−17.8°C) and below in both the wrought and fully recrystallized conditions. Depending on the nature of the dispersion, some alloys also provided tensile strengths as high as 35,000 to 40,000 psi at 1900°F (1038°C). Addition of 4 at.% molybdenum to the dispersed-carbide alloys increased the tensile strength at 1900°F to about 60,000 psi but raised the ductile-to-brittle transition temperature to 300 and 400°F. The highest strengths were observed in a Cr−6 at.% W−0.10 at.% Y alloy, which had tensile

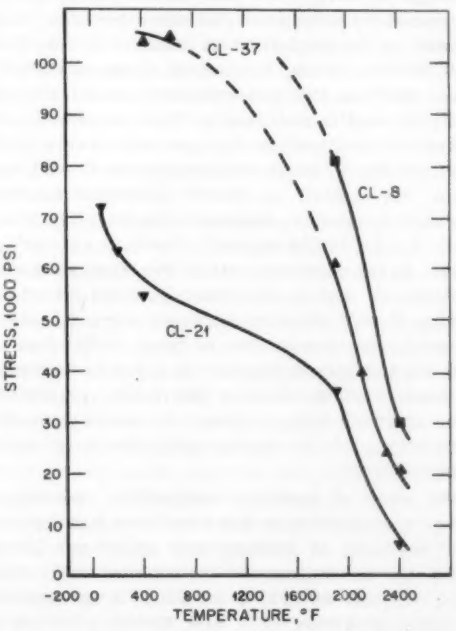

Fig. III-14 Tensile strengths of strongest chromium-base alloys of each general type after 2000°F, 1-hr annealing.[72] Strain rate = 0.03 min^{-1}, ■, Cl-8, 6 W−0.10 Y; ▲, Cl-37, 4 Mo−0.05 Y−0.3 Hf−0.3 Zr−0.4 C; ▼, Cl-21, 0.05 Y−0.3 Hf−0.3 Zr−0.4 C.

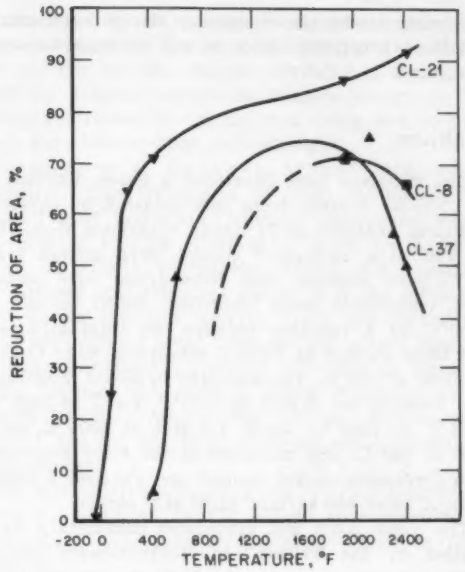

Fig. III-15 Tensile ductility of strongest chromium-base alloys of each general type after 2000°F, 1-hr annealing.[72] Alloy composition is the same as in Fig. III-14.

strengths of 81,000 and 30,100 psi at 1900 and 2400°F (1038 and 1316°C), respectively. Tungsten was definitely superior to molybdenum with respect to strengthening but appeared to have a more adverse effect on workability.

Substitution of cobalt for much of the rhenium in ductile Cr−35 at.% Re alloys resulted in cold workability in single-phase alloys in the cast condition. These Cr−Re−Co compositions, however, were subject to profuse sigma precipitation and consequent embrittlement upon aging at 1600 to 1800°F (871 to 982°C) owing to a rapid decrease in the cobalt solvus with decreasing temperature. Such alloys, therefore, did not appear to be practical.

Dilute Cr−Y alloys with NbC, TaC, and TiC additions had finely dispersed carbides and exhibited attractive strength characteristics. The oxidation−nitridation resistance of such alloys, however, was markedly inferior to those with ZrC or HfC dispersions. Their reliable use will require a more effective means of preventing nitrogen embrittlement than that afforded by yttrium.

Additions of lanthanum were shown to be effective in preventing nitridation in complex alloys containing carbides, as well as in simple Cr−La and Cr−Mo−La compositions. Somewhat higher concentrations of lanthanum were required to promote nitridation resistance in alloys with NbC or TaC dispersions than in alloys with zirconium-rich carbides. Because of a low solubility in chromium and some evidence of a low eutectic temperature, potential problems in con-

solidating lanthanum-containing alloys were established. A beneficial effect on air oxidation behavior was noted.

Niobium

The Russians have developed a phase diagram of the Nb–Ni system from data obtained by physicochemical analysis of 31 alloys containing from 26.5 to 100 at.% niobium.[73] Alloys were melted from 99.7% pure niobium and N-00-grade pure nickel. Two compounds were identified: Nb_5Ni formed at 1350°C by a reaction between two solid solutions, and NbNi formed at 1570°C dissolving 49 to 61 at.% niobium at 800°C. The solubility of nickel in niobium was found to be: 8 at.% at 1570°C, 4 at.% at 1400°C, 2 at.% at 1200°C, about 1.5 at.% at 1000°C, and 1 at.% at 800°C. The hardness of the alloy increased with increasing nickel content and reached a maximum of about 640 kg/mm^2 at 40 at.% nickel.

The yield point and associated parameters were studied by the British[74] in electron-beam-refined niobium containing amounts of oxygen ranging from 150 to 800 ppm. Specimens were tested at room temperature and at strain rates from 5×10^{-5} to 2×10^{-1}/sec. The upper yield stress (σ_u), lower yield stress (σ_i), and the k_y parameter measure of dislocation pinning showed a linear relation with oxygen content of the form $\sigma = \sigma_0 + \alpha C$, where σ represents the stress parameters, σ_0 is their value at zero oxygen content, α is the increment per ppm oxygen, and C is the oxygen concentration in ppm (by weight). The oxygen dependence of σ_u, σ_y, and σ_i decreased linearly with increase in strain rate, whereas that of $\sigma_u - \sigma_y$ and the k_y parameter increased linearly with increasing strain rate. The strain-rate dependence of the yield point and associated parameters can be expressed by the equation $\sigma = A + A' \log \dot{\epsilon}$. In general, the values of A for any parameter and strain-rate range are increased and those of A' are decreased with increasing oxygen content. The dislocation velocity exponent (n) showed a relation with oxygen concentration of the form $n = 9.2 + 6.9 \times 10^{-3} C^{1.3}$.

It was shown that the yield drop was due to dislocation multiplication and that the k_y parameter represented the critical stress required to operate dislocation-generation sources ahead of the Lueders band front. The density of mobile dislocations at the upper yield stress decreased with increasing content of oxygen, whereas their velocity and the stress corresponding to unit velocity of dislocations increased with increasing oxygen content.

Experiments to purify niobium with respect to interstitial impurities were conducted by the Germans.[75] The content of interstitially dissolved impurity atoms was reduced to about 10 at. ppm from 3800 at. ppm by annealing in high vacuum. Niobium specimens thus treated did not show a measurable recovery of electrical resistivity after plastic deformation and subsequent tempering between room temperature and 360°C. Instead a small continuous decrease in resistivity was observed. However, treatment with oxygen after purification resulted in a pronounced recovery between 100 and 200°C. Within the concentration range investigated, the total recovery of residual resistivity at 230°C was found to depend linearly on the oxygen content and amounted to 8.5% of the additional resistivity due to oxygen. Another recovery stage related to nitrogen was found in niobium between 275 and 360°C. The observed recovery behavior was interpreted by assuming that the impurity atoms migrated to lattice defects in characteristic temperature ranges, thus contributing less to the resistivity than if interstitially dissolved. The resistivity recovery of a purified specimen was approximately 1.6 times the additional resistivity caused by residual impurities. Only about 10% of this latter resistivity annealed out when the specimens were treated with gas. Therefore an interpretation based on the migration of oxygen or nitrogen does not apply in this case. The observed recovery may be due to annealing of structural point defects produced during deformation.

Niobium alloys containing 5 to 80 wt.% tantalum, 2.5 to 80 wt.% vanadium, and 5 to 41 wt.% titanium were melted in an argon-atmosphere arc furnace by Russian workers,[76] and their elastic properties were measured by ultrasonic and other methods. An increase in the proportion of tantalum in Nb–Ta alloys led to a marked increase in elastic modulus (E), shear modulus (G), and volumetric modulus of elasticity (Q) and to decrease in Poisson ratio (μ). The effect of vanadium on niobium was more complex, i. e., in Nb–V alloys containing up to 40 wt.% vanadium, the moduli E and G increased markedly, whereas μ sharply decreased. In the alloy with 40 wt.% V, $E = 14{,}730$ kg/mm^2, $G = 5440$ kg/mm^2, $\mu = 0.355$. As the vanadium content was increased further, however, E and G decreased. Niobium alloys containing 5 wt.% titanium displayed some increase in E and G, but any further increase in titanium content led to a steady decrease in E and G. An analysis of these findings reveals interesting regularities; e.g., in every case, a change in one of these characteristics led to an opposite change in another characteristic.

The effect of tantalum, molybdenum, and tungsten on the microstructure and room- and high-temperature hardness of niobium-base alloys was investigated by the Russians.[77] Arc-melted alloy ingots were annealed at 1700°C for 50 hr. It was found that the microstructure of a cast Nb–Ta alloy had the typical structure of a single-phase solid solution. With increasing tantalum content, the substructure became more distinct. As-cast Nb–5 wt.% Ta–5 wt.% Mo and Nb–10 wt.% Ta–5 wt.% Mo alloys also exhibited a single-phase structure, with elongated

grains and traces of dendritic segregation. A noticeable segregation of impurities was observed in Nb–5 wt.% Ta–5 wt.% W and Nb–10 wt.% Ta–5 wt.% W alloys. The hardness of a Nb–10 wt.% Ta alloy at 20 and 1000°C was 180 and 105 HV, respectively. Additional alloying with 5 wt.% molybdenum or 5 wt.% tungsten increased the hardness at corresponding temperatures to 198 and 127 HV or to 192 and 120 HV, compared with 150 and 90 HV for unalloyed niobium. The creep rates (calculated from the results of hot-hardness tests) of alloys containing molybdenum and tantalum were the lowest, and those of alloys containing tantalum and tungsten were the highest.

The Russians[78] investigated the Nb–Ru system by means of microscopic and X-ray diffraction analysis, by hardness and microhardness determinations at 50 to 700°C, and by thermal-conductivity measurements at 25 to 500°C. Homogenized alloy specimens were quenched in water from 1500°C after soaking for 10 hr. The alloys corresponding to the compound NbRu at the minimum of the solidus line exhibited a solid solution, whereas the other alloys had a dendritic nature. Alloys containing up to 56 at.% ruthenium were polyhedric. The Vickers hardness of annealed and quenched specimens did not differ markedly. The 40 at.% ruthenium alloy exhibited a volume-centered cubic lattice, whereas a 42 at.% ruthenium alloy had an ordered tetragonal lattice. The high-temperature modification was close-packed hexagonal. In the range of compositions studied, the minimum of the solidus line, the electrical-conductivity curve, and the temperature coefficient of the electrical resistivity, the maximum of the hardness curve, and the transition from face-centered cubic to tetragonal all correspond to the same composition, about 40 at.% ruthenium.

The sorption kinetics and mechanical properties of dilute Nb–H solutions were investigated at the University of Oklahoma.[79] The sorption kinetics, as measured by a thermal-equilibrium technique, were found to be sensitive to surface condition and insensitive to grain size. The sorption rate was adequately described by a diffusion-controlled reaction in the temperature range 600 to 750°C, provided that the metal surface was abraded to remove effects of chemical etching. Below 600°C a surface step reaction apparently controlled the sorption process, rather than bulk diffusion. Hydrogen was found to have little effect on the strength of niobium in the temperature range 77 to 300°K. The ductility of hydrogenated niobium, however, was sensitive to hydrogen concentration, temperature, and microstructure. In fact, hydrogenated niobium was observed to undergo a ductile–brittle–ductile transition as the temperature was lowered from 300 to 77°K. Crack formation appeared to be due to a hydride precipitation in localized regions of high hydrogen concentration. Diffusion of hydrogen to the microcracks from the surrounding regions was apparently responsible for crack propagation. It was considered that (1) hydrogen adsorbs on the internal surfaces of a microcrack and thereby lowers the surface energy or (2) hydrogen diffuses to the tip of a crack and results in a lower niobium-atom bond strength.

Investigators at General Atomic[80] are using internal-friction techniques to study the microflow properties of materials. Niobium specimens were deformed in torsion to about 0.5% at 150°K by a series of slowly increasing stress–strain loops. The desired unidirectional plastic flow was accumulated during the last quarter cycle and served to break dislocations away from pinning points. Specimen characterization involved determining the internal friction and modulus defect spectrum as a function of temperature. The internal friction decreased and the specimen stiffened with increasing temperatures.

The internal-friction spectrum (Q^{-1}) for a niobium specimen is shown in Fig. III-16 as a function of temperature with various annealing states as parameters.

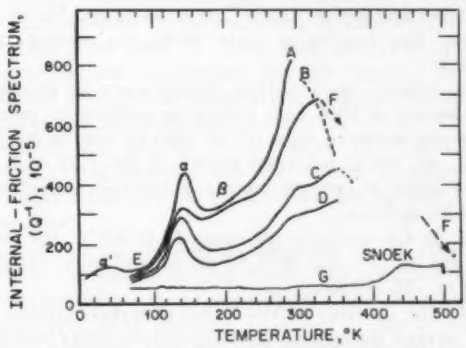

Fig. III-16 Effect of temperature on internal friction of niobium.[80] Torsional deformation is 0.5% at 150°K; strain amplitude $\epsilon_m = 8 \times 10^{-5}$; letters denote different states of annealing.

Investigators at Battelle–Columbus[81] conducted a program to improve the strength and ductility of niobium alloys by mechanical twinning. In the materials investigated it was not possible to introduce mechanical twins without introducing cracks that weakened the materials. Twin strengthening did not occur at elevated temperature in tensile tests on polycrystalline niobium, Nb–40 wt.% V, and FS-85.

Niobium and tantalum alloys were aged for 100 and 1000 hr and tensile tested at Westinghouse Astronuclear.[82] Alternate base and weld-metal specimens were tested over a wide range of conditions to provide a thorough screening of the alloys. The alloys were aged in the postweld-annealed condition and demonstrated generally excellent stability, with only

one alloy, D-43, displaying a consistent time–temperature-dependent overaging and consequent loss in strength. The loss in strength in D-43 was not surprising considering the apparent optimized preaged strength of the particular material employed in this program. The alloys FS-85, C-129Y, and SCb-291 displayed excellent stability with little change in tensile properties. Very slight losses in tensile strength were exhibited in T-111 and T-222, and no change in 2500° F (1371° C) properties was noted.

Wah Chang[83] has compiled data on a number of niobium-base alloys which may be of interest for reactor application. Physical and mechanical property data are given for the following alloys:

WC-103	(Nb–10 wt.% Hf–1 wt.% Ti–0.7 wt.% Zr)
WC-129 Y	(Nb–10 wt.% Hf–10 wt.% W–0.2 wt.% Y)
WC-1 Zr	(Nb–1 wt.% Zr)
Cb-752	(Nb–10 wt.% W–2.5 wt.% Zr)
D-43	(Nb–10 wt.% W–1.0 wt.% Zr)
SCb-291	(Nb–10 wt.% W–10 wt.% Ta)
Cb-132 M	(Nb–20 wt.% Ta–15 wt.% W–5 wt.% Mo–1.5 wt.% Zr)
FS-85	(Nb–27.5 wt.% Ta–11.0 wt.% W–0.9 wt.% Zr)

Investigators at Knolls[84] have examined Nb–Si alloys. The results of their study are summarized below:

1. Silicon is a potent strengthener in niobium. Additions of 2000 ppm silicon to niobium increased the hot hardness from 15 to 1000 kg/mm^2 at 900°C.
2. At 790°C the yield stress of Nb–0.22 wt.% Si was about 45,000 psi compared with less than 10,000 psi for niobium.
3. In the temperature range 25 to 800°C, the yield stress of Nb–0.2 wt.% Si decreased from ~55,000 psi to ~35,000 psi.
4. The ductility of Nb–Si was adversely influenced by oxygen throughout the temperature range investigated.

The tensile properties of the Nb–Si alloys are illustrated in Fig. III-17. Difficulties were encountered in the tests at 650 and 790°C owing to oxygen contamination of the specimens. This problem was solved through a modification in the testing procedure, which involved a more effective flow of inert gas in the furnace during testing.

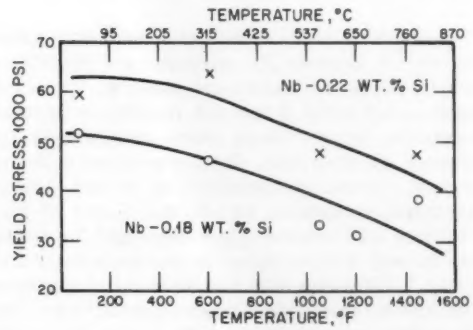

Fig. III-17 Yield stress of Nb–0.18 and 0.22 wt.% Si as a function of temperature.[14]

Molybdenum

The effect of deformation at 195 to 473°K on the electrical resistivity of high-purity molybdenum single crystals was determined by investigators at Rice University.[85] The point-defect resistivity as a function of strain was given by

$$\Delta\rho_{pd} = \Delta\rho_0\,\epsilon^m \qquad m = \begin{matrix}1.0 \text{ at } 195°K \\ 1.3 \text{ at } 273°K\end{matrix}$$

Annealing of these point defects did not affect the flow stress. The specific resistivity of dislocations in molybdenum crystals on the basis of the dislocation-density measurements by Lawley and Gaigher was -5.8×10^{-19} ohm-cm^3. This value tended to decrease with strain at higher deformation temperatures. The applied stress at low temperatures and sufficiently high strains was linear with the square root of the dislocation density.

Molybdenum single crystals were also deformed[86] in direct shear over the temperature range 78 to 400°K. All tests were conducted in a manner that placed maximum shear stress on the $(0\,1\,1)-[1\,\bar{1}\,1]$ slip system. The effects of impurity concentration on the shear stress–strain curve were determined. With additions of very minute quantities of impurities, the mechanical properties changed drastically, but the effect of impurities decreased as the amount of impurities increased. The influence of impurities was also found to decrease as the temperature of deformation increased.

The effects of C, B, Zr, and Ti additions to electron-beam-melted molybdenum and the mechanisms for improvement of its ductility by melting with the additional elements were studied by the Japanese.[87] Bend tests, measurements of intergranular fracture stresses, and observations of fracture surfaces were made. The ductility of molybdenum ingots at room temperature was improved by electron-beam melting with the optimum amounts of carbon, boron, and titanium, respectively. However, the addition of zirconium did not improve the ductility. Ingot ductility was dependent on the strengthening of grain boundaries. From fractographic observations, carbon and boron additions appeared to increase the intergranular fracture strength by the suitable amounts of intergranular precipitates. With titanium additions it was assumed that grain boundaries were strengthened by eliminating the segregation of some harmful impurities. The degree of improvement in ductility of molybdenum ingots by

additional elements depended on two opposing effects of the added elements, i.e., the lowering of ductility of matrix and the strengthening of grain boundary.

The solubility of carbon in molybdenum, tungsten, and rhenium was determined with the isothermal carburizing method by the Germans.[88] In the Re–C system, no carbide layer was found on the sample surface. The maximum solubility of carbon at the eutectic temperature amounted to 1.1 at.% in molybdenum (2180°C), 0.7 at.% in tungsten (2710°C), and 4.9 at.% in rhenium (2450°C). With molybdenum and tungsten the solubility of carbon exceeded the values previously found by the usual means. The maximum solubility of carbon found for rhenium was lower than the formerly reported value of 11.9 at.% carbon. The eutectic temperature of the three-phase equilibrium ($\alpha + \beta$ + solid) for molybdenum, tungsten, and rhenium was determined by melting experiments and compared with the values taken from the literature.

Specimens of cast and forged molybdenum were diffusion-coated with chromium, packed in chromium powder, and held at 1350 to 1600°C for 10 to 25 hr by the Russians[89] to study solid solubility in the Cr–Mo system. The diffusion layer was found to consist of an external zone with columnar grains oriented in the direction of diffusion flow, a hard middle zone with similar grains that could hardly be etched and had equal atomic contents of chromium and molybdenum, and an inner zone with polyhedral grains. Analysis of these results showed the external zone to be a solid solution with variable concentration of components and a bcc lattice, and the middle zone had a tetragonal lattice. X-ray structural analysis of annealed alloy powders revealed the presence of tetragonal-lattice lines and other odd lines that disappeared under the effect of deformation. The appearance of a tetragonal lattice in Cr–Mo alloys may be associated with ordering of the solid solution. The lines of a tetragonal lattice in all the alloys studied could be caused by dendritic heterogeneity.

In other Russian studies,[90] electron-beam-melted molybdenum (99% purity), as cast or vacuum annealed at 700 to 1500°C for 45 min, was subjected to bend tests to determine the effect of the annealing temperature on the metal structure and ductility. The as-cast specimens failed in a brittle manner at a bend angle of 30°, but specimens annealed at 900 and 1200°C sustained a bend angle of 180° without failure. Specimens annealed at 1400 and 1500°C first cracked at a bend angle of 150 and 60° and failed along the grain boundary at a bend angle of 175 and 60°, respectively. Electron microscope examination revealed the presence of molybdenum oxides and carbides at the grain boundaries in the as-cast specimens and within the grains at a distance of 1 to 2 mm from the grain boundaries in the specimens annealed at 1300 to 1400°C. This high ductility in molybdenum annealed at 900 to 1200°C was brought about by eliminating impurities from the polygonal grain boundaries. Lower ductility in molybdenum annealed at 1500°C was believed to be caused by microporosity, which was observed in the specimens and probably resulted from coagulation of vacancies or vaporization of molybdenum trioxide from the grain boundaries.

The recrystallization temperature and rupture strength of vacuum arc-melted molybdenum-base alloys with 0.25 or 0.5 at.% C, Ti, Zr, or Hf were investigated by the Russians.[91] Rough machined alloy ingots, after being heated in an argon atmosphere at 1700°C for 3 hr, were forged first into 40-mm-square bars and then, at 1400 and 1200°C, into rods 16 mm in diameter. The recrystallization temperature of the alloys was determined by measuring the HRC microhardness of the alloys vacuum annealed at 900 to 1200°C for 1 hr. The 100-hr rupture strength was measured in vacuum at 1400°C on alloys vacuum annealed at 2000°C for 3 hr. It was found that increasing the carbon content from 0.25 to 0.5 at.% did not raise the recrystallization temperature (1000°C) or rupture strength of molybdenum. However, in molybdenum alloyed with 0.25 at.% carbon, the addition of 0.25 at.% zirconium, hafnium, or titanium increased the temperature of the beginning of alloy recrystallization from 1000 to 1400, 1300, and 1100°C, respectively, and the rupture strength from 2.8 to 9.0, 3.5, and 2.9 kg/mm^2, respectively. The corresponding figures for molybdenum alloyed with 0.5 at.% C and and 0.5 at.% Zr, Hf, or Ti were 1600, 1800, and 1300°C, respectively, and the rupture strength increased from 2.0 to 10, 9.5, and 5.0 kg/mm^2, respectively.

A series of oriented molybdenum single crystals 4 mm in diameter and 80 to 100 mm long were stretched at a rate of about 1 mm/min. Mechanical properties were strongly dependent on the orientation.[92] Crystals with the axis oriented in the region bounded by (0 1 2), (0 1 1), (1 1 1), and (1 1 2) exhibited a high ductility and deformed with multiple necking with a total elongation of 1.5 to 7%. Crystals with the axis oriented in the region bounded by (0 1 2), (1 1 2), and (0 0 1) had a low ductility and failed in a brittle manner by cleavage along the plane of the cube with 1 to 2% elongation. The group of ductile crystals with the axis oriented close to (0 1 1) deformed locally, with a reduction of area of over 90% at a total elongation of about 2%. Crystals with the axis oriented close to (1 1 1) deformed uniformly, with necking beginning at a total elongation of about 7%. In all cases, deformation proceeded by multiple slip. It was concluded that no dislocation blocking occurred during the plastic yield of crystals with the axis oriented close to (0 1 1); blocking did occur when the crystal axis was oriented close to (1 1 1), but it was overcome by growing stresses. In crystals with the axis close to (0 0 1), the blocking of dislocations prevented yielding altogether and finally led to brittle fracture.

The phase diagram of the tertiary system, Mo–Fe–Si, was studied at 800°C by Russian investigators.[93] The study involved 133 individual samples prepared by fusing mixtures of the elements in an electric arc furnace. The lattice parameters were determined by the X-ray technique. The existence of $MoFe_2Si_2$ was confirmed, and its crystal structure was found to belong to the rhombic system. The existence of two other compounds, Mo_3FeSi and Mo_5Fe_3Si, and of the $(Mo_{0.17}Fe_{0.83})_5Si_3$ phase was also established. The previously reported compound Mo–Fe–Si was found to be a binary solid solution based on $MoFe_2$ stabilized by silicon. The solubility of silicon in the Mo–Fe mu phase was about 13.5 at.%, and the solubility of molybdenum and iron in the binary silicides was very low. The stabilizing effect of the silicon on various lambda and mu phases was associated with the increased electron concentration when silicon was dissolved in such binary compounds as $MoFe_2$ or $MoFe_{1.3}$ (Mo_2Fe_3).

The Russians[94] have also studied 120 alloys of the Mo–Co–Si system. Alloys were melted from 99.9%-pure molybdenum, 99.98%-pure cobalt, and 99.99%-pure silicon. A phase-equilibrium diagram of the system at 800°C was plotted on the basis of data obtained by physicochemical analysis. The existence of the MoCoSi compound with a homogeneity region extending from 15 to 30 at.% silicon was confirmed. Two previously unknown compounds, $Mo_5Co_3Si_2$ (a = 11.06 A, c = 19.89 A) and Mo_3CoSi (a = 12.70 A, c = 4.85 A), were found. The solubility of cobalt in MoSi was about 3 at.% and that in Mo_5Si_3 and Mo_3Si was about 5 at.%. The solubility of silicon in Mo_6Co_7 and $MoCo_3$ was 12 at.% and less than 5 at.%, respectively. The solubility of molybdenum in silicides was insignificant.

Tantalum

The mechanical and physical properties of several tantalum alloys were compiled by Wah Chang.[83] The alloys described in this work include WC-111 (Ta–8 wt.% W–2 wt.% Hf), WC-222 (Ta–10 wt.% W–2.5 wt.% Hf–0.1 wt.% C), Ta–10 wt.% W, and Ta–30 wt.% Nb–7.5 wt.% V.

Tungsten

Electron-beam and arc-melted tungsten and tungsten alloys were evaluated for ductility, strength, recrystallization, and grain-growth characteristics by investigators at Lewis.[95] Sheet fabricated from electron-beam-melted tungsten alloys with 1.9 to 9.1% rhenium exhibited, in the worked condition, ductile–brittle bend transition temperatures as low as −75 to −100°F (−59 to −75°C), as compared with 235°F (113°C) for unalloyed tungsten (electropolished). Sheet fabricated from arc-melted alloys was less ductile, with bend transition temperatures of 50 to 280°F (10 to 138°C). Annealing at 3600°F (1980°C) significantly increased the ductile–brittle bend transition temperatures of both electron-beam and arc-melted alloys. Transition temperatures of about 400°F (204°C) were observed for alloys with 2 to 4% rhenium. High-rhenium alloys with 24 and 26% rhenium had transition temperatures of 350 to 375°F (177 to 190°C) after similar annealing treatments.

Alloying with 1.9 to 9.1% rhenium raised the recrystallization temperature of the electron-beam-melted tungsten by 600 to 800°F (316 to 427°C), whereas the grain-growth rates were significantly reduced. Rhenium additions up to 9.1% strengthened tungsten at elevated temperatures in both short-time tensile and long-time creep tests. The alloys with 24 and 26% rhenium had tensile strengths similar to the 9.1%-rhenium alloys, but they were considerably weaker in creep. Strengths of these alloys approximated those of unalloyed tungsten.

Investigators at United Nuclear[96] found that the thermal conductivity of solid tungsten varied from 76 Btu/(hr)(ft)(°F) at 3000°F (1649°C) to 66 Btu/(hr)(ft)(°F) at 5000°F (2760°C). Thermal conductivities of porous tungsten were 10 to 15% of the values for nonporous material.

The physical and mechanical properties of several tungsten-base materials containing rhenium have been summarized by General Electric.[97] Tensile and creep-rupture data where reported for W–25 at.% Re–30 at.% Mo, W–30 at.% Re–30 at.% Mo, and W–25 wt.% Re, where available. Similarly thermal expansion, thermal conductivity, and enthalpy for these alloys were given.

Tungsten ingots with and without small amounts of aluminum, silicon, and potassium were prepared by General Electric[98] investigators by conventional powder-metallurgy techniques and hot rolled to 0.001-in.-thick sheet. The ingots were either (1) initially cross rolled and then straight rolled, (2) straight rolled only or straight rolled and then cross rolled. Total reduction was 99.8%. Samples of the sheets were annealed in vacuo at temperatures from 1200 to 2200°C. Substructures and textures were determined by transmission electron microscopy and X-ray diffraction. The doping agents formed particles of mullite ($Al_6Si_2O_{13}$) which, on rolling, appeared to form strings of particles aligned parallel to the rolling direction. These strings of particles were associated with an increase in the recrystallization temperature from 1400°C for undoped sheet to 2000°C for doped sheet. The particles also limited lateral grain growth while allowing growth parallel to the rolling direction, which resulted in the formation by primary recrystallization of large, highly elongated grains of specific preferred orientation. The undoped sheet recrystallized to small equiaxed grains. The preferred orientations of the large grains were determined from axis density plots to be $(1\bar{1}3)$, (691),

(0 1 3), (3 6 2), (1 1 0), and (3 0 4) for the initially cross rolled and then straight-rolled materials. These orientations are similar to the orientations of the large elongated grains in doped and heavily drawn tungsten wire. The nucleation of the large grains appeared to occur by recovery of certain of the polygonized regions of specific orientation, followed by strain-induced boundary migration.

Microscopic, microhardness, thermal, and X-ray-phase analyses were made by the Russians[99] on polythermal cross sections of ternary W–Zr–Ti alloys. The ratio of tungsten to zirconium was maintained at 4:1 and 1:1, with addition of titanium ranging from 10 to 30 wt.%. Isothermal cross sections were constructed at 1500 and 1000°C. Combined solubility of tungsten and zirconium in beta-titanium solid solutions was reduced with decreasing temperature (thus the solubility across the Ti–W_2Zr cross section was 43 to 44 wt.% at 1500°C and 35 to 36 wt.% at 1000°C). Additions of titanium increased tungsten diffusion into beta zirconium at 1500 and 1000°C.

Russian workers[100] studied the phase composition of several W–LaB_6 alloys (1 to 50 mole % LaB_6) by X-ray techniques. Microhardness, specific electrical resistivity from 293 to 1273°K, and thermal emission parameters and emanation coefficients from 1200 to 1950°K were determined for various W–LaB_6 alloys. The alloy samples were prepared by hot pressing of suitable W + LaB_6 mixtures in an argon atmosphere. It was found that during the interaction between tungsten and LaB_6, a simultaneous formation of two borides, W_2B and WB, and a decomposition of LaB_6 occurred. These processes were accompanied by an increase in the specific electrical resistivity of the samples. It was also noted that the addition of as little as 1 mole % LaB_6 to tungsten resulted in a sharp decline in the work function. This effect was explained in terms of the declining statistical weight of the stable d^5 configurations in the tungsten atoms, leading in turn to an easy thermal excitation of the nonlocalized electrons.

Vanadium

An attempt was made by Russian investigators[101] to determine the influence of niobium on solid-state transformations in V–Ta alloys in the region of the metallic compound TaV_2. Both annealed (ordered) and quenched (from 1000, 1150, 1250, and 1400°C) alloys were investigated by physicochemical techniques that included microscopic and high-temperature contactless thermal analyses, hardness and microhardness measurements, and determination of temperatures of starting fusion. On the basis of the data obtained, phase diagrams of the V–Ta–Nb system in a radial section with a constant ratio (at.%) of V:Ta = 2.1 and in two polythermal sections (with 10 and 5 at.% niobium) were plotted, and the distribution of the phase regions was established in the ternary system at various temperatures. According to X-ray data, the crystal structure and lattice constants of the ternary ordered phase did not differ from those of the metallic compound TaV_2.

The V–Ta alloys form a continuous series[102] of solid solutions, with the solidus and liquidus lines reaching a minimum at 1825°C with 15 at.% Ta. The magnetic susceptibility depends on the temperature, according to the Curie–Weiss law, and measured values indicated that the *d* electrons remain localized. The compound TaV_2 appeared to form on long annealing of the 2:1 V–Ta mixture. This compound was shown by X-ray analysis to have a hexagonal structure similar to that of the crystalline phase of $MgZn_2$, with $a = 5.058$ A, $c = 8.250$ A, and $c/a = 1.631$. Magnetic susceptibility was not temperature dependent. Concentration and temperature limits for the existence of TaV_2 in a binary system were shown graphically, along with photomicrographs of the microstructures.

The effects of the molybdenum additions to the V–Ta system were studied.[103] At high temperatures molybdenum solubility was unlimited, as shown by the solidus line of the phase diagram, the absence of breaks in the hardness curves, and the absence of thermal effects from 1400 to 1600°C on the differential heating curve of annealed alloys. An X-ray analysis showed that a regularizing process occurred which was related to formation of a crystalline phase with a structure similar to that of TaV_2 formed in the binary V–Ta system. Phase diagrams for the V–Ta–Mo system were constructed.

The effects of the gettering agents aluminum, silicon, and yttrium on vanadium were evaluated by Combustion Engineering.[104] Two 100-g button ingots containing each gettering concentration were melted in a nonconsumable-electrode tungsten-arc furnace; one of the buttons was then remelted using electron-beam melting. The buttons from both melting processes were evaluated for chemistry, hardness, and microstructure. Yttrium was the most effective gettering agent for removing oxygen in vanadium. Nitrogen was not removed by either melting process nor were the gettering agents effective. Yttrium can be effectively removed from vanadium by electron-beam melting. Carbon was removed during electron-beam melting by combining with oxygen to form CO or CO_2. Yttrium additions of 1 wt.% reduced the interstitial content after arc and electron-beam melting from 1800 ppm to 790 ppm.

Room-temperature tensile tests[105] (strain to rupture) were conducted on sheet samples of V–40 wt.% Ti, V–15 wt.% Ti–5 wt.% Cr, and V–20 wt.% Ti. All samples were annealed for 1 hr at 700, 900, or 1350°C, with the V–Ti–Cr alloy also receiving a 1500°C treatment. The results are shown in Table III-7. The strength and elongation for V–40 wt.% Ti are apparently reduced by the 1350°C anneal. For

the V–15 Ti–5 Cr alloy, the tensile strength was relatively unaffected by their prior heat-treatment. However, the elastic modulus, elongation, type of fracture, and hardness reflect the influence of heat-treatment. The 900°C fully recrystallized structure would be selected for optimum short-time, room-temperature, mechanical-property behavior. Creep and creep rupture cannot be extrapolated from these data. One might expect that a material containing a structure similar to that shown for the 1500°C anneal would be desirable for increasing the creep strength of the alloy, particularly if the dispersed phase was composed of finer particles. However, fabrication was affected in the reverse order. The annealing treatments for V–20 wt.% Ti had only a moderate effect on the alloy's tensile properties.

Table III-7 ROOM-TEMPERATURE TENSILE RESULTS FOR V–20 AND 40 WT.% Ti AND V–15 WT.% Ti–5 WT.% Cr ANNEALED AT VARIOUS TEMPERATURES[105]

Alloy	Annealing temp., °C	Elastic modulus, 10^6 psi	Yield stress, 1000 psi	Ultimate tensile stress, 1000 psi	Elongation, %	Type of fracture
V–20 Ti	700	17.55	84	96.5	15.6	Ductile
	900	16.05	75.1	88	18.7	Ductile
	1350	17.45	74	96	12.5	Brittle
V–40 Ti	900	14.10	59.7	63	25	Ductile
	1350	13.40	97.35	98.9	8.1	Brittle
V–15 Ti–5 Cr	700	13.90	85.8	97.8	23	Ductile
	900	18.90	80.2	96.2	26.5	Ductile
	1350	18.50	86	100	10.2	Brittle
	1500	14.00	83.9	92.3	7.8	Brittle

*Tensile tests were run on 1.5-mm-thick (0.060-in.) sheet samples. The strain rate was 0.5 mm/min (0.02 in./min), and the gauge length was 25 mm (1 in.).

Tensile tests were run on 0.292-in.-OD by 0.016-in.-wall tubing of V–15 wt.% Ti–7.5 wt.% Cr and, for comparison purposes, 304 stainless steel. The results of these tests are summarized in Table III-8. With both materials in an as-drawn condition, the 304 stainless steel had a higher ultimate strength at room temperature than did the ternary alloy. However, the V–15 wt.% Ti–7.5 wt.% Cr alloy exhibited a higher strength than did the stainless steel when both were in the fully annealed condition. Annealing the V–Ti–Cr alloy at 1250°C resulted in an insignificant drop in the room-temperature ultimate strength.

In the 650°C tests, the ternary alloys was stronger than the 304 stainless steel in the as-drawn condition and half again as strong in the annealed condition. Annealing the V–Ti–Cr alloy at 1250°C resulted in a slight drop in strength compared with the values obtained on material annealed at 850°C. Between room temperature and 650°C, there was a much more marked decrease in strength for the annealed stainless steel than for the annealed ternary alloy.

(J. A. DeMastry)

Table III-8 RESULTS OF ROOM-TEMPERATURE AND 650°C TENSILE TESTS ON V–15 Ti–7.5 Cr AND 304 STAINLESS-STEEL TUBING[105]

(Nominal Tube Size Is 0.292 in. in Outside Diameter by 0.016 in. in Wall Thickness)

Material, wt.%	Condition	Average ultimate tensile strength,* 1000 psi	
		Room temperature	650°C
V–15 Ti–7.5 Cr	As drawn	143.2	116.6
V–15 Ti–7.5 Cr	850°C anneal	108.6	92
V–15 Ti–7.5 Cr	1250°C anneal	107.5	85.9
Type 304 S.S.	As drawn	168.7	98.1
Type 304 S.S.	Annealed	93.8	59.3

*Average of three tests, except for V–15 Ti–7.5 Cr, 850°C anneal, tested at 650°C, which is an average of two tests.

Metallurgy of Common Cladding and Structural Materials

Light Metals

The effect of cold work[106] on the hardness of SAP alloys containing various amounts of Al_2O_3 is illustrated in Fig. III-18. Figure III-19 shows the recovery of cold work in SAP alloys at various annealing temperatures. The recovery temperature is significantly increased with increasing Al_2O_3 content and becomes more distinct with increasing Al_2O_3 content.

Zirconium and Zirconium Alloys

The surface morphology of high-purity zirconium, which had been fractured at room temperature and –196°C, was studied by electron fractography.[107] It was concluded that each dimple appearing on the fracture surface represented the extent of propagation of an individual microcrack.

The influence of vacuum (10^{-6} to 10^{-1} mm Hg) on the creep rate of beta zirconium in the 1100 to 1300°C range has been investigated.[108] It was found

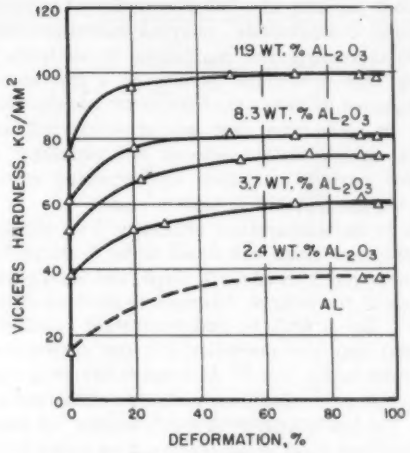

Fig. III-18 Increase of Vickers hardness vs. the deformation degree for alloys with different Al_2O_3 content.[106]

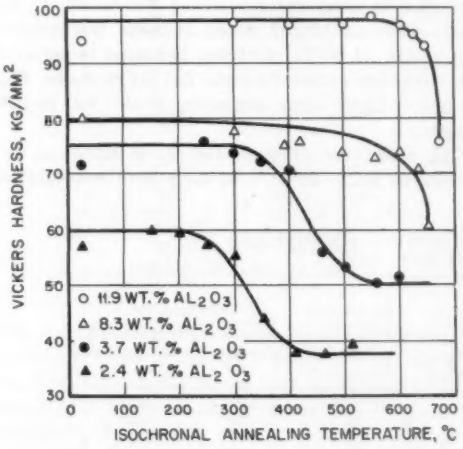

Fig. III-19 Change of Vickers hardness vs. the annealing temperature for alloys with different amounts of Al_2O_3 after 95% deformation.[106]

that, as the vacuum was changed from 10^{-5} to 10^{-4} mm Hg, the creep rate diminished, the ductility was drastically reduced, and the time to rupture was decreased. These effects were attributed to pickup of oxygen atoms at the grain boundaries.

The effects of additions up to 4.2 at.% oxygen on the mechanical properties of zirconium in the −196 to 425°C range have been determined.[109] Additions of large amounts of oxygen resulted in tensile strengths of up to 120,000 psi, but the ductility was drastically reduced. However, at test temperatures above room temperature, the degree of ductility loss was minor. The addition of oxygen generally inhibited twinning and, with large amounts of oxygen additions, twins were observed only in the $\{10\bar{1}2\}$ planes. Oxygen was also found to promote cross slip and cause clustering of slip lines.

The microstructure of cold-rolled Zircaloy-4 sheet has been characterized by electron-transmission microscopy and X-ray diffraction techniques.[110] The substructure of the strained material consisted of a dense cellular-dislocation arrangement, which was heterogeneous after strains as low as 2.5%. Most of the work hardening as well as the change in structure takes place in the first 10% of straining with only minor changes at higher strains. The yield stress of the prestrained Zircaloy-4 sheet was found to be a linear function of the square root of dislocation density, as predicted by work-hardening theories.

Zirconium hydride platelets in Zircaloy-2 have been observed to precipitate along the grain boundaries only if a properly orientated habit plane is available along the grain boundary.[111] However, precipitation at secondary habit planes may occur near grain boundaries since this lowers the strain energy of the system. No zirconium hydride precipitates were observed on twin boundaries. The possibilities of placing habit planes, which result in precipitation of hydride platelets, along the grain boundaries by various manufacturing processes were discussed.

A Canadian patent[112] has been issued for a Zr−3 wt.% Cu alloy that demonstrated considerably better corrosion and creep resistance for applications in CO_2 at elevated temperatures than does unalloyed zirconium. The slow diffusion of uranium in this alloy provides an advantage for its use as a cladding material. The fabrication, heat-treatment, and performance of Zr−2.5 wt.% Nb pressure tubes for water-cooled power reactors has also been thoroughly evaluated.[113] It was concluded that these pressure tubes are more than adequate for their intended functions.

Pressure-Vessel Steels

A greater degree of precipitation strengthening[114] was obtained in a low-alloy steel (0.11 wt.% C, 0.74 wt.% Mn, and 0.02 wt.% Nb) by tempering at 580°C rather than at 635°C. This strengthening was due to a finer precipitate of NbC particles. However, the lower tempering temperature was found to result in considerably higher ductile-to-brittle transition-temperature shifts. The lower tempering temperature resulted in precipitation of the carbide particles at dislocation lines, which caused pinning of the dislocations and reduced the toughness of the steel. The higher tempering temperature resulted in a more general distribution of the carbide particles and, therefore, the number of mobile dislocations was considerably higher and the steel exhibited a higher toughness. These findings[115] were supported to some degree by another study on 8-in. sections of A-302

YB steel which showed that the best impact and tensile properties were imparted by tempering the steel at 650°C for 1 to 1.4 hr. The properties of the quenched and tempered material were significantly better than those of the quenched, normalized, and tempered material. The better properties of the quenched and tempered material were attributed to better distribution and shape of the carbide particles.

Stainless Steels

The precipitation of carbides in F. V. 548 stainless steel has been studied by the British.[116] The F. V. 548 composition corresponds to 316 stainless steel stabilized with about 2 wt.% niobium. Increasing the solution-annealing temperature from 1075 to 1150°C and then aging at 850°C causes the NbC particles in this alloy to be considerably smaller and more randomly distributed. These fine NbC particles were found to be remarkably stable after heating for 1000 hr at 650 and 750°C when compared with the NbC particles in 20 wt.% Cr–25 wt.% Ni niobium-stabilized stainless steel. No large M_6C particles were found at the grain boundaries unless the material was cold worked before aging at 750°C. The solubility[117] of NbC particles in a 20 Cr–25 Ni niobium-stabilized stainless steel is not affected by varying boron contents of 2 to 75 ppm. An extremely fine dispersion of carbide particles in 304 stainless steel can be obtained[33] by cold-working the steel 20% at liquid-nitrogen temperature (–196°C) and heating to 650°C. The cold working at –196°C transforms some of the austenite to martensite, whereas subsequent heating at 650°C reverts the martensite to austenite. Repeating this procedure results in a fine structure accompanied by removal of the prior austenite boundaries. It is believed that this structure will be resistant to irradiation-induced embrittlement since the fine carbide particles are expected to act as traps for the embrittling helium atoms.

The room-temperature solubility[118] of nitrogen in 304 stainless steel was found to be 0.125 wt.%. Excess nitrogen formed CrN, Cr_2N, and Si_3N_4 particles throughout the matrix. Attempts to produce ultrapure 18 wt.% Cr–8 wt.% Ni stainless steel resulted in a material that was martensitic if the carbon content was sufficiently low.[119] At least 0.007 wt.% carbon was required to obtain an austenitic structure in this alloy. The low-cyclic-fatigue properties[50] of annealed 348 stainless steel in the temperature range of 150 to 816°C have been determined, and these are given in Table III-9.

The shape of Ni_3Ti particles[120] in precipitation-hardened stainless steels is usually cubic when precipitated at temperatures above 750 to 800°C. However, after prolonged times at these temperatures, the shape of Ni_3Ti particles becomes lamellar and the particles richer in iron. The laves phase, Fe_2Ti, is precipitated after annealing in the 800 to 900°C range.

The effects of titanium and boron additions in an Fe–15 wt.% Cr–20 wt.% Ni alloy have been studied.[121]

Table III-9 LOW-CYCLE FATIGUE-TEST* RESULTS[50] FOR ANNEALED 348 STAINLESS STEEL FROM 150 TO 816°C

Temp., °C	Axial strain			Diametral strain			Axial stress	Fatigue life	
	Total strain range (Δ_t), %	Plastic strain range ($\Delta_{\epsilon p}$), %	Elastic strain range ($\Delta_{\epsilon e}$), %	Total strain range (Δ_d), %	Plastic strain range ($\Delta_{\epsilon dp}$), %	Elastic strain range ($\Delta_{\epsilon de}$), %	Stress range at $N_f/2$ (Δ_σ), kg/mm²	Cycles to fracture (N_f)	Cycles to 5% load-reduction point (N_5)
150	1.72	1.32	0.40	0.78	0.66	0.12	73.9	2984	2984
150	1.72	1.32	0.40	0.78	0.66	0.12	71.4	4696	4665
300	1.72	1.32	0.40	0.78	0.66	0.12	64.5	2408	2390
300	1.73	1.36	0.37	0.79	0.68	0.11	63.1	2575	2540
400	1.74	1.34	0.40	0.79	0.67	0.12	68.8	2496	2430
400	1.72	1.32	0.40	0.78	0.66	0.12	67.8	2732	2690
500	1.73	1.29	0.44	0.78	0.65	0.13	63.6	1910	1910
500	1.74	1.27	0.47	0.78	0.64	0.14	67.6	1912	1840
500	1.74	1.29	0.45	0.78	0.65	0.13	62.3	2160	2160
600	1.70	1.31	0.39	0.77	0.65	0.12	66.3	870	820
600	1.71	1.35	0.36	0.77	0.66	0.11	63.0	1002	950
600	1.73	1.34	0.37	0.79	0.68	0.11	62.7	1304	1260
650	1.74	1.35	0.39	0.80	0.68	0.12	57.4	834	815
650	1.76	1.36	0.40	0.80	0.68	0.12	58.1	895	841
650	1.68	1.28	0.40	0.76	0.64	0.12	57.7	1024	980
700	1.72	1.32	0.40	0.79	0.66	0.13	54.4	740	660
700	1.70	1.33	0.37	0.78	0.67	0.11	52.4	768	730
750	1.73	1.40	0.33	0.80	0.70	0.10	50.9	531	420
750	1.68	1.36	0.32	0.77	0.68	0.09	48.4	538	420
750	1.67	1.36	0.31	0.77	0.68	0.09	45.6	576	520
816†	1.63	1.41	0.22	0.77	0.70	0.07	39.1	290	230
816	1.63	1.43	0.20	0.78	0.72	0.06	37.8	304	220
816†	1.63	1.41	0.22	0.77	0.70	0.07	41.1	304	230

*Control mode: diametral strain. Mode shape: triangular with zero mean strain. Diametral strain range: 0.78% (nominal value). Cyclic rate: 400 cycles/hr. Starting condition: compression first.
†Cyclic rate: 356 cycles/hr.

Table III-10 TENSILE DATA* FOR Fe–Cr–Al–Y ALLOYS[50]

Alloy designation†	Test temp., °C	Yield strength psi	Yield strength kg/cm²	Ultimate strength psi	Ultimate strength kg/cm²	Elongation, %
1361 DS‡	RT	114,620	8060	118,180	8310	1.1
	RT	115,450	8120	120,520	8480	2.8
	RT	116,440	8190	120,470	8470	2.4
	RT			122,300	8600	2.8
	550	32,500	2290	53,840	3790	6.0
	550	35,520	2500	50,070	3520	6.8
	550	§		64,750	4550	19.0
	750	6,270	440	11,470	810	50.3
	750			12,720	900	44.2
1541	RT¶	56,000	3940	77,000	5480	23.0
	650¶	17,000	1200	18,300	1290	71.2
	750¶	10,600	750	10,600	750	107.0
2541	RT	51,200	3600	75,300	5290	
	650¶	16,600	1170	20,000	1410	70.0
	750¶	9,600	680	9,600	680	110.7

*All tests conducted in air.
†Nominal compositions (wt.%): 1361, Fe–13 Cr–6 Al–1 Y; 1541, Fe–15 Cr–4 Al–1 Y; 2541, Fe–25 Cr–4 Al–1 Y.
‡1361 DS data at crosshead speed of 0.005 min^{-1}.
§No extensometer.
¶Harwell data. Crosshead speed of 0.012 min^{-1}.

Table III-11 CREEP-RUPTURE DATA* FOR ANNEALED 1361 DS SHEET[50]

Test temp., °C	Stress psi	Stress kg/cm²	Time to 1% elongation, hr	Test time, hr	Total elongation, %	Test status
550	15,000	1050	3.8	111.0	40.3	Ruptured
550	10,000	700	11.5	458.1	6.4	Terminated
550	6,000	420	47.5	2125.6		†
550	6,000	420	180.0	561.6	1.4	Terminated
750	3,000	210	1172.2	1317.4	1.4	Terminated
750	3,000	210	1146.0	1221.9	1.1	Terminated

*Composition of Alloy 1361 is Fe–13 Cr–6 Al–1 Y.
†Removal from creep stand at 1% elongation and continued testing in a rupture stand. Specimen still intact at 2125.6 hr.

The titanium additions varied from 2 to 3.8 wt.%; two boron additions (0.022 and 0.48 wt.%) were used, with the titanium content being held constant at 3.7 wt.%. Boron was found to precipitate as small platelets of hexagonal TiB_2 which were relatively stable during aging at elevated temperatures. Titanium formed spherical gamma-prime (fcc Ni_3Ti) particles that grew in size and transformed to cellular eta particles (hcp Ni_3Ti) during prolonged aging. Both the rate of particle coarsening and rate of transformation of the Ni_3Ti particles were favored by the increased titanium content and the presence of cold work. Additions of boron retarded the cellular grain-boundary precipitation of eta particles.

Considerable development of oxidation-resistant iron-base alloys has been conducted by General Electric.[50] The tensile properties of ferritic Fe–Cr–Al–Y alloys at room and elevated temperatures are given in Table III-10. These alloys are characterized by rather low ductility at room temperature, which may be due to notch sensitivity of the material since the fracture originated at extensometer knife edges. The creep-rupture properties of Alloy 1361 at 550 and 750°C are shown in Table III-11, and the impact strengths of various alloys are illustrated in Fig. III-20. The creep-rupture tests show that Alloy 1361 exhibits considerable creep strength at temperatures up to 750°C. Heating of the specimens for 50 hr at 450°C before testing resulted in reduced impact

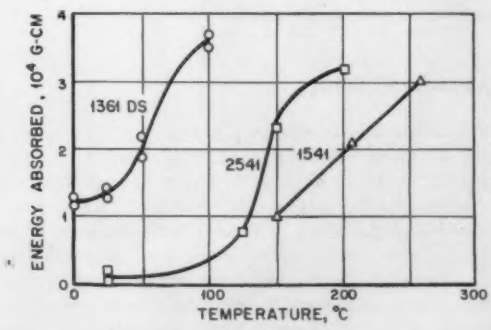

Fig. III-20 Impact strength of 1361 DS alloy compared with strengths of 2541 and 1541 alloys.[50]

Table III-12 TENSILE DATA FOR BINARY IRON-BASE ALLOYS[50]

Composition (balance iron), at.%	Test temperature, °C	Yield strength		Tensile strength		Elongation in 2.54 cm, %
		psi	kg/cm²	psi	kg/cm²	
5 Al	RT	19,000	1340	36,900	2,590	14.8
10 Al	RT	32,800	2310	50,100	3,520	14.4
15 Al	RT	49,900	3520	61,700	4,340	13.5
20 Al	RT			63,800	4,490	1.8
5.5 V	RT	22,500	1580	47,000	3,300	28.8
13 V	RT	34,200	2410	57,100	4,020	27.3
17 V	RT	51,600	3630	71,400	5,020	18.8
0.1 Ti	RT	18,200	1280	37,800	2,660	34.3
3 Ti	RT	29,000	2040	52,300	3,680	26.1
5 Ti	RT	35,900	2520	58,700	4,130	25.6
0.1 Be	RT	25,200	1770	29,200	2,050	31.0
0.75 Be	RT	21,500	1510	41,000	2,880	23.3
3 Be	RT	49,700	3490	74,700	5,250	25.6
11 Be	RT	77,400	5440	151,100	10,620	21.0
16 Be	RT	82,400	5790	163,400	11,490	14.8
5 Al	750	4,200	300	6,000	420	62.4
10 Al	750	6,200	440	7,800	550	101.4
15 Al	750	4,800	340	5,900	410	75.1
20 Al	750			6,400	450	52.7
3.5 V	750	3,700	260	5,600	390	39.8
5.5 V	750	4,000	280	5,900	410	50.3
13 V	750	6,200	440	9,400	660	66.0
17 V	750	9,200	650	11,300	790	50.3
22 V	750			10,600	750	54.9
0.1 Ti	750	3,400	240	5,200	370	26.0
3 Ti	750	13,600	960	15,400	1,080	17.8
5 Ti	750	14,000	980	15,500	1,090	32.4
0.75 Be	750	3,900	270	6,400	450	31.7
3 Be	750	6,300	440	12,500	880	46.3
11 Be	750	14,000	980	19,400	1,360	6.9
16 Be	750	12,900	910	19,400	1,360	63.4
Iron	750	1,000	70	1,600	110	14.5
304 stainless steel	750	15,100	1060	26,700	1,880	51.0

strength, which was attributed to the formation of a fine alpha-prime precipitate. A patent has been issued to the USAEC for an alloy that is corrosion resistant to elevated-temperature steam.[122] The composition of the alloy is 0 to 15 wt.% Cr, 0.5 to 12 wt.% Al, and 0.1 to 3.0 wt.% Y, with the balance being iron.

Tensile properties of various binary iron-base alloys at room temperature and 750°C are given in Table III-12. In these studies the effects of various amounts of Al, V, Ti, and Be on the tensile properties of iron were determined.

Nickel-Base Alloys

The formation of sigma phase in Ni–Co–Cr–Al–Ti–C alloys at 900°C has been investigated.[123] Additions of up to 10 wt.% of titanium or aluminum did not result in sigma formation provided that only one of the elements was present. If both elements were present, the sigma phase formed at total titanium and aluminum content of less than 10 wt.%. The sigma phase was found to originate in areas where the carbon had been depleted by formation of chromium-rich carbides. It was also found that the electron vacancy/atom ratio concept of sigma-phase formation can be used, but the phase and composition changes at each temperature should be considered.

Figure III-21 illustrates the specific-heat change as a function of temperature for INOR-8 (Hastelloy-N).[124] The anomalous rise in the specific heat at about 550°C is attributed to the dispersion of short-range

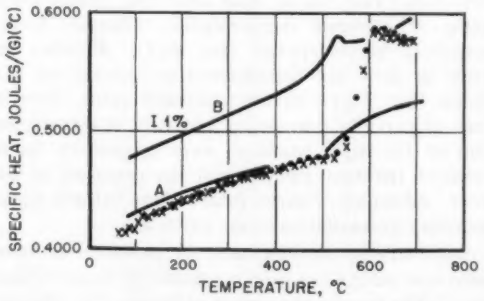

Fig. III-21 Specific heat of nickel-base alloys[124] from 50 to 700°C. K is the energy input rate that is essentially constant during measurement. ●, INOR-8, K = 123 joules/(g)(hr) (4.5°C/min at 300°C); ×, INOR-8, K = 49 joules/(g)(hr) (2°C/min at 300°C); A, Ni–15 wt.% Mo, K = 50 to 123 (2 to 4.5°C/min at 300°C); B, Ni–10 wt.% Cr, K = 70 to 180 (2 to 6°C/min at 310°C).

order, which takes place at that temperature. Curves A and B in Fig. III-21 illustrate the same phenomenon in binary nickel alloys, only the magnitude of the change is considerably less than in the more complex INOR-8. A comprehensive report on the physical and mechanical properties of Soviet superalloys has been published by Defense Metals Information Center.[125] This report discusses the physical and mechanical properties of 36 nickel-base alloys and three cobalt-base alloys. (M. Kangilaski)

Nonfuel Refractories

Several Russian investigators have examined the conditions for preparing various carbide materials. Samsonov, Makarenko, and Krushinskii[126] studied the conditions of formation of solid solutions of the carbides WC–ScC in the mole ratio from 1:4 to 4:1 in vacuo at 1000 to 2000°C. The formation of WC–TiC–ScC solid solutions by carbon reduction of the appropriate oxides was investigated in vacuo and in hydrogen in the 1000 to 2500°C range. It was found that the optimum conditions for preparing a solid solution containing 20 mole % ScC with maximum microhardness were obtained by heating a stoichiometric mixture of oxides with carbon at 1900°C for 1 hr. In the case of reduction in vacuo, WC–TiC–ScC solid solutions were obtained most readily by heating a suitable oxide and carbon mixture for 1 hr at 2000°C. Carbidization in a Tamman furnace was accomplished by either a two-time heating of a $WC-TiO_2-Sc_2O_3-C$ mixture for 1 hr at 2100°C or heating of a $W-Sc_2O_3-TiO_2-C$ mixture for 1 hr at 2500°C. In general, the presence of ScC increases the hardness of the other transition-element carbides.

Preparation of NbC from niobium and NH_3 was studied in the range 1200 to 1700°C for 1 to 8 hr. The preparation of $NbN_{0.3}C_{0.7}$ from NbO_5, carbon, and nitrogen and from NbO_5 and C_2 in an NH_3 atmosphere was studied in the 1000 to 1700°C range for 1 to 2 hr.[127] Generally, higher temperatures and longer reaction times led to higher nitrogen content in the NbC product. The experimental data as well as the thermodynamic calculations showed that, above 1620°C, NbC with less than 0.1 wt. % oxygen can be prepared from NbO_5 in an NH_3 atmosphere. The experimental data and the thermodynamic calculations also showed that niobium carbonitride with as little as 0.01 wt.% oxygen can be prepared from NbO_5, carbon, and NH_3. In general, the formation of nitrides and carbonitrides in NH_3 atmospheres was faster than in nitrogen atmospheres. This was explained in terms of the high reactivity of nitrogen atoms readily generated on oxide surfaces by the dissociation of ammonia.

Kraus[128] examined the effect of the average grain size (1 to 3 μ) of WC and cobalt binder-phase content (6 to 25 wt.%) on X-ray measurements of macrostresses in sintered carbides. A comparison of X-ray measurements with the stresses calculated theoretically from the corresponding deflections and mean elastic constants showed that the values of the stresses determined by X-ray were systematically lower. This difference increased as the mean grain size of WC or cobalt content increased.

The thermodynamic properties of several carbides and nitrides have been determined recently by Russian investigators. Voitovich[129] calculated the reduced thermodynamic potentials of several carbides and nitrides at 298, 500, 1000, 1500, and 2000°K. Bolgar, Guseva, and Fesenko[130] determined the values of the enthalpy of ZrC and HfC over the temperature range from 1300 to 2500°K. On the basis of the results obtained in this work and data in the literature, the enthalpy, heat capacity, entropy, and reduced potentials of the investigated carbides were determined over the range 298 to 2500°K.

The complex silico–silicide–boride–oxide coating was developed by Sazonova and Komarova[131] for the protection of B_4C against oxidation and when in contact with quartz, corundum, BeO_2, $MoSi_2$, and C–Fe alloys in various atmospheres at 1200°C for over 300 hr. The physicochemical reactions taking place between the silico–silicide–boride–oxide coating and its components, the backing material, and gas media during fusing of the coating on the B_4C had decisive effects on the protection properties of the coating.

Researchers at the Tokyo University have examined the effects of carbon content on the properties of vacuum sintered WC–TiC–Co alloys.[132] The composition of the specimens was strictly controlled to contain 10 wt. % cobalt and 6 to 25 wt. % TiC and provide a three-phase material ($WC + \beta + \gamma$). The relation between the properties of the sintered alloys and the carbon content or the TiC content was investigated. The lattice parameters of the gamma and beta phases showed a regular change in the three-phase region due to the change in composition in both phases. The tungsten content in the binder phase of the three-phase alloys varied from about 2 to 10 wt. %, depending on the carbon content. The amount of tungsten and carbon dissolved in the binder phase corresponded to the values in WC–Co alloys. The addition of TiC resulted in an extreme extension of the three-phase range due to the change in carbon content in the beta phase. The properties, such as transverse-rupture strength and magnetic saturation, varied regularly within the three-phase region.

The effect of carbon content on certain electrophysical and thermophysical properties of ZrC was studied by Avgustinik et al.[133] The dependence of electrical resistivity, absolute thermal electromotive force (emf), Hall coefficient, and thermal conductivity of ZrC was determined for carbon contents of 36 to 48 at.%. The ZrC samples were prepared by fusing high-purity zirconium and carbon at 1800°C in vacuo, followed by sintering at 2200°C. It was found that free

electrons acted as current carriers within ZrC. The electrical resistivity, thermal emf, and Hall coefficient were found to decline and the thermal conductivity was found to increase with decreasing contents of the combined carbon in ZrC. This phenomenon was related to the release of a portion of the zirconium electrons from the localized metal–carbon bonds. The specific resistivity and absolute thermal emf were found to increase linearly with increasing temperature. The slope of these lines was observed to decrease with decreasing carbon content in $Zr(CO_3)_2$, because of the decline in the effective mass of the conduction electrons.

Investigators at the Albany Metallurgy Research Center are evaluating the potential of spin casting high-melting-point metal–carbon alloys.[134] Currently, properties are being determined for castings of these alloys with nominal dimensions of 0.635 by 1.27 by 7.61 cm. Tests include thermal expansion, bend-rupture hot hardness, oxidation, and electrical resistivity. The castings normally exhibit some porosity and microcracks, and, generally, the cracks are shallow and appear on the side walls and the bottom of the castings. Spectrographic analyses of these materials have shown the principal impurities to be iron (200 to 400 ppm) and silicon (200 to 300 ppm). The ho hardness values for ZrC and TiC are given in Table III-13. Plots of log hardness vs. temperature showed that the TaC–C and HfC specimens exhibited a linear change in hardness with temperature. All other alloys showed a sharper drop in hardness from 20 to about 400°C; the hardness then gradually decreased linearly with temperature. Heating to 1500°C reduced the hardness of all specimens to values ranging from 10 to 28% of their room-temperature hardness.

The hot-hardness values at 20, 500, 1000, and 1500°C and at the free-carbon levels tested are shown in Table III-14. Plots of log hardness vs. free-carbon content showed that there was only a slight variation in hardness with increasing free-carbon content for hypoeutectic compositions. The results of this work show that:

1. The variation in hardness of each metal–carbon alloy with increasing free-carbon content diminishes with increasing temperature.

2. At room temperature the DPH hardness of the eutectic compositions decreases in the following order: ZrC–C (1050), TaC–C (802) HfC–C (630), and NbC–C (522). However, at 500, 1000, and 1500°C, the order is ZrC–C, HfC, and TaC, or NbC.

3. Between 500 and 1500°C the eutectic structures of TaC–C and ZrC–C are harder than the corresponding hypereutectic structures.

Table III-13 HOT HARDNESS (DPH) FOR ZrC AND TiC CASTINGS[134]

Temp., °C	ZrC		TiC	
	20.3 wt. % C	17.3 wt. % C	20.3 wt. % C	18.5 wt. % C
RT	1048		934	
RT	1058	1122	834	1372
200	662	824	735	854
300	644	684*	536	676
400	496	580	434	506
500	366	444	338	416
600	290	388	290	372
700	224	362†	276	328
800	332	362	264	312
900	224	344	272	276
1000	228	324	234	258
1100	240	302	204	228
1200	200	290	192	208
1300	186	290	182	194
1400	236	264		
1500	228	226‡		170

*At 319°C.
†At 716°C.
‡At 1482°C.

Table III-14 VARIATION IN HOT HARDNESS OF CAST CARBIDES WITH FREE-CARBON CONTENT[134]

Material	Free carbon, wt. %	Hot hardness, DPH at indicated temperature			
		20°C	500°C	1000°C	1500°C
HfC	0	1868	676*	361*	183
	1.7	1218	514*	261*	158
	6.6	630	429*	252*	166
TaC	0.2†	934	438	248	144
	0.3‡	678	398	218	120
	1.4	746*	434	242	141
	2.6	802	376	218	128
	3.4	431*	332	162	120
NbC	1.4	962	366	226	156
	2.8	649*	350	212	136
	2.8	824	338	198	120
	5.2	522*	290	200	142
ZrC	5.7	1122	444	324	226
	7.1	834	472	332	224
	8.1†	1142	486	366	250
	8.1‡	1006	508	366	254
	8.7	1038	366	228	228
TiC	0	1372	416	258	170
	0.3	834	338	234	155

*Calculated using equations in report for quarter ending December 1966.
†First heating.
‡Second heating.

The linear-oxidation rates of several carbide materials (listed in Table III-15) were obtained by manually monitoring the change in weight of specimens in static air between 472 and 1005°C.

The properties of the carbide systems ZrC–NbC, TaC–HfC, ZrC–HfC, and TaC–ZrC have been studied by several Russian investigators. Barentseva, Paderno, and Paderno[135] determined the resistivity and Hall constants of the alloys ZrC–NbC and TaC–HfC at room temperature. Maximums were found in the curves showing the dependence of these properties on the ratio of the carbide components. Andrievskii et al.[136] found a maximum in the fusion point in the systems TaC–ZrC and TaC–HfC (TaC · 1 ZrC, 3890°C and 4 TaC · 1 HfC, 3990°C); no maximum was found in the ZrC–HfC system. A microstructural in-

Table III-15 RESULTS OF AIR-OXIDATION TESTS ON NbC, ZrC, AND TiC CASTINGS[134]

Material	Carbon, wt. %	Temp., °C	Time, hr	Linear oxidation rate, mg/(min)(dm²)	Remarks
NbC	17.6	510	3	61.6	Oxidized to powder; no solid piece left
		552	7	19.9	
		605	4	41	
NbC-4	15.3	472	4	0	
		506	6	3.1	Thin adherent gray film
		553	6	5.5	Gray film
		610	5½	20.8	Thick white layer on specimen
ZrC	17.3	555	5½	0.65	Thin adherent gray film
		603	5½	3.1	Adherent nearly white film
		704	5	22.75	Adherent white film
TiC	18.5	610	4	0	Slight loss in weight
		695	2½	0	Slight loss in weight
		790	5½	0	Slight loss in weight
		900	6	1.0	Yellow film
		952	5½	1.5	Yellow film
		1005	5	6.3	Purplish film

vestigation showed that the absence of a maximum in this system was not connected with the presence of free carbon in the samples. In the systems TaC–ZrC and TaC–HfC, considerable decarbonization of the samples was noted on heating to temperatures close to the fusion points. It was assumed that the high fusion points for the composition 4 TaC · 1 HfC and 8TaC · 1 ZrC are a result of a shift in stoichiometry during the experiment.

Paderno et al.[137] studied the thermal expansion of hot-pressed ZrC, HfC, NbC, and TaC in the temperature range 293 to 3173°K. The thermal expansion was measured in a vacuum chamber (10^{-2} mm Hg) in which the carbide samples (8 mm in diameter and 15 to 18 mm in length) were heated electrically. Individual carbide samples had the following porosities: ZrC, 19 to 24%; HfC, 22 to 28%; NbC, 13 to 18%; and TaC, 27%. Table III-16 gives the average values of the thermal-expansion coefficients for the various carbides. The thermal conductivity and electrical resistance of these carbides were also determined in this temperature range.[138]

Workers at Los Alamos have studied the reaction of TaC_x with rhenium.[139] Various starting compositions yielded several reaction products and structures that exhibited a wide range of homogeneity. Mixtures of finely powdered rhenium metal and characterized tantalum carbides of different compositions were used as starting materials. The samples were heated in a helium atmosphere using a graphite crucible with the interior and exterior surfaces coated with tantalum carbide to minimize contamination by the transport of graphite vapor. The results of these tests are listed in Table III-17. It was assumed from the sharpness of the X-ray diffraction peaks that the phases examined were equilibrium compositions.

The reactions between various carbides of the transition metals and their oxides were investigated by Kosolapova, Fedorus, and Kuz'ma.[140] The oxide–carbon systems of Ti, Zr, Hf, V, Nb, and Cr with their carbides were examined in 100°C intervals over the range 1000 to 2000°C at 10^{-3} mm Hg by using chemical and X-ray analyses. At 1000 to 2000°C, in the TiO_2–TiC and ZrO_2–ZrC systems, the reaction proceeded up to the formation of MC_xO_{1-x} oxycarbides, whereas no reaction was observed in the HfO_2–HfC system. Carbides of Group V metals, VC and NbC, reacted with the corresponding oxides to form the metals via stages of formation of lower oxides and carbides. The formation of chromium by the reaction of Cr_3C_2 with Cr_2O_3 was observed at 1200°C. Further increases in temperature led to an increase in the yield of pure chromium, reaching 96% in the vicinity of the melting point of chromium. It was concluded that the difference in the nature of the reactions of

Table III-16 THERMAL-EXPANSION COEFFICIENTS FOR SEVERAL CARBIDE MATERIALS[132]

Specimen	Temp. range, °K	Expansion coefficient, 10^{-6}/°C	Specimen	Temp. range, °K	Expansion coefficient, 10^{-6}/°K
ZrC	293–773	6.74	HfC	293–773	6.60
	293–873	6.80		293–973	6.62
	293–973	6.86		293–1173	6.76
	293–1123	6.93		293–1373	6.79
	293–1273	6.99		293–1673	7.00
	293–1573	7.20		293–1873	7.21
	293–1773	7.43		293–2073	7.47
	293–1973	7.70		293–2273	7.61
	293–2173	8.10		293–2573	7.76
	293–2573	8.77		293–2873	7.90
	293–2873	9.30		293–3173	8.01
	293–3173	9.61			
NbC	293–773	6.65	TaC	293–773	6.29
	293–873	6.70		293–873	6.41
	293–973	6.76		293–973	6.52
	293–1123	6.84		293–1123	6.61
	293–1273	6.88		293–1273	6.64
	293–1473	6.90		293–1473	6.67
	293–1673	6.92		293–1673	6.89
	293–1873	7.15		293–1873	7.29
	293–2073	7.41		293–2073	7.59
	293–2273	7.57		293–2273	7.94
	293–2573	7.76		293–2573	8.20
	293–2873	7.92		293–2873	8.61
	293–3173	8.02		293–3173	8.81

Table III-17 TaC–RHENIUM REACTION PRODUCTS[139]

Starting composition, mole %	Observed melting temp., °C (±25)	Phases present after melting
80 $TaC_{0.94}$ + Re	2655	$TaC_{0.90}$ + Re
80 $TaC_{0.70}$ + Re	2730	$TaC_{0.74}$ + X phase (a_0 = 9.743 A, ~65 at % Re)
20 $TaC_{0.70}$ + Re	2700	$TaC_{0.92}$ + X phase (a_0 = 9.623 A, ~78 at % Re)
80 $TaC_{0.485}$ + Re	2775	Ta–Re solid solution (a_0 = 3.182 A, ~$Ta_{0.55}Re_{0.45}$) + $TaC_{0.70}$ + X phase (small amount)

Group IV, V, and VI transition-metal oxides with carbides is due to the difference in the electronic structure of the metal atoms forming these oxides and carbides.

A means of improving the thermal-shock resistance of TaC was developed by Hivert.[141] Impregnating porous TaC structures with copper or silver improved the thermal-shock resistance and reduced the rate of oxidation in air.

The properties of TaB_2–ZrB_2–Cr alloys have been measured by Dergunova et al.[142] The alloys containing 20, 25, and 30 vol. % ZrB_2 and 3 to 10 vol. % chromium were fabricated by hot pressing at 2100 to 2200°C under a pressure of 220 kg/cm^2 and subsequent homogenization at 2000°C in an argon atmosphere. The porosity of alloys varied from 0.5 to 4% depending on the composition. The alloys consisted mainly of (1) a solid solution of ZrB_2 in TaB_2 with a microhardness of 2900 to 3300 kg/mm^2 and (2) a solid solution of CrB in TaB_2 with a microhardness of 1000 to 1200 kg/mm^2. In addition, fine grains of a third phase, probably CrB, were observed along the second-phase grain boundaries. The composition dependence of the melting temperature of TaB_2–ZrB_2–Cr alloys was shown. Increasing the chromium content from 3 to 10% lowered the strength (hardness) of the alloys both at room temperature and at elevated temperatures but increased their oxidation resistance. (W. C. Chard)

Concrete

Concrete containing a special aggregate has been used for some time as nonload-bearing biological shielding to attenuate both gamma and neutron radiation. More recently, concrete has been employed in load-bearing roles in prestressed-concrete pressure vessels (PCPV). Presently, countries having an active technical interest in the development of PCPV's include Czechoslovakia, France, Germany, Sweden, Britain, United States, USSR, Australia, and Austria.

The preliminary testing and data analyses leading to the selection of concrete for the British Wylfa prestressed-concrete pressure-vessel reactor have been described.[143] A crushed-limestone aggregate was chosen for the concrete used in construction of the spherical Wylfa vessel. The maximum designed operating temperature of the concrete is 95° F (35° C). (D. R. Lankard)

Ceramic Technology

Russian scientists[144] studying the Sm_2O_3–Cr_2O_3 phase diagram in argon at 1000 to 2400°C found only one compound, $SmCrO_3$, which melts congruently at 2300 ± 30°C. This compound forms eutectics with Sm_2O_3 (80 mole %), melting at 1980 ± 30°C, and with Cr_2O_3 (84 mole %), melting at 2080 ± 30°C. No solid solutions were detected.

The same group studied[145] the systems Y_2O_3–Cr_2O_3 and Gd_2O_3–Cr_2O_3.[146] One compound, $YCrO_3$, melting at 2310 ± 30°C, was found in the Y_2O_3–Cr_2O_3 system. The eutectics, at 28 and 80 mole % Cr_2O_3, melted at 2020 ± 30° and 2070 ± 30°C, respectively. In the Gd_2O_3–Cr_2O_3 system, one compound, $GdCrO_3$, was found. The eutectics, at 23 and 85 mole % Cr_2O_3, had melting points of 2060 ± 20 and 2120 ± 30°C, respectively.

Workers at Northwestern[147] have observed considerable strengthening of sapphire single crystals doped with 0.5 cation % titanium. If this technique could be applied to polycrystalline alumina ceramics, it would represent a forward step. The investigators suggest that precipitate particles interfere with the local plastic deformation, which they considered necessary for crack propagation. (H. D. Sheets)

References

1. S. Kass, The Corrosion and Hydrogen-Absorption Characteristics of Zirconium Alloys Containing Iron, Chromium, Tin, and Niobium, USAEC Report WAPD-TM-543, Westinghouse Electric Corporation, Bettis Atomic Power Laboratory, February 1967.
2. K. Drefahl, H. Richter, and W. Ruckdechel, Further Development of the ZrNb3Sn1 Zirconium Alloy with Reference to Its Use for Cladding in Water-Cooled Reactors, USAEC-Euratom Report EURAEC-1725, Metallgesellschaft A. G., June 23, 1966.
3. P. Patriarca (Comp.), Oak Ridge National Laboratory, unpublished, June 1966.
4. P. Patriarca (Comp.), Oak Ridge National Laboratory, unpublished, May 1967.
5. Atomic Energy of Canada Limited, unpublished, 1967.
6. B. Cox, The Use of Electrical Methods for Investigating the Growth and Breakdown of Oxide Films on Zirconium Alloys, Canadian Report AECL-2668, January 1967.
7. F. W. Albaugh, S. H. Bush, J. J. Cadwell, D. R. deHalas, and D. C. Worlton, Battelle–Northwest, unpublished, March 1967.
8. J. T. Dunn, Wear Rates of Metals and Oxides in 80 and 160°F High-Purity Water, Canadian Report AECL-2602, August 1966.
9. J. E. Draley and W. E. Ruther, Corrosion of Aluminum Alloys by Flowing High-Temperature Water, USAEC Report ANL-7227, Argonne National Laboratory, January 1967.
10. D. G. Tskhvirashvili, L. E. Vasadze and A. S. Tsukh, Distribution of Construction Materials and Neutron Ir-

radiation, *At. Energ. (USSR)*, 21(4): 300-302 (October 1966).

11. A. A. Kot, *Water and Water Treatment in Nuclear Power Plants*, Atomizdat, Moscow, 1964. (USAEC Report AEC-tr-6629.)
12. J. E. Antill, M. J. Bennett, G. H. Chaffey, K. A. Peakall, and J. B. Warburton, Some Aspects of the Corrosion of a 20 Percent Cr/25 Percent Ni/Nb Stainless Steel at Elevated Temperatures, British Report AERE-R-5377, January 1967.
13. C. R. Bergen, Elk River Reactor Operations Analysis Program Final Report: Task 615. Corrosion Samples and Tests Evaporator Water Boxes, USAEC Report ACNP-66542, Allis-Chalmers Mfg. Co., June 1966.
14. S. P. Gibson, W. Evans, and R. D. Watson, Chloride Stress-Corrosion Cracking in Threaded 300 Series Stainless-Steel Components, Canadian Report AECL-2878, May 1967.
15. H. L. Logan and M. J. McBee, Stress-Corrosion Cracking of Cold-Reduced Austenitic Stainless Steels, *Mater. Res. Stand.*, 7(4): 137-145 (April 1967).
16. J. F. Gibbons, L. E. Anderson, R. W. Knapp, F. T. Grubelich, and W. J. Mordarski, Advanced BONUS Core Development Program, Final Report, USAEC Report CEND-265, Combustion Engineering, Inc., Feb. 28, 1966.
17. D. A. Kubose, M. G. Lai, H. A. Goya, and H. I. Cordova, Measurement of Seawater Corrosion of SNAP Container Alloys Using Radioactive Tracer Techniques, USAEC Report USNRDL-TR-1092, Naval Radiological Defense Laboratory, Oct. 10, 1966.
18. P. N. Walsh, J. M. Quets, and R. A. Graff, Kinetics of the Oxygen–Tungsten Reaction at High Temperatures, *J. Chem. Phys.*, 46: 1144-1153 (Feb. 1, 1967).
19. Papers presented at International Research Symposium on Oxidation of Metals, Brussels, Belgium, October 6–8, 1965, CONF-651082.
    a. J. E. Battles, G. R. St. Pierre, and R. Speiser, Reaction of Water Vapor and Tungsten, pp. 213-221.
    b. D. Cismaru and A. Geangu-Moisin, Oxidation of Tungsten at High Temperatures: Kinetics of the System W–CO_2, pp. 222-227.
    c. F. Degreve and J. Drowart, Study of the Mass Behavior of the Oxidation of Tantalum, pp. 204-212.
    d. W. M. M. Huijbregts and S. M. J. Brabers, Oxidation of Niobium and of Niobium Coated with Aluminum in Steam and Steam–Air Mixtures, pp. 61-69.
20. E. Fromm and H. Jehn, Steady States During Annealing of Niobium and Tantalum in Oxygen, *Z. Metallk.*, 58: 61-66 (January 1967).
21. E. Fromm and H. Jehn, Steady States During Heat-Treatment of Niobium and Tantalum Under Water Vapor, *Z. Metallk.*, 58: 120-124 (February 1967).
22. L. M. Adelsberg, G. R. St. Pierre, and R. Speiser, Kinetics of the Oxidation of Tantalum by Water Vapor, *Trans. AIME, Met. Soc.*, 239: 490-496 (April 1967).
23. M. I. Gavrilyuk, V. T. Ershova, and V. A. Konstantinov, Reaction of Tantalum with Nitrogen and Air, *Metalloved. Term. Obrab. Metal.*, 12: 37-40 (December 1966).
24. R. F. Voitovich, Oxidation Rate of Niobium–Iron and Niobium–Cobalt Alloys at High Temperatures, *Zh. Prikl. Khim.*, 39: 1418-1422 (June 1966).
25. N. Terao, Structure of Tantalum Oxides, *J. Appl. Phys. (Japan)*, 6: 21-34 (January 1967).
26. S. Steeb and J. Renner, Electron-Diffraction Investigations on the Stratification of Oxygen Atoms in Niobium and Tantalum, *Metall.*, 21: 93-97 (February 1967).
27. J. Van Landuyt, Electron Microscopic Investigation of Phenomena Associated with Solid Solution of Oxygen in Niobium, USAEC–Euratom Report EURAEC-1184 (EUR-2022.*e*), Centre d'Étude de l'Énergie Nucléaire, April, 1965.
28. J. Niebuhr, The Lower Oxides of Niobium, *J. Less-Common Metals*, 11: 191-203 (September 1966).
29. V. L. Hill and J. J. Rausch, Protective Coatings for Tantalum-Base Alloys, Report AFML-TR-64-354 (Pt.2), Illinois Institute of Technology Research Institute, October 1965.
30. M. R. Licciardello and B. Ohnysty, Development of Composite Structures for High-Temperature Operation, Report AFFDL-TR-67-54, Solar, April 1967.
31. P. Kofstad and S. Espevik, Oxidation of Tantalum Coated with Aluminum and Aluminum–Chromium Alloys, *J. Less-Common Metals*, 12: 117-138 (February 1967).
32. B. Lux, P. Stecher, and N. Perlhefter, Protection of Niobium from Oxidation by a $NbSi_2$ Coating Impregnated with SnAl (in French), *Ann. Mines*, pp. 802-821 (October–November 1966).
33. J. R. Weeks (Comp.), Brookhaven National Laboratory, unpublished, 1967.
34. Argonne National Laboratory, Reactor Development Program Progress Report, April 1967, USAEC Report ANL-7329, June 16, 1967.
35. Argonne National Laboratory, Reactor Development Program Progress Report, May 1967, USAEC Report ANL-7342, June 30, 1967.
36. L. Champeix, W. Graff, and J. Sannier, Effect of Various Additives on the Compatibility of Zirconium with Liquid Sodium, in *Study of the Corrosion and Protection of Zirconium and Its Alloys* (in French), pp. 63-65, University Press of France, 1966.
37. A. W. Thorley and C. Tyzack, The Corrosion Behaviour of Iron and Nickel-Based Alloys in High-Temperature Sodium, British Report TRG-Report-1356 (or NP-16413), Oct. 17, 1966.
38. R. L. Carter, The Problem of Core Graphite Contamination by Sodium in a Calandria Type SGR, USAEC Report NAA-SR-Memo-3697, Atomics International, 1957.
39. R. B. Hinze, Sodium Purity Requirements (A Review and Evaluation), USAEC Report NAA-SR-Memo-12394, Atomics International, Liquid Metal Engineering Center, May 10, 1967.
40. Atomics International, Liquid Metal Engineering Center Quarterly Technical Progress Report for January–March 1967, USAEC Report NAA-SR-12416, May 5, 1967.
41. H. Susskind and W. Becker, Behavior of Fuel Claddings Under Load and with Thermal Cycling in Sodium, USAEC Report BNL-50010 (T-433), Brookhaven National Laboratory, June 1966.
42. H. Derow and B. E. Farwell, SNAP-8 Materials Semiannual Report, January–June 1966, Report NASA-CR-72156 (or N67-18985), Aerojet-General Corporation, July 1966.
43. J. Boulton, Some Aspects of Materials in Organic-Cooled Reactors (A Summary of Canadian Experience), Canadian Report AECL-2640, May 1966.
44. R. L. Klueh and D. H. Jansen, Effects of Liquid and Vapor Cesium on Structural Materials, USAEC Report ORNL-TM-1813, Oak Ridge National Laboratory, June 1967.
45. H. C. Young and A. G. Grindell, Summary of Design and Test Experience with Cesium and Potassium Components and Systems for Space Power Plants, USAEC Report ORNL-TM-1833, Oak Ridge National Laboratory, June 1967.
46. *Nucl. Appl.*, 3(2): 71-134 (February 1967).
    a. J. H. DeVan and C. E. Sessions, Mass Transfer of Niobium-Base Alloys in Flowing Nonisothermal Lithium, pp. 102-109.
    b. J. A. DeMastry, Corrosion Studies of Tungsten, Molybdenum, and Rhenium in Lithium, pp. 127-134.
    c. A. J. Romano, A. H. Fleitman, and C. J. Klamut, Evaluation of Li, Na, K, Rb, and Cs Boiling and Condensing in Nb–1% Zr Capsules, pp. 110-116.

d. K. Goldmann, N. Hyman, S. Kostman, and J. McKee, Carbon and Nitrogen Transfer in a Type 316 Stainless-Steel, Nb–1% Zr, Liquid-Potassium System, pp. 117-126.
47. J. R. Weeks (Comp.), The U. S. Program on Corrosion by Liquid Sodium, USAEC Report BNL-11265, Brookhaven National Laboratory, Apr. 18, 1967.
48. S. H. Fenney, Bibliography on Liquid Metals, 1964–1965, British Report TRG-Inf. Ser.-312(R)(Suppl. 1), November 1966.
49. Argonne National Laboratory, Reactor Development Program Progress Report, February 1967, USAEC Report ANL-7308, Mar. 28, 1967.
50. General Electric Company, Nuclear Materials and Propulsion Operation, High-Temperature Materials Programs, Part A, Annual Report No. 6, USAEC Report GEMP-475A, Mar. 31, 1967.
51. L. Baker, Jr., and L. C. Just, Studies of Metal–Water Reactions at High Temperatures. III. Experimental and Theoretical Studies of the Zirconium–Water Reactions, USAEC Report ANL-6548, Argonne National Laboratory, May 1962.
52. A. W. Lemmon, Jr., Studies Relating to the Reaction Between Zirconium and Water at High Temperatures, USAEC Report BMI-1154, Battelle Memorial Institute, Columbus Laboratories, Jan. 3, 1957.
53. W. A. Bostrom, The High Temperature Oxidation of Zircaloy in H_2O, USAEC Report WAPD-104, Westinghouse Electric Corporation, Bettis Atomic Power Laboratory, Mar. 19, 1954.
54. W. J. O'Donnell, Fracture of Cylindrical Fuel Rod Cladding Due to Plastic Instability, USAEC Report WAPD-TM-651, Westinghouse Electric Corporation, Bettis Atomic Power Laboratory, April 1967.
55. J. W. Weber, Plastic Stability of Zircaloy-2 Fuel Cladding, USAEC Report BNWL-SA-653, Battelle–Northwest, July 1966.
56. H. D. Gronbeck, ETR Radiation Damage Surveillance Programs. Progress Report II, USAEC Report IN-1036, Idaho Nuclear Corporation, February 1967.
57. P. J. Harrop and J. N. Wanklyn, The Embrittlement of Oxide Films on Zirconium by Neutron Irradiation, *J. Nucl. Mater.*, 21: 310-316 (1967).
58. R. B. Roy and B. Solly, Embrittlement of Neutron Irradiated 20 Cr–25 Ni–Nb Austenitic Steel at 650°C, *J. Iron Steel Inst. (London)*, 205: 58-61 (January 1967).
59. R. B. Roy and B. Solly, High-Temperature Tensile Properties of Unirradiated and Neutron-Irradiated 20 Cr–35 Ni Austenitic Steel, Swedish Report AE-260, December 1966.
60. H. J. Busboom, F. A. Comprelli, and C. N. Spalaris, Radiation Damage in Incoloy 800, *Nucl. Appl.*, 2: 486-488 (December 1966).
61. Reference deleted.
62. Argonne National Laboratory, Reactor Development Program Progress Report, March 1967, USAEC Report ANL-7317, Apr. 28, 1967.
63. E. T. Wessel, Variations in the Embrittlement of Irradiated Pressure Vessel Steels, in *Proceedings of the First International Conference on Fracture*, Vol. 3, pp. 1971-1986, 1966.
64. G. Östberg and H. Mogard, Progress Report on Reactor Materials and Fuel Elements, July 1, 1966–January 31, 1967, Swedish Report S-362, March 1967.
65. E. B. Norris, Influence of Neutron Irradiation on the Properties of Steels and Welds Typical of the ERR Pressure Vessel, USAEC Report SWRI-1228P4-28, Southwest Research Institute, Jan. 24, 1967.
66. C. R. Brinkman and J. M. Beeston, Axial Fatigue of Pre- and Postirradiated A-302B and A-212B Steels, USAEC Report IN-1052, Idaho Nuclear Corporation, January 1967.
67. J. L. Brimhall and B. Mastel, Neutron Irradiation Effects in FCC, BCC, and CPH Metals, USAEC Report BNWL-361, Battelle–Northwest, February 1967.
68. Oak Ridge National Laboratory, Solid State Division Annual Progress Report for Period Ending December 31, 1966, USAEC Report ORNL-4098, March 1967.
69. Oak Ridge National Laboratory, Radiation Metallurgy Section, Solid State Division Progress Report for Period Ending January 1967, USAEC Report ORNL-4097, April 1967.
70. K. Shiraishi and T. Murata, Electron Microscope Observation of Gas Bubbles in Neutron-Irradiated Al–Li Alloys, *J. Nucl. Sci. Technol. (Tokyo)*, 3: 466-472 (November 1966).
71. F. J. A. den Broeder and W. G. Burgers, The Existence of a Chromium–Molybdenum A15 Structure, *Acta Crystallogr.*, 21: 1003-1004 (Dec. 10, 1966).
72. J. W. Clark and C. S. Wukusick, Development of High-Temperature Chromium Alloys, Report NASA-CR-80657 (N67-13536), General Electric Company, Materials Development Laboratory Operation, Apr. 22, 1966.
73. I. I. Kornilov and E. N. Pylaeva, Niobium–Nickel System, *Izv. Akad. Nauk SSSR, Metally*, No. 5: 132-136 (September–October 1966).
74. Z. C. Szkopiak, Yield-Point Phenomenon in Electron-Beam Refined Niobium, *Proceedings of Conference on Physical Basis of Yield Fracture*, pp. 108-118, Institute of Physics and Physical Society, 1966.
75. R. J. Dinter, High-Vacuum Purification of Niobium and Tantalum and Its Influence on the Electric Resistivity, *Z. Metallk.*, 58: 70-75 (January 1967).
76. I. M. Nedyukha and V. G. Chernyi, Elastic Properties of the Alloys of Niobium with Tantalum, Vanadium, and Titanium, *Fiz. Metal. Metalloved.*, 22: 114-117 (July 1966).
77. E. V. Vasil'eva, D. A. Prokoshkin, and L. M. Belova, Structure and Properties of Niobium–Tantalum Alloys Containing Tungsten and Molybdenum, *Metalloved. Term. Obrab. Metal.*, No. 12: 21-24 (December 1966).
78. L. A. Panteleimonov, O. P. Nesterova, Z. A. Guts, K. G. Akhmetzyanov, and I. G. Sokolova, *Vestn. Mosk. Univ., Ser. II, Khim.*, No. 6: 57-62 (November–December 1965).
79. T. G. Oakwood and R. D. Daniels, Sorption Kinetics and Mechanical Properties of Dilute Columbium–Hydrogen Solutions, USAEC Report ORO-2570-10, Oklahoma University Research Institute, February 1967.
80. T. A. Trozera and T. E. Firle, A Program of Basic Research on Mechanical Properties of Reactor Materials, USAEC Report GA-7661, General Atomic Division, General Dynamics Corp., January 1967.
81. J. W. Edington, Improvement of Creep Strength and Low-Temperature Ductility of Refractory Metals by Means of Mechanical Twinning, Report NASA-CR-79710 (N67-10893), Battelle Memorial Institute, Columbus Laboratories, Oct. 15, 1966.
82. G. G. Lessmann, Effect of 1000-Hour Thermal Exposures on Tensile Properties of Refractory Metal Alloys, Report WANL-PR-(P)-012, Westinghouse Electric Corporation, Astronuclear Laboratory, January 1967.
83. Wah Chang Corporation, Columbium and Tantalum Alloys (Technical Information), USAEC file no. NP-16657 (Vol. II), August 1966.
84. C. D. Calhoun, Preliminary Study of Niobium–Silicon Alloys, USAEC Report KAPL-M-6574, Knolls Atomic Power Laboratory, January 1966.
85. L. D. Whitmire and F. R. Brotzen, The Effects of Deformation on the Electrical Resistivity of Molybdenum Single Crystals, Report NASA-CR-77029 (N66-33405), Rice University, December 1966.
86. L. D. Whitmire, Effects of Impurities on the Plastic Deformation of Molybdenum Single Crystals, Thesis, Rice University, 1966.
87. K. Tsuya and N. Aritomi, Effects of Some Additional Elements on the Ductility of Electron-Beam-Melted Molybdenum Ingots, *Nippon Kinzoku Gakkaishi*, 30: 952-958 (1966).

88. E. Gebhardt, E. Fromm, and U. Roy, The Solubility of Carbon in Molybdenum, Tungsten, and Rhenium, *Z. Metallk.*, 57: 732-736 (October 1966).
89. D. A. Prokoshkin and O. I. Sedunova, Ordered Solid Solution in the Chromium–Molybdenum System, *Izv. Vyssh. Ucheb. Zaved., Mashinostr.*, No. 7: 116-119 (1966).
90. Yu. B. Malevskii and D. B. Novikova, Effect of the Annealing Temperature on the Structure and Properties of Cast Molybdenum, *Metalloved. Term. Obrab. Metal.*, No. 12: 50-53 (December 1966).
91. N. N. Morgunova, Effect of Titanium, Zirconium, and Hafnium on the Properties of Molybdenum with Carbon, *Metalloved. Term. Obrab. Metal.*, No. 12: 40-44 (December 1966).
92. N. V. Ageev, A. A. Babareko, G. E. Chuprikov, and N. N. Bokareva, Mechanism of the Plastic Deformation of Differently Oriented Molybdenum Single Crystals Under Tension, *Izv. Akad. Nauk SSSR, Metally*, No. 4: 84-89 (July–August 1966).
93. R. V. Skolozdra and E. I. Gladyshevskii, System Mo–Fe–Si, *Izv. Akad. Nauk SSSR, Neorgan. Materialy*, 2: 1448-1453 (August 1966).
94. R. V. Skolozdra, E. T. Gladyshevskii, and Y. P. Yarmolyuk, Ternary Mo–Co–Si System, *Izv. Akad. Nauk SSSR, Metally.*, No. 5: 148:151 (September–October 1966).
95. W. D. Klopp, W. R. Wetzke, and P. L. Raffa, Mechanical Properties of Dilute Tungsten–Rhenium Alloys, Report NASA-TN-D-3483 (N66-37031), National Aeronautics and Space Administration, Lewis Research Center, September 1966.
96. S. L. Israel, T. D. Hawkins, and S. C. Hyman, Thermal Properties of Solid and Porous Tungsten at Temperatures to 5000°F, Report NASA-CR-402 (N66-19519), United Nuclear Corp., March 1966.
97. P. N. Flagella (Comp.), Some Physical and Mechanical Properties of W–25 At. % Re–30 At. % Mo W–30 At. % Re–30 At. % Mo and W–25 Wt. % Re, USAEC Report GEMP-497, General Electric Company, Nuclear Materials and Propulsion Operation, Mar. 21, 1967.
98. J. L. Walter, Growth and Preferred Orientations of Large Elongated Grains in Doped Tungsten Sheet, *Trans. Met. Soc. AIME*, 239: 272-286 (February 1967).
99. A. M. Zakharov and E. M. Savitskii, Constitution Diagram of the Ternary W–Zr–Ti Alloy, *Izv. Akad. Nauk SSSR, Metally.*, No. 5: 159–168 (September–October 1966).
100. G. V. Samsonov, Yu. K. Lapshov, I. A. Podchernyaeva, V. S. Fomenko, Yu. I. Erosov, and E. M. Dudnik, Some Physical Properties of the W–LaB_6 Alloys, *Izv. Akad. Nauk SSSR, Neorgan. Materialy*, 2: 1454-1459 (August 1966).
101. A. T. Grigor'ev, E. M. Sokolovskaya, A. P. Nefedov, and I. G. Sokolova, Effect of Niobium on Solid-State Transformations in Alloys of Vanadium–Tantalum System, *Izv. Akad. Nauk SSSR, Metally.*, No. 3: 183-192 (May–June 1966).
102. A. P. Nefedov, E. M. Sokolovskaya, A. T. Grigor'ev, V. I. Chechernikov, I. G. Sokolova, and L. A. Guzei, Solid-State Phase Transformations in Vanadium–Tantalum Alloys, *Vestn. Mosk. Univ., Ser. II, Khim.*, No. 5: 42-47 (September–October 1965).
103. A. T. Grigor'ev, E. M. Sokolovskaya, A. P. Nefedov, and N. G. Sokolova, Effects of Molybdenum on Solid-State Transitions in Vanadium–Tantalum Alloys, *Vestn. Mosk. Univ., Ser. II, Khim.*, No. 4: 44-49 (July–August 1965).
104. Y. S. Shen, S. Worcester, and S. S. Christopher, Vanadium Purification, USAEC Report CEND-3742-293, Combustion Engineering, Inc., January 1967.
105. W. C. Kramer, W. R. Burt, Jr., F. I. Karasek, J. E. Flinn, and R. M. Mayfield, Vanadium Alloy Screening Studies and Fabrication of V–15 Wt. % Ti–7.5 Wt. % Cr Tubing for Nuclear Fuel Cladding, USAEC Report ANL-7206, Argonne National Laboratory, August 1966.
106. G. Fiorito and W. Schule, Recovery of Work Hardening of SAP Alloys, *J. Nucl. Mater.*, 21: 61-69 (1967).
107. C. J. Beevers, Interpretation of Fracture Surface Observations, *Acta Met.*, 15: 432-434 (February 1967).
108. E. A. Abromyan, L. I. Ivanov, N. S. Kudryatsev, and V. A. Yanushkevich, Influence of a Vacuum on the High-Temperature Creep of Beta Zirconium (in Russian), *Fiz.-Khim. Mekh. Mater.*, No. 4: 422-423 (July–August 1966).
109. D. H. Baldwin, Investigation of the Effect of Oxygen on the Tensile Deformation of Zirconium, Thesis, University of Florida, 1966.
110. E. N. Aqua and C. M. Owens, The Microstructural Characterization of Cold Rolled Zircaloy-4 Sheet, *Trans. Met. Soc. AIME*, 239: 155-161 (February 1967).
111. V. S. Arunachalam, B. Lehtinen, and G. Östberg, The Orientation of Zirconium Hydride on Grain Boundaries in Zircaloy-2, *J. Nucl. Mater.*, 21: 241-248 (1967).
112. P. Baque and R. Oanas, Ternary Alloy of Zirconium, Canadian Patent No. 750,318, Jan. 10, 1967.
113. W. Evans, J. E. LeSurf, and W. R. Thomas, Heat-Treated Zr–2.5% Nb Pressure Tubes for Water-Cooled Power Reactors, Canadian Report AECL-2890, May 1967.
114. J. H. Bucher, The Toughness of Ferritic Steel Strengthened by Precipitation of CbC, *Trans. Met. Soc. AIME*, 239(4): 478-485 (April 1967).
115. S. Nagashima and N. Mori, Studies on Tempering Characteristics of A-302YB (in Japanese), *Tetsu To Hagane*, 51: 2037-2039 (October 1965).
116. A. F. Rowcliffe, J. P. Shepherd, and A. C. Wilkinson, Precipitation in F. V. 548 Stainless Steel, British Report TRG-Report-1357(*c*), 1967.
117. M. Deighton, Solubility of NbC in 20% Cr–25% Ni Stainless Steel, *J. Iron Steel Inst. (London)*, 205: 535-538 (May 1967).
118. Virginia Polytechnic Institute, The Influence of Nitrogen Additions on Phase Relations in AISI Type 304, Summary Report 438-A, USAEC–Euratom Report EURAEC-1716, August 1966.
119. G. Chaudron, Annual Report on Studies of Stainless Steels, July 1, 1965–June 30, 1966, Special Report No. 2, USAEC–Euratom Report EURAEC-1797.
120. N. F. Lashko and K. P. Sorokina, Characteristic Features of the Phase Composition of Heat-Resistant Steels and Alloys of the Fe–Ni–Cr–Ti and Mo–W–B System (in Russian), *Fiz. Metal Metalloved.*, 22: 66-72 (July 1966).
121. D. Dulieu and B. Aronsson, Structure and Mechanical Properties of Pure 15% Cr–20% Ni Austenites Hardened with Titanium and Some Observations on the Influence of Boron Additions, *Jernkontorets Ann.*, 150: 787-817 (1966).
122. Embrittlement Resistant Iron–Chromium–Aluminum–Yttrium Alloys, U. S. Patent No. 3,298,826, to USAEC, Jan. 17, 1967.
123. J. R. Mihalisin, Sigma Formation in Nickel-Rich Nickel – Cobalt – Chromium – Aluminum – Titanium – Carbon Alloys at 1650°F, *Trans. Met. Soc. AIME*, 239(2): 180-193 (February 1967).
124. C. R. Brooks and E. E. Stansbury, The Specific Heat from 50 to 700°C of a Nominal Ni (16 Wt. % Mo, 7 Wt. % Cr, 5 Wt. % Fe) Alloy, *J. Nucl. Mater.*, 20: 332-333 (1966).
125. J. Prock, Jr., and H. J. Wagner, A Primer on Soviet Superalloys, Report DMIC-235, Battelle Memorial Institute, Defense Metals Information Center, Dec. 20, 1966.
126. G. V. Samsonov, G. N. Makarenko, and A. N. Krushinskii, Investigation of the Conditions of Formation of Solid Solutions of Carbides Involving Scandium Carbide, in *Vysokotemperaturnye Neorganicheskie Soedineniya*, pp. 250-256, Izdatel'stvo Naukova Dumka, Kiev, 1965.
127. G. A. Meerson, E. M. Rakitskaya, V. N. Bulgakov, and A. S. Ladygo, Investigation of the Conditions for the Preparation of Niobium Carbide and Niobium Carbo-

nitride from Niobium Pentoxide, *Izv. Akad. Nauk SSSR, Neorgan. Materialy*, 2: 1429-1433 (August 1966).

128. I. Kraus, On the Question of the Influence of the Average Grain Size of WC and the Content of the Binding Cobalt Phase on X-Ray Measurements of Macrostresses in Sintered Carbides of the System WC–Co, *Czech. J. Phys.*, B17: 249-258 (1967).
129. R. F. Voitovich, Calculation of Reduced Thermodynamic Potentials of Some Carbides and Nitrides, *Porosh. Met., Akad. Nauk Ukr. SSR*, No. 2: 40-43 (February 1967).
130. A. S. Bolgar, E. A. Guseva, and V. V. Fesenko, Thermodynamic Properties of Zirconium and Hafnium Carbides over the Range of 298 to 2500°K, *Porosh. Met., Akad. Nauk Ukr. SSR*, No. 1: 40-43 (January 1967).
131. M. V. Sazonóva and G. N. Komarova, Protection of Boron Carbide Against Oxidation and Reaction with Various Materials at 1200°C in Air Atmosphere, *Zh. Prikl. Khim.*, 39: 2662-2669 (December 1966).
132. H. Suzuki and K. Hayashi, Effects of the Carbon Content on the Properties of WC–TiC–Co Alloys, *Trans. Jap. Inst. Metals*, 7: 199-203 (July 1966).
133. A. I. Avgustinik, D. A. Golikova, G. M. Klimashin, V. S. Neshpor, S. S. Ordan, and V. A. Snetkova, The Dependence of Certain Electro- and Thermophysical Properties of Zirconium Monocarbide on Carbon Content in the Homogeneity Region, Report NASA-TT-F-10448 (N67-15845) [from *Izv. Akad. Nauk SSSR, Neorgan. Materialy*, 2(8): 1439-1444 (1966)].
134. Albany Metallurgy Research Center, Bureau of Mines, Quarterly Metallurgy Progress Report No. 34, January 1–March 31, 1967, USAEC Report USBM-RC-1288.
135. I. G. Barantseva, V. N. Paderno, and Yu. B. Paderno, Some Physical Properties of Alloys of the ZrC–NbC and TaC–HfC Systems, *Porosh. Met. Akad. Nauk Ukr. SSR*, No. 2: 70-73 (February 1967).
136. R. A. Andrievskii, N. S. Strel'nikova, N. I. Poltoratskii, E. D. Kharkhardin, and V. S. Smirnov, Fusion Point in the Systems ZrC–HfC, TaC–ZrC, TaC–HfC, *Porosh. Met. Akad. Nauk Ukr. SSR*, No. 1: 85-88 (January 1967).
137. Yu. B. Paderno, E. M. Dudnik, T. V. Andreeva, I. G. Barantseva, and V. L. Yupko, Measurement of the Coefficient of Thermal Expansion of ZrC, HfC, NbC, and TaC at High Temperatures, USAEC Report AEC-tr-6867 (from *Vysokotemperaturnye Neorganicheskie Soedineniya*, pp. 293-296, Akademiya Nauk Ukrainski SSR, Kiev, 1965).
138. Yu. B. Paderno, I. G. Barantseva, and V. L. Yupko, Determination of Thermal Conductivity and Electric Resistance of ZrC, HfC, NbC, and TaC at High Temperatures, in *Vysokotemperaturnye Neorganicheskie Soedineniya*, pp. 199-204, Izdatel'stvo Naukova Dumka, Kiev, 1965.
139. N. H. Krikoran, T. C. Wallace, M. C. Krupka, and C. L. Radosevich, The Reaction of Some Noble and Transition Metals with Refractory Carbides, *J. Nucl. Mater.*, 21: 236-238 (1967).
140. T. Ya. Kosolapova, V. B. Fedorus, and Yu. B. Kuz'ma, Interaction Between Carbides of Transition Metals and Their Oxides, Report NASA-TT-F-10447 (N67-15690) [from *Izv. Akad. Nauk SSSR, Neorgan. Materialy*, 2(8): 1516-1523 (1966)].
141. A. Hivert, A Refractory Material Resistant to Thermal Shock: Impregnated Tantalum Carbide, Report NASA-TT-F-10249 (N67-10206) [from paper presented at Conference on Materials for Use in Space, Paris Feb. 7–11, 1966].
142. V. S. Dergunova, P. L. Timonin, A. N. Kuzin, and V. Z. Tseitlin, Properties of Tantalum Diboride–Zirconium Diboride Alloys Containing Chromium, *Tsvetn. Metal.*, No. 12: 84-86 (December 1966).
143. R. D. Browne, Properties of Concrete in Reactor Vessels, in Proceedings of the Conference on Prestressed Concrete Pressure Vessels, held at Churchhouse, London, Mar. 13–17, 1967, Group C, Paper B, pp. 11-31.
144. V. N. Pavlikov, L. M. Lopato, Z. A. Yaremenko, and A. V. Shevchenko, Phase Diagram of the Sm_2O_3–Cr_2O_3 System, *Izv. Akad. Nauk SSSR, Neorgan. Materialy*, 2: 1055-1057 (June 1966).
145. V. N. Pavlikov, L. M. Lopato, and S. G. Tresvyatskii, Study of the Phase Diagram of the Y_2O_3–Cr_2O_3 System, *Izv. Akad. Nauk SSSR, Neorgan. Materialy*, 2: 1244-1247 (July 1966).
146. A. V. Shevchenko, L. M. Lopato, and S. G. Tresvyatskii, Phase Diagram of the Gd_2O_3–Cr_2O_3 System, *Izv. Akad. Nauk SSSR, Neorgan. Materialy*, 2: 1240-1243 (July 1966).
147. S. H. Hsu, W. Kobes, and M. E. Fine, Strengthening of Sapphire by Precipitates Containing Titanium, *J. Amer. Ceram. Soc.*, 50(3): 149-152 (March 1967).

Section IV

Reactor Materials

Special Fabrication Techniques

Cast and Wrought Materials

Melting and Casting Processes

The National Lead Company of Ohio[1] has made changes in their induction-melting and casting procedures for the production of 8- and 9-in.-diameter solid uranium ingots to significantly improve soundness. The new furnace cycle being employed is outlined below:

Operation	Crucible power, kw	Mold power, kw	Time, min
Heating	159	15	60
	90	0*	50
	0	0	5
Pour	-	-	-
Cool	-	-	90

*Previously 15 kw in routine practice.

This furnace cycle differed from the old cycle in that mold heating was used only during the first hour of the heating period. Other changes included (1) removing insulation from bottom regions of the mold, (2) maintaining a clearance of about ½ in. between the crucible bottom and the top of the mold (for more efficient radiant heat transfer), and (3) employing a cup on all ingots so that the level of metal in the mold after pouring was approximately 3 in. from the top.

The consumable-electrode arc melting of uranium has also been described by National Lead.[2] Electrodes for arc melting were produced by vacuum-induction melting uranium feedstock and casting into 5½-, 8-, and 9-in.-diameter molds. These electrodes were then arc melted in a vacuum into production-size ingots, 7, 7⅜, and 11 in. in diameter. Metallographic studies on resulting arc-melted castings showed that the inclusions were finely divided and evenly distributed. Chemical analyses indicated that no chemical refinement, except for a small reduction in hydrogen content, could be attributed to the arc-melting process. It was observed that fuel cores fabricated from arc-melted uranium performed as well as cores from regular induction-melted stock in both cladding and reactor tests.

Melting and casting studies on refractory-metal–graphite alloys are being conducted at two sites. Battelle–Columbus[3] is developing a subscale manufacturing process for the preparation of these alloys for environmental-, physical-, and mechanical-property determinations. Several HfC + C and ZrC + C compositions up to 2½ in. in diameter and 6 in. long have been prepared by skull arc melting and drop casting. Consumable-electrode arc melting has also been examined for these alloys, but cracks have occurred in all castings prepared to date. The Bureau of Mines[4] is preparing smaller castings of HfC + C, ZrC + C, NbC + C, and TaC + C for hot-hardness, air-oxidation, thermal-expansion, and resistivity measurements. Some property data have been obtained on these materials.

Fabrication of Cast Structures

On the basis of results of screening tests at Argonne[5] involving a number of alloys, a V–15 wt.% Ti–7.5 wt.% Cr alloy emerged as a promising cladding candidate for sodium-cooled fast reactors. The following fabrication procedures were employed on this alloy. Consolidation involved consumable-electrode arc melting of compacted electrodes followed by arc remelting. The double-melted ingots were broken down by extrusion, and then reextruded into rod, sheet bar, and tube blanks. Rod and sheet products were easily cold rolled to finished sizes. Extruded tube blanks were processed by swaging, tube reducing, and drawing. Some early processing problems were solved, and high yields were realized in the production of reactor-grade tubing.

A new method has been developed by Reactive Metals, Inc.,[6] for producing coextrusion billets of uranium. The method, termed the "upset-forge" process, involves extruding the ingot to a size smaller than that of the finished billet, correcting any existing defects, and then deforming the billet in a closed container to the required size and shape of a finished billet. The advantage of this process is that metal is removed only where actual defects are present, and thus the total machining time and scrap losses are reduced. Fifty-two billets, each approximately 2.8 in. in inside diameter and 6.95 in. in outside diameter were prepared. An average yield of about 75% of the original starting weight was realized.

The French[7] have summarized the fabrication of fuel elements in their country. The greater part of their industrial activities in this area is divided among three families of fuel elements: those with

metallic uranium as their base, those with oxides as their base, and those which are laminated. The principal steps in the fabrication of these three types of elements are discussed.

The fabrication and evaluation of 3.25-in.-ID, 0.120-in.-wall, cold-worked Zr–2.5 wt.% Nb pressure tubes have been described by Chalk River.[8] The tubes were made by an extrusion and drawing process similar to that employed on Zircaloy-2, except that in some cases an annealing treatment was also used between the extrusion and drawing steps. Tubes fabricated without the annealing treatment were found to be much stronger than those which were annealed. The ultimate tensile strength of the strongest tube exceeded 70,000 psi at 300°C. A postfabrication anneal at 400°C for 72 hr had little effect on the ultimate tensile strength of the strongest tubes, but the 0.2% yield strength decreased by up to 24%. Annealing at 500°C for 10 hr weakened all the tubes.

The Cyclops Corp. has developed a fabrication schedule for the production of vacuum arc-melted tungsten sheet. This schedule is shown in Table IV-1.

Table IV-1 FINALIZED FABRICATION SCHEDULE FOR THE PRODUCTION OF ARC-MELTED TUNGSTEN SHEET[9]

Process*	Temp., °F	Target finish gauge, in. 0.060	0.040	0.020
Breakdown rolling	2300	0.800	0.540	0.280
Recrystallization anneal, 1 hr	2500–2700			
Intermediate rolling	2300	0.360	0.200	0.110
Stress-relieve anneal, 1 hr	2000			
Intermediate rolling (continued)	2000	0.120	0.120	
Final rolling†	1400	0.060	0.040	0.020
Roller level	1200–1400			
Descale, then stress-relieve anneal	1700			

*Ingots were initially vacuum arc melted in a 9½-in.-diameter crucible and conditioned to a 8-in.-diameter billets for extrusion. These were extruded to 2- by 6-in. sheet bar at 3000 to 3500°F and conditioned prior to rolling, as shown above.

†Individual sheet cross rolled to 1:1 ratio separately, using 1095 steel cover plates. Total reductions in rolling were 92 to 94% after recrystallization and 80 to 85% after stress relief.

The objective of this work was to prepare 36- by 96-in. sheet 0.020, 0.040, and 0.060 in. thick, but the goal has not yet been realized because of severe problems with surface condition and cracking owing to the processing sequences investigated.[9]

The Russians[10] have examined techniques for cladding niobium on steel. Niobium-clad steel sheets were produced by rolling packs consisting of steel plate (9 to 12 mm thick) and niobium sheet (2 mm thick) in a vacuum (4×10^{-5} mm Hg) mill equipped with steel rolls (166 mm in diameter) at 900 to 1200°C with reductions of 10 to 40% per pass. The width of packs was 50 mm, and the length was 140 mm. Strength of the bond between the cladding and base metals increased with increasing rolling temperature. The shear strength was 10 kg/mm^2 after 30% reduction at 900 to 1000°C, and 21 to 23 kg/mm^2 after the same reduction at 1100 to 1200°C. The bond strength also increased with increasing reduction per pass. After 10% reduction at 1100°C, the bond strength did not exceed 10 kg/mm^2; and, after 30 to 40% reduction, it reached 25 kg/mm^2. However, high reduction led to a nonuniform deformation of the layers. Therefore, to ensure reliable bonds and more uniform deformation, the workers found it best to roll at 1100 to 1200°C with 10 to 15% reduction per pass and 30 to 40% total reduction.

The effects of cold rolling, direction of rolling, and annealing on the mechanical properties of niobium at room and high temperature were also investigated by the Russians.[11] Niobium ingots, 75 mm in diameter and 150 mm long, melted in a vacuum arc furnace and homogenized at 1800°C in an argon atmosphere for 10 hr, were extruded at 1500°C into sheet bars 35 to 40 mm thick. After reheating to 1500°C, the bars were rolled to a thickness of 12 to 15 mm, conditioned by machining, vacuum annealed, and then rolled into sheet 1 mm thick at about 150°C. Sheet specimens (50 by 10 by 1 mm) were then cold rolled with 50, 70, 80, 90, or 99% reduction without process annealing. It was found that cold rolling with a reduction of more than 70% significantly strengthened niobium. Specimens rolled with 90% reduction and tested at 20 to 1500°C had tensile strengths ranging from 77.2 kg/mm^2 at the lowest temperature to 7.5 kg/mm^2 at the highest temperature. The corresponding values for specimens annealed at 1300°C for 1 hr were 51 and 7.5 kg/mm^2, respectively. Cold rolling produced considerable anisotropy of strength and ductility, which, however, was completely eliminated by annealing at 1300°C for 1 hr. Annealing at 1500 to 1800°C increased the grain size from 0.06 to 0.9 mm.

In another Russian study[12] the recrystallization behavior of commercial-grade niobium produced in the USSR, Nb–4 wt.% Mo, and Mo–0.15 wt.% Zr was investigated. Extruded, rolled, and annealed alloy sheets were cold rolled to 80 to 90% reduction and then vacuum annealed at 500 to 1500°C for 2 hr. It was found that the temperature of the beginning of recrystallization for niobium was 1050°C, whereas that of the alloys was 1150°C. In alloys deformed by stretching, the temperature of the beginning of recrystallization was 100 to 200°C higher than that for rolled alloys, owing to a more uniform deformation in stretching. The entire recrystallization range for the niobium alloy was found to be 100 to 150°C, and that for the molybdenum alloy, 200 to 250°C. Annealing of deformed niobium alloys in vacuum of 1×10^{-4} mm Hg brought about a significant absorption of oxygen, which increased with increasing temperature; at 1400°C the amount of absorbed oxygen reached 0.1%. Annealing of molybdenum alloys under the same conditions did not produce a similar effect, apparently because of a different type of oxidation. Stresses of the first order up to 10 to 15 kg/mm^2 were developed

as a result of stretching and were nonuniformly distributed along the length of specimens in the Nb–Mo alloy. No such phenomena were observed in the Mo–Zr alloy. (S. G. Nelson)

Powder-Metallurgy Materials

Several studies have been concerned with the fundamental aspects of the sintering process. At the University of Florida,[13] investigators performed studies on the evolution of structure during sintering, the rate at which the structure evolves, and the relations that operate in the interplay between structure and kinetics. The application of topological techniques of quantitative metallography to the study of sintering systems provided fairly detailed, reliable, and significant information about the variation of several geometric parameters as sintering proceeds. The average velocity of the pore–solid interface was introduced as a new function for monitoring sintering rate.

A theory on the sintering of wires by surface diffusion has been formulated at Bettis.[14] A convergent, stable, finite-difference solution has been developed for the case of two-dimensional shape changes due to surface diffusion induced by capillarity. This solution was applied specifically to the case of an infinite line of wires and a wire on a plane.

A bibliography concerned with the vibratory compaction of metal and ceramic powders has been compiled by the British.[15] In other work,[16] outlined in a British patent, a method was devised for vibratorily compacting bodies, such as spheres, of varying diameters to produce a uniform configuration. A selected size range of particles of a ceramic material was subjected to axial vibration within a container until a close-packed configuration was attained. A screen was provided for exerting pressure to maintain the particles in the close-packed configuration while a smaller size range of ceramic particles was introduced. During introduction of smaller particles, the container was vibrated in both axial and radial modes. For this method of packing, the diameter of the smaller size particles should be less than one-quarter the mean diameter of the other particles.

British[17] investigators have utilized a unique device for the compaction of refractory-metal powders. The desired shapes were achieved by using opposing magnetic fields produced in coaxial conductors. High pressures over long lengths were attained in consolidating tubes and other shapes by this process.

A method[18] of semicontinuous pressure sintering was developed at Boeing and Nuclear Metals wherein a ceramic powder was encapsulated in a metal tube and subsequently densified by combinations of rolling, swaging, and drawing at various temperatures. Requirements for development of the process were established and essentially met.

Large sheets of unalloyed tungsten were fabricated in programs[9] conducted in support of the Materials Advisory Board Refractory Metals Sheet Rolling Program. Six contracts covered the development of practices for producing large sheets from unalloyed tungsten, including powder-metallurgy techniques.

Submicron tungsten has been consolidated by high-pressure techniques at Lawrence Radiation Laboratory.[19] The production of ingots of sound microstructure has permitted quantitative densification analysis of submicron tungsten using both belt and piston-cylinder high-pressure apparatus. Pressure, temperature, and time ranges were 0.4 to 35 kbars, 600 to 1400°C, and 10 sec to 20 min, respectively. Under 23 kbars, 1170°C, and 10 min, sound ingots within 0.4% of theoretical density were obtained. Pressures ranging from 30 to about 1.4 kbars at 1080°C and 10 min resulted in equivalent densities, with a sharp break in density occurring near 1 kbar. A density maximum near 1100°C has been correlated with the onset of grain growth under pressure. Over a mean particle-size range of 0.25 to 7.0 μ, ingot gas content appears to be the primary determinant of end-point density. Close agreement was obtained with theoretical end-point-density predictions based on the plastic-flow densification mechanism. Self-diffusion and activation-energy data calculated from 23-kbar processing agreed closely with data obtained from pressureless sintering.

An investigation of two-phase W–Re alloys for ionizer applications has been completed by TRW Systems.[20] The laboratory program involved a study of the microstructure as a function of alloy composition over the range from 25 to 45 wt.% rhenium. It was demonstrated that alloys in the range from 36 to 38 wt.% rhenium had the optimum proportions and configurations of the tungsten solid solution and the sigma-phase alloy components. An extensive investigation of techniques for removing the sigma-phase component indicated that an electrolytic etching technique was optimum in terms of reproducibility and efficiency. Cesium-ionization tests were performed using a button-shaped emitter with a diameter of approximately ⅛ in.

A program[21] is in progress at Oak Ridge to study the problems and parameters associated with primary SAP-alloy billet fabrication. The objective of this work is to arrive at a more reliable and consistent product having the strength of a commercial 10 wt.% Al_2O_3–SAP alloy. General process steps of importance are feed-powder characterization, dispersion preparation, and consolidation. Work is continuing to optimize these steps.

Other researchers are involved with the fabrication of SAP alloys for application in the Heavy-Water Organic-Cooled Reactor (HWOCR). Atomics Inter-

national and Combustion Engineering[22] are investigating the effect of extrusion ratios of 1000:1 and 30:1 on cladding specimens of SAP 930 and XAP001. Tube extrusion blanks were cut from $7\frac{3}{4}$-in.-diameter billets, and after extrusion the tubing represented a reduction of 30:1 from the powder compact stage. Blanks were taken from the billets so that the final extrusion direction was both parallel and transverse to the initial billet extrusion axis in order to determine whether "cross-extrusion" would affect the mechanical properties of the tubing. Approximately 25 ft of tube representing each orientation was obtained for each alloy. The metallographic structures produced were compared with those of materials produced under normal fabrication procedures. It was found that the homogeneity of the SAP 930 alloy with the light reduction shows greater variation from previously examined material than does the XAP001 tube with a corresponding light reduction. Transmission electron microscopy, short-time tensile tests, and creep-rupture tests are being conducted.

A process for making steam-corrosion-resistant Fe–Cr–Al–Y alloys is the subject of a U. S. patent.[23] The dispersion-strengthened alloy consists of an Fe–Cr–Y matrix and a finely dispersed phase of iron and yttrium with a maximum diameter no greater than 5 μ. The preferred method for making such an alloy is by atomization of a molten composition to form an alloy powder having the described metallurgical structure and yttrium-containing dispersed phase.

Canadian[24] investigators have studied the fabrication and mechanical properties of sintered Zr–Y_2O_3 dispersions. Various stages in the development of a route for fabricating these dispersions are described, together with the improvements in stress-rupture properties resulting from each stage. The best properties were achieved with a 5 vol.% dispersion of fused, crushed, and sized (0.5 μ in.) Y_2O_3 particles, which was subjected to a double cycle of fabrication with an intermediate rehydriding step. The rupture time and minimum creep rate of this material at 500°C were improved by a factor of about 10 over the corresponding properties for sintered zirconium. This improvement is ascribed to the stabilizing effects of the particles on the grain structure. No strength contribution from direct dislocation–particle interaction was detectable. (C. A. MacMillan)

Pressure Bonding

Hot pressing of dissimilar-metal transition joints have been investigated by Atomics International and Combustion Engineering.[22] For SAP-alloy–steel transition joints of the HWOCR configuration, a knife edge on the steel component was first plated with 0.2 mil of nickel and then vapor plated with 0.5 to 2.0 mils of tungsten. Hot pressing was accomplished at 1025 ± 15°F (552 ± 8°C) for 5 min with a 50-ton load. Finished joints of this type exhibited ultimate strengths to 34,400 and 11,200 psi at room temperature and 750°F (399°C), respectively. Thermal treatment for 30 min at 950 and 1000°F (510 and 538°C) did not result in a strength decrease, but degradation of the tungsten and reaction of the SAP alloy with both the tungsten and steel was observed. Zirconium-alloy–steel joints were also hot pressed by this technique at temperatures of 1100 to 1600°F (593 to 871°C). No intermetallic compound was formed during hot pressing for the required 5 min. However, heat-treating for 30 min at 1600°F did produce an intermetallic, with indications that the chromium from the steel was the most rapidly diffusing species.

Dissimilar-metal foils have been used to promote interdiffusion in beryllium, molybdenum, and tungsten structures below their respective recrystallization temperatures.[25] Beryllium has been bonded at 1330°F (721°C) with an aluminum intermediate layer and at 1625°F (885°C) with a copper intermediate layer. Both nickel and titanium were effective intermediate layers for bonding molybdenum at 1700 and 1680°F (927 and 916°C), respectively. Tungsten has been joined at 1700°F with niobium and nickel foils. With each materials system, postbond treatments were conducted at higher temperatures to assess diffusion damage as a function of service temperature.

(S. W. Porembka)

Plating

Nonelectrolytic Chemical Plating

The use of chemical vapor deposition for the preparation of refractory-metal parts and cladding continues to receive attention. Near-optimum conditions for the deposition of rhenium on copper substrates by hydrogen reduction of rhenium hexafluoride were established by experiments conducted at the Bureau of Mines.[26] High-purity deposits of nearly 90% of theoretical density were produced at 250°C with an ReF_6 flow rate of 5 g/hr, a hydrogen-to-ReF_6 volume ratio of 25:1, and a total pressure of 1 atm. Attempts to codeposit rhenium and tungsten were unsuccessful in this work owing to the difference in the optimum temperature of reduction for the two compounds. The lowest pressure studied was 600 torrs.

Oak Ridge workers[27] continued their study of the same reactions at 600 to 900°C and at lower pressures (3 to 10 torrs). Refinements included a vapor injector and moving mandrels. Rhenium and W–Re alloys (7 and 22 wt.% rhenium) having compositional uniformity were obtained. Rhenium-rich deposits produced in the range 600 to 900°C were noncoherent.

(E. H. Hall)

Electroplating

Battelle–Columbus researchers reviewed cleaning and electroplating processes that eliminate or reduce

the danger of delayed stress failure caused by hydrogen entry into ultrahigh-strength steels.[28] Although dry mechanical cleaning, solvent cleaning, vapor degreasing, and anodic alkaline cleaning are considered nonembrittling, examples of hydrogen pickup have been noted. Water vapor in the atmosphere can be absorbed during mechanical cleaning. Also, steel can pick up hydrogen in rinse waters after anodic alkaline cleaning. Anodic treatments in acid minimize embrittlement but do not completely prevent it for high-carbon steels.

A nonaqueous dimethylformamide solution for plating cadmium avoids embrittlement, but the need for baking after plating is questionable. A brush plating process approved for cadmium-plate repair apparently requires no baking after plating. The popular Delta process employing a titanium salt includes a bake cycle, but the cycle can be shortened. Baking is also required after nickel plating or chromium plating. Stress relief by baking prior to chromium plating is recommended. Baking after plating with chromium, zinc, or cadmium does not always overcome the tendency for hydrogen stress cracking, however. Chromium with a dense crack pattern is recommended in place of chromium with fewer cracks for accelerating hydrogen removal and avoiding stress cracking of the steel.

Battelle–Northwest electrochemists reviewed their process for electroplating nickel on uranium in a paper prepared for presentation at a meeting of the American Electroplaters' Society.[29] The nickel electroplate (<0.001 in.) is a diffusion barrier between the uranium core and an aluminum cladding. Nickel plate with reduced porosity was obtained when the uranium was anodically treated with an improved sulfuric–hydrochloric acid solution and plated in a sulfamate bath containing bromide ions in place of chloride ions for promoting nickel-anode dissolution.

The effectiveness of a composite of chromium and nickel electroplates for protecting molybdenum at high temperatures has been noted by the Russians.[30] A coating with a thickness of 180 μ (0.0045 in.) prevented molybdenum oxidation for 300 hr at 900°C. Silver and gold electroplates were investigated as barriers for the diffusion of molybdenum into nickel in order to reduce the thickness of the final electroplated metal (nickel) in the system. Research in the United States on such barriers was reported 11 years ago.[31] (W. H. Safranek)

Explosion Forming

The explosive sizing of tubes was investigated at Battelle–Columbus.[32] Welded Zircaloy tubes 6 in. in diameter and 10 in. long with 0.062-in.-thick walls (and similar stainless-steel tubes used in preliminary mockup tests) were expanded by a central linear explosive charge in a water transfer medium against a steel female die. The stainless-steel preliminary test samples were sized satisfactorily by this technique without weld damage. However, difficulty was encountered in both sizing and reducing ovality in Zircaloy tubular samples. This behavior was attributed to the inhomogeneous plastic deformation of the welds, heat-affected zone, and unaffected base metal, particularly at the higher levels of explosive strain rates. The best results were obtained by repetitive small sizing steps, minimizing strain rate, and shock-hardening the weld regions with contact charges prior to the standoff sizing operation. Because of design changes and the more favorable results obtained by thermal sizing, investigation of the explosive method was discontinued.

It was concluded that the corrosion resistance and mechanical properties of Zircaloy are not adversely affected as a result of explosively sizing the preforms or explosively strengthening the preform welds prior to sizing. Table IV-2 presents the properties of shock-hardened Zircaloy-welded coupons. The explosive-shocked coupons exhibited weld strengthening as they all failed during tensile testing outside the weld areas.

Table IV-2 TENSILE TEST RESULTS FOR ZIRCALOY AFTER EXPLOSIVE TREATMENT, WELDING, OR SIZING[32]

Sample	Treatment	Tensile strength, psi	Elongation in 2 in., %
E-1	Shocked with contact charge of 1 g/sq. in. of Detasheet	73,500	23
E-3	Shocked with 3 g/sq. in.	75,750	23
E-5	Shocked with 5 g/sq. in.	78,400	20
E-1H	E-1 plus 4 hr at 1200°F in argon	73,000	35
E-3H	E-3 plus heat-treatment	72,600	34
E-5H	E-5 plus heat-treatment	71,400	31
	Zirconium sheet as-welded	70,250	43
		69,500	43
	Experimental-sized base metal	71,500	56
	Experimental-sized weld area	68,400	37
		69,500	36

Midwest Research Institute has surveyed the state of the art of high-energy rate forming (HERF).[33] The several literature surveys published in this area during the early 1960's have been updated, and the increased, maturing interest in HERF as a metalworking tool manifested during the last several years was summarized. Several of their conclusions about the future of these processes are especially interesting.

1. For the short-term future—the next 3 to 5 years—the greatest growth potential appears to be in the contact operations: welding, cladding, and strengthening. This field is rapidly moving from an empirical and experimental basis toward standard industrial processes.

2. The potential for use of explosive-forming technology is greatest at present in emerging nations having a huge labor force yet lacking the capital tools to compete with heavily industrialized countries.

(H. S. Gurev)

Welding and Brazing

Welding

Martin has reported on a feasibility study of the thermochemical vapor-deposition process for joining several different alloys.[34] Of the alloys tested, stainless steel provided the only good joints. Aluminum, titanium, and beryllium were not successfully joined by this technique, and it was concluded that special techniques were needed to minimize microcracks and voids. The usefulness of thermochemical vapor deposition for joining molybdenum was demonstrated several years ago by the same organization.

Magnetic force welding, which is used widely to join precious-metal contacts to buses, etc., has been under study at Atomics International and Battelle–Northwest for the welding of fuel-element components.[22,35] The process has the advantage of minimizing the loss of corrosion resistance and cracking caused by impurities in the reactive and refractory metals. Investigations to date at Battelle–Northwest have covered stainless steel, stainless-steel–UO_2 cermets, Incoloy, nickel, tantalum, beryllium, tungsten, tungsten–UO_2 cermets, TD nickel, thoriated tungsten, molybdenum, and graphite. Most of these materials have been satisfactorily welded. Welds of SAP aluminum to SAP aluminum under test at Atomics International have been found to be 100% efficient. It was observed that the advantages of magnetic force welding make it particularly applicable to isotope encapsulation.

Some interesting comparative data on the mechanical properties of several welded aluminum sheet and plate alloys have been developed by Douglas Aircraft in stress-corrosion studies.[36] Table IV-3 and Fig. IV-1 present these data. The objective of this program was to provide engineering data on threshold levels of stress for a 500-hr corrosive-medium exposure. The stress-corrosion work in this program is not far enough along for meaningful results.

A microstructural study of simulated weld-heat-affected zones in René 41 has been completed by Northrop Corp.[37] No new criteria are given for the successful welding of René 41, but a better understanding of effects on the microstructure can be derived from the results. The development work required to establish the procedures for welding the forged parts for the nozzle of the Phoebus-2 rocket was outlined by Aerojet-General.[38] The study included nondestructive testing, welding-operator qualification, filler-metal qualification (Hastelloy X), and repair welding.

Brazing

The feasibility of inert-atmosphere brazing of X7005 honeycomb sandwich structures using No. 719 brazing alloy followed by heat-treating and quenching was demonstrated in a 3-year program at Aeronca.[39] Optimum results were obtained when the base metal was clad with the brazing alloy. Two new brazing alloys that show promise were also identified. Brazing alloys from the Al–Ge–Si–Zn and Al–Ge–Si–Ag systems can be used at about 1000° F (538° C) and do not diffuse into the base metal as much as commercially available materials.

Avco is investigating the fabrication of complex aluminum header-to-tube heat exchangers by brazing without a flux.[40] Commercial brazing alloys are being used in this program. Perhaps the most important item of general interest revealed by this study is the discovery that extruded, thin-wall tubing can contain surface defects that are revealed only during brazing. Others have reported similar experience when salt-bath dip-brazing 6061 aluminum, which can be related only to the condition of the filler wire used. Capillary flow can vary considerably even when wetting behavior is good. Vacuum heat-treatment of the filler

Table IV-3 TIG DCSP PARAMETERS FOR WELDING ALUMINUM SHEET AND PLATE[36]

Base metal		Filler wire			Tungsten electrode			Weld travel,	Current,	Arc voltage,	Shield gas		Joint design and pass sequence
Alloy	Thickness, in.	Alloy	Diameter, in.	Speed, in./min	Type	Diameter, in.	Tip, in.	in./min	amp	volts	Type	Flow, cfh	
2219	0.125	2319	1/16	81	2% TH	1/8	1/16	43	210	12.5	He	50	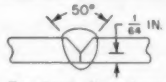
2014	0.080	4043	1/16	65	2% TH	1/8	1/16	43	125	13	He	75	
7002	0.125	5180	1/16	75	2% TH	1/8	Point	17	140	13	He	40	For 7002 alloy sheet
7106	0.090	5180	1/16	66	2% TH	1/8	Point	42	150	11	He	40	
2024	0.080	4145	1/16	66	2% TH	1/8	Point	44	125	13	He	40	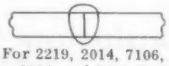
7039	0.125	5039	1/16	22	2% TH	1/8	Point	12	165	10	He	125	For 2219, 2014, 7106, 2024, and 7039 sheet
2219	0.75	2319	1/16	10	2% TH	5/32	5/64	6	385	12	He	125	
7039	1	5039	1/16	10	2% TH	3/16	5/64	4	590	11	He	100	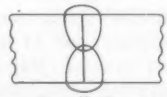
2014	1	4043	1/16	15	2% TH	3/16	3/32	4	590	12	He	100	
2024	1	4145	1/16	11	2% TH	3/16	3/32	6	590	12	He	100	For all plate

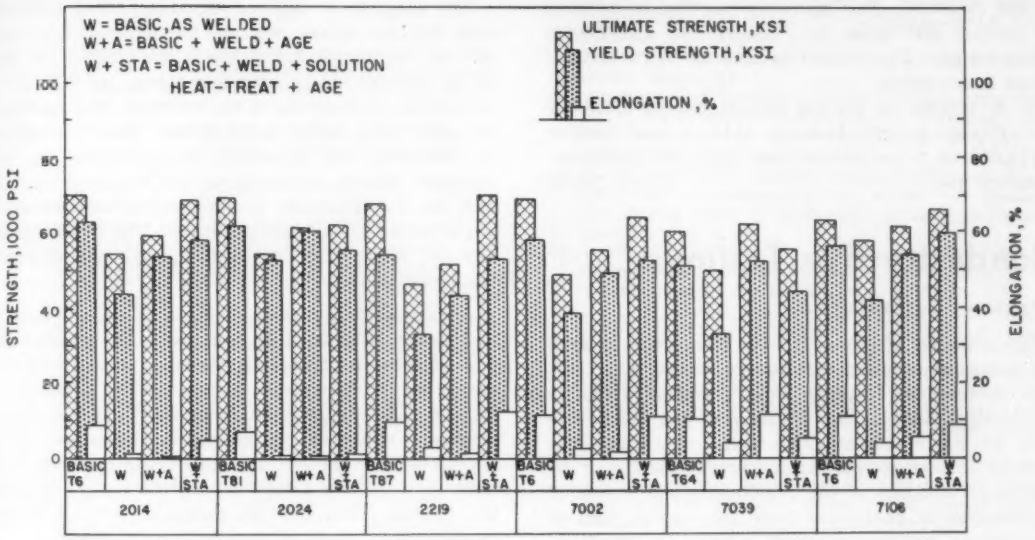

Fig. IV-1 Effect of welding and postweld heat-treatment on tensile properties of aluminum-sheet alloys.[36]

wire may improve the capillary flow when this situation is encountered.

The use of vacuum brazing to fabricate aluminum assemblies, which requires that no postbrazing cleaning operations be incorporated, has proved feasible at Martin.[41] Complex assembly parts were prepared after the usual cleaning methods by brazing with commercial filler alloy in a 10^{-6}-torr vacuum. At the end of the brazing cycle, the assemblies were quenched in helium. The gaseous quench technique eliminates possible flux residues inherent in other aluminum brazing techniques and also prevents the formation of other compounds on the aluminum.

Gaseous quenching has been shown beneficial for aluminum brazing, but it has also been shown as the probable cause of cracking in other systems. When Westinghouse brazed 304 stainless steel with the GE8100 filler metal, the brazed joint contained centerline cracks if the gas atmosphere flow rate was too high.[42] Induction-brazed joints made in hydrogen with a flow rate of 20 to 30 cfh cracked. When the flow was reduced to 5 to 7 cfh, no cracking occurred.

The practical parameters for brazing a number of high-temperature alloys have been defined by Monsanto Research Corp.[43] The materials covered are tantalum, Ta–10 wt.% W, molybdenum, tungsten, 304 stainless steel, Haynes 25, Hastelloy C, Waspalloy, TD nickel, and U–10 wt.% Mo. Vacuum brazing with nine different filler metals melting over the range 800 to 2000°C was studied. Procedure, test standards, wetting characteristics, preparation methods, and joint-strength relations were shown by the data presented.

General Electric (GE) investigators have expanded previous research on TD-nickel joining to TD nickel–chromium.[44] The ultimate objective of this work is to produce jet-engine and aerospace components from the new dispersion-strengthened alloys. Oxidation studies of brazed joints in TD nickel–chromium indicated that this alloy reacts differently than TD nickel. The TD nickel is subject to external preferential oxidation, but the new alloy is not. Brazed joints in TD nickel–chromium fail as a result of internal preferential oxidation of the brazing alloy at the joint interface. To overcome the internal oxidation, the workers developed a new brazing alloy by adding silicon to one of the alloys that GE previously found best for use with TD nickel. The new alloy, called TD-50 (Ni–20 Cr–10 Si–9 Mo–21 Fe–2 Co, by weight), produced joints in TD nickel–chromium that were not subject to gross internal oxidation.

A study of new zirconium-base brazing alloys for use on Zircaloy has produced promising results.[45,46] An evaluation of the corrosion resistance for reactor applications of 68 alloys has identified 14 promising compositions. After 500-hr pressurized-water exposures, among the promising alloys are Zr–15 wt.% Cr, Zr–18 wt.% Cr, Zr–24 wt.% Cr, Zr–12 wt.% Fe, Zr–15.8 wt.% Fe, Zr–21 wt.% Fe, Zr–15 wt.% Cu, Zr–32.5 wt.% Mn, and Zr–4.5 wt.% Si.

Researchers in the USSR have developed a new technique for preparing refractory metals for brazing and soldering.[47] Best results were obtained by thinly coating the joint surface with finely divided MoO_3 or WO_2 powder and then reducing the oxide in hydrogen

at 850 to 900°C. This operation can then be followed by joining with most tin-, copper-, or silver-base filler metals. The method is also useful for making joints in ceramics.

U. S. patents on brazing include number 3,316,069 on refractory-metal-brazing alloys and number 3,316,086 on a manganese-base alloy for high-temperature use. (R. M. Evans)

Nondestructive Testing

Ultrasonic Techniques

Researchers at Boeing[48] have found that, despite its simplicity, the tap test has proved to be a valuable method of locating loosely bonded areas in honeycomb sandwich materials. A device was developed to strike a honeycomb with a controlled, repetitive impact to permit inspection aurally or by electronic analysis of the resultant sound waves. A microphone is positioned near the impact point of the plunger, and the resultant output is filtered and displayed on an oscilloscope. The number and spacing of successive rebounds that the plunger undergoes after each initial impact can be used to detect loose bonding associated with sonic damage or faulty adhesive splices in honeycomb specimens.

To measure the elastic properties of 304 stainless steel as a function of temperature up to 1000°C, Argonne[49] employed a buffer rod, which is threaded to "clean up" reflections, and attached the specimen by means of a threaded coupling. They obtained good coupling between the specimen and the buffer rod first by machining the mating surfaces flat and polishing to a 3-μ finish and then by tightening the threaded coupling to approach a forced mechanical bond. (D. Ensminger)

NDT Techniques Other Than Ultrasonics

Nondestructive flaw detection through the use of acoustic emissions has been studied by Phillips Petroleum.[50] The object of this work was to develop a safeguards system for diagnostic examination of reactor pressure vessels and primary-loop flaw analysis. The test program involved large-scale, complex reactor-vessel testing, supplemented by laboratory-scale tensile tests. Acoustic signals were successfully detected, recorded, and analyzed from two complex embrittled pressure vessels tested under conditions of applied stress. Two types of acoustic emission occurred in the stressed metals: high-amplitude bursts or pulses, and continuous high-frequency random emissions. These were recorded on magnetic tape which was then analyzed by instrumentation systems designed to relate the detected acoustic-signal characteristics to the stress, stress rate, and flaw size.

The continuous type of signal appeared instantly with the first stress, whereas the detection threshold for the burst-type signal was in the range 0.1 to 30% of the normal vessel operating stress and 0.02 to 5% of nominal yield stress of the material. The presence of a flaw in a metal under stress was evidenced by an unusually low threshold of appearance for the acoustic signals, by occurrence of the burst signals, and by the increase in the continuous-emission-signal intensity with applied stress. The burst signals allowed location of the flaw through triangulation techniques.

Additional study of the neutron television system and image intensifier at Argonne[49] has included the use of neutron radiographic motion pictures to examine the flow of metal during casting. A sample of Wood's metal chosen to simulate ^{235}U was photographed as it was poured into an aluminum block containing a mold pattern. Although similar studies have been made by X ray, the neutron method permits the heavier metals to be studied in greater thicknesses when a range of transmission is needed.

The nondestructive testing of brazed joints by three methods has been compared in work done by the Japanese.[51] The methods were Gd-M direct-exposure neutron radiography, indium-transfer neutron radiography, and X-radiography. The base metal used was 304 stainless steel. Brazing alloys containing thermal-neutron-sensitive elements (boron, silver, cadmium, etc.) were chosen. As standard brazing faults, the brazing-alloy foils which varied in thickness from 0.0126 to 0.0762 mm and contained various holes were sandwiched between the base metals whose thicknesses varied from 1.59 to 6.35 mm. The diameter and width of brazed-joint faults were compared by means of a hole-type radiographic penetrameter. The relation between the hole diameter and width was in accordance with Criscuol's equation for the thickness between 0.0254 and 0.0762 mm in X-ray radiography and in the indium transfer method. Neutron radiography permitted excellent detection when the Gd 0.0127-mm-M (single) direct-exposure method was used on the brazing alloy. The In-AA transfer method gave results comparable with X-radiographs for detection of faults. Both of the neutron methods gave poor results for those foils which contained only silver as a neutron-sensitive element.

Ultrasonic methods were advantageous in detecting nonbonds in diffusion-bonded samples. However, small faults about 1.6 mm in diameter could not be shown clearly in 12.7-mm-thick specimens, especially near the edges. The Gd-M direct method was recommended for these faults in thermal-neutron-sensitive brazing alloys. This work complements some similar U. S. work previously reported in the Spring 1966 issue of this Review (Vol. 9, No. 1, page 70).

(A. F. Leatherman)

References

1. J. R. Maynord and W. M. Fink, Production of Mark VE Inner and Outer Ingots by Revised Casting Procedures, USAEC Report NLCO-989, National Lead Co. of Ohio, January 1967.
2. R. L. Schardt, Consumable-Electrode Arc Melting of Uranium, USAEC Report NLCO-916, National Lead Co. of Ohio, March 1967.
3. E. L. Foster, S. G. Nelson, D. E. Price, W. J. Hilldebrand, D. P. Moak, and J. Allen, Development of a Subscale Manufacturing Process for the Fabrication of Hypereutectic Transition-Metal Carbide Castings, Interim Engineering Progress Report No. 4, April 1–June 30, 1967, USAEC file no. NP-16855, Battelle–Columbus, July 14, 1967.
4. Bureau of Mines, Albany Metallurgy Research Center, Quarterly Metallurgy Progress Report No. 34, January 1–March 31, 1967, USAEC Report USBM-RC-1288, March 1967.
5. W. C. Kramer, W. R. Burt, Jr., F. J. Karasek, J. E. Flinn, and R. M. Mayfield, Vanadium Alloy Screening Studies and Fabrication of V–15 Wt.% Ti–7.5 Wt.% Cr Tubing for Nuclear Fuel Cladding, USAEC Report ANL-7206, Argonne National Laboratory, August 1966.
6. Reactive Metals, Inc., Annual Progress Summary on Uranium Fabrication, 1966, USAEC Report RMI-8, Apr. 20, 1967.
7. The Fabrication of Fuel Elements in France, *Bull. Inform. A. T. E. N. (Ass. Tech. Energ. Nucl.)*, No. 63: 12-20 (January–February 1967).
8. B. A. Cheadle and W. Evans, The Fabrication and Metallurgical Evaluation of 3¼-in.-I.D. Cold-Worked Zirconium–2.5 Percent Niobium Pressure Tubes, Canadian Report AECL-2652, December 1966.
9. D. J. Maykuth, Summary of Contractor Results in Support of the Refractory Metals Sheet Rolling Program, Report DMIC-231, Battelle Memorial Institute, Defense Metals Information Center, Dec. 1, 1966.
10. Yu. I. Krivonosov, F. E. Dolzhenkov, O. A. Myakshin, and L. A. Zakharov, Cladding of Steel with Niobium by Vacuum Rolling, *Tsvetn. Metal.*, No. 12: 88-89 (December 1966).
11. L. P. Zhorova and G. V. Zakharova, Effect of Cold Plastic Deformation and Annealing on the Mechanical Properties of Niobium Sheets, *Metalloved. Term. Obrab. Metal.*, No. 12: 28-31 (December 1966).
12. S. S. Gorelik, E. N. Spektor, and T. A. Burdasova, Structural Changes During Annealing of Deformed Niobium and Its Alloys, *Metalloved. Term. Obrab. Metal.*, No. 12: 24-28 (December 1966).
13. University of Florida, Topological Study of the Sintering Process, Annual Progress Report, February 1967, USAEC Report ORO-2581-1.
14. F. A. Nichols, Theory of the Sintering of Wires by Surface Diffusion, USAEC Report WAPD-T-1965, Westinghouse Electric Corp., Bettis Atomic Power Laboratory, January 1967.
15. P. J. Jones (Comp.), Vibratory Compaction of Metal and Ceramic Powders, A Bibliography, British Report AERE-Bib-153, February 1967.
16. Method and Apparatus for Vibratory Compaction, British Patent 1,051,954, Dec. 21, 1966.
17. Method and Device for Consolidating Refractory Metal Powders, British Patent 1,050,722, Dec. 7, 1966.
18. R. W. Rice and J. G. Hunt, Semi-Continuous Pressure Sintering, Summary Report, May 3, 1965–April 29, 1966, Report AD-638453, Boeing Co. and Nuclear Metals, Inc., May 1966.
19. G. E. Zima and J. F. Lakner, High-Pressure Consolidation of Submicron Tungsten, USAEC Report UCRL-50172, University of California, Lawrence Radiation Laboratory, Dec. 28, 1966.
20. M. E. Kirkpatrick and R. A. Mendelson, Investigation of Two-Phase Tungsten–Rhenium Alloys for Ionizer Applications, Report NASA-CR-54694 (N66-32186), TRW Systems, July 1966.
21. P. Patriarca, Oak Ridge National Laboratory, unpublished, March 1967.
22. Atomics International and Combustion Engineering, Inc., Heavy Water Organic Cooled Reactor, Quarterly Technical Progress Report, January–March 1966, USAEC Report AI-CE-31, May 15, 1966.
23. C. S. Wukcusick, Steam Corrosion Resistant Iron–Chromium–Aluminum–Yttrium Alloys and Process for Making Same, U. S. Patent 3,293,007, to USAEC, Dec. 20, 1966.
24. J. Rezek and B. G. Childs, Fabrication and Mechanical Properties of Sintered Zirconium–Yttria Dispersions, Canadian Report AECL-2633, January 1967.
25. A. T. D'Annessa, Diffusion Bonding Beryllium, Molybdenum, and Tungsten, *Metal Progr.*, 91(2): 71-74 (February 1967).
26. F. W. Hoertel and J. G. Donaldson, Rhenium and Rhenium–Tungsten Deposition by Thermochemical Reduction of the Hexafluorides — A Preliminary Study, USAEC Report BMI-6915, Bureau of Mines, August 1966.
27. J. I. Federer, A. C. Schaffhauser, and C. F. Leitten, Thermochemical Deposition and Evaluation of Rhenium and Tungsten–Rhenium Alloys, USAEC Report ORNL-P-2745, Oak Ridge National Laboratory, 1965.
28. T. P. Groenveld, E. E. Fletcher, and A. R. Elsea, A Review of the Literature on Cleaning, Pickling, and Electroplating Processes and Relief Treatments to Minimize Hydrogen Embrittlement on Ultrahigh-Strength Steels, Special Report, Battelle–Columbus, Oct. 15, 1966.
29. J. R. Lundquist, R. L. Braun, and R. W. Stromatt, Nickel Plating Uranium: Review of Laboratory Studies, USAEC Report BNWL-SA-1030, Battelle–Northwest, Jan. 16, 1967.
30. I. M. Kvokova and V. I. Lainer, Heat-Resistant Galvanic Electroplating of Molybdenum and Tungsten in *Zharostoikie Pokrytiya*, pp. 100-107, Izdatel'stvo Nauka, Leningrad and Moscow, 1965.
31. W. H. Safranek and G. R. Schaer, Properties of Electrodeposits at Elevated Temperatures, *Tech. Proc. Amer. Electroplaters' Soc.*, 43: 105-117 (1956).
32. J. H. Suldan and R. J. Krahn, Sizing of Zircaloy Structurals, USAEC Report WAPD-TM-620, Westinghouse Electric Corp., Bettis Atomic Power Laboratory, February 1967.
33. M. C. Noland, H. M. Gadberry, J. B. Loser, and E. C. Sneegas, High-Velocity Metalworking, Report NASA-SP-5062, National Aeronautics and Space Administration, 1967.
34. R. Wilson, Intermolecular Bonding of Various Metals and Alloys by Thermochemical Vapor Deposition, Report NASA-CR-80721, Martin Co., November 1966.
35. R. F. Boolen, Magnetic Force Welding Applications at Battelle–Northwest, USAEC Report BNWL-422, Battelle–Northwest, May 1967.
36. R. V. Turley, C. H. Avery, and E. Dash, Stress Corrosion Susceptibility of Welded Aluminum Alloys, Second Quarterly Progress Report, Report DAC-33545, Douglas Aircraft Co., Inc., Jan. 18, 1967.
37. K. C. Wu and R. E. Herfert, Microstructural Studies of René 41 Simulated Weld Heat-Affected Zones, *Welding J.* (N. Y.), 46(1): 32s-38s (January 1967).
38. C. W. Fletcher, F. J. Flens, and L. F. Glasier, Jr., Welding of Thick Sections of Hastelloy X for the Phoebus-2 Nozzle, *Welding J.* (N. Y.), 46(4): 290-303 (April 1967).
39. B. E. Kramer and D. Y. Potter, Development of High Strength, Brazed Aluminum, Honeycomb Sandwich Composites Adaptable for Both Elevated and Cryogenic Temperature Applications — Volume I, Brazing Alloy Development and Selection; Volume II, Manufacturing and Testing, Final Report, Aeronca, Inc., Sept. 30, 1966.

40. Avco Corp., Development and/or Establishment of Processes to Fluxless Braze Complex Structures of Aluminum Alloys, Interim Engineering Progress Report, September 16–December 15, 1966, Report IR-8-317(6).
41. M. M. Schwartz, F. B. Gurtner, and P. K. Shutt, Jr., Vacuum (or Fluxless) Brazing–Gas Quenching of 6061 Aluminum Alloy, Report EATR-4085, Edgewood Arsenal, March 1967.
42. S. Kaufman, Westinghouse Electric Corp., private communication, August 1967.
43. W. P. Robbins, Brazing Superalloys and Refractory Metals, USAEC Report MLM-1322, Mound Laboratory, Mar. 10, 1967.
44. R. E. Yount, R. E. Kutchera, and D. L. Keller, Development of Joining Techniques for TD Nickel–Chromium, Interim Progress Report, October 1, 1966–January 1, 1967, Report IR-4-8-211A, General Electric Company, Flight Propulsion Division.
45. Illinois Institute of Technology Research Institute, Research on Zircaloy Braze Alloy Development, Quarterly Report, January 1–March 31, 1967, USAEC Report IITRI-578P29-11 (EURAEC-1841), Apr. 17, 1967.
46. Illinois Institute of Technology Research Institute, Research on Zircaloy Braze Alloy Development, Quarterly Report October 1–December 31, 1966, USAEC Report IITRI-578P29-8 (EURAEC-1810), Jan. 17, 1967.
47. Z. V. Nikiforova, B. M. Nesterov, and O. A. Sharov, Welding Molybdenum and Tungsten by Tin Base Solder, *Svar. Proizv.*, No. 3: 19-22 (March 1967).
48. H. A. Johnson and C. L. Etheridge, Nondestructive Test Development for Advanced Airplanes, *J. Mater.*, 1(4): 823-836 (December 1966).
49. Argonne National Laboratory, Reactor Development Program Progress Report, USAEC Report ANL-7329, April 1967.
50. D. L. Parry, Nondestructive Flaw Detection by Use of Acoustic Emissions, USAEC Report IDO-17230, Phillips Petroleum Company, April 1967.
51. A. Kanno, The Nondestructive Testing of Brazed Joints, *Papers Ship Res. Inst. (Japan)*, 8: 1-23 (November 1965).

Index

Reactor Materials

Volume 10

Note: The page range for each of the four issues of Vol. 10 is as follows:

No. 1, pages 1 to 67
No. 2, pages 69 to 133
No. 3, pages 135 to 202
No. 4, pages 203 to 266

36 NKhTYu
  strength, Mo effects on, 46

A

Acoustic-emission testing, 264
Actinides
  electrodeposition, 127
AGC-200 braze alloy
  properties, 131
AGC-201 braze alloy
  properties, 131
AL80
  fatigue properties, 114
  recrystallization, 53
Alkali-metal hydrides
  heats of formation, 221
Alkali metals
  corrosive effects, 32, 96
Alloy 16-25-6
  compatibility with PuC–UC mixtures, 73
Alloy 713C
  mechanical properties, 47
Alloy 713LC
  mechanical properties, 47
Alloy 718
  mechanical properties, welding effects on, 128
Alloy 1361 DS
  tensile properties, 247–48
Alloy 1541
  impact strength, 247–48
Alloy 2541
  impact strength, 247–48
Alloys
  diffusion in body-centered cubic, 179
  fracture mechanics, 114
  mechanical properties, effects of material removal on, 53
  nitridation in carbide-containing, La effects in, 237
  zone melting, 194
Alloys (braze)
  (see Braze alloys)
  properties of AGC-200 and AGC-201, 131
  for refractory metals, 199
Alloys (dispersion strengthened)
  compaction, 62
Alloys (hydrided)
  thermal conductivity, H/Zr-ratio effect on, 221
Alloys (powdered)
  sintering, 197
Alloys (refractory)
  coatings for, 27–28
Alloys (refractory metal)
  corrosion, 31–32, 101
  diffusion studies, 54
  explosive bonding, 64
  extrusion, lubricants for, 123
  thermal expansion, linear, 110
Alloys (super-)
  deformation, 111
Aluminum
  bonding, 197, 262
  compatibility with metals, 180
  compatibility with UN, 12
  corrosion, 95
  electrical conductivity, Zr effects on, 53
  explosive spot welding, 64
  mechanical properties, Zr effects on, 53
  recrystallization temperature, Zr-addition and annealing effects on, 112
Aluminum (irradiated)
  corrosion, 226
Aluminum (molten)
  reaction with water, 166
Aluminum (SiO_2-fiber reinforced)(irradiated)
  fracture strength, 41
Aluminum-alloy coatings
  for Mo and Nb, 162
Aluminum-alloy joints (Al alloy(SAP)-steel)
  hot pressing, 260
Aluminum-alloy plates
  mechanical properties of welded, 262
Aluminum-alloy plates (Al–U)
  preparation of, containing Al–B_4C-dispersion foils, 91
Aluminum-alloy plates (Al–U)(irradiated)
  performance of, containing Al–B_4C-dispersion foils, 91
Aluminum-alloy sheet
  mechanical-properties of welded, 262
Aluminum-alloy tubes (6061-T6)
  corrosion, 94–95
Aluminum alloys
  brazing, 262–63
  corrosion, 93–95, 225–26
  fracture toughness, 45
  stress-corrosion cracking, 26
Aluminum alloys (1S)
  hot-press bonding to Zircaloy-2, 197
Aluminum alloys (356)(irradiated)
  mechanical properties, 232
Aluminum alloys (2024)(irradiated)
  mechanical properties, 232
Aluminum alloys (2219)
  corrosion, 94
Aluminum alloys (2219)(irradiated)
  corrosion, 94
Aluminum alloys (6061)
  brazing, 262–63
  coating with Ni, 127
  corrosion, 94
Aluminum alloys (6061)(irradiated)
  mechanical properties, 232–33
Aluminum alloys (6061-0)
  drawing, vibration effects on, 124
Aluminum alloys (Al–Be)
  corrosion, 160
Aluminum alloys (Al–Cr–Fe–Y)
  corrosion, 226, 248
  metallurgy, 46–47
  oxidation, 26–27, 46–47
  production of corrosion-resistant, 260
  tensile properties, 247–48
Aluminum alloys (Al–Cr–Fe–Y)(irradiated)
  embrittlement, 170
  mechanical properties, 37
Aluminum alloys (Al–Cr–Ni–Ti)
  crystal structure, W effects on, 177
Aluminum alloys (Al–Cu)(irradiated)
  dislocation movement, 106
Aluminum alloys (Al–Fe)
  Fe diffusion in, 54
  sintering, 230
  tensile properties, 248
Aluminum alloys (Al–Fe–U)
  phase studies, 69
Aluminum alloys (Al–Li)(irradiated)
  He bubbles in, 236
  rare-gas diffusion in, 16
Aluminum alloys (Al–Mo–Sn–Zr)
  corrosion, 229
Aluminum alloys (Al–Np)
  preparation, 121
Aluminum alloys (Al–Nb)
  phase studies, 51
Aluminum alloys (Al–Nb–Ti)
  mechanical properties, 113
Aluminum alloys (Al–Sn–Ti)
  reaction with H, 221
Aluminum alloys (Al–Ti–V)
  drawing, vibration effects on, 124
  reaction with H, 220–21
  strength, 43
Aluminum alloys (Al–U)
  ignition, 15
  oxidation, 69
  production, 121, 137–38, 194
Aluminum alloys (Al–V)
  corrosion, 99
  sintering, 230
Aluminum alloys (Al–Zr)
  corrosion, 229
Aluminum alloys (irradiated)
  properties, 232–33
Aluminum alloys (SAP)
  corrosion, 230

fabrication, 259-60
hardness, cold-work effects on, 244
powder metallurgy, 125
production, 61
reaction with UC, 209
strain hardening, 179
structure, 61-62
Aluminum alloys (X8001)
corrosion, 94
Aluminum composites
tensile strength of electrodeposited, 127
Aluminum composites (Al–Sn–W)
corrosion, 161
Aluminum couples
corrosion, 94
Aluminum-dispersion control rods (Al–Eu_2O_3)(irradiated)
performance, 92
Aluminum-dispersion control rods (Al–$Eu_{5.3}MoO_{11}$)(irradiated)
performance, 92
Aluminum dispersions (Al–Al_2O_3)
evaluation, 125
Aluminum dispersions (Al–B_4C)
preparation, 91
Aluminum dispersions (Al–U aluminide) (irradiated)
swelling, porosity effects on, 74
Aluminum dispersions (Al–UO_2)(irradiated)
swelling, 74, 214
Aluminum dispersions (Al–UO_2–ZrO_2)(Al clad)(irradiated)
stability, 9
Aluminum dispersions (Al–U_3O_8)
development, 141
Aluminum dispersions (Al–U_3O_8)(Al clad) (irradiated)
stability, 9
Aluminum dispersions (Al–U_3O_8)(irradiated)
swelling, porosity effects on, 74
Aluminum dispersions (Al–UAl_3)
swelling, 141
Aluminum intermetallic compounds (UAl_2) (irradiated)
swelling, 214
Aluminum oxide
corrosion, 103
dispersion strengthening, 115
He diffusion in, 54
powder metallurgy, 61
self-diffusion in, 54
Aluminum oxide compacts (Al_2O_3–Gd_2O_3)
fabrication and thermal expansion, 223
Aluminum oxide dispersions (Al–Al_2O_3)
evaluation, 125
Aluminum oxide single crystals
He diffusion in, 54
Aluminum oxide systems (Al–Al_2O_3)
strain hardening, 179
Aluminum systems (Al–Al_2O_3)
strain hardening, 179
Aluminum systems (Al–C–Cr–Co–Ni–Ti)
sigma-phase formation, 248
Aluminum systems (Al–Ge–Si–Ag)
use for brazing, 262
Aluminum systems (Al–Ge–Si–Zn)
use for brazing, 262
ANM-16
corrosion, 103
AR 213
hardening mechanisms, 45-46
AS-55
corrosion, 101

B

B-66
coating with Cr–Si–Ti, 162
corrosion, 101
creep properties, 42
strength, 43
welding, 129-30
Beryllium
analysis for C, 86
bonding, 262
brazing, 218-19
brittle behavior of extruded, 220
characterization, 156
combustion gases, 84
compatibility with metals, 180
corrosion, 84, 94-95
deformation, 111
diffusion bonding, 260
electroforming, 154
fabrication, 84-86, 219
handling, safety practices for, 21
hot rolling, 123
impact behavior, 22
interdiffusion with U, 1
joining, 21, 86
machining, 21, 85, 219
mechanical properties, 20-22, 53, 84, 155-56
metal removal, 85
metallurgy, conference on, 86
physical metallurgy, 21-22
powder metallurgy, 21
production, 154-55, 219
surface treatment, 85
tensile properties, 219
twin-precipitate interaction, 84
welding, 86, 262
Beryllium (chromate coated)
oxidation, 220
Beryllium (irradiated)
compression properties, 156
gas release, 156
hardness, 86
impact properties, 86
mechanical properties, 106
properties, 22
Beryllium-alloy sheet (Be–Cu)
development of solid-solution-strengthened, 219
Beryllium alloys
(see also IN-102)
corrosion, 95
forming, 85
production, 156
Beryllium alloys (Al–Be)
corrosion, 160
Beryllium alloys (Be–Cu)
metallurgy, mechanical, 155
production by splat cooling, 219
tensile properties, 219
Beryllium alloys (Be–Fe)
tensile properties, 248
Beryllium alloys (Be–Ni)
metallurgy, mechanical, 155
Beryllium alloys (Be–Th)
hot hardness, 8
Beryllium alloys (Be–Ti)
phase studies, 21
Beryllium alloys (Be–U)
ignition, 15
Beryllium alloys (QMV)
corrosion, 94
Beryllium bicrystals
metallurgy, mechanical, 155
Beryllium compacts
coatings on, plating of, 63
Beryllium composites (Be–graphite)
hot pressing, 20
Beryllium couples (Al–Be)
corrosion, 94
Beryllium couples (Be–stainless steel (304))
stress-corrosion cracking, 94
Beryllium fluoride systems (BeF_2–LiF–ThF_4–UF_4–ZrF_4)(molten)
corrosive effects, 103
Beryllium forgings
anisotrophy, 219-20
Beryllium ingots
casting and hot working, 85
Beryllium oxide
orientation, 114
self-diffusion in, 54
thermal diffusivity, 88
Beryllium oxide (irradiated)
compatibility with irradiated graphite, 153-54
performance, 87-88
thermal diffusivity, 88
Beryllium oxide dispersions (BeO–UO_2) (irradiated)
fission-product retention, 156
Beryllium oxide powder
pore structure, 220
properties, impurity effects on, 22
Beryllium oxide systems (BeO–PuO_2–UO_2)
phase studies, 140
Beryllium powder
metallurgy, 21
Beryllium sheet
fabrication, 85
properties, thermal-treatment effects on, 85-86
Beryllium single crystals
metallurgy, mechanical, 155
preparation, 21
Beryllium wire
mechanical properties, 85
production, 84-85
Bismuth (molten)
corrosive effects, 103
Bismuth alloys (Bi–Pb)(molten)
corrosive and erosive effects, 30-31
Bismuth alloys (Bi–Ni–Sn)
wear, 225
Bismuth alloys (Bi–Na)(molten)
corrosive effects, 103
Bismuth alloys (Bi–U)
ignition, 15
Boiling detectors (incipient)
ultrasonic testing, 200
Bonding (pressure), 62, 126, 197-98, 260
Bonds
heat-transfer and ultrasonic-transmission properties, correlation of, 64
nondestructive testing of diffusion, 264
ultrasonic testing, 200
Borides
thermal conductivity and thermal expansion of di-, 222
Borides (refractory)
fabrication, 185-86
preparation, 185-86
reactions in liquid media, 116-17
reactions with metals, 116
wettability by molten metals, 116
Boron carbide
protective coating for, 249
Boron carbide dispersions (Al–B_4C)
preparation, 91
Boron carbide systems (B_4C–Cu)
fabrication and properties, 24-25
Boron carbide systems (B_4C–SiC–TiC)
properties, high-temperature, 187
Boron composites (B–graphite)
hot pressing, 20
Boron composites (B–Ti)
fabrication by hot isostatic pressing, 198
Boron mixtures (B–graphite)(irradiated)
dimensional changes, 222
Braze alloys
corrosion, 102-3, 229

development, 262-64
properties of AGC-200 and AGC-201, 131
for refractory metals, 199
use, 262-64
Brazed joints
nondestructive testing, 264
Brazing, 199, 262-64
Bronze powder
sintering, 197

C

C-129Y
tensile properties, aging effects on, 240
welding, 129-30
C-129Y (coated)
evaluation, 28
Cadmium alloys (Cd-In-Ag)(Ni plated) (irradiated)
oxidation and tensile properties, 24
Cadmium alloys (Cd-In-Ag)(stainless-steel clad)
fabrication, 24
Calcium oxide-system rods ($CaO-UO_2-ZrO_2$)
fabrication, 12
Calcium oxide systems ($CaO-UO_2-ZrO_2$)
thermal conductivity, 143
Carbide castings (metal)
properties, 250
Carbide powders
production, 61
Carbides
thermodynamic properties, 249
Carbides (cemented)
properties, 186-87
Carbides (metal)
free energy of formation, 102
hot pressing, 61
spin casting, 250
Carbides (refractory)
fabrication, 185-86
preparation, 185-86
reactions in liquid media, 116-17
reactions with metals, 116
wettability by molten metals, 116
Carbides (transition metal)
elastic properties, 115
reactions with oxides, 251-52
Carbon
(see also Graphite)
diffusion in Mo_2C, 179
diffusion in Nb carbide, 179
diffusion in Nb-Zr alloy, 54
diffusion in NbC, 54
diffusion in Ta carbide, 179
diffusion in ZrC, 179
solubility in molten Pu, 4, 205
Carbon (irradiated)
contraction of glassy, 217
Carbon (pyrolytic)(irradiated)
dimensional changes, 218
Carbon coatings (pyrolytic)
(see Coatings (PyC))
Carbon composites (C-NbC)
deformation, 116
Carbon materials
fission-product diffusion in, 54
Carbon systems (Al-C-Cr-Co-Ni-Ti)
sigma-phase formation, 248
Carbon systems (C-Cr-Hf-Mo-Y-Zr)
tensile properties, 237
Carbon systems (C-HfC)
melting, casting, and properties, 257
Carbon systems (C-Mo)
recrystallization temperature and rupture strength, 241
Carbon systems (C-Mo-U)
phase relations, PuC-addition effects on, 77
Carbon systems (C-NbC)
melting, casting, and properties, 257
Carbon systems (C-Pu-U)
phase studies, 207-8
Carbon systems (C-Si-U)
phase studies, 144
Carbon systems (C-TaC)
melting, casting, and properties, 257
Carbon systems (C-Th)
properties, 209-10
Carbon systems (C-Ti-U)
phase relations, PuC-addition effects on, 77
Carbon systems (C-U)
ignition, 15
Carbon systems (C-U-Zr)
phase relations, PuC-addition effects on, 77
Carbon systems (C-Zr)
production and properties, 115-16
Carbon systems (C-ZrC)
melting, casting, and properties, 257
Cast materials
fabrication, 194-96, 257-59
melting, 194
working, 122-24
Casting, 59-60, 121-22, 257
Cb-132
thermal-mechanical processing, 50
Cb-132M
corrosion, 164
mechanical and physical properties, 240
Cb-752
mechanical and physical properties, 240
welding, 130
Cb-753
corrosion, 101
creep properties, 42
mechanical properties, 50
physical properties, 50
Ceramic dispersions (ceramic-metal)
development, 141
Ceramic powders
sintering and vibratory compaction, 259
Ceramics
fission-product diffusion in, 54
forming methods, 63
joining, 264
technology, 54, 114-15, 189, 252
Ceramics (irradiated)
properties, 16-17, 213-15
Cerium
oxidation, 27
Cerium alloys (Ce-Co-Pu)(molten)
corrosive effects, 31
fission-gas venting, 4-5
Cerium alloys (Ce-Fe-Pu)
phase studies, 139
Cerium alloys (Ce-Ni-Pu)
phase studies, 139
Cerium alloys (Ce-Pu)
density, 205
Cerium alloys (Ce-U)
ignition, 15
Cerium dioxide
thermal diffusion in UO_2, 209
Cerium dioxide systems (CeO_2-UO_2)
diffusion in, 180
Cerium oxide
self-diffusion in, 54
Cerium-system microspheres (Ce-O-Pu) (W-coated)
preparation, 7
Cermets
strength, 10
Cermets (oxide)
preparation of infiltrated, 125-26
Cesium
corrosive effects, 32, 103, 230
Cesium hydride
heat of formation, 221
Chemical plating
(see Plating)
Chromium
compatibility with UN, 12
corrosion, 96, 98, 100
diffusion in Ni alloys, 179-80
ductility, 45
electroplating on Mo, 261
fabrication, 123
mechanical behavior, 123
metallurgy, 236-38
properties, 183
self-diffusion in, 179
sintering, 230
Chromium-alloy sheet (Cr-Ti-V)
tensile properties, 243-44
Chromium-alloy tubing (Cr-Ti-V)
burst testing, 181-82
fabrication, 196, 257
tensile properties, 244
Chromium alloys
ductility, 123
mechanical properties, 45
properties, 183
wetting in molten Na, 101
Chromium alloys (Al-Cr-Fe-Y)
corrosion, 226, 248
metallurgy, 46-47
oxidation, 26-27, 46-47
production of corrosion-resistant, 260
tensile properties, 247-48
Chromium alloys (Al-Cr-Fe-Y)(irradiated)
embrittlement, 170
mechanical properties, 37
Chromium alloys (Al-Cr-Ni-Ti)
crystal structure, W effects on, 177
Chromium alloys (Cr-Co-Re)
workability, 237
Chromium alloys (Cr-Hf)
phase studies, 24
Chromium alloys (Cr-Fe)(irradiated)
embrittlement, 170
Chromium alloys (Cr-Fe-Ni)
B effects on, 246-47
sigma-phase precipitation, (Fe,Cr), 109
strength, Mo effects on, 176
Ti effects on, 246-47
zone melting, 194
Chromium alloys (Cr-Fe-Ni-Nb)
hardening by precipitation, 177
Chromium alloys (Cr-Fe-Nb-Sn-Zr)
corrosion, 225
Chromium alloys (Cr-Fe-Zr)
preparation, 122
Chromium alloys (Cr-La)
nitridation in carbide-containing, 237
Chromium alloys (Cr-La-Mo)
nitridation in carbide-containing, 237
Chromium alloys (Cr-Mo)
solid solubility in, 241
structure, 236-37
Chromium alloys (Cr-Mo-Nb)
phase studies, 111
Chromium alloys (Cr-Ni)
Cr diffusion in, 179
corrosion, 96, 98
specific heat, temperature effects on, 248-49
strength, effects of Mo and Nb on, 47
Chromium alloys (Cr-Ni alloy (TD))
brazing, 263
Chromium alloys (Cr-Ni-Pd)
corrosion, 103
Chromium alloys (Cr-Nb)
oxidation, 161
Chromium alloys (Cr-Re)
oxidation, 95-96

Chromium alloys (Cr–Ta)
creep properties, N effects on, 183
Chromium alloys (Cr–Ti–V)
compatibility with PuC–UC mixtures, 73
corrosion, 163, 228
tensile properties, 114
Chromium alloys (Cr–Ti–V)(irradiated)
tensile properties, 234
Chromium alloys (Cr–W)
decomposition, 111
Chromium alloys (Cr–W–Y)
tensile properties, 237
Chromium alloys (Cr–U)
ignition, 15
pearlitic reaction, 4
Chromium alloys (Cr–V)
corrosion, 99, 163, 228
Chromium alloys (Cr–Y)
carbide-dispersion effects, 237
Chromium alloys (Cr–Zr)
use for brazing, 263
Chromium boride
production, 188
Chromium carbide
Young's modulus, 115
Chromium dicarbide
reaction with Cr_2O_3, 251–52
Chromium plate
dispersoids in, 63
Chromium sesquioxide
reaction with Cr_3C_2, 251–52
Chromium sesquioxide systems (Cr_2O_3–Gd_2O_3)
phase studies, 252
Chromium sesquioxide systems (Cr_2O_3–Sm_2O_3)
phase studies, 252
Chromium sesquioxide systems (Cr_2O_3–Y_2O_3)
phase studies, 252
Chromium systems (Al–C–Cr–Co–Ni–Ti)
sigma-phase formation, 248
Chromium systems (C–Cr–Hf–Mo–Y–Zr)
tensile properties, 237
Chromium systems (C–Cr–Hf–Y–Zr)
tensile properties, 237
Chromium systems (C–Cr–Re)
phase studies, 52
Chromium systems (Cr–Fe–Si–Ti–V)
fused-slurry coatings developed from, 161
Chromium systems (Cr–TaB_2–ZrB_2)
fabrication and properties, 252
Cladding
eddy-current testing, 132
Cladding (Zircaloy-2)
hydride embrittlement, 175
Cladding (Zr alloy)
evaluation, 175
Cladding materials, 26–58, 93–120, 158–93, 225–56
Coast Metals 50
corrosion, 102–3
Coast Metals 52
corrosion, 102–3
Coast NP
corrosion, 229
Coatings
corrosion, 95
deposition of, 62–64
for B_4C, 249
for Nb–Zr alloys, 162
for refractories, 27–28
for T-222, 162
for Ta–W alloys, 162
Coatings (Al alloy)
for Mo and Nb, 162
Coatings (Cr–Si–Ti)
for B-66, 162
Coatings (Hf–Ta)
for Ta–W alloys, 228
Coatings (HfO_2)
for Ta–W alloys and W, 227–28
Coatings (Ni)
deposition, 10, 127
Coatings (PyC)
deposition, 10, 74–75, 142
stress–strain properties, relation to density, 10
Coatings (silicide), 28, 161–62
Coatings (ThO_2)
for Ta–W alloys and W, 227–28
Coatings (Vitro Cr–Mo–Si)
for Nb–Zr alloys, 162
Cobalt alloys
(see also AR 213 and L-605)
corrosion, 228, 230
fabrication, 122
Cobalt alloys (Ce–Co–Pu)(molten)
corrosive effects, 31
fission-gas venting, 4–5
Cobalt alloys (Cr–Co–Re)
workability, 237
Cobalt alloys (Co–Fe–U)
phase studies, 71
Cobalt alloys (Co–Mo)
properties, addition effects on, 47
Cobalt alloys (Co–Nb)
oxidation, 227
phase studies, 51
Cobalt alloys (Co–Y)
phase studies, 47
Cobalt composites (Co–Thornel)
fabrication by hot isostatic pressing, 198
Cobalt-powder mixtures (Co–W carbide)
compacting and sintering, 61
Cobalt superalloys
mechanical and physical properties, 249
Cobalt systems (Al–C–Cr–Co–Ni–Ti)
sigma-phase formation, 248
Cobalt systems (Co–Mo–Si)
phase studies, 242
Cobalt systems (Co–TaC–WC)
properties and structure, 186
Cobalt systems (Co–TiC–WC)
properties, C effects on, 249
strength, 187
Cobalt systems (Co–WC)
macrostresses in, 249
properties of sintered, 115
strength, 187
Cold working, 60–61
cast materials, 122–24
Composites (fiber reinforced)
hot isostatic pressing, 198
Compounds (refractory)
reactions in liquid media, 116–17
reactions with metals, 116
wettability by molten metals, 116
Computer codes and programs
for fuel studies, 212–15
Concrete
properties in pressure vessels, 252
Construction materials
corrosion, 32
Control materials, 217–24
Coolants (alkali metal)
corrosive effects, 96
Coolants (organic)
corrosive effects, 31, 93, 230
fouling effects, 165–66
Copper
drawing, vibration effects on, 124
interdiffusion with U, 203
zone melting, 194
Copper (braze bonded)
heat-transfer and ultrasonic-transmission properties, correlation of, 64
Copper (irradiated)
defect clusters, 173–74, 236
dislocation movement, 106
embrittlement, 171
Ni diffusion into, 106
Copper-alloy sheet (Be–Cu)
development of solid-solution-strengthened, 219
Copper alloys (Al–Cu)(irradiated)
dislocation movement, 106
Copper alloys (Be–Cu)
metallurgy, mechanical, 155
production by splat cooling, 219
tensile properties, 219
Copper alloys (Cu–Fe–Zr)
hydriding, 230
Copper alloys (Cu–Mo–Zr)
corrosion, heat-treatment effects on, 93
Copper alloys (Cu–Nb–Zr)(irradiated)
tensile properties, 168
Copper alloys (Cu–U)
ignition, 15
oxidation, 15, 69
Copper alloys (Cu–Zr)
corrosion, 228–29
development, 245
use for brazing, 263
Copper composites (Cu–W)
corrosion, 161
Copper single crystals (irradiated)
critical shear stress, 173–74
Copper systems (B_4C–Cu)
fabrication and properties, 24–25
Cores
fission-product release, 149
reactivity, crud effects on, 159
Crusilite A (irradiated)
lattice damage, 187

D

D-11
corrosion, 101
D-14
corrosion, 101
D-36
welding, 130
D-43
corrosion, 100–1
mechanical properties, 240
physical properties, 240
stress–rupture properties, heat-treatment effects on, 50
tensile properties, aging effects on, 239–40
welding, 129–30
D-43 (coated)
evaluation, 28
D-43 (silicide coated)
oxidation, 161
Diffusion bonds
nondestructive testing, 264
Disil coatings
evaluation on Nb alloys, 28
Durak KA coatings
evaluation on Nb alloys, 28
for Nb–Zr alloys, 162
Dysprosium
oxidation, 27
Dysprosium oxide
Young's modulus, 54
Dysprosium oxide dispersions (Dy_2O_3–Ni)
stability, 25
Dysprosium oxide dispersions (Dy_2O_3–Ni)
(Inconel 600 clad)
fabrication and stability, 25

E

Eddy-current testing, 65, 132, 200
Electron-beam zone refiner
  characteristics, 194
Electroplating
    (see Plating)
Erbium
  oxidation, 27
Erbium hydride
  thermodynamic properties, 221
Erbium oxide
  O self-diffusion in, 114-15
  Young's modulus, 54
Europium
  burnup in irradiated Eu_2O_3-stainless steel dispersions, 223
  oxidation, 27
Europium molybdenum oxide-dispersion control rods (Al-$Eu_{1.3}MoO_{4.1}$)(irradiated)
  performance, 92
Europium oxide
  compatibility with stainless steel, 222-23
  corrosion, 223
Europium oxide cermets (Eu_2O_3-stainless steel)
  corrosion, 25
Europium oxide cermets (Eu_2O_3-stainless steel-TiO_2)
  corrosion, 25
Europium oxide-dispersion control rods (Al-Eu_2O_3)(irradiated)
  performance, 92
Europium oxide dispersions (Eu_2O_3-stainless steel)(irradiated)
  behavior, 222
  burnup of Eu, 223
Europium oxide microspheres
  preparation and properties, 91
Europium oxide mixtures (Eu_2O_3-TiO_2)
  corrosion, 25
Experimental Boiling Water Reactor Core IA
  fuel, irradiation performance of, 71
Explosion forming, 261
Explosive metalworking, 127-28

F

F-48
  corrosion, 101
Fabrication
  special techniques, 59-67, 121-33, 194-202, 257-66
Facings
  corrosion of hard, 229
Fertile materials, 1-19, 69-82, 135-51, 203-16
Films
  properties, 225
Fluoride salts (fused)
  corrosive effects, 103-4
Foils
  coating of, 199
  preparation of Mo and Re, 196
Forming (explosion), 261
FS-60
  corrosion, 101
FS-85
  corrosion, 101
  creep-rupture properties, 42
  mechanical properties, 239-40
  physical properties, 240
  welding, 130
FS-85 sheets
  explosive bonding, 64
Fuel elements (clad)
  pressure bonding, 62
Fuel elements (irradiated)
  growth and swelling in cylindrical, 79
Fuel materials, 1-19, 69-82, 135-51, 203-16
    (see also Nonfuel materials and specific fuel materials)
Fuels
  fabrication in France, 257-58
  reactions with water, 211
Fuels (carbide-oxide)(irradiated)
  fission-gas retention, 214
Fuels (coated particle), 10-11, 74-75, 142-43
Fuels (dispersion)(irradiated)
  swelling, porosity effects on, 74
Fuels (hydride)
  thermal conductivity, H/Zr-ratio effect on, 221
Fuels (irradiated)
  burnup analysis, 148-49, 213
  fission-product behavior, 149, 212-14
Fuels (molten)
  corrosive effects, 31-32
Fuels (molten)(irradiated)
  fission-product release, 212
Fuels (oxide)(Zircaloy clad)(irradiated)
  evaluation, computer program for, 214-15
Fused fluoride salts
  corrosive effects, 103-4

G

Gadolinium
  oxidation, 27, 91
  solubility in W, 91
Gadolinium alloys (Gd-Mo)
  phase studies, 91
Gadolinium alloys (Gd-Pu-Y)
  phase studies, 139
Gadolinium oxide compacts (Al_2O_3-Gd_2O_3)
  fabrication and thermal expansion, 223
Gadolinium sesquioxide systems (Cr_2O_3-Gd_2O_3)
  phase studies, 252
Gallium alloys (Ga-Pu)
  delta-phase stability, 72
GE 2541
  corrosion, 226
General Electric J8100
  corrosion, 102-3
General Electric J8300
  corrosion, 102-3
Germanium systems (Al-Ge-Si-Ag)
  use for brazing, 262
Germanium systems (Al-Ge-Si-Zn)
  use for brazing, 262
Gold
  reactions with UC and UN, 209
Gold (irradiated)
  damage, 42
  defect clusters, 174
Gold alloys
    (see ANM-16)
Graphite
    (see also Carbon)
  analysis, 20
  compatibility with Li, 30
  compatibility with Na, 229
  cracks, eddy-current investigation of, 83-84
  fabrication, 218
  fracture toughness, 154
  magnetic force welding, 262
  mechanical properties, degassing effects on, 154
  out-of-plane waves, velocity of, 84
  radiography, 217
  reactions with Nb, 179
  thermal conductivity, 84
Graphite (irradiated)
  compatibility with irradiated BeO, 153-54
  creep, 83
  dimensional changes in boronated, 222
  properties, 152-54, 217-18
  strain absorption, 83
Graphite (polycrystalline)
  thermal expansion, 20
Graphite (pyrolytic)(irradiated)
  dimensional changes, 217
Graphite (TSGBF)
  expansion, Na effects on, 29
Graphite (TSX)
  expansion, Na effects on, 29
Graphite coatings
  deposition, 75, 142
Graphite composites (graphite-metal)
  hot pressing, 20, 198
Graphite composites (graphite-NbC)
  thermal expansion, 116
Graphite joints (graphite-Hastelloy N)
  corrosion, 103
Graphite joints (graphite-Mo)
  corrosion, 103
Graphite systems (graphite-refractory metal)
  melting and casting, 257

H

Hafnium
  elastic moduli, temperature effects on, 24
  grain growth, 221-22
Hafnium (irradiated)
  mechanical properties, 41
Hafnium-alloy coatings (Hf-Ta)
  for Ta-W alloys, 228
Hafnium alloys (Cr-Hf)
  phase studies, 24
Hafnium alloys (Hf-Mo)
  aging, 111
  recrystallization temperature, 241
  rupture strength, 241
Hafnium alloys (Hf-Mo-Ta)
  oxidation, 222
Hafnium alloys (Hf-Nb)
  high-temperature properties, W- and Y-addition effects on, 111
Hafnium alloys (Hf-Nb-Ti-W)
  mechanical properties and oxidation, 49
Hafnium alloys (Hf-Ta)
  phase studies and properties, 222
Hafnium alloys (Hf-Ta-W)
  thermal conductivity, 110
Hafnium alloys (Hf-Ta-Zr)
  oxidation, 222
Hafnium carbide
  stoichiometry, 186
Hafnium composites (graphite-Hf)
  hot pressing, 20
Hafnium diboride
  fabrication, 188
  hot hardness, 188
  oxidation of zone-melted, 117
  thermal expansion, 223
Hafnium dioxide
  reaction with HfC, 251-52
Hafnium dioxide coatings
  for Ta-W alloys and W, 227-28
Hafnium dioxide composites (HfO_2-W)
  strength, 183
Hafnium monocarbide
  properties, 115, 249, 251-52
Hafnium monocarbide castings
  hot hardness, 59, 250
  oxidation, 250
Hafnium monocarbide-system castings (C-HfC)
  hardness and stress relieving, 186

Hafnium monocarbide systems (C–HfC)
  eutectic temperature, 186
  melting and casting, 257
  properties, 257
Hafnium monocarbide systems (HfC–TaC)
  properties, 250-51
Hafnium monocarbide systems (HfC–ZrC)
  fusion point, 250-51
Hafnium oxide
  self-diffusion in, 54
Hafnium systems (C–Cr–Hf–Mo–Y–Zr)
  tensile properties, 237
Hafnium systems (C–Cr–Hf–Y–Zr)
  tensile properties, 237
Hafnium systems (C–Hf–Nb)
  phase studies, 51
Hafnium systems (C–Hf–Ta)
  phase studies, 51
Hafnium systems (C–Hf–W)
  fabrication and preparation, 52
Hafnium systems (Hf–Nb–N)
  precipitation hardening, 50
Hastelloy B
  mass transfer, 98-99
Hastelloy C
  brazing, 263
  corrosion, 226, 229
  mechanical properties, 47
Hastelloy N
  corrosion, 31-32, 226
  creep-rupture properties, 182
  specific heat, temperature effects on, 248-49
Hastelloy N (irradiated)
  creep-rupture properties, 171-72
  embrittlement, 106
  stress-rupture properties, 234
Hastelloy N joints (graphite–Hastelloy N)
  corrosion, 103
Hastelloy W
  aging effects on weld-metal, 109
  mass transfer, 98-99
Hastelloy X
  aging effects on weld-metal, 109
  corrosion, 160, 226
  evaporation in He, 94
Hastelloy X nozzles
  welding, 262
Hastelloy X weld joints
  aging effects, 129
Hastelloy X-280
  aging effects on welded, 109
Hastelloy X-280 (irradiated)
  rupture and tensile properties, 37
Haynes 25
  brazing, 263
  corrosion, 226
  evaporation in He, 94
Haynes 25 weld joints
  aging effects, 129
Haynes 56
  compatibility with PuC–UC mixtures, 73
  compatibility with $Pu_{0.2}U_{0.8}C$, 12
Haynes Stellite-25
  aging effects on welded, 109-10
  mechanical properties, effects of Fe and Si on, 47
HB-40
  corrosive effects, 31, 230
Holmium
  oxidation, 27
Holmium tetraboride
  fabrication and hot hardness, 188
Honeycomb materials
  tap testing, 264
Hot working, 60-61
  cast materials, 122-24
HT 60
  embrittlement of welded joints, 46
Hydride fuels
  thermal conductivity, H/Zr-ratio effect on, 221
Hydrides (alkali metal)
  heats of formation, 221
Hydrogen systems (H–La)
  phase studies, 22, 88-89
Hydrogen systems (H–N–Zr)
  phase studies, 89
Hydrogen systems (H–U)
  ignition, 15
HYMU-80
  corrosion, 31-32

I

IN-100
  mechanical properties, 47
IN-102
  corrosion, 226
  fabrication, 219
Incipient boiling detectors
  ultrasonic testing, 200
Incoloy
  corrosion, 230
  magnetic force welding, 262
Incoloy 800
  corrosion, 160, 228
Incoloy 800 (irradiated)
  tensile properties, 233-34
Inconel
  mass transfer, 98-99
  stress-corrosion cracking, 159
Inconel 600
  corrosion, 31-32, 226
  explosive bonding, 64
Inconel 600 joints (Inconel 600–Zircaloy-2) (irradiated)
  tensile properties, 39-40
Inconel 600 tubes
  stress-corrosion cracking, 94
Inconel 625
  compatibility with PuC–UC mixtures, 73
  corrosion, 226
Inconel 718
  mechanical properties, 47
Inconel 800
  corrosion, 226
Inconel X
  corrosion, 160
  mass transfer, 98-99
Inconel X (irradiated)
  mechanical properties, 234
Inconel X-550
  corrosion, 99
Inconel X-750
  corrosion, 99
  mechanical properties, 47
Indium (molten)
  corrosive effects, 230
Indium alloys (Cd–In–Ag)(Ni plated) (irradiated)
  oxidation and tensile properties, 24
Indium alloys (Cd–In–Ag)(stainless-steel clad)
  fabrication, 24
INOR-8
  specific heat, temperature effects on, 248-49
INOR-8 (irradiated)
  creep-rupture properties, 171-72
Iridium
  compatibility with molten PuO_2, 140
  diffusion studies, 54
  interdiffusion with Ta, 180
  oxidation, 160
  powder metallurgy, 197
  reaction with UC, 209
Iridium (irradiated)
  defect clusters, 174
Iridium-alloy coatings
  for Ta alloys, 161-62
Iridium alloys (Ir–Rh)
  oxidation, 160
Iridium alloys (Ir–W)
  powder metallurgy, 197
Iridium-system coatings
  for Ta alloys, 161
Iron
  corrosion, 103
  diffusion in Al–Fe alloy, 54
  strain aging, effect of stress on, 111-12
  tensile properties, 248
  wetting in molten Na, 101
  zone melting, 194
Iron (Armco)
  corrosion, 96, 98
  penetration by molten Fe–U eutectics and U, 135
Iron (irradiated)
  annealing kinetics, 236
  damage, 41-42
  electrical resistivity, 106
  hardness, 173
  yield stress, 234-35
Iron alloys
  (see also Haynes 56)
  compatibility with $Pu_{0.2}U_{0.8}C$, 12
  oxidation, 247
  wetting in molten Na, 101
Iron alloys (Al–Cr–Fe–Y)
  corrosion, 226, 248
  metallurgy, 46-47
  oxidation, 26-27, 46-47
  production of corrosion-resistant, 260
  tensile properties, 247-48
Iron alloys (Al–Cr–Fe–Y)(irradiated)
  embrittlement, 170
  mechanical properties, 37
Iron alloys (Al–Fe)
  Fe diffusion in, 54
  sintering, 230
  tensile properties, 248
Iron alloys (Al–Fe–U)
  phase studies, 69
Iron alloys (Be–Fe)
  tensile properties, 248
Iron alloys (Ce–Fe–Pu)
  phase studies, 139
Iron alloys (Cr–Fe)(irradiated)
  embrittlement, 170
Iron alloys (Cr–Fe–Ni)
  B effects on, 246-47
  sigma-phase precipitation, (Fe,Cr), 109
  strength, Mo effects on, 176
  Ti effects on, 246-47
  zone melting, 194
Iron alloys (Cr–Fe–Ni–Nb)
  hardening by precipitation, 177
Iron alloys (Cr–Fe–Nb–Sn–Zr)
  corrosion, 225
Iron alloys (Cr–Fe–Zr)
  preparation, 122
Iron alloys (Co–Fe–U)
  phase studies, 71
Iron alloys (Cu–Fe–Zr)
  hydriding, 230
Iron alloys (Fe–Nd)
  phase studies, 24
Iron alloys (Fe–Ni)
  wetting in molten Na, 101
  zone melting, 194
Iron alloys (Fe–Ni–Nb–Sn–Zr)
  hydriding, 230
Iron alloys (Fe–Ni–W)
  fabricability, 52

Iron alloys (Fe–Nb)
oxidation, 227
Iron alloys (Fe–Ti)
tensile properties, 248
Iron alloys (Fe–U)
ignition, 15
Iron alloys (Fe–U)(molten)
penetration of Armco Fe by, 135
Iron alloys (Fe–V)
tensile properties, 248
Iron alloys (Fe–Zr)
use for brazing, 263
Iron alloys (irradiated)
phase transformations, 106
Iron systems (Cr–Fe–Si–Ti–V)
fused-slurry coatings developed from, 161
Iron systems (Fe–Mo–Si)
phase studies, 242
Iron systems (Fe–Si–U)
phase studies, 69

J

Joining, 128-31
Joints (brazed)
nondestructive testing, 264

K

K-95
corrosion, 229

L

L-605
embrittlement reduction, 110
mechanical properties, 47, 114
Lanthanide oxide microspheres
preparation and properties, 91
Lanthanides
oxidation, 27
Lanthanum
oxidation, 27
Lanthanum alloys
consolidation, 237-38
Lanthanum alloys (Cr–La)
nitridation in carbide-containing, 237
Lanthanum alloys (Cr–La–Mo)
nitridation in carbide-containing, 237
Lanthanum hexaboride
fabrication and hot hardness, 188
Lanthanum hexaboride systems (LaB_6–W)
phase studies and physical properties, 243
Lanthanum systems (H–La)
phase studies, 22, 88-89
Lead (molten)
corrosive effects, 103
Lead alloys (Bi–Pb)(molten)
corrosive and erosive effects, 30-31
Lead alloys (Pb–U)
ignition, 15
Lead combinations (Pb–LiH)
gamma-ray attenuation, 221
Lithium
corrosive effects, 30, 32, 102, 230
effects on corrosive effects of Na, 163
Lithium alloys (Al–Li)(irradiated)
He bubbles in, 236
rare-gas diffusion in, 16
Lithium carbides
identification using X-ray diffraction, 30
Lithium deuteride
compressibility, 157
heat of formation, 221
Lithium fluoride systems (BeF_2–LiF–ThF_4–UF_4–ZrF_4)(molten)
corrosive effects, 103
Lithium fluoride systems (LiF–UF_4)(molten)
corrosive effects, 103-4
Lithium hydride
compatibility with W alloy and ZrH_2, 221
compressibility, 157
heat of formation, 221
neutron attenuation, 221
Lithium hydride combinations (Pb–LiH)
gamma-ray attenuation, 221
Loops (molten K)
incipient boiling detector, 64
Loops (primary)
acoustic-emission testing, 264
Lutetium
oxidation, 27

M

Magnesium
compatibility with metals, 180
corrosion, 95
Magnesium alloys
(see AL80, MN70, ZR55, and ZR57)
corrosion, 95
patent for improved, 112
Magnesium alloys (Mg–Y)
oxidation and strength, 53
Magnesium oxide
extrusion, 126
reactions with H_2PO_3F, 115
self-diffusion in, 54
Magnesium oxide powder
sintering, 189
Magnox AL80
(see AL80)
Manganese
self-diffusion in, 179
Manganese alloys
(see also MN70)
use for brazing, 264
Manganese alloys (Mn–Zr)
use for brazing, 263
Melting, 59-60, 121-22, 194, 257
Mercury
corrosive effects, 30
Metal carbide castings
properties, 250
Metal carbides
free energy of formation, 102
hot pressing, 61
spin casting, 250
Metal carbides (transition-)
elastic properties, 115
reactions with oxides, 251-52
Metal composites (graphite-metal)
hot pressing, 20
Metal diborides (transition-)
thermal conductivity, 222
Metal dispersions (ceramic-metal)
development, 141
Metal hydrides (alkali-)
heats of formation, 221
Metal oxide microspheres
preparation, 12
Metal oxides
self-diffusion in, 54
Metal oxides (transition-)
reactions with carbides, 251-52
Metal powders
(see Powder metallurgy)
Metal systems (refractory-)(graphite–refractory metal)
melting and casting, 257
Metallurgy (powder)
(see Powder metallurgy)
Metals
compatibility studies, 180
corrosion of chromized, 159
deformation processing, 60
diffusion in, 54, 179
embrittlement, 166
fission-product migration in, 54
hot-press bonding of dissimilar, 197
hot rolling, 123
inert-gas behavior with respect to, 54, 147-48
mechanical properties, effects of material removal on, 53
reactions with refractory compounds, 116
reactions with water, 32-33, 104, 166-67, 230-32
working, 60, 127-28
zone melting, 194
Metals (alkali)
corrosive effects, 32, 96
Metals (irradiated)
coalescence of spheres by surface diffusion, 16
embrittlement and damage recovery, 106
fission-fragment tracks in, 16
point defects, 236
Metals (molten)
bibliographies, 32, 230
casting, nondestructive examination during, 264
compatibility and corrosive effects, 32
embrittlement effects on metals, 166
wetting of refractory compounds by, 116
Metals (refractory)
analyses for interstitial elements, comparison of chemical, 110
brazing, 199, 263-64
coating of, 62-63, 198-99
compatibility with metals, 180
corrosion, 27-28, 226-27, 230
deformation, 111
diffusion studies, 54
extrusion, 123-24, 196
melting, electron-beam, 60
metallurgy, 236-44
soldering, 263-64
Metals (refractory)(coated)
corrosion, 227-28
Metals (transition)
conductivity, electrical and thermal, 222
MN70
fatigue properties, 114
Moderator materials, 20-23, 83-90, 152-57, 217-24
Molybdenum
Al-alloy coatings for, 162
bonding, 262
brazing, 199, 263
C solubility in, 241
compatibility with Li, 30
corrosion, 100, 103
crystallization, vibration effects on, 195
deposition, 126-27
diffusion bonding, 260
diffusion studies, 54
ductility, melting techniques for improving, 59-60
ductility, addition effects on, 111, 240-41
ductility, annealing effects on, 241
electroplating Cr and Ni on, 261
extrusion, lubricants for, 123
hot workability, addition effects on, 52
mechanical properties, 178, 195
melting, 60, 194
oxidation, 96
passivity, 96
K diffusion in, 30
magnetic force welding, 262
metallurgy, 240-42

reactions with UC–ZrC system, 145
recrystallization, metal-addition effects on, 111
solubility in molten Pu, 4
solubility in UN, 77
structure, annealing effects on, 241
thermal conductivity, grain-size effects on, 178
twinning, Re-addition effects on, 111
U diffusion in, 135
zone refining, 121-22, 194
Molybdenum (irradiated)
defect clusters, 42, 172-73, 236
mechanical properties, 172
tensile properties, 41
Molybdenum-alloy tubing
fabrication, 124-25, 196-97
Molybdenum alloys
(see also TZC and TZM)
extrusion, lubricants for, 123
precipitation-hardenable, patent for, 178
Molybdenum alloys (Al–Mo–Sn–Zr)
corrosion, 229
Molybdenum alloys (Cr–La–Mo)
nitridation in carbide-containing, 237
Molybdenum alloys (Cr–Mo)
solid solubility in, 241
Molybdenum alloys (Cr–Mo)
structure, 236-37
Molybdenum alloys (Cr–Mo–Nb)
phase studies, 111
Molybdenum alloys (Co–Mo)
properties, addition effects on, 47
Molybdenum alloys (Cu–Mo–Zr)
corrosion, heat-treatment effects on, 93
Molybdenum alloys (Gd–Mo)
phase studies, 91
Molybdenum alloys (Hf–Mo)
aging, 111
recrystallization temperature, 241
rupture strength, 241
Molybdenum alloys (Hf–Mo–Ta)
oxidation, 222
Molybdenum alloys (Mo–Ni)
specific heat, temperature effects on, 248-49
Molybdenum alloys (Mo–Nb)
Nb self-diffusion in, 180
recrystallization, fabrication effects on, 258-59
Molybdenum alloys (Mo–Nb–Ta–W)
creep mechanism, 50-51
Molybdenum alloys (Mo–Nb–Ti–U–Zr)
tensile properties, 137
Molybdenum alloys (Mo–Nb–Zr)
phase studies, 111
Molybdenum alloys (Mo–Pu–U)
compatibility with stainless steel 304L and thermal expansion, 6
Molybdenum alloys (Mo–Re)
corrosion, 103
Molybdenum alloys (Mo–Re–W)
creep properties, 183-84
development, 179
ductility, 52
mechanical properties, 242
physical properties, 242
powder metallurgy, 124
Molybdenum alloys (Mo–Ta–V)
phase studies, 243
Molybdenum alloys (Mo–Ti)
aging, 111
cavitation, 30
extrusion, lubricants for, 123
recrystallization temperature, 241
rupture strength, 241
Molybdenum alloys (Mo–Ti–Zr)
corrosion, 161
phase studies, 111
Molybdenum alloys (Mo–W)
corrosion, 103
diffusion studies, 54
preparation by vapor deposition, 198
Molybdenum alloys (Mo–U)
brazing, 263
ignition, 15
structure, 4, 135
Molybdenum alloys (Mo–U)(irradiated)
properties, 16
Molybdenum alloys (Mo–V)
corrosion, 99
Molybdenum alloys (Mo–Y)
oxidation, 96
Molybdenum alloys (Mo–Zr)
aging, 111
corrosion, 161
recrystallization, fabrication effects on, 258-59
recrystallization temperature, 241
rupture strength, 241
Molybdenum billets
evaluation for forging, 60
Molybdenum boride
production, 188
Molybdenum braze alloys (Mo–Re–Ru)
patent for, 199
Molybdenum carbide
C diffusion in, 179
Young's modulus, 115
Molybdenum coatings
deposition of, 63
Molybdenum composites (graphite–Mo)
hot pressing, 20
Molybdenum disilicide
slip casting, 62
Molybdenum disilicide-system powders ($MoSi_2$–ZrB_2)
sintering, 188
Molybdenum foil
preparation, 196
Molybdenum joints (graphite–Mo)
corrosion, 103
Molybdenum sheet
development of high-ductility, 52-53
Molybdenum single crystals
deformation, 240-41
mechanical properties, orientation effects on, 111
Molybdenum systems (C–Cr–Hf–Mo–Y–Zr)
tensile properties, 237
Molybdenum systems (C–Mo)
recrystallization temperature and rupture strength, 241
Molybdenum systems (C–Mo–W–Y)
corrosion, 161
Molybdenum systems (C–Mo–U)
phase relations, PuC-addition effects on, 77
Molybdenum systems (Co–Mo–Si)
phase studies, 242
Molybdenum systems (Fe–Mo–Si)
phase studies, 242
Molybdenum tubing
fabrication, 196
Monel K-500
mechanical properties, 47
Multimet
corrosion, 228

N

NaK
corrosive effects, 32
Neodymium
oxidation, 27
Neodymium alloys (Fe–Nd)
phase studies, 24
Neodymium alloys (Nd–Pu–Y)
phase studies, 139
Neptunium
electrodeposition, 63
Neptunium alloys (Al–Np)
preparation, 121
Neutron radiography, 65, 131-32, 264
Nickel
compatibility with UN, 12
corrosion, 27, 94, 96, 98, 103
deposition, 62-63, 127
electroplating on Mo and U, 261
magnetic force welding, 262
mechanical properties, 47
reaction with steam, 230
wetting in molten Na, 101
zone melting, 194
Nickel (irradiated)
critical shear stress, 174
defect clusters, 42, 236
Nickel-63
diffusion into irradiated Cu, 106
Nickel 200
corrosion, 160
Nickel 201
corrosion, 27, 160
Nickel alloys
(see also Alloy 713C, Alloy 713LC, Alloy 718, Hastelloy..., Haynes 25, HYMU-80, Incoloy 800, Inconel..., INOR-8, Monel K-500, Nickel 200, Nickel 201, Nimonic PE16, PDRL-120, Rene 41, TD-50, Udimet 500, and Waspaloy)
corrosion, 100, 226, 228
fabrication, 122
mass transfer, 98-99
mechanical properties, 45, 47
metallurgy, 248-49
wetting in molten Na, 101
Nickel alloys (Al–Cr–Ni–Ti)
crystal structure, W effects on, 177
Nickel alloys (Be–Ni)
metallurgy, mechanical, 155
Nickel alloys (Bi–Ni–Sn)
wear, 225
Nickel alloys (Ce–Ni–Pu)
phase studies, 139
Nickel alloys (Cr–Fe–Ni)
B effects on, 246-47
sigma-phase precipitation, (Fe,Cr), 109
strength, Mo effects on, 176
Ti effects on, 246-47
zone melting, 194
Nickel alloys (Cr–Fe–Ni–Nb)
hardening by precipitation, 177
Nickel alloys (Cr–Ni)
Cr diffusion in, 179
corrosion, 96, 98
specific heat, temperature effects on, 248-49
strength, effects of Mo and Nb on, 47
Nickel alloys (Cr–Ni alloy (TD))
brazing, 263
Nickel alloys (Cr–Ni–Pd)
corrosion, 103
Nickel alloys (dispersion strengthened)
compaction, 62
Nickel alloys (Fe–Ni)
wetting in molten Na, 101
zone melting, 194
Nickel alloys (Fe–Ni–Nb–Sn–Zr)
hydriding, 230
Nickel alloys (Fe–Ni–W)
fabricability, 52
Nickel alloys (irradiated)
ductility, 34-35

mechanical properties, 233-34
Nickel alloys (Mo–Ni)
specific heat, temperature effects on, 248-49
Nickel alloys (Ni–Nb)
hardness, 238
phase studies, 177, 238
Nickel alloys (Ni–U)
ignition, 15
Nickel alloys (TD)
bonding, 126
brazing, 263
Cr diffusion in, 179-80
magnetic force welding, 262
strength, 43
Nickel coatings
deposition, 10, 127
Nickel composites (graphite–Ni)
fabrication by hot isostatic pressing, 198
Nickel couples (Al–Ni)
corrosion, 94
Nickel-dispersion sheet (Ni–ThO_2)
cold rolling and annealing, 177
Nickel dispersions (Dy_2O_3–Ni)
stability, 25
Nickel dispersions (Dy_2O_3–Ni) (Inconel 600 clad)
fabrication and stability, 25
Nickel monocarbide (irradiated)
behavior, 187-88
Nickel oxide
self-diffusion in, 54
Nickel superalloys
mechanical and physical properties, 249
Nickel systems (Al–C–Cr–Co–Ni–Ti)
sigma-phase formation, 248
Nicrobraz 10
corrosion, 102-3
Nicrobraz 30
corrosion, 229
Nicrobraz 50
corrosion, 102-3, 229
Nimonic 80A
corrosion, 228
Nimonic PE16 (irradiated)
ductility, 37
Niobium
absorption of O and water, 227
coating of, with Al alloys, 162
coating of, with $NbSi_2$, 63
compatibility with K, 29
corrosion, 95, 100, 103-4, 164
diffusion studies, 54
electrical resistivity, 238
extrusion, 123, 125
H solubility in, 110-111
internal friction, 239
mechanical properties, 110, 113, 239, 258
metallurgy, 238-40
microflow properties, 239
oxidation, 160-61, 227
preparation, 195
purification, 238
reactions with graphite, 179
recrystallization, fabrication effects on, 258
recovery in cold-worked, 110
self-diffusion in Mo–Nb alloys, 180
solid-solution hardening, 178
solubility in molten Pu, 4
strain aging, effect of stress on, 111-12
U diffusion in, 135
yield point, 238
yield stress, zone-purification effects on, 112
zone melting, 194
Niobium (Al–Sn–$NbSi_2$ coated)
oxidation, 228
Niobium (fluoride coated)
oxidation, 96
Niobium (irradiated)
hardening, 236
Niobium-alloy pressure tubes (Nb–Zr)
evaluation, 245, 258
fabrication, 258
Niobium-alloy sheets (Nb–Ta)
explosive bonding, 64
Niobium-alloy sheets (Nb–Zr)
explosive bonding, 64
Niobium-alloy tubing (Nb–Zr)
fabrication, 196
Niobium alloys
(see also AS-55, B-66, C-129Y, Cb-132, Cb-132M, Cb-752, Cb-753, D-11, D-14, D-36, D-43, F-48, FS-85, S-291, and X-34)
corrosion, 95
ductility, 49
extrusion, lubricants for, 123
fabricability, 49-50
mechanical properties, 49, 239-40
physical properties, 240
strength, 49
tensile properties, aging effects on, 239-40
welding, 129-30
Niobium alloys (Al–Nb)
phase studies, 51
Niobium alloys (Al–Nb–Ti)
mechanical properties, 113
Niobium alloys (Cr–Fe–Ni–Nb)
hardening by precipitation, 177
Niobium alloys (Cr–Fe–Nb–Sn–Zr)
corrosion, 225
Niobium alloys (Cr–Mo–Nb)
phase studies, 111
Niobium alloys (Cr–Nb)
oxidation, 161
Niobium alloys (Co–Nb)
oxidation, 227
phase studies, 51
Niobium alloys (Cu–Nb–Zr) (irradiated)
tensile properties, 168
Niobium alloys (Hf–Nb)
high-temperature properties, W- and Y-addition effects on, 111
Niobium alloys (Hf–Nb–Ti–W)
mechanical properties and oxidation, 49
Niobium alloys (Fe–Ni–Nb–Sn–Zr)
hydriding, 230
Niobium alloys (Fe–Nb)
oxidation, 227
Niobium alloys (Mo–Nb)
Nb self-diffusion in, 180
recrystallization, fabrication effects on, 258-59
Niobium alloys (Mo–Nb–Ta–W)
creep mechanism, 50-51
Niobium alloys (Mo–Nb–Ti–U–Zr)
tensile properties, 137
Niobium alloys (Mo–Nb–Zr)
phase studies, 111
Niobium alloys (Ni–Nb)
hardness, 238
phase studies, 177, 238
Niobium alloys (Nb–Re)
H solubility in, 111
Niobium alloys (Nb–Re–Zr)
oxidation and scale formation, 95
Niobium alloys (Nb–Ru)
phase studies and structure, 239
Niobium alloys (Nb–Ta)
properties and structure, 238-39
Niobium alloys (Nb–Ta–V)
mechanical properties, 242
phase studies, 243
physical properties, 242
strength, 43
Niobium alloys (Nb–Sn–Zr)
corrosion, 93, 225
Niobium alloys (Nb–Ti)
corrosion, 101
elastic properties, 238
Niobium alloys (Nb–Ti–V)
strength, 43
Niobium alloys (Nb–Ti–Zr)
corrosion, 164
Niobium alloys (Nb–W)
diffusion in, 180
oxidation, 161
thermal conductivity, 110, 178
Niobium alloys (Nb–W–Zr)
Be-induced second phase, annealing effects on, 111
Niobium alloys (Nb–U)
ignition, 15
metastable phases, 204
tensile properties, 71
Niobium alloys (Nb–U–Zr)
phase transformation, 71
reaction with water, 15
Niobium alloys (Nb–U–Zr) (Zircaloy-2 clad) (irradiated)
performance, 71
Niobium alloys (Nb–V)
corrosion, 164
ductile–brittle transition, 42, 113
elastic properties, 238
mechanical properties, mechanical-twinning effects on, 239
strain hardening, 184
strength, 43
yield point, Ti effects on, 179
Niobium alloys (Nb–V) (irradiated)
twinning, 172
Niobium alloys (Nb–Zr)
beta-phase decomposition, 51
carbide-layer growth on, 54
C diffusion in, 54
cavitation, 30
coatings for, 162
compatibility with K, 29-30
corrosion, 164-66
creep rate, aging effects on, 176
ductility, 48
hydriding, 31, 93, 230
H supersaturation, 109
mechanical properties, 108-9
mechanical properties, O effects on, 111, 175-76
mechanical properties, Na-exposure effects on, 99
oxidation, 95
oxide films on, potential on, 225
phase transformation, 175
scale formation, 95
strength, Be-addition effects on, 111
thermal expansion, H effects on, 48
Zr hydride-platelet orientation, 109
Niobium alloys (Nb–Zr) (hydrided) (irradiated)
impact properties, 39
Niobium alloys (Nb–Zr) (irradiated)
creep properties, 39, 168
tensile properties of heat-treated, 39
Niobium carbide
C diffusion in, 179
stoichiometry, 186
Young's modulus, 115
Niobium carbonitride
preparation, 249
Niobium cladding
fabrication on steel, 258
Niobium composites (graphite–Nb)
hot pressing, 20
Niobium diboride
fabrication, 188
hot hardness, 188

thermal expansion, 223
Niobium disilicide coatings
application on Nb, 63
Niobium monocarbide
C diffusion in, 54
deformation, 116
elastic properties, 115
electrical resistance, 115, 251
preparation, 249
reaction with Nb oxide, 251-52
thermal conductivity, 251
thermal expansion, 251
Niobium monocarbide castings
hot hardness, 59, 250
oxidation, 59, 250-51
Niobium monocarbide composites (C–NbC)
deformation, 116
Niobium monocarbide composites (graphite–NbC)
thermal expansion, 116
Niobium monocarbide-system castings (C–NbC)
hardness and stress relieving, 186
Niobium monocarbide systems (C–NbC)
eutectic temperature, 186
melting and casting, 257
properties, 257
Niobium monocarbide systems (NbC–ZrC)
Hall constant and resistivity, 250
Niobium oxide
composition, 227
evaporation of volatile, 227
reaction with NbC, 251-52
structure, 227
Niobium single crystals
preparation, 122
Niobium single crystals (irradiated)
plastic deformation, 173
Niobium solid solutions (Nb–Ti–V)
oxidation, 95
Niobium systems
fabrication, 52
Niobium systems (C–Hf–Nb)
phase studies, 51
Niobium systems (C–Nb–Ti)
phase studies, 51
Niobium systems (C–Nb–W)
fabrication and preparation, 52
Niobium systems (C–Nb–Zr)
phase studies, 51
Niobium systems (Hf–Nb–N)
precipitation hardening, 50
Niobium systems (H–Nb)
mechanical properties and sorption kinetics, 239
Niobium systems (H–Nb–Zr)
phase studies, 22-23
Niobium systems (Nb–Si)
hot hardness, 184
mechanical properties, 240
Niobium tubing
fabrication, 196
Nitrides
thermodynamic potential, 249
Nitrides (refractory)
fabrication, 185-86
preparation, 185-86
reactions in liquid media, 116-17
reactions with metals, 116
wettability by molten metals, 116
Nitrogen systems (H–N–Zr)
phase studies, 89
Nondestructive testing, 64-65, 131-32, 200, 254
Nonfuel materials
refractory, 115-17, 185-89, 249-52
Nonfuel materials (irradiated)
fission-product diffusion in, 54
properties, 104-6, 167-74
Nuclear poisons, 24-25, 65, 91-92, 221-23

O

Organic coolants
corrosive effects, 31, 93, 230
fouling effects, 165-66
Osmium-alloy coatings (Ir–Os)
for Ta alloys, 161
Oxide cermets
preparation of infiltrated, 125-26
Oxide films
potential on, on Zr and Zr alloys, 225
Oxide fuels
homogeneity measurement by fission-track counting, 65
Na logging, 29
Oxide fuels (irradiated)
fission-gas swelling, 80
swelling and temperature calculation, 149
Oxide fuels (metal clad)(irradiated)
analysis of, computer programs for, 80
Oxide microspheres
preparation of metal, 12
Oxides
wear of, on Zr alloys, 225
Oxides (metal)
self-diffusion in, 54
Oxides (refractory)
reactions with metals, 116
Oxides (transition metal)
reactions with carbides, 251-52
Ozhennite 0.5
hydriding, 230

P

Palladium alloys (Cr–Ni–Pd)
corrosion, 103
Palladium alloys (Pd–U)
ignition, 15
PDRL-120 (irradiated)
mechanical properties, 172
PFR-32 coatings
evaluation on Nb alloys, 28
Plastics (polyformaldehyde)
corrosion, 94
Plating, 62-64, 126-27, 198-99, 260-61
Platinum (irradiated)
yield strength, 174
Platinum alloys (Pt–U)
ignition, 15
Plutonium
compatibility with metals, 180
diffusion in UO_2, 73
electrodeposition, 127
electrorefining, 205
endothermic reaction in, 139
grain growth, 5
heat capacity, 139, 205
oxidation, 205
phase transformation, 5
pickup in UO_2 microspheres, 206
properties, 7
Plutonium (molten)
solubility of elements in, 4, 139, 205
Plutonium alloys
measurement of alpha Pu, 5
properties, 7
Plutonium alloys (Ce–Co–Pu)(molten)
corrosive effects, 31
fission-gas venting, 4-5
Plutonium alloys (Ce–Fe–Pu)
phase studies, 139
Plutonium alloys (Ce–Ni–Pu)
phase studies, 139
Plutonium alloys (Ce–Pu)
density, 205
Plutonium alloys (Gd–Pu–Y)
phase studies, 139
Plutonium alloys (Ga–Pu)
delta-phase stability, 72
Plutonium alloys (molten)
corrosive effects, 31
Plutonium alloys (Mo–Pu–U)
compatibility with stainless steel 304L and thermal expansion, 6
Plutonium alloys (Nd–Pu–Y)
phase studies, 139
Plutonium alloys (Pu–Th–U)
liquidus surface and phase studies, 8
Plutonium alloys (Pu–Th–U)(irradiated)
burnup, 8
Plutonium alloys (Pu–Th–U)(Ti–V alloy clad)(irradiated)
behavior, 205
Plutonium alloys (Pu–Ti–U)
phase studies, 5
properties, 138
solid-state reactions, 5
thermal conductivity, 5
thermal properties, 72
Plutonium alloys (Pu–Ti–U)(Ti–V-alloy clad)(irradiated)
behavior, 138-39
Plutonium alloys (Pu–U)
development for fast breeder fuel, 5
elastic modulus, 6
thermal properties, 71
Plutonium alloys (Pu–U–Zr)
phase studies, 205
preparation, 205
properties, 138
thermal conductivity, 5
Plutonium alloys (Pu–U–Zr)(Ti–V-alloy clad)(irradiated)
behavior, 138-39
Plutonium arsenide
preparation, 140
Plutonium carbide systems (Pu carbide–U carbide)
compatibility with Fe alloys, 12
compatibility with stainless steel (304), 207
preparation, 73
Plutonium carbide systems (Pu carbide–U carbide)(irradiated)
behavior, 207
Plutonium compounds
properties, 7
Plutonium dioxide
etching, chemical, 7
evaporation, 206
Plutonium dioxide (irradiated)
properties, 140
Plutonium dioxide (molten)
compatibility with Ir, 140
Plutonium dioxide microspheres
preparation, 7
Plutonium dioxide microspheres (W coated)
preparation, 7
Plutonium dioxide mixtures (PuO_2–ThO_2)
preparation, 7
Plutonium dioxide mixtures (PuO_2–UO_2)
preparation, 7
Plutonium dioxide mixtures (PuO_2–UO_2) (irradiated)
behavior, 141
compatibility with Na, 29
Plutonium dioxide pellets
preparation by sintering, 73
Plutonium dioxide powder
sintering, 73

Plutonium dioxide solid solutions (PuO_2–UO_2)
oxidation, 7
Plutonium dioxide-system pellets (PuO_2–UO_2)
preparation by sintering, 74
Plutonium dioxide systems (BeO–PuO_2–UO_2)
phase studies, 140
Plutonium dioxide systems (PuO_2–UO_2)
phase studies, 73
Plutonium dioxide systems (PuO_2–UO_2) (irradiated)
fission-product behavior, 214
Plutonium dioxide systems (PuO_2–UO_2) (stainless-steel (316) clad)(irradiated)
properties, 7
Plutonium isotopes (^{238}Pu)
data sheets, 205
Plutonium monocarbide
compatibility with SiC, 72–73
reaction with N, 77, 207
thermal properties, 141
Plutonium monocarbide-mixture powders
sintering, 211
Plutonium monocarbide mixtures (PuC–UC)
compatibility with cladding materials, 73
Plutonium monocarbide systems (PuC–PuN–UC–UN)
phase studies, 144–45
Plutonium monocarbide systems (PuC–UC)
compatibility with cladding materials, 77
phase studies, 144–45
Plutonium monocarbide systems (PuC–UC) (clad)(irradiated)
stability, 13, 210
Plutonium monocarbide systems (PuC–UC) (irradiated)
behavior, 210
Plutonium mononitride
O solubility in, 145
Plutonium mononitride-mixture powders
sintering, 211
Plutonium mononitride systems (PuC–PuN–UC–UN)
phase studies, 144–45
Plutonium mononitride systems (PuN–UC)
phase studies, 144–45
Plutonium mononitride systems (PuN–UN)
phase studies, 144–45
Plutonium monophosphide
preparation, 205
properties, 205–6
Plutonium monophosphide powder
sintering, 205
Plutonium monosulfide
preparation, 205
properties, 205–6
Plutonium monosulfide powder
sintering, 205
Plutonium monoxide systems (PuO–UO)
properties and synthesis, 7
Plutonium nitride systems (Pu nitride–U nitride)
thermal conductivity, 206–7
thermal diffusivity, 206
Plutonium oxide systems (Pu oxide–U oxide)
thermal conductivity and thermal diffusivity, 206
Plutonium oxycarbides
volatility, 140
Plutonium reduction products
electrodeposition, 63
Plutonium sesquicarbide
compatibility with SiC, 73
Plutonium-system microspheres (Ce–O–Pu) (W-coated)
preparation, 7
Plutonium systems (C–Pu–U)
phase studies, 207–8
Plutonium systems (O–Pu–U)
compatibility with Na, 29
corrosive effects, 29–30, 32, 102–3, 165, 230
Polyformaldehyde plastic
corrosion, 94
Potassium
corrosive effects, 29–30, 32, 102–3, 165, 230
diffusion in Mo, 30
Potassium alloys (NaK)
corrosive effects, 32
Potassium chloride eutectics (KCl–UCl_3) (molten)
corrosive effects, 31–32
Potassium deuteride
heat of formation, 221
Potassium hydride
heat of formation, 221
Powder metallurgy, 61–62, 124–26, 196–98, 259–60
Powders (nonmetallic)
coatings on, deposition of, 63
Praseodymium
oxidation, 27, 160
Praseodymium oxide
self-diffusion in, 54
Praseodymium oxide microspheres
preparation and properties, 91
Precipitates
inert-gas-bubble binding to, 16
Pressure bonding, 62, 126, 197–98, 260
Pressure vessels
properties of concrete in, 252
steel in, 234–36, 245–46
testing, 182, 264
Primary loops
acoustic-emission testing, 264
Promethium
oxidation, 27
Protactinium
diffusion in Th, 208
Pyrolytic carbon coatings
(see Coatings (PyC))

R

Radiation effects
Be, 22, 86, 106, 156
fuel materials, 15–17, 79–80, 147–49, 205, 212–15
nonfuel materials, 54, 104–6, 167–74
structural materials, 33–42, 232–36
Radiography, 65, 131–32, 264
Rare-earth compounds
review of refractory, 186
Rare-earth nitrides
preparation, 59
Rare-earth silicides
oxidation, 188–89
Reactors (high-temperature gas-cooled)
fission-product release from core, metallic, 149
Reduction vessels
cracking in stainless-steel, 123
Refiner
characteristics of electron-beam zone, 194
Refractories (nonfueled), 115–17, 185–89, 249–52
Refractory-alloy sheets
explosive bonding, 64
Refractory alloys
coatings for, 27–28
Refractory compounds
reactions in liquid media, 116–17
reactions with metals, 116
wettability by molten metals, 116
Refractory-metal alloys
(see Alloys (refractory metal))
Refractory-metal foils
coating of, 199
Refractory-metal powders
compaction, 259
Refractory-metal systems (graphite–refractory metal)
melting and casting, 257
Refractory metals
(see Metals (refractory))
Rene 41
corrosion, 160
mechanical properties, 47
microstructure of simulated weld-heat-affected zones in, 262
strength, 43
Rhenium
C solubility in, 241
corrosion, 27, 226
deposition, 126, 260
diffusion, 54
reaction with Ta carbide, 251
reaction with UC, 145
reactions with UC–ZrC system, 145
recrystallization temperature, 52
solubility in molten Pu, 4, 205
Rhenium (irradiated)
defect clusters, 236
Rhenium-alloy tubing
fabrication, 60–61, 124–25, 196–97
Rhenium alloys
properties, 52
Rhenium alloys (Cr–Co–Re)
workability, 237
Rhenium alloys (Cr–Re)
oxidation, 95–96
Rhenium alloys (Mo–Re)
corrosion, 103
Rhenium alloys (Mo–Re–W)
creep properties, 183–84
development, 179
ductility, 52
mechanical properties, 242
physical properties, 242
powder metallurgy, 124
Rhenium alloys (Nb–Re)
H solubility in, 111
Rhenium alloys (Nb–Re–Zr)
oxidation and scale formation, 95
Rhenium alloys (Re–Ta)
H solubility in, 111
Rhenium alloys (Re–W)
corrosion, 101
deposition, 126–27, 198, 260
diffusion, 54
ductility, ThO_2-dispersion effects on, 52
emissivity, 110
evaluation for ionizer applications, 259
fractographic studies, 52
mechanical properties, 242
physical properties, 242
powder metallurgy, 124, 197
reactions with UC, 145
reactions with UC–ZrC system, 145
thermal conductivity, 110
Rhenium alloys (Re–U)
structure and transformation, 204
Rhenium braze alloys (Mo–Re–Ru)
patent for, 199
Rhenium foil
preparation, 196
Rhenium systems (C–Cr–Re)
phase studies, 52
Rhodium
reaction with UC, 209
Rhodium-alloy coatings (Ir–Rh)
for Ta alloys, 161–62

Rhodium alloys (Ir–Rh)
oxidation, 160
Rhodium alloys (Rh–U)
ignition, 15
Rubidium
corrosive effects, 230
Rubidium hydride
heat of formation, 221
Ruthenium alloys (Nb–Ru)
phase studies and structure, 239
Ruthenium alloys (Ru–U)
ignition, 15
Ruthenium braze alloys (Mo–Re–Ru)
patent for, 199
Rutile
electrical conductivity, 189

S

S-1
corrosion, 228
S-291
corrosion, 101
S8DR
fuel, H/Zr-ratio effect on thermal conductivity of, 221
Salts (fused fluoride)
corrosive effects, 103-4
Samarium
oxidation, 27
Samarium sesquioxide mixtures (Sm_2O_3–UO_2)
impaction, 127-28
Samarium sesquioxide systems (Cr_2O_3–Sm_2O_3)
phase studies, 252
Santowax OM
corrosive effects, 230
SAP
(see Aluminum alloys (SAP))
Sapphire single crystals
strengthening with Ti, 252
Saxton Reactor
reactivity, crud effects on, 159
Scandium
diffusion in Ti, 179
Scandium monocarbide solid solutions (ScC–TiC–WC)
formation, 249
Scandium silicide
oxidation, 188
SCb-291
properties, 240
Silicide coatings, 28, 161-62
Silicon
solubility in Pu carbide, 73
Silicon carbide (irradiated)
lattice damage, 187
Silicon coatings
deposition of, 63
Silicon dioxide
self-diffusion in, 54
Silicon monocarbide
compatibility with Pu carbide, 72-73
reactions in liquid media, 116
Silicon monocarbide coatings
deposition on fuel particles, 142
Silicon monocarbide systems (B_4C–SiC–TiC)
properties, high-temperature, 187
Silicon nitride whiskers
metallizing of, 62
Silicon systems (Al–Ge–Si–Ag)
use for brazing, 262
Silicon systems (Al–Ge–Si–Zn)
use for brazing, 262
Silicon systems (C–Si–U)
phase studies, 144
Silicon systems (Cr–Fe–Si–Ti–V)
fused-slurry coatings developed from, 161
Silicon systems (Co–Mo–Si)
phase studies, 242
Silicon systems (Fe–Mo–Si)
phase studies, 242
Silicon systems (Fe–Si–U)
phase studies, 69
Silicon systems (Nb–Si)
hot hardness, 184
mechanical properties, 240
Silicon systems (Si–U)
ignition, 15
Silicon systems (Si–Zr)
use for brazing, 263
Silver
diffusion in Ti, 179
Silver alloys (Ag–U)
ignition, 15
Silver alloys (Cd–In–Ag)(Ni plated) (irradiated)
oxidation and tensile properties, 24
Silver alloys (Cd–In–Ag)(stainless-steel clad)
fabrication, 24
Silver composites (Ag–W)
corrosion, 161
Silver systems (Al–Ge–Si–Ag)
use for brazing, 262
Sintering, 259
162-65, 228-30
Sodium
corrosive effects, 28-29, 32, 96-102, 162-65, 228-30
Sodium alloys (Bi–Na)(molten)
corrosive effects, 103
Sodium alloys (NaK)
corrosive effects, 32
Sodium deuteride
heat of formation, 221
Sodium hydride
heat of formation, 221
Sodium pastes
corrosive effects, 101-2
Solids (irradiated)
rare-gas diffusion in, 213
Stainless steel
B effects on, 246-47
bonding, 262
braze alloys for, 131
carburization, 100
casting of precipitation-hardenable, 122
compatibility with Eu_2O_3, 222-23
corrosion, 26-27, 96, 98, 100, 226
crud deposition on, 159
ductility, ultrasonic-vibration effects on, 121
magnetic force welding, 262
mass transfer, 98-99
melting of precipitation-hardenable, 122
metallurgy, 246-48
Ni_3Ti-particle shape in precipitation-hardened, 246
stress–corrosion cracking, 26, 94
structure, annealing effects on, 121
Ti effects on, 246-47
Stainless-steel (17-4 pH) couples (Al–stainless steel(17-4 pH))
corrosion, 94
Stainless steel (18-10)
mechanical properties, C effects on, 112
Stainless steel (20-25 Nb)
grain growth, Y effects on, 177
Stainless steel (36 NKhTYu)
strength, Mo effects on, 46
Stainless steel (300 series)
sintering, 229-30
Stainless steel (301)
stress-corrosion cracking, 226
Stainless steel (304)
brazing, 263
carbide-particle dispersion in, 246
carburization, 28
cavitation, 30
compatibility with Pu carbide–U carbide system, 12, 207
compatibility with UN, 12
corrosion, 94-95, 101-2, 159-60, 162-63, 231-32
creep properties, 112
fatigue properties, 182
interdiffusion with U_2Ti, 205
mass transfer, 98-99
mechanical properties, N effects on, 177
mechanical properties, Na-exposure effects on, 99
N solubility in, 109, 246
oxide-film structure, 27
rupture, 45
sensitization, 100
stress–corrosion cracking, 159, 226
tensile properties, 244, 248
ultrasonic testing, 264
Stainless steel (304)(irradiated)
damage in, adjacent to UO_2, 171
mechanical properties, 35-36, 170
Stainless-steel (304) brazed joints
nondestructive testing, 264
Stainless-steel (304) couples (Al–stainless steel(304))
corrosion, 94
Stainless-steel (304) couples (Be–stainless steel(304))
stress–corrosion cracking, 94
Stainless-steel (304) dispersions (stainless steel (304)–UO_2)
mechanical properties, 9
Stainless-steel (304) piping
stress–corrosion cracking, 159
Stainless-steel (304) tubing
burst testing, 181
tensile properties, 244
Stainless-steel (304) tubing (irradiated)
mechanical properties, 171
Stainless steel 304L
compatibility with Mo–Pu–U alloys, 6
Stainless steel (304L)(irradiated)
tensile properties, annealing effects on, 104
Stainless steel (310)
mass transfer, 98-99
stress-corrosion cracking, 226
Stainless-steel (310) reduction vessels
cracking, 123
Stainless steel (316)
carburization, 28
cavitation, 30
compatibility with K, 29
corrosion, 28, 103, 162-65, 228
creep properties, 112
mass transfer, 98-99
reaction with In, 230
rupture, 45
stress-corrosion cracking, 226
Stainless steel (316)(irradiated)
ductility, 34
mechanical properties, 171
Stainless-steel (316) weld joints
aging effects, 129
Stainless steel (316L)(irradiated)
bubble formation, 104-5
Stainless steel (318)
creep properties, 112-13
Stainless steel (321)
corrosion, 163
explosive bonding, 64
stress-corrosion cracking, 226

Stainless steel (330)
mass transfer, 98-99
Stainless steel (347)
explosive bonding, 64
mass transfer, 98-99
stress-corrosion cracking, 159
Stainless-steel (347) reduction vessels
performance, 123
Stainless steel (348)
fatigue properties of annealed, 246
Stainless steel (348)(irradiated)
defect clusters and mechanical properties, 174
Stainless steel (400 series)
sintering, 229-30
Stainless steel (406)
corrosion, 226
Stainless steel (410)
corrosion, 163
Stainless steel (416)
corrosion, 94
hot-press bonding to Zircaloy-2, 197
Stainless steel (420)
stress-corrosion cracking, 94
Stainless-steel (420) couples (Al-stainless steel(420))
corrosion, 94
Stainless steel (430)
corrosion, 160
mass transfer, 98-99
Stainless steel (A-286)
precipitation during aging, 176-77
Stainless steel (austenitic)
corrosion, 102
hardness, Ta effects on, 176
mechanical properties, C effects on, 112
phase stability, Ti effects on, 46
properties, 177
Stainless steel (austenitic)(irradiated)
bubble formation, 104-5
ductility, 35
tensile properties, 104
Stainless steel (Cr)
corrosion, 95
Stainless steel (Cr-Fe-Ni)
phase stability, Ti effects on, 46
Stainless steel (Cr-Ni)
corrosion, 95
NbC solubility in, 246
production, 246
Stainless steel (Cr-Ni)(irradiated)
bubble formation, 104-5
Stainless steel (Cr-Ni-Nb)(irradiated)
oxidation, 160
Stainless steel (Cr-Ni-Nb-Y)
corrosion, 226
Stainless steel (F. V. 548)
carbide precipitation, 246
Stainless steel (irradiated)
defect structures, 174
ductility, 34-35, 104
failure, 233
tensile properties, 36-37
Stainless steel (molten)
reaction with water, 166
Stainless-steel cermet pellets (stainless steel-UO_2)
fabrication, 74
Stainless-steel cermet pellets (stainless steel-UO_2)(irradiated)
performance, 74
Stainless-steel cermets (Eu_2O_3-stainless steel)
corrosion, 25
Stainless-steel cermets (Eu_2O_3-stainless steel-TiO_2)
corrosion, 25
Stainless-steel cermets (stainless steel-UO_2)
magnetic force welding, 262
Stainless-steel dispersions (Eu_2O_3-stainless steel)(irradiated)
behavior and burnup of Eu, 222
Stainless-steel dispersions (stainless steel-UO_2)
development, 9
Stainless-steel dispersions (stainless steel-UO_2)(irradiated)
swelling, porosity effects on, 74
Stainless-steel dispersions (stainless steel-UO_2-ZrB_2)(stainless-steel(347)clad)(irradiated)
damage, 208-9
Stainless-steel powder
sintering, 197
Stainless-steel tubing
explosive sizing, 261
thickness measurement using ultrasonics, 64
Steel
chromizing, 63
cladding with Nb, 258
corrosion, 100, 226, 230
electroplating on, 260-61
embrittlement, 46
fatigue, 46
fracture mechanics, 114
fracture toughness, 45
impact strength of welded joints, Al effects on, 46
mass transfer, 99
welding, 199-200
Steel welds
ultrasonic testing, 131
Steel (212B)(irradiated)
failure, catastrophic delayed, 40
Steel (1020)
corrosion, 103
Steel (4340)
drawing, vibration effects on, 124
extrusion, lubricants for, 123
Steel (A 105-II)(irradiated)
mechanical properties, 235
Steel (A-201B) pressure vessels
testing, 182
Steel (A-212B)(irradiated)
annealing kinetics, 236
axial fatigue properties, 169-70
embrittlement, 105
mechanical properties, 235
yield-strength recovery, 234
Steel (A-302B)
fracture toughness, 180-81
Steel (A-302B)(irradiated)
embrittlement, 105, 234
mechanical properties, 169, 235
Steel (A-302B) pressure vessels
testing, 182
Steel (A-302YB)
tempering, 245-46
Steel (A-350F1(modified))(irradiated)
embrittlement, 105
Steel (A-350LF3)(irradiated)
embrittlement, 105
Steel (A-387D) pressure vessels
testing, 182
Steel (Al-Ni)
welding, 199
Steel (AMS 6435)
welding, 199
Steel (austenitic)
corrosion, 96, 98, 102
development of high-strength, 109
fretting, 100
hardening by precipitation, 177
Steel (carbon)
cavitation, 30
corrosion, 95, 102
Steel (carbon)(irradiated)
corrosion, 226
electrical resistivity, 106
embrittlement, 105
Steel (carbon) tubing
corrosion, 159
Steel (Cr)
corrosion, 96, 98
decarburization, 98
Steel (Cr-Co-Mo-Ni)
welding, 199
Steel (Cr-Mo)
mechanical properties, Na effects on, 28
Steel (Cr-Mo-Ni)
embrittlement of welded joints, 46
Steel (Cr-Ni)
sigma-phase precipitation, (Fe,Cr), 109
Steel (Cr-Ni-Si)
corrosion, 96, 98
Steel (Croloy 2 1/4)
corrosion, 162-63
Steel (D-6ac)
welding, 199
Steel (ferritic)
corrosion, 96, 98, 100, 162
development, 100
mechanical properties, Na effects on, 28
Steel (Fortiweld)(irradiated)
transition temperature, B effects on, 235
Steel (high alloy)
development of high-strength, 109
Steel (high strength)
development, 109
welding, 64, 199
Steel (HP-9-4-20)
welding, 199
Steel (HP-9-4-25)
welding, 199
Steel (HY-80)(irradiated)
embrittlement, 105
Steel (HY-180/210)
welding, 199
Steel (low alloy)
corrosion, 95
decarburization, 98
development, 109
improvements, 46
precipitation strengthening, 245
welding, 199
Steel (low alloy)(irradiated)
embrittlement, 105
fatigue properties, 105
tensile properties, 40
Steel (low carbon)
compatibility with Bi-Pb alloy, 30
corrosion, 103
impact strength, U effects on, 46
Zr solubility on, 46
Steel (low carbon)(irradiated)
fatigue properties, 105
Steel (low carbon) tubes
failure, 46
Steel (Mn)(irradiated)
fatigue properties, 105
Steel (Mn-Mo)
notch toughness, 46
Steel (maraging)
fracture toughness, 45
Steel (martensitic)
welding, 199
Steel (mild)
corrosion, 27
hot-press bonding to Al, 197
Steel (mild)(irradiated)
damage, 42
Steel (Ni)
welding, 199-200
Steel (Nb stabilized)
decarburization, 98
Steel (pressure vessel)
metallurgy, 245-46

Steel (pressure vessel)(irradiated)
properties, 234-36
Steel (SA-192) tubing
corrosion, 159
Steel (SA-212B)(irradiated)
fatigue properties, 105
Steel (SA-302B)(irradiated)
fatigue properties, 105
Steel (Si-killed carbon)(irradiated)
annealing kinetics, 236
Steel (T-1) pressure vessels
testing, 182
Steel (Ti stabilized)
decarburization, 98
Steel (tool)
corrosion, 229
Steel (Vascojet X2)
welding, 199
Steel joints
hot pressing, 260
Stellite-3
corrosion, 229
Stellite 6B
corrosion, 164, 229
Structural materials, 26-58, 93-120, 158-93, 225-56
Superalloys
deformation, 111
Sylcor Sn–Al coatings
for Nb–Zr alloys, 162
Sylvania A
creep-rupture properties, 43

T

T-111
annealing, 178
cavitation, 30
corrosion, 100-1
tensile properties, aging effects on, 240
welding, 130
T-222
cavitation, 30
coatings for, 162
corrosion, 101, 164
creep-rupture properties, 42-43
tensile properties, aging effects on, 240
T-222 (disilicide coated)
oxidation, 28
T-222 sheets
explosive bonding, 64
Tantalum
ablation, 161
absorption of O and water, 227
brazing, 263
coating, 198-99
compatibility with Li, 30
corrosion, 27, 31, 100-3
diffusion, 54
extrusion, 125
hydriding, destructive, 29
H solubility in, 110-11
interdiffusion with Ir, 180
magnetic force welding, 262
oxidation, 95, 160-61, 227
reaction with N, 227
solubility in molten Pu, 4, 205
strain aging, effect of stress on, 111-12
Ta_2O_5-scale formation on, 227
Tantalum (coated)
oxidation, 96, 228
Tantalum (irradiated)
hardness, 173
Tantalum-alloy coatings (Hf–Ta)
for Ta–W alloys, 228
Tantalum-alloy sheets (Nb–Ta)
explosive bonding, 64
Tantalum alloys
(see FS-60, T-111, and T-222)
age-hardenable, 111
coating, 27-28, 161-62, 198-99, 227
fabricability, 49-50
grain growth, Y and rare-earth effects on, 178
mechanical properties, 49, 242
physical properties, 242
tensile properties, aging effects on, 239-40
Tantalum alloys (Cr–Ta)
creep properties, N effects on, 183
Tantalum alloys (Hf–Mo–Ta)
oxidation, 222
Tantalum alloys (Hf–Ta)
hardness, oxidation, and phase studies, 222
Tantalum alloys (Hf–Ta coated)
oxidation, 227
Tantalum alloys (Hf–Ta–W)
thermal conductivity, 110
Tantalum alloys (Hf–Ta–Zr)
oxidation, 222
Tantalum alloys (Mo–Nb–Ta–W)
creep mechanism, 50-51
Tantalum alloys (Mo–Ta–V)
phase studies, 243
Tantalum alloys (Nb–Ta)
properties and structure, 238-39
Tantalum alloys (Nb–Ta–V)
mechanical properties, 242
phase studies, 243
physical properties, 242
strength, 43
Tantalum alloys (Re–Ta)
H solubility in, 111
Tantalum alloys (Ta–W)
brazing, 263
coatings for, 162, 227-28
corrosion, 31
fabricability, 50
mechanical properties, 242
physical properties, 242
strength, 50
weldability, 50
Tantalum alloys (Ta–W)(coated)
oxidation, 27, 228
Tantalum alloys (Ta–U)
ignition, 15
Tantalum alloys (Ta–V)
solid-state transformations, 243
Tantalum braze alloys (Ta–Ti–V)
patent for, 199
Tantalum carbide
C diffusion in, 179
reaction with Re, 251
stoichiometry, 186
Tantalum composites (graphite–Ta)
hot pressing, 20
Tantalum composites (Ta–W–Zr)
strength, 183
Tantalum diboride
thermal expansion, 223
Tantalum diboride systems (Cr–TaB_2–ZrB_2)
fabrication and properties, 252
Tantalum dioxide
formation, 227
Tantalum monocarbide
deformation, 116
elastic properties, 115
electrical resistance, 115, 251
oxidation, Cu and Ag effects on, 252
thermal properties, 251-52
Tantalum monocarbide (irradiated)
behavior, 187-88
Tantalum monocarbide castings
hot hardness, 59, 250
oxidation, 59
Tantalum monocarbide single crystals
growth parameters, 59
Tantalum monocarbide-system castings (C–TaC)
hardness and stress relieving, 186
Tantalum monocarbide systems (C–TaC)
eutectic temperature, 186
melting and casting, 257
properties, 257
Tantalum monocarbide systems (Co–TaC–WC)
properties and structure, 186
Tantalum monocarbide systems (HfC–TaC)
fusion point, 250-51
Hall constant, 250
resistivity, 250
Tantalum monocarbide systems (TaC–ZrC)
fusion point, 250-51
Tantalum monoxide
formation, 227
Tantalum oxide
composition, 227
evaporation of volatile, 227
structure, 227
Tantalum oxide (Ta_2O_5)
scale formation on Ta, 227
Tantalum single crystals
oxidation, 95
Tantalum systems (C–Hf–Ta)
phase studies, 51
Tantalum tubing
fabrication, 196
TD-50
use for brazing; 263
Terbium
oxidation, 27
Terbium oxide
self-diffusion in, 54
Terphenyls
corrosive effects, 93, 230
Testing (nondestructive), 64-65, 131-32, 200, 264
Thermal-wave transducers
use in nondestructive testing, 200
Thorium
compatibility studies, 74, 180
diffusion in, 208
heat content, 8
heat of fusion, 8
heat of phase transformation, 8
thermal conductivity, 74
utilization, 8
Thorium (molten)
heat content, 8
Thorium-alloy particles (Th–U)(coated)
use at high temperatures, 142-43
Thorium alloys (Be–Th)
hot hardness, 8
Thorium alloys (Pu–Th–U)
liquidus surface and phase studies, 8
Thorium alloys (Pu–Th–U)(irradiated)
burnup, 8
Thorium alloys (Pu–Th–U)(Ti–V alloy clad)(irradiated)
behavior, 205
Thorium alloys (Th–U)(irradiated)
annealing effects on, 8
Thorium alloys (Th–U)(Ti–V alloy clad)(irradiated)
behavior, 205
Thorium alloys (Th–U–Zr)(Zircaloy-2 clad)(irradiated)
behavior, 141, 208
Thorium alloys (Th–Zr)
hot hardness, 8
Thorium boride
thermal expansion, 146
Thorium carbide
thermal expansion, 146

Thorium carbide-system fuel particles (Th carbide–U carbide)(PyC coated) (irradiated)
performance, 143
Thorium composites (graphite–Th)
hot pressing, 20
Thorium compounds (refractory)
thermal expansion, 146
Thorium dicarbide particles (PyC coated) (irradiated)
performance, 143
Thorium dicarbide-system particles (ThC_2–UC_2)(PyC coated)
use at high temperatures, 142
Thorium dicarbide-system particles (ThC_2–UC_2)(PyC coated)(irradiated)
stability, 10-11
Thorium dioxide
corrosion, 31
extrusion, 209
thermal conductivity, 143
thermal expansion, 146
thermodynamic data, 75-76
Thorium dioxide (irradiated)
rare-gas behavior in, 213
Thorium dioxide coatings
for Ta–W alloys and W, 227-28
Thorium dioxide composites (ThO_2–W)
corrosion, 161
Thorium dioxide-dispersion sheet (Ni–ThO_2)
cold rolling and annealing, 177
Thorium dioxide microspheres
preparation, 12
Thorium dioxide mixtures (PuO_2–ThO_2)
preparation, 7
Thorium dioxide mixtures (ThO_2–UO_2)
impaction, 127-28
Thorium dioxide particles (PyC coated) (irradiated)
performance, 143
Thorium dioxide pellets
fabrication, 12
Thorium dioxide powder
sintering, TiO_2-addition effects on, 144
Thorium dioxide-system particles (ThO_2–UO_2)(PyC coated)(irradiated)
stability, 10-11
Thorium dioxide systems (O_2–ThO_2–UO_2)
thermal conductivity, 143
Thorium dioxide systems (ThO_2–W)
creep–rupture properties, 43
tensile properties, 44
Thorium dioxide systems (ThO_2–UO_2)
compatibility with Th, 74
thermal conductivity, 11-12, 143
Thorium dioxide tubes
fabrication by slip casting, 144
Thorium monocarbide
reaction with Au, 209
Thorium monocarbide-mixture powders
sintering, 211
Thorium monocarbide systems (ThC–UC)
compatibility with Th, 74
Thorium mononitride
thermal expansion, 146
Thorium mononitride-mixture powders
sintering, 211
Thorium monosulfide
thermal expansion, 146
Thorium phosphide
thermal expansion, 146
Thorium systems (C–Th)
phase studies, 8, 74
properties, 209-10
Thorium tetrafluoride systems (BeF_2–LiF–ThF_4–UF_4–ZrF_4)(molten)
corrosive effects, 103
Thornel composites (Co–Thornel)
fabrication by hot isostatic pressing, 198
Thulium
oxidation, 27
solubility in molten Pu, 139
Tin alloys (Al–Mo–Sn–Zr)
corrosion, 229
Tin alloys (Al–Sn–Ti)
reaction with H, 221
Tin alloys (Bi–Ni–Sn)
wear, 225
Tin alloys (Cr–Fe–Nb–Sn–Zr)
corrosion, 225
Tin alloys (Fe–Ni–Nb–Sn–Zr)
hydriding, 230
Tin alloys (Nb–Sn–Zr)
corrosion, 93, 225
Tin composites (Al–Sn–W)
corrosion, 161
Titanium
bonding, 262
compatibility with metals, 180
corrosion, 95, 100
diffusion in Ti–V alloys, 179
explosive spot welding, 64
melting, 60, 194
reaction with H, 220-21
Sc diffusion in, 179
Ag diffusion in, 179
stress–corrosion cracking, 95
U diffusion in, 135
Titanium-alloy sheet (Cr–Ti–V)
tensile properties, 243-44
Titanium-alloy sheet (Ti–V)
tensile properties, 243-44
Titanium-alloy tubing (Cr–Ti–V)
burst testing, 181-82
fabrication, 196, 257
tensile properties, 244
Titanium-alloy tubing (Ti–V)
drawing, 122-23
Titanium alloys
corrosion, 95
fracture toughness, 45
stress–corrosion cracking, 95
Titanium alloys (Al–Cr–Ni–Ti)
crystal structure, W effects on, 177
Titanium alloys (Al–Nb–Ti)
mechanical properties, 113
Titanium alloys (Al–Sn–Ti)
reaction with H, 221
Titanium alloys (Al–Ti–V)
drawing, vibration effects on, 124
reaction with H, 220-21
strength, 43
Titanium alloys (Be–Ti)
phase studies, 21
Titanium alloys (Cr–Ti–V)
compatibility with PuC–UC mixtures, 73
corrosion, 163, 228
tensile properties, 114
Titanium alloys (Cr–Ti–V)(irradiated)
tensile properties, 234
Titanium alloys (Hf–Nb–Ti–W)
mechanical properties and oxidation, 49
Titanium alloys (Fe–Ti)
tensile properties, 248
Titanium alloys (Mo–Nb–Ti–U–Zr)
tensile properties, 137
Titanium alloys (Mo–Ti)
aging, 111
cavitation, 30
extrusion, lubricants for, 123
recrystallization temperature, 241
rupture strength, 241
Titanium alloys (Mo–Ti–Zr)
corrosion, 161
phase studies, 111
Titanium alloys (Nb–Ti)
corrosion, 101
elastic properties, 238
Titanium alloys (Nb–Ti–V)
strength, 43
Titanium alloys (Nb–Ti–Zr)
corrosion, 164
Titanium alloys (Pu–Ti–U)
phase studies, 5
properties, 138
solid-state reactions, 5
thermal conductivity, 5
thermal properties, 72
Titanium alloys (Pu–Ti–U)(Ti–V-alloy clad) (irradiated)
behavior, 138-39
Titanium alloys (Ti–W–Zr)
phase studies, 243
Titanium alloys (Ti–U)
ignition, 15
Titanium alloys (Ti–V)
corrosion, 99, 163-64, 228
mechanical properties, Na-exposure effects on, 99
production, 122
Ti diffusion in, 179
V diffusion in, 179
Titanium alloys (Ti–V)(irradiated)
tensile properties, 41, 234
Titanium braze alloys (Ta–Ti–V)
patent for, 199
Titanium carbide
oxidation, 229
reactions in liquid media, 116-17
stoichiometry, 186
Young's modulus, 115
Titanium composites
hot pressing, 20, 198
Titanium diboride
reactions in liquid media, 116-17
thermal expansion, 223
Titanium dioxide
reaction with TiC, 251-52
Titanium dioxide cermets (Eu_2O_3–stainless steel–TiO_2)
corrosion, 25
Titanium dioxide mixtures (Eu_2O_3–TiO_2)
corrosion, 25
Titanium hydride
lattice parameters, 157
Titanium hydride (irradiated)
strength, 89
Titanium hydride systems (Ti hydride–V)
production, 89
Titanium intermetallic compounds (U_2Ti)
interdiffusion with stainless steel (304), 205
Titanium monocarbide
elastic properties, 115
reactions in liquid media, 116
reaction with TiO_2, 251-52
Titanium monocarbide (irradiated)
behavior, 187-88
Titanium monocarbide castings
hot hardness, 250
oxidation, 250-51
Titanium monocarbide solid solutions (ScC–TiC–WC)
formation, 249
Titanium monocarbide systems (B_4C–SiC–TiC)
properties, high-temperature, 187
Titanium monocarbide systems (C–TiC)
strength, 187
Titanium monocarbide systems (Co–TiC–WC)
properties, C effects on, 249
strength, 187
Titanium monocarbide systems (TiC–WC)
properties, Cr_2C_3-addition effects on, 115
Titanium nitride
reactions in liquid media, 116-17

Titanium oxide
self-diffusion in, 54
Titanium solid solutions (Nb–Ti–V)
oxidation, 95
Titanium systems (Al–C–Cr–Co–Ni–Ti)
sigma-phase formation, 248
Titanium systems (C–Nb–Ti)
phase studies, 51
Titanium systems (C–Ti–U)
phase relations, PuC-addition effects on, 77
Titanium systems (Cr–Fe–Si–Ti–V)
fused-slurry coatings developed from, 161
Transducers (thermal wave)
use in nondestructive testing, 200
Transition-metal carbides
elastic properties, 115
reactions with oxides, 251-52
Transition-metal diborides
thermal conductivity, 222
Transition-metal oxides
reactions with carbides, 251-52
Transition metals
conductivity, electrical and thermal, 222
Tubing
eddy-current testing, 65, 132
fabrication, 124-25, 196
Tungsten
brazing, 199, 263
C solubility in, 241
corrosion, 31, 103, 161, 229
creep-rupture properties, 43
deposition, 126-27, 198, 260
diffusion, 54
diffusion bonding, 180, 260
electron-beam melting, 194
extrusion, lubricants for, 123
fractographic studies, 52
Gd solubility in, 91
grain refinement, additive effects on, 121
HfO_2 coatings for, 227-28
magnetic force welding, 262
mechanical properties, 53, 111, 178-79, 242
metallurgy, 242-43
oxidation, 96, 161, 226-27
permeability of sintered, 197
properties of vapor-deposited, 195
reaction with UC, 145
reactions with UC–ZrC system, 145
recrystallization, annealing effects on, 111
self-diffusion in, 180
solubility in molten Pu, 4, 205
surface diffusion in, 180
tensile properties, 44
thermal conductivity, 242
ThO_2 coatings for, 227-28
volatilization, 227
Young's modulus, 115
zone melting, 194
Tungsten (Durak B coated)
corrosion, 161
Tungsten (fluoride coated)
oxidation, 96
Tungsten (Hf–Ir–Ta coated)
oxidation, 227
Tungsten (irradiated)
dislocation loops, 174
electrical conductivity, 173
Tungsten (thoriated)
magnetic force welding, 262
Tungsten (ZrB_2 coated)
corrosion, 161
Tungsten-alloy tubing
fabrication, 60-61, 124-25, 196-97
Tungsten alloys
compatibility with LiH, 221
creep-rupture properties, 43
deposition, 126, 198-99
development, 52
extrusion, lubricants for, 123
fabrication, 52
preparation, 52
Tungsten alloys (Cr–W)
decomposition, 111
Tungsten alloys (Cr–W–Y)
tensile properties, 237
Tungsten alloys (Hf–Nb–Ti–W)
mechanical properties and oxidation, 49
Tungsten alloys (Hf–Ta–W)
thermal conductivity, 110
Tungsten alloys (Ir–W)
powder metallurgy, 197
Tungsten alloys (Fe–Ni–W)
fabricability, 52
Tungsten alloys (Mo–Nb–Ta–W)
creep properties, 50-51
Tungsten alloys (Mo–Re–W)
creep properties, 183-84
development, 179
ductility, 52
mechanical properties, 242
physical properties, 242
powder metallurgy, 124
Tungsten alloys (Mo–W)
corrosion, 103
diffusion studies, 54
preparation by vapor deposition, 198
Tungsten alloys (Nb–W)
diffusion in, 180
oxidation, 161
thermal conductivity, 110, 178
Tungsten alloys (Nb–W–Zr)
Be-induced second phase, annealing effects on, 111
Tungsten alloys (Re–W)
corrosion, 101
deposition, 126-27, 198, 260
diffusion, 54
ductility, ThO_2-dispersion effects on, 52
emissivity, 110
evaluation for ionizer applications, 259
fractographic studies, 52
mechanical properties, 242
physical properties, 242
powder metallurgy, 124, 197
reactions with UC, 145
reactions with UC–ZrC system, 145
thermal conductivity, 110
Tungsten alloys (Ta–W)
brazing, 263
coatings for, 162, 227-28
corrosion, 31
fabricability, 50
mechanical properties, 242
physical properties, 242
strength, 50
weldability, 50
Tungsten alloys (Ta–W)(coated)
oxidation, 27, 228
Tungsten alloys (TCD)
creep-rupture properties, 43
Tungsten alloys (Ti–W–Zr)
phase studies, 243
Tungsten billets
evaluation for forging, 60
Tungsten carbide-powder mixtures (Co–W carbide)
compacting and sintering, 61
Tungsten cermets (W–UO_2)
magnetic force welding, 262
Tungsten cladding
deposition on U–Zr carbides, 63
Tungsten coatings
deposition of, 63
Tungsten composites
corrosion, 161
extrusion of fibered, 111
strength, 183
Tungsten dioxide
volatilization, 227
Tungsten dispersions
stability, 43-44
strength, 183
Tungsten honeycomb (W–UO_2)
fabrication, 127
Tungsten ingots
preparation, 242
Tungsten monocarbide
corrosion, 229
preparation, 115
properties, 115
Tungsten monocarbide (irradiated)
behavior, 187-88
Tungsten monocarbide solid solutions (ScC–TiC–WC)
formation, 249
Tungsten monocarbide solid solutions (ScC–WC)
formation, 249
Tungsten monocarbide systems (Co–TaC–WC)
properties and structure, 186
Tungsten monocarbide systems (Co–TiC–WC)
properties, C effects on, 249
strength, 187
Tungsten monocarbide systems (Co–WC)
macrostresses in, 249
properties of sintered, 115
strength, 187
Tungsten monocarbide systems (TiC–WC)
properties, Cr_2C_3-addition effects on, 115
Tungsten oxide ($W_{18}O_{49}$)
volatilization, 227
Tungsten powder
consolidation, 125, 259
Tungsten sheet
fabrication, 258-59
grains in, 242-43
joining by vapor deposition, 198
mechanical properties, 114
preparation, 242
properties, 183
Tungsten single-crystal sheet
fabrication, 60
Tungsten single crystals
ductile–brittle transition, 44-45
mechanical properties, impurity effects on, 51-52
Tungsten systems
(see Sylvania A)
Tungsten systems (C–Hf–W)
fabrication and preparation, 52
Tungsten systems (C–Mo–W–Y)
corrosion, 161
Tungsten systems (C–Nb–W)
fabrication and preparation, 52
Tungsten systems (C–W–Zr)
fabrication and preparation, 52
Tungsten systems (LaB_6–W)
phase studies and physical properties, 243
Tungsten systems (ThO_2–W)
creep-rupture properties, 43
tensile properties, 44
Tungsten trioxide
volatilization, 227
Tungsten tubing
fabrication, 60-61, 124, 196-97
production by vapor deposition, 198
Tungsten wire
stress–rupture properties, 114
TZC
fatigue, 42
TZM
corrosion, 101, 164
fatigue, 42

pack-cementation-coating processes for, 198
TZM sheet
mechanical properties, 114
properties, 183

U

Udimet 500
mechanical properties, 47
Ultrasonic testing, 64, 131, 200, 264
UMCO-51
corrosion, 228
Uranium
arc melting, 257
compatibility with metals, 180
compressive behavior, 135
creep properties, 1, 69
density, heat-treatment effects on, 2
development review, 71
diffusion in metals, 135
diffusion in Th, 208
diffusion in UO_2, 73, 76
electrodeposition, 63, 127
electroplating Ni on, 261
electropolishing, 199, 203
extrusion, 203
flow, grain-size effects on, 2
fracture stress, grain-size effects on, 2
heat capacity, 135
ignition, 15
inclusions in, identification of, 1, 69
interdiffusion with Be, 1
interdiffusion with Cu, 203
metallography, electron, 69
microstructure, 1
oxidation, 15, 69, 203
phase transformation, 1-2, 135
pitting, 2
plastic deformation, 2
production, 135
reaction with steam, 14
reaction with water, 14-15, 78-79
texture, 135
Wiedeman–Franz ratio, 135
zone refining, 135
Uranium (adjusted)
density, heat-treatment effects on, 2
hot hardness, 69
phase transformation, 69, 71
thermal conductivity, 2
Uranium (enriched)(irradiated)
swelling, 1-2
Uranium (irradiated)
cracking, grain-boundary, 1
creep, 69
fission-gas bubbles in, 148
growth, 69
properties, 15-16
reaction with water, 78
swelling, 3-4, 136-37, 212
U-atom emission, 80
Uranium (molten)
corrosive effects, 31, 166
penetration of Armco Fe by, 135
reaction with water, 14
Uranium (molten)(irradiated)
radioiodine release, 212
Uranium-alloy particles (Th–U)(coated)
use at high temperatures, 142-43
Uranium-alloy plates (Al–U)
preparation of, containing Al–B_4C-dispersion foils, 91
Uranium-alloy plates (Al–U)(irradiated)
performance of, containing Al–B_4C-dispersion foils, 91
Uranium alloys
(see also Uranium (adjusted))
creep, microstructure effects on, 4
development review, 71
hot hardness of dilute, 203
ignition, 15
oxidation, 15, 69
phase transformation, 71
recrystallization of dilute, 203
texture evaluation, 69
Uranium alloys (Al–Fe–U)
phase studies, 69
Uranium alloys (Al–U)
ignition, 15
oxidation, 69
production, 121, 137-38, 194
Uranium alloys (Cr–U)
ignition, 15
pearlitic reaction, 4
Uranium alloys (Co–Fe–U)
phase studies, 71
Uranium alloys (Fe–U)(molten)
penetration of Armco Fe by, 135
Uranium alloys (irradiated)
swelling, 3-4, 136-37
Uranium alloys (Mo–Nb–Ti–U–Zr)
tensile properties, 137
Uranium alloys (Mo–Pu–U)
compatibility with stainless steel 304L and thermal expansion, 6
Uranium alloys (Mo–U)
brazing, 263
ignition, 15
structure, 4, 135
Uranium alloys (Mo–U)(irradiated)
properties, 16
Uranium alloys (Nb–U)
ignition, 15
metastable phases, 204
tensile properties, 71
Uranium alloys (Nb–U–Zr)
phase transformation, 71
reaction with water, 15
Uranium alloys (Nb–U–Zr)(Zircaloy-2 clad)(irradiated)
performance, 71
Uranium alloys (Pu–Th–U)
liquidus surface and phase studies, 8
Uranium alloys (Pu–Th–U)(irradiated)
burnup, 8
Uranium alloys (Pu–Th–U)(Ti–V alloy clad)(irradiated)
behavior, 205
Uranium alloys (Pu–Ti–U)
phase studies, 5
properties, 138
solid-state reactions, 5
thermal conductivity, 5
thermal properties, 72
Uranium alloys (Pu–Ti–U)(Ti–V-alloy clad)(irradiated)
behavior, 138-39
Uranium alloys (Pu–U)
development for fast breeder fuel, 5
elastic modulus, 6
thermal properties, 71
Uranium alloys (Pu–U–Zr)
phase studies, 205
preparation, 205
properties, 138
thermal conductivity, 5
Uranium alloys (Pu–U–Zr)(Ti–V-alloy clad)(irradiated)
behavior, 138-39
Uranium alloys (Re–U)
structure and transformation, 204
Uranium alloys (Th–U)(irradiated)
annealing effects on, 8
Uranium alloys (Th–U)(Ti–V-alloy clad)(irradiated)
behavior, 205
Uranium alloys (Th–U–Zr)(Zircaloy-2 clad)(irradiated)
behavior, 141, 208
Uranium alloys (U–V)
grain refinement and mechanical properties, 203-4
Uranium alloys (U–Zr)
ignition, 15
structure, 4
Uranium aluminide
preparation, 121
Uranium aluminide dispersions (Al–U aluminide)(irradiated)
swelling, porosity effects on, 74
Uranium billets
production of coextrusion, 257
Uranium carbide
preparation, 59
Young's modulus, 115
Uranium carbide-mixture powders
sintering, 211
Uranium carbide pellets
preparation from powder, 78
Uranium carbide-system fuel particles (Th carbide–U carbide)(PyC coated)(irradiated)
performance, 143
Uranium carbide systems (Pu carbide–U carbide)
compatibility with Fe alloys, 12
compatibility with stainless steel (304), 207
preparation, 73
Uranium carbide systems (Pu carbide–U carbide)(irradiated)
behavior, 207
Uranium carbide systems (U carbide–Zr carbide)
cladding with W by vapor deposition, 63
Uranium castings
production, 195
Uranium composites (graphite–U)
hot pressing, 20
Uranium crystals
electrical resistivity and growth, 135
Uranium crystals (irradiated)
electrical resistivity, 135, 148
Uranium diboride
compatibility with Th, 74
Uranium dicarbide
energy of formation, 12-13
thermal expansion, 13
Uranium dicarbide particles
corrosion by HCl, 10
production of porous spherical, 211
use at high temperatures, 142
Uranium dicarbide particles (PyC coated)(irradiated)
stability, 10-11
Uranium dicarbide-system particles (ThC_2–UC_2)(PyC coated)
use at high temperatures, 142
Uranium dicarbide-system particles (ThC_2–UC_2)(PyC coated)(irradiated)
stability, 10-11
Uranium dioxide
CeO_2 thermal diffusion in, 209
extrusion, 209
heat capacity, 11
heat transfer, 75
impaction, 127-28
Pu diffusion in, 73
reaction with steam, 147, 211
self-diffusion in, 54
thermal conductivity, 12, 75, 143

thermodynamic data, 75-76
U diffusion in, 73, 76
Uranium dioxide (irradiated)
compatibility with Na, 29
fission-product behavior, 75, 149, 211-14
fission products in, of mass 140, 80
heat transfer, 75
inclusions in, microanalysis of, 214
knock-out for fission fragments, 75
porosity, 149
thermal conductivity, 75, 149
U-atom emission, 80, 143-44, 214
U self-diffusion in, metal-addition effects on, 149
Uranium dioxide (molten)
reaction with water, 147
Uranium dioxide (molten)(irradiated)
vaporization, 212
Uranium dioxide (Nb coated)(irradiated)
swelling, 214
Uranium dioxide (Nb–Zr-alloy clad)
corrosion, 31
Uranium dioxide (refractory-material clad)
diffusion studies, 54
Uranium dioxide (Zircaloy-2 clad)(molten)
reactions with water, 167
Uranium dioxide–cermet pellets (stainless steel–UO_2)
fabrication, 74
Uranium dioxide–cermet pellets (stainless steel–UO_2)(irradiated)
performance, 74
Uranium dioxide cermets (stainless steel–UO_2)
magnetic force welding, 262
Uranium dioxide cermets (W–UO_2)
magnetic force welding, 262
Uranium dioxide coatings
vapor plating of, 63
Uranium dioxide dispersions (Al–UO_2)(irradiated)
swelling, 74, 214
Uranium dioxide dispersions (Al–UO_2–ZrO_2)(Al clad)(irradiated)
stability, 9
Uranium dioxide dispersions (BeO–UO_2)(irradiated)
fission-product retention, 156
Uranium dioxide dispersions (stainless steel–UO_2)
development, 9
Uranium dioxide dispersions (stainless steel–UO_2)(irradiated)
swelling, porosity effects on, 74
Uranium dioxide dispersions (stainless steel–UO_2–ZrB_2)(stainless-steel(347) clad)(irradiated)
damage, 208-9
Uranium dioxide dispersions (stainless steel(304)–UO_2)
mechanical properties, 9
Uranium dioxide films (irradiated)
fission-fragment damage, 16-17
Uranium dioxide honeycomb (W–UO_2)
fabrication, 127
Uranium dioxide microspheres
Pu pickup, 206
preparation, 12
Uranium dioxide mixtures (PuO_2–UO_2)
preparation, 7
Uranium dioxide mixtures (PuO_2–UO_2)(irradiated)
behavior, 141
compatibility with Na, 29
Uranium dioxide mixtures (Sm_2O_3–UO_2)
impaction, 127-28
Uranium dioxide mixtures (ThO_2–UO_2)
impaction, 127-28
Uranium dioxide particles
fabrication, 76
Ni coatings, application of, 10
Uranium dioxide particles (PyC coated)(irradiated)
stability, 10-11
Uranium dioxide pastes (Na–UO_2)
corrosive effects, 101-2
Uranium dioxide pellets
N release from sintered, 11
Uranium dioxide plates
production, 76
Uranium dioxide powder
production, 209
sintering, 61, 76, 144
Uranium dioxide single crystals (irradiated)
^{85}Kr diffusion in, 16
Uranium dioxide solid solutions (PuO_2–UO_2)
oxidation, 7
Uranium dioxide–system particles (ThO_2–UO_2)(PyC coated)(irradiated)
stability, 10-11
Uranium dioxide–system pellets (PuO_2–UO_2)
preparation by sintering, 74
Uranium dioxide–system rods (CaO–UO_2–ZrO_2)
fabrication, 12
Uranium dioxide–system rods (UO_2–ZrO_2)
fabrication, 12
Uranium dioxide systems (BeO–PuO_2–UO_2)
phase studies, 140
Uranium dioxide systems (CeO_2–UO_2)
diffusion in, 180
Uranium dioxide systems (O_2–ThO_2–UO_2)
thermal conductivity, 143
Uranium dioxide systems (PuO_2–UO_2)
phase studies, 73
Uranium dioxide systems (PuO_2–UO_2)(irradiated)
fission-product behavior, 214
Uranium dioxide systems (PuO_2–UO_2)(stainless-steel (316) clad)(irradiated)
properties, 7
Uranium dioxide systems (ThO_2–UO_2)
compatibility with Th, 74
thermal conductivity, 11-12, 143
Uranium dioxide systems (U–UO_2)
phase studies, 136
Uranium dioxide systems (UO_2–ZrO_2)
thermal conductivity, 143
Uranium dispersions (U–UC)(Zircaloy-2 clad)(irradiated)
stability, 2-3
Uranium fuel materials (irradiated)
properties, 2, 138, 205
Uranium hydride
reaction with water, 79
Uranium ingots
production, 257
Uranium intermetallic compounds
preparation and testing, 121
Uranium intermetallic compounds (UAl_2)(irradiated)
swelling, 214
Uranium intermetallic compounds (UAl_3)(irradiated)
swelling, 214
Uranium intermetallic compounds (U_2Tl)
interdiffusion with stainless steel (304), 205
Uranium isotopes (^{235}U)
charged-particle emission, 213
Uranium monoarsenide
crystal structure, melting point, and solubility in UP and US, 77
Uranium monocarbide
C activity in, 77
compatibility with cladding materials, 77
elastic properties, 115
elongation, 145
energy of formation, 12-13
hydrolysis, O-addition effects on, 77
impaction, 127-28
oxidation, 12
powder metallurgy, 61
preparation, 77-78, 211
PyC coatings, application of, 10
reaction with Au, 209
reaction with Ir, 209
reaction with N, 77, 207
reaction with Re, 145
reaction with Re–W alloy, 145
reaction with Rh, 209
reaction with SAP, 209
reaction with W, 145
zone melting, 59
Uranium monocarbide (irradiated)
gas-bubble dragging, 213
microstructure, 145-46
performance, 77, 210
porosity, 149
rare-gas diffusion in, 213
swelling, 13
Uranium monocarbide (SAP clad)(irradiated)
performance, 77
Uranium monocarbide (stainless-steel clad)(irradiated)
performance, 77, 210
Uranium monocarbide coatings
vapor plating of, 63
Uranium monocarbide crystals
preparation, 121
Uranium monocarbide dispersions (U–UC)(Zircaloy-2 clad)(irradiated)
stability, 2-3
Uranium monocarbide mixtures (PuC–UC)
compatibility with cladding materials, 73
Uranium monocarbide particles (carbide coated)
use at high temperatures, 142
Uranium monocarbide pastes (Na–UC)
corrosive effects, 101-2
Uranium monocarbide powder
sintering, 211
Uranium monocarbide single crystals (irradiated)
^{85}Kr diffusion in, 16
Uranium monocarbide solid solutions (UC–UN)
phase relations, U oxide effects on, 77
Uranium monocarbide–system particles (UC–ZrC)(PyC coated)
use at high temperatures, 142
Uranium monocarbide–system powder (UC–UN)
sintering, 211
Uranium monocarbide systems (PuC–PuN–UC–UN)
phase studies, 144-45
Uranium monocarbide systems (PuC–UC)
compatibility with cladding materials, 77
phase studies, 144-45
Uranium monocarbide systems (PuC–UC)(clad)(irradiated)
stability, 13, 210
Uranium monocarbide systems (PuC–UC)(irradiated)
behavior, 210
Uranium monocarbide systems (PuN–UC)
phase studies, 144-45
Uranium monocarbide systems (ThC–UC)
compatibility with Th, 74
Uranium monocarbide systems (UC–UN)
phase studies, 144-45
Uranium monocarbide systems (UC–ZrC)
preparation, 211
production, 13

reactions with Mo, Re, Re–W alloy, and W, 145
Uranium monocarbide systems (UC–ZrC) (refractory-material clad)
diffusion, 54
Uranium monocarbide systems (UC–ZrC) (W clad)
electron emission, 145
Uranium mononitride
compatibility with metals and alloys, 12
evaporation, 210
impaction, 127–28
Mo solubility in, 77
O solubility in, 145
preparation, 13
production, 211
reaction with Au, 209
sublimation, 12
Uranium mononitride (irradiated)
fission-gas-bubble sizes, 210
Uranium mononitride dispersions
development, 146–47
Uranium mononitride particles
production of spherical, 13
Uranium mononitride pastes (Na–UN)
corrosive effects, 101–2
Uranium mononitride powder
sintering, 146, 211
synthesization, 146
Uranium mononitride single crystals (irradiated)
fission-gas-bubble sizes, 210–11
Uranium mononitride solid solutions (UC–UN)
phase relations, U oxide effects on, 77
Uranium mononitride–system powder (UC–UN)
sintering, 211
Uranium mononitride systems (PuC–PuN–UC–UN)
phase studies, 144–45
Uranium mononitride systems (PuN–UN)
phase studies, 144–45
Uranium mononitride systems (PuN–UN) (irradiated)
performance, 77
Uranium mononitride systems (UC–UN)
phase studies, 144–45
Uranium monophosphide
compatibility with Th, 74
modulus of elasticity, 13
properties, 77
synthesis by impaction, 128
UAs solubility in, 77
vapor pressure, 77
Uranium monosulfide
compatibility with Th, 74
UAs solubility in, 77
vapor pressure, 77
Uranium monoxide systems (PuO–UO)
properties and synthesis, 7
Uranium nitride–mixture powders
sintering, 211
Uranium nitride pellets
preparation from powder, 78
Uranium nitride systems (Pu nitride–U nitride)
thermal conductivity and thermal diffusivity, 206–7
Uranium octoxide (irradiated)
swelling, 214
Uranium octoxide dispersions ($Al–U_3O_8$)
development, 141
Uranium octoxide dispersions ($Al–U_3O_8$) (Al clad)(irradiated)
stability, 9
Uranium octoxide dispersions ($Al–U_3O_8$) (irradiated)
swelling, porosity effects on, 74
Uranium oxide
melting point, 11
Uranium oxide (irradiated)
thermal conductivity, 149
Uranium oxide pellets
preparation from powder, 78
Uranium oxide systems (Pu oxide–U oxide)
thermal conductivity and thermal diffusivity, 206
Uranium powder
sintering, 203
Uranium sesquicarbide
energy of formation, 12–13
thermal expansion, 13
Uranium silicide
preparation, 121
Uranium silicide (U_3Si_2)(irradiated)
swelling, 214
Uranium silicide pellets
preparation from powder, 78
Uranium single crystals
preparation, 1
Uranium sulfide
synthesis by impaction, 128
Uranium systems (C–Mo–U)
phase relations, PuC-addition effects on, 77
Uranium systems (C–N–O–U)
thermodynamic properties, 145
Uranium systems (C–O–U)
phase studies, 12
Uranium systems (C–Pu–U)
phase studies, 207–8
Uranium systems (C–Si–U)
phase studies, 144
Uranium systems (C–Ti–U)
phase relations, PuC-addition effects on, 77
Uranium systems (C–U)
ignition, 15
Uranium systems (C–U–Zr)
phase relations, PuC-addition effects on, 77
Uranium systems (H–U)
ignition, 15
Uranium systems (H–U–Zr)
properties, 22
Uranium systems (Fe–Si–U)
phase studies, 69
Uranium systems (irradiated)
swelling, 136–37
Uranium systems (O–Pu–U)
compatibility with Na, 29
Uranium systems (Si–U)
ignition, 15
Uranium systems ($U–UAl_2–UFe_2–UMn_2$)
phase studies, 71
Uranium systems ($U–UO_2$)
phase studies, 136
Uranium tetraboride
compatibility with Th, 74
Uranium tetrafluoride systems ($BeF_2–LiF–ThF_4–UF_4–ZrF_4$)(molten)
corrosive effects, 103
Uranium tetrafluoride systems ($LiF–UF_4$)(molten)
corrosive effects, 103–4
Uranium trialuminide dispersions ($Al–UAl_3$)
swelling, 141
Uranium trichloride eutectics ($KCl–UCl_3$) (molten)
corrosive effects, 31–32
Uranium tubing (clad)
fabrication, 126

V

Valoy
corrosion, 93
oxidation, 93, 231
Vanadium
corrosion, 100, 163, 228
diffusion in Ti–V alloys, 179
metallurgy, 243–44
purification, 194, 243
yield point, Ti effects on, 179
zone melting, 194
Vanadium-alloy sheet (Cr–Ti–V)
tensile properties, 243–44
Vanadium-alloy sheet (Ti–V)
tensile properties, 243–44
Vanadium-alloy tubing (Cr–Ti–V)
burst testing, 181–82
fabrication, 196, 257
tensile properties, 244
Vanadium-alloy tubing (Ti–V)
drawing, 122–23
Vanadium alloys
corrosion, 99, 228, 230
development, 43
ductile–brittle transition, 113
mechanical-property assessment, 194
weldability assessment, 194
Vanadium alloys (Al–Ti–V)
drawing, vibration effects on, 124
reaction with H, 220–21
strength, 43
Vanadium alloys (Al–V)
corrosion, 99
sintering, 230
Vanadium alloys (Cr–Ti–V)
compatibility with PuC–UC mixtures, 73
corrosion, 163, 228
tensile properties, 114
Vanadium alloys (Cr–Ti–V)(irradiated)
tensile properties, 234
Vanadium alloys (Cr–V)
corrosion, 99, 163, 228
Vanadium alloys (Fe–V)
tensile properties, 248
Vanadium alloys (irradiated)
tensile properties, 234
Vanadium alloys (Mo–Ta–V)
phase studies, 243
Vanadium alloys (Mo–V)
corrosion, 99
Vanadium alloys (Nb–Ta–V)
mechanical properties, 242
phase studies, 243
physical properties, 242
strength, 43
Vanadium alloys (Nb–Ti–V)
strength, 43
Vanadium alloys (Nb–V)
corrosion, 164
ductile–brittle transition, 42, 113
elastic properties, 238
mechanical properties, mechanical-twinning effects on, 239
strain hardening, 184
strength, 43
yield point, Ti effects on, 179
Vanadium alloys (Nb–V)(irradiated)
twinning, 172
Vanadium alloys (Ta–V)
solid-state transformations, 243
Vanadium alloys (Ti–V)
corrosion, 99, 163–64, 228
mechanical properties, Na-exposure effects on, 99
production, 122
Ti diffusion in, 179
V diffusion in, 179
Vanadium alloys (Ti–V)(irradiated)
tensile properties, 41, 234
Vanadium alloys (U–V)
grain refinement, 203–4
ignition, 15

mechanical properties, 203-4
Vanadium alloys (V–Zr)
corrosion, 99
Vanadium braze alloys (Ta–Ti–V)
patent for, 199
Vanadium hydride
production, 89
Vanadium monocarbide
reaction with V oxide, 251-52
Vanadium monocarbide systems (C–VC)
eutectic temperature, 186
Vanadium oxide
reaction with VC, 251-52
Vanadium solid solutions (Nb–Ti–V)
oxidation, 95
Vanadium systems (Cr–Fe–Si–Ti–V)
fused-slurry coatings developed from, 161
Vanadium systems (Ti hydride–V)
production, 89
Vessels
(see Pressure vessels)

W

Waspaloy
brazing, 263
mechanical properties, 47
WC-1 Zr
mechanical and physical properties, 240
WC-103
mechanical and physical properties, 240
WC-111
mechanical and physical properties, 242
WC-129Y
mechanical and physical properties, 240
WC-222
mechanical and physical properties, 242
Welding, 199-200, 262
Wires
sintering, 259
Working
cast materials, 122-24
explosive, 127-28
hot and cold, 60-61
Wrought materials
fabrication, 257-59

X

X-34
corrosion, 101
X-280 weld joints
aging effects, 129
X7005
brazing, 262
X8001
corrosion, 94
X radiography, 264

Y

Ytterbium
oxidation, 27
Yttrium
corrosion, 166
fabrication, 123
mechanical behavior, 123
Yttrium-alloy hydrides
cladding with Cr, 156-57
Yttrium alloys (Al–Cr–Fe–Y)
corrosion, 226, 248
metallurgy, 46-47
oxidation, 26-27, 46-47
production of corrosion-resistant, 260
tensile properties, 247-48
Yttrium alloys (Al–Cr–Fe–Y)(irradiated)
embrittlement, 170
mechanical properties, 37
Yttrium alloys (Cr–W–Y)
tensile properties, 237
Yttrium alloys (Cr–Y)
carbide-dispersion effects, 237
Yttrium alloys (Co–Y)
phase studies, 47
Yttrium alloys (Gd–Pu–Y)
phase studies, 139
Yttrium alloys (Mg–Y)
oxidation and strength, 53
Yttrium alloys (Mo–Y)
oxidation, 96
Yttrium alloys (Nd–Pu–Y)
phase studies, 139
Yttrium disilicide
oxidation, 188
Yttrium hydride
cladding with Cr, 156-57
Yttrium hydride (fueled)(Mo–Re-alloy clad)
(irradiated)
performance, 89
Yttrium oxide
O self-diffusion in, 114-15
preparation and sintering, 189
Yttrium rods
fabrication, 123
Yttrium sesquioxide systems (Cr_2O_3–Y_2O_3)
phase studies, 252
Yttrium sesquioxide dispersions (Y_2O_3–Zr)
fabrication and mechanical properties
of sintered, 260
Yttrium single crystals
deformation, 123
Yttrium systems (C–Cr–Hf–Mo–Y–Zr)
tensile properties, 237
Yttrium systems (C–Cr–Hf–Y–Zr)
tensile properties, 237
Yttrium systems (C–Mo–W–Y)
corrosion, 161
Yttrium tubing
fabrication, 123

Z

Zinc oxide
self-diffusion in, 54
Zinc systems (Al–Ge–Si–Zn)
use for brazing, 262
Zircaloy
brazing, 263
crud deposition on, 159
impact properties, 48, 175
plating on, 63-64
pressure bonding, 62
reaction with steam, 32-33
Zircaloy (irradiated)
corrosion, 93
Zircaloy structurals
sizing, 195-96
Zircaloy tubing
explosive sizing, 261
Zircaloy-2
compatibility with Bi–Pb alloy, 30
compatibility with UN, 12
contamination by F, 26
corrosion, 26, 93, 158
hot-press bonding to 1S Al and stainless
steel (416), 197
hydride orientation, 175
hydriding, 31, 93, 230
H terminal solubility in, 47-48
microindentation properties of hydrided,
156
oxidation, 93, 231
oxide-film measurement, 26
oxide films on, potential on, 225
strength, 108
thermal expansion, H effects on, 48
toughness, H effects on, 108-9
Zr hydride-platelet orientation, 245
Zircaloy-2 (hydrided)(irradiated)
impact properties, 39
Zircaloy-2 (irradiated)
corrosion, 158
creep properties, 39, 168
mechanical properties, 232
rupture, 39
tensile properties, 37, 39-40
Zircaloy-2 cladding
hydride embrittlement, 175
Zircaloy-2 cladding (irradiated)
failure, 232
Zircaloy-2 joints (Inconel 600–Zircaloy-2)
(irradiated)
tensile properties, 39-40
Zircaloy-2 single crystals
growth, 196
production, 175
Zircaloy-2 tubing
drawing, 122
mechanical properties, preferred-
orientation effects on, 107-8
texture, fabrication effects on, 108
Zr hydride-platelet orientation, fabrica-
tion effects on, 108
Zircaloy-2 tubing (irradiated)
burst strength, 106, 167-68
Zircaloy-4
corrosion, 158
hydriding, 31, 93, 230
H solubility in, 108
oxidation in steam, 231
thermal conductivity, 107
thermal expansion, H effects on, 48
Zircaloy-4 (irradiated)
mechanical properties, 167
Zircaloy-4 (molten)
reaction with water, 166
Zircaloy-4 sheet
microstructure, 245
tensile properties, 185
Zircaloy-4 tubing
cladding inside with Al and SAP, 195
mechanical properties, 185
properties, 175
Zirconium
anodized films on, electrical conductivity
of, 225
anodizing, 158-59
compatibility with metals, 180
compatibility with UN, 12
corrosion, 95
creep properties, vacuum effects on,
184-85, 244-45
deformation of annealed, 107
ductility, H effects on, 48
embrittlement by Zr hydride platelets, 108
evaluation, 175
fracture of, containing Zr hydride
precipitates, 49
hydride platelets in, 48-49
hydriding, 29, 88
H solubility in, 108
H supersaturation, Nb-addition effects
on, 109
mechanical properties, O effects on, 245
mechanical properties, prestraining
effects on, 106-7
melting, electron-beam, 60
metallurgy, 244-45
oxidation, 93, 158, 231
oxide films on, potential on, 225
properties, 47
reaction with steam, 32, 166-67, 231

structure, tension effects on, 107
surface morphology, 244
tensile properties, 48
thermal expansion, 107
U diffusion in, 135
yield point, 107
zone refining, O and Fe redistribution during, 122
Zirconium (irradiated)
corrosion, 158
creep properties, 168
Zirconium (molten)
reaction with water, 166
Zirconium-alloy sheets (Nb–Zr)
explosive bonding, 64
Zirconium-alloy joints (steel-Zr alloy)
hot pressing, 260
Zirconium-alloy tubing
cladding inside with Al and SAP, 195
Zirconium-alloy tubing (Nb–Zr)
evaluation, 245, 248
fabrication, 196, 258
Zirconium alloys
(see also Valoy, Zircaloy, ZR55, and ZR57)
corrosion, 26, 31, 95, 225, 228-30
evaluation, 175
hydriding, 47-48
mechanical properties, 107
metallurgy, 244-45
oxidation in steam, 231
oxides on, wear of, 225
reactions with H, 23
use for brazing, 263
use for cladding, 175
Zr hydride-platelet formation, 47
Zirconium alloys (Al–Mo–Sn–Zr)
corrosion, 229
Zirconium alloys (Al–Zr)
corrosion, 229
Zirconium alloys (Cr–Fe–Nb–Sn–Zr)
corrosion, 225
Zirconium alloys (Cr–Fe–Zr)
preparation, 122
Zirconium alloys (Cr–Zr)
use for brazing, 263
Zirconium alloys (Cu–Fe–Zr)
hydriding, 230
Zirconium alloys (Cu–Mo–Zr)
corrosion, heat-treatment effects on, 93
Zirconium alloys (Cu–Nb–Zr)(irradiated)
tensile properties, 168
Zirconium alloys (Cu–Zr)
corrosion, 228-29
development, 245
use for brazing, 263
Zirconium alloys (Hf–Ta–Zr)
oxidation, 222
Zirconium alloys (Fe–Ni–Nb–Sn–Zr)
hydriding, 230
Zirconium alloys (Fe–Zr)
use for brazing, 263
Zirconium alloys (irradiated)
behavior, 167
corrosion, 225
hydriding, 225
properties, 232-33
Zirconium alloys (Mn–Zr)
use for brazing, 263
Zirconium alloys (Mo–Nb–Ti–U–Zr)
tensile properties, 137
Zirconium alloys (Mo–Nb–Zr)
phase studies, 111
Zirconium alloys (Mo–Ti–Zr)
corrosion, 161
phase studies, 111
Zirconium alloys (Mo–Zr)
aging, 111
corrosion, 161
recrystallization, fabrication effects on, 258-59
recrystallization temperature, 241
rupture strength, 241
Zirconium alloys (Nb–Re–Zr)
oxidation and scale formation, 95
Zirconium alloys (Nb–Sn–Zr)
corrosion, 93, 225
Zirconium alloys (Nb–Ti–Zr)
corrosion, 164
Zirconium alloys (Nb–W–Zr)
Be-induced second phase, annealing effects on, 111
Zirconium alloys (Nb–U–Zr)
phase transformation, 71
reaction with water, 15
Zirconium alloys (Nb–U–Zr)(Zircaloy-2 clad)(irradiated)
performance, 71
Zirconium alloys (Nb–Zr)
beta-phase decomposition, 51
carbide-layer growth on, 54
C diffusion in, 54
cavitation, 30
coatings for, 162
compatibility with K, 29-30
corrosion, 164-66
creep rate, aging effects on, 176
ductility, 48
hydriding, 31, 93, 230
H supersaturation, 109
mechanical properties, 108-9
mechanical properties, O effects on, 111, 175-76
mechanical properties, Na-exposure effects on, 99
oxidation, 95
oxide films on, potential on, 225
phase transformation, 175
scale formation, 95
strength, Be-addition effects on, 111
thermal expansion, H effects on, 48
Zr hydride-platelet orientation, 109
Zirconium alloys (Nb–Zr)(hydrided)(irradiated)
impact properties, 39
Zirconium alloys (Nb–Zr)(irradiated)
creep properties, 39, 168
tensile properties of heat-treated, 39
Zirconium alloys (Pu–U–Zr)
phase studies, 205
preparation, 205
properties, 138
thermal conductivity, 5
Zirconium alloys (Pu–U–Zr)(Ti–V-alloy clad)(irradiated)
behavior, 138-39
Zirconium alloys (Th–U–Zr)(Zircaloy-2 clad)(irradiated)
behavior, 141, 208
Zirconium alloys (Th–Zr)
hot hardness, 8
Zirconium alloys (Ti–W–Zr)
phase studies, 243
Zirconium alloys (U–Zr)
ignition, 15
structure, 4
Zirconium alloys (V–Zr)
corrosion, 99
Zirconium boride
production, 188
Zirconium carbide
production, 115-16
properties, 115-16
reactions in liquid media, 116-17
stoichiometry, 186
Zirconium carbide systems (U carbide–Zr carbide)
cladding with W by vapor deposition, 63
Zirconium composites (graphite–Zr)
hot pressing, 20
Zirconium composites (Ta–W–Zr)
strength, 183
Zirconium diboride
corrosion, 31
fabrication, 188
grain growth during sintering, 25
hot hardness, 188
oxidation of zone-melted, 117
reactions in liquid media, 116-17
thermal expansion, 223
Zirconium diboride dispersions (stainless steel–UO_2–ZrB_2)(stainless-steel(347) clad)(irradiated)
damage, 208-9
Zirconium diboride-system powders ($MoSi_2$–ZrB_2)
sintering, 188
Zirconium diboride systems (Cr–TaB_2–ZrB_2)
fabrication and properties, 252
Zirconium dioxide
bonding with H_2PO_3F, 115
extrusion, 123, 126
reaction with ZrC, 251-52
Zirconium dioxide composites (W–ZrO_2)
strength, 183
Zirconium dioxide dispersions (Al–UO_2–ZrO_2)(Al clad)(irradiated)
stability, 9
Zirconium dioxide films
crack and pore measurement and potential on, 225
Zirconium dioxide films (irradiated)
embrittlement, 232
Zirconium dioxide microspheres
preparation, 12
Zirconium dioxide-system rods (CaO–UO_2–ZrO_2)
fabrication, 12
Zirconium dioxide-system rods (UO_2–ZrO_2)
fabrication, 12
Zirconium dioxide systems (CaO–UO_2–ZrO_2)
thermal conductivity, 143
Zirconium dioxide systems (UO_2–ZrO_2)
thermal conductivity, 143
Zirconium dispersions (Y_2O_3–Zr)
fabrication and mechanical properties of sintered, 260
Zirconium hydride
compatibility with LiH, 221
H absorption in porous beds of, 156
tensile properties, 48
Zirconium hydride (Al–Cr–Fe-alloy clad)
testing, 88
Zirconium hydride platelets
in Zr, 48-49
orientation in Zircaloy-2, 245
Zirconium intermetallic compounds
reactions with H, 23
Zirconium monocarbide
C diffusion in, 179
elastic properties, 115, 186
properties, 249-51
reactions in liquid media, 116
reaction with ZrO_2, 251-52
Zirconium monocarbide (irradiated)
behavior, 187-88
Zirconium monocarbide castings
hot hardness, 59, 250
oxidation, 59, 250-51
Zirconium monocarbide coatings
deposition on fuel particles, 142
Zirconium monocarbide plates
fabrication, 186
Zirconium monocarbide-system castings (C–ZrC)
hardness and stress-relieving, 186

Zirconium monocarbide-system particles (UC–ZrC)(PyC coated)
use at high temperatures, 142
Zirconium monocarbide systems (C–ZrC)
eutectic temperature, 186
melting and casting, 257
properties, 257
Zirconium monocarbide systems (HfC–ZrC)
fusion point, 250-51
Zirconium monocarbide systems (NbC–ZrC)
Hall constant and resistivity, 250
Zirconium monocarbide systems (TaC–ZrC)
fusion point, 250-51
Zirconium monocarbide systems (UC–ZrC)
preparation, 211
production, 13
reactions with Mo, Re, Re–W alloy, and W, 145
Zirconium monocarbide systems (UC–ZrC) (refractory-material clad)
diffusion, 54
Zirconium monocarbide systems (UC–ZrC) (W clad)
electron emission, 145
Zirconium nitride
reactions in liquid media, 116-17
Zirconium single crystals
oxidation, 26
Zirconium systems (C–Cr–Hf–Mo–Y–Zr)
tensile properties, 237
Zirconium systems (C–Cr–Hf–Y–Zr)
tensile properties, 237
Zirconium systems (C–Nb–Zr)
phase studies, 51
Zirconium systems (C–W–Zr)
fabrication and preparation, 52
Zirconium systems (C–U–Zr)
phase relations, PuC-addition effects on, 77
Zirconium systems (C–Zr)
production and properties, 115-16
Zirconium systems (H–Nb–Zr)
phase studies, 22-23
Zirconium systems (H–N–Zr)
phase studies, 89
Zirconium systems (H–U–Zr)
properties, 22
Zirconium systems (Si–Zr)
use for brazing, 263
Zirconium tetrafluoride systems (BeF_2–LiF–ThF_4–UF_4–ZrF_4)(molten)
corrosive effects, 103
Zirconium tubing
drawing, 122
Zone refiner
characteristics of electron-beam, 194
ZR55
fatigue properties, 114
ZR57
fatigue properties, 114

LEGAL NOTICE

This journal was prepared under the sponsorship of the U. S. Atomic Energy Commission. Neither the United States, nor the Commission, nor any person acting on behalf of the Commission:

A. Makes any warranty or representation, expressed or implied, with respect to the accuracy, completeness, or usefulness of the information contained in this journal, or that the use of any information, apparatus, method, or process disclosed in this journal may not infringe privately owned rights; or

B. Assumes any liabilities with respect to the use of, or for damages resulting from the use of any information, apparatus, method, or process disclosed in this journal.

As used in the above, "person acting on behalf of the Commission" includes any employee or contractor of the Commission, or employee of such contractor, to the extent that such employee or contractor of the Commission, or employee of such contractor prepares, disseminates, or provides access to, any information pursuant to his employment or contract with the Commission, or his employment with such contractor.

NUCLEAR SCIENCE ABSTRACTS

The U. S. Atomic Energy Commission, Division of Technical Information, publishes *Nuclear Science Abstracts* (*NSA*), a semimonthly journal containing abstracts of the literature of nuclear science and engineering.

NSA covers (1) research reports of the U. S. Atomic Energy Commission and its contractors; (2) research reports of government agencies, universities, and industrial research organizations on a worldwide basis; and (3) translations, patents, books, and articles appearing in technical and scientific journals.

Complete indexes covering subject, author, source, and report number are included in each issue. These are cumulated quarterly, semiannually, and annually providing a detailed and convenient key to the literature.

Availability of *NSA*

SALE *NSA* is available on subscription from the Superintendent of Documents, U. S. Government Printing Office, Washington, D. C., 20402, at $30.00 per year for the semimonthly abstract issues and $22.00 per year for the four cumulated-index issues. Subscriptions are postpaid within the United States, Canada, Mexico, and all Central and South American countries, except Argentina, Brazil, Guyana, French Guiana, Surinam, and British Honduras. Subscribers in these Central and South American countries, and in all other countries throughout the world, should remit $37.00 per year for subscriptions to semimonthly abstract issues and $25.00 per year for the four cumulated-index issues.

EXCHANGE *NSA* is also available on an exchange basis to universities, research institutions, industrial firms, and publishers of scientific information. Inquiries should be directed to the Division of Technical Information Extension, U. S. Atomic Energy Commission, P. O. Box 62, Oak Ridge, Tennessee, 37830.

TECHNICAL PROGRESS REVIEWS may be purchased from Superintendent of Documents, U. S. Government Printing Office, Washington, D. C., 20402. *Nuclear Safety* at $3.50 per year (six issues) for each subscription or $0.60 per issue; each of the other journals at $2.50 per year (four issues) or $0.70 per issue. The use of the coupon below will facilitate the handling of your order.

POSTAGE AND REMITTANCE: Postpaid within the United States, Canada, Mexico, and all Central and South American countries except Argentina, Brazil, Guyana, French Guiana, Surinam, and British Honduras. For these Central and South American countries and all other countries: add, for each annual subscription, $1.00 for *Nuclear Safety* and $0.75 for each of the other journals; for single issues, add one-fourth of the single-issue price. Payment should be by check, money order, or document coupons, and MUST accompany order. Remittances from foreign countries should be made by international money order or draft on an American bank payable to the Superintendent of Documents or by UNESCO book coupons.

order form

SUPERINTENDENT OF DOCUMENTS
U. S. GOVERNMENT PRINTING OFFICE
WASHINGTON, D. C., 20402

Enclosed:

document coupons ☐ check ☐ money order ☐

Charge to Superintendent of Documents No. _____

Please send a one-year subscription to

☐ ISOTOPES AND RADIATION TECHNOLOGY
☐ NUCLEAR SAFETY
☐ REACTOR AND FUEL-PROCESSING TECHNOLOGY
☐ REACTOR MATERIALS

SUPERINTENDENT OF DOCUMENTS
U. S. GOVERNMENT PRINTING OFFICE
WASHINGTON, D. C., 20402

(Print clearly)

_____
Name

_____
Street
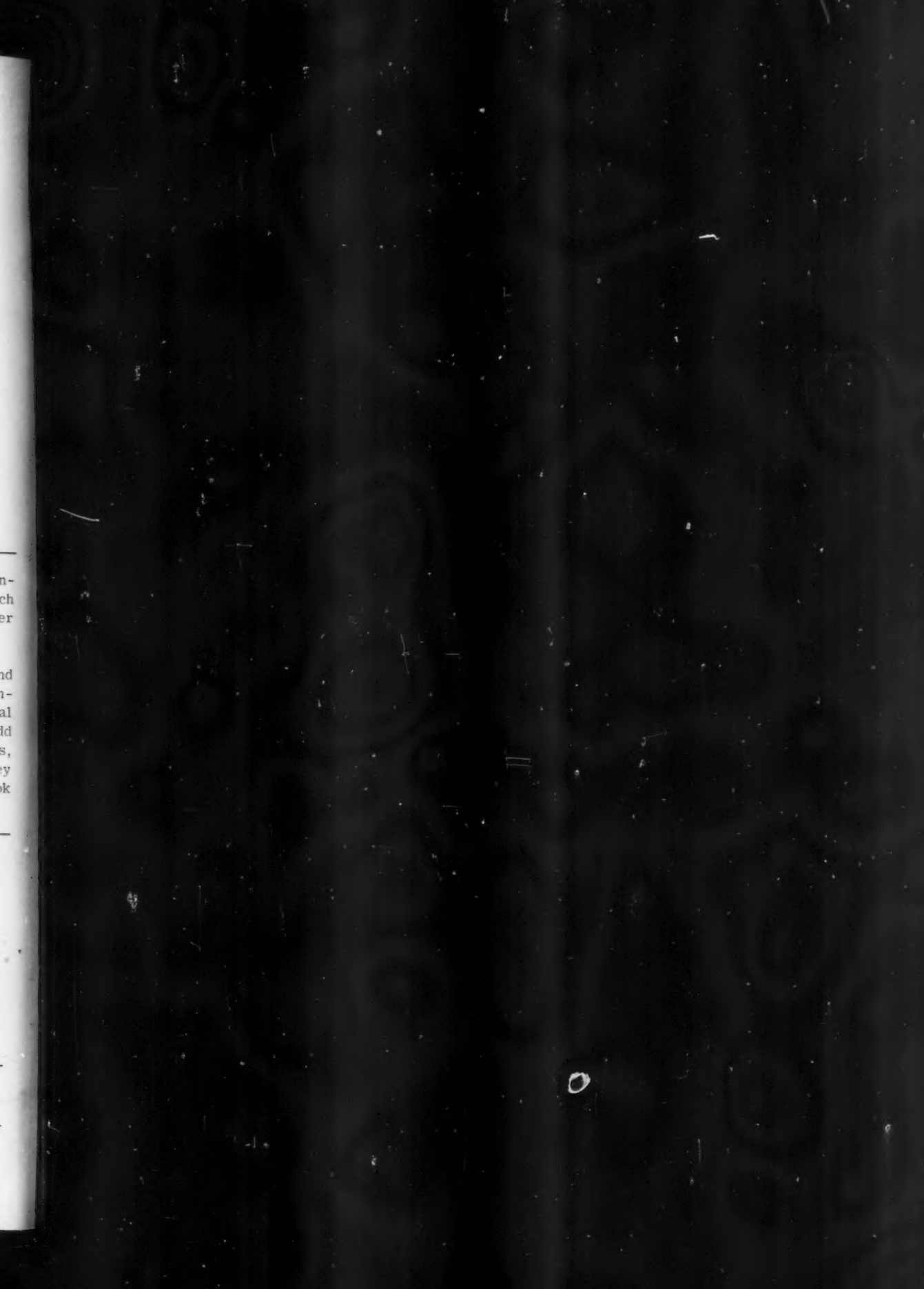
_____
City, State, ZIP Code